GKSS
FORSCHUNGSZENTRUM
in der HELMHOLTZ-GEMEINSCHAFT

Local Reinforcement of Magnesium Components by Friction Processing: Determination of Bonding Mechanisms and Assessment of Joint Properties

(Vom Promotionausschuss der Technischen Universität Hamburg-Harburg als Dissertation angenommene Arbeit)

Author:
G.A. Pinheiro

ISSN 0344-9629

HELMHOLTZ
| GEMEINSCHAFT

wissen
schafft
nutzen

GKSS 2008/12

GKSS 2008/12

Local Reinforcement of Magnesium Components by Friction Processing: Determination of Bonding Mechanisms and Assessment of Joint Properties

(Vom Promotionausschuss der Technischen Universität Hamburg-Harburg als Dissertation angenommene Arbeit)

Author:

G. A. Pinheiro

(Institute of Materials Research)

GKSS-Forschungszentrum Geesthacht GmbH · Geesthacht · 2008

Die Berichte der GKSS werden kostenlos abgegeben.
The delivery of the GKSS reports is free of charge.

Anforderungen/Requests:

GKSS-Forschungszentrum Geesthacht GmbH
Bibliothek/Library
Postfach 11 60
21494 Geesthacht
Germany
Fax.: +49 4152 87-17 17

Als Manuskript vervielfältigt.

ISSN 0344-9629

GKSS-Forschungszentrum Geesthacht GmbH · Telefon (04152) 87-0
Max-Planck-Straße 1 · 21502 Geesthacht / Postfach 11 60 · 21494 Geesthacht

GKSS 2008/12

Local Reinforcement of Magnesium Components by Friction Processing: Determination of Bonding Mechanisms and Assessment of Joint Properties

(Vom Promotionausschuss der Technischen Universität Hamburg-Harburg als Dissertation angenommene Arbeit)

Gustavo Alves Pinheiro

189 pages with 103 figures and 32 tables

Abstract

The development of new creep-resistant and cost effective die casting magnesium alloys, such as AE, MRI, MEZ, ACM, AXJ, AJ, WE, have emerged as an alternative, to fulfil the modern demands in structurally relevant applications, such as engine blocks, gears and converter boxes. However, in most cases, magnesium components are screwed with aluminium and steel bolts, which lead the screwed joints to lose the preload force, due to relaxation. This barrier thereby limits the broad use of magnesium within this segment and should somehow find an adequate solution to help overcome this limitation. Furthermore, together with alloy development and the addition of reinforcement (MMCs), local material engineering processes have been conceived and are considered a method to improve the properties and therefore expand the number of potential applications for magnesium alloys. In this context, Friction Welding (FW) and particularly Friction Hydro Pillar Processing (FHPP), which can be described as a drill and fill process, appear to be an alternative to make the use of magnesium more widespread. For this reason, FHPP is intended to be used, to locally reinforce the mechanically fastened magnesium components. With this approach, regions submitted to the stresses imposed by tightening forces can be compensated by the use of a material with superior properties. It is not required to fabricate the whole structure from an expensive material, thus saving costs and thereby satisfying the economic pressures of an increasingly competitive global market.

In the present work, a preliminary experimental matrix was defined and used to determine the optimal welding conditions for each specific material combination selected. Further, elaborate experimental techniques are used to describe the process parameters-microstructure-properties relationships and the consequent mechanisms leading to bonding in FHPP welds in similar and dissimilar configurations. The welds were performed using a hydraulic powered friction welding machine, originally designed and built as a portable stud welding unit, delivering up to 40 kN welding force and 8000 rpm. All welds were monitored, analysed and evaluated using a purpose-built data recording system. AZ91, AE42 and MRI230D magnesium grades were used in the experimental programme. The results obtained in the course of this study have shown the feasibility of FHPP to produce high strength welds with mechanical properties comparable to those of the base material. Defects, such as porosity or lack of bonding, were not observed. Furthermore, the welding pressure rather than the upsetting was found to have a major influence in the final weldment. The influence of process parameters on heat generation and bonding quality is similar to that known from rotational friction welding. It could be demonstrated that for dissimilar MRI230D to AZ91D and for similar AZ91D to AZ91D welds, the consumable member is fully plasticised across the bore of the hole and throughout the thickness of the workpiece. However, for AE42 to AZ91D welds, the stud was not completely plasticised across the bore of the hole and significant microstructural changes were restricted to a narrow area around the bonding line. Hardness profiles indicate a substantial reduction in scattering, as soon as the stud material is reached. Hardening or softening phenomena were not observed. Transverse tensile and pull-out testing confirmed the feasibility of the process to produce high strength welds, with failures taking place outside the welded area in most of the cases. Joint performance, in terms of creep and bolt load retention, was also tested and showed promising results. Although creep properties were demonstrated to be inferior within the extruded material, in comparison with the base materials (BM), the creep resistances of reinforced samples were always superior to those of purely unreinforced AZ91D-T6. The strength of the reinforced joint in both tensile and compressive BLR tests was elevated relative to the BM, achieving in some cases 93 % of BM values.

Lokale Verstärkung von Magnesiumkomponenten mittels „Friction Hydro Pillar Processing": Bestimmung der Bindemechanismen und Bewertung der Verbindungseigenschaften

Zusammenfassung

Die Entwicklung neuer kriechbeständiger und kostengünstiger Magnesiumdruckgusslegierungen wie AE, MRI, MEZ, ACM, AXJ, AJ und WE hat sich als Alternative zur Erfüllung der tatsächlichen Forderungen der strukturell relevanten Anwendungen, wie bei Motorblöcken und Getrieben, erwiesen. Allerdings sind Magnesiumbauteile in den meisten Fällen mit Aluminium- und Stahlschrauben zu verschrauben. Die unterschiedlichen thermischen Eigenschaften führen bei den betriebsbedingten Lastwechseln dazu, dass die verschraubte Verbindung aufgrund der Relaxation die Vorspannkraft verliert. Diese Problematik begrenzt damit die Verbreitung von Magnesiumlegierungen in diesem Segment. Legierungsentwicklung und Partikelverstärkung (MMCs) sowie lokale Werkstoffprozesse wurden in letzter Zeit als Methoden zur Verbesserung der Eigenschaften entwickelt. In diesem Zusammenhang stellt sich das Reibschweißen besonders in Form des Friction Hydro Pillar Processing (FHPP) als eine der modernsten und geeignetesten Option vor. In diesem Schweißverfahren wird ein Bolzen unter Rotation in eine Bohrung eingeführt. An der Kontaktstelle wird aufgrund des aufgebrachten hohen axialen Drucks Reibungshitze generiert. Das Bolzenmaterial wird dadurch plastifiziert und durch die örtlichen hohen Temperaturen eine metallische Verbindung zum Grundmaterial hergestellt. Das Ziel dieser hier dargestellten Arbeit ist die lokale Verstärkung von Magnesiumbauteilen mittels Einbringen einer festeren Magnesiumlegierung (GKSS-Patent n°. 816 p Gk 3.03). Durch diesen Ansatz können die einwirkenden Kräfte im beanspruchten Bereich durch die Einbringung eines Werkstoffs mit festeren mechanischen Eigenschaften besser aufgenommen werden. Einerseits muss die ganze Struktur nicht aus einem teuren Material hergestellt werden, und andererseits können Kosten eingespart werden, um sich dem wirtschaftlichen Druck eines zunehmend wettbewerbsorientierten globalen Marktes anzupassen.

In der vorliegenden Arbeit wurde in erster Linie ein Schweißparameterbereich definiert und untersucht, um die optimalen Schweißbedingungen für jede spezifische Materialkombination festzustellen. Außerdem wurden experimentelle Techniken zur Beschreibung der Korrelationen zwischen den Prozessparametern, Mikrostruktur sowie der daraus resultierenden mechanischen Eigenschaften und den zugrunde liegenden Bindemechanismen in FHPP-Schweißnähten in artgleichen und -ungleichen Konfigurationen. Die Schweißungen wurden mit einer hydraulischen Reibschweißmaschine, welche ursprünglich als portable Bolzenschweißeinheit ausgelegt wurde, durchgeführt. Sie generiert eine axiale Schweißkraft bis zu 40 kN bei einer Drehzahl bis zu 8000 U/min. Alle Schweißungen wurden mit einem speziell dafür entwickelten Datenaufzeichnungsgerät überwacht, analysiert und bewertet. Die Magnesiumlegierungen AZ91, AE42 und MRI230D wurden in dem experimentellen Programm untersucht. Die Ergebnisse, die im Verlauf dieser Studie gewonnen wurden, haben gezeigt, dass mittels FHPP hochfeste Schweißungen mit mechanischen Eigenschaften, vergleichbar denen des höherfesten Grundwerkstoffs produziert werden können. Schweißfehler, wie Porositäten oder Bindedefekte, konnten nicht beobachtet werden. Die axiale Schweißkraft weist dabei einen wesentlich größeren Einfluss als die Gesamtverkürzung auf die Qualität der Schweißung auf. Der Einfluss von Prozessparametern auf die Wärmeerzeugung und Bindungseigenschaften erwies sich als vergleichbar zu den beim Rotations-Reibschweißen beobachteten Effekten. Für artungleiche Verbindungen MRI230D auf AZ91D und für artgleiche AZ91D-Verbindungen konnte die vollständige Plastifizierung des Verstärkungsmaterials über den gesamten Verbindungsquerschnitt nachgewiesen werden. Im Gegensatz dazu wurde für die artungleiche Verbindung AE42 auf AZ91D keine vollständige Plastifizierung erreicht. In diesem Fall konnten lediglich in einem engen Bereich um die Bindelinie deutliche mikrostrukturelle Veränderungen beobachtet werden. Härteprofile zeigen eine deutliche Reduzierung der Streuung, sobald das extrudierte Material erreicht wird. Härt- oder Erweichungsphänomene wurden nicht festgestellt. Querzug- und Pull-out-Tests bestätigten die Tauglichkeit des Verfahrens zur Herstellung von Schweißverbindungen hoher Festigkeit. Das Versagen erfolgte in den meisten Fällen außerhalb des geschweißten Bereiches. Die Belastbarkeit der Verbindungen in Bezug auf Kriech- und Spannungsrelaxationsbeständigkeit wurde getestet und zeigte viel versprechende Ergebnisse. Obwohl die Kriecheigenschaften der extrudierten Materialien nicht die der Ausgangswerkstoffe erreichten, konnte ein deutlich erhöhter Kriechwiderstand der verstärkten Proben gegenüber dem reinen unverstärkten AZ91D-T6-Grundmaterial nachgewiesen werden. Die Festigkeit der verstärkten Verbindungen, relativ zu den Grundwerkstoffen während des Spannungsrelaxationstests sowohl unter Zug- als auch Druckbelastung, erreichte in einigen Fällen 93 % der Werte der Grundwerkstoffe der Verstärkungsmaterialien.

Manuscript received / Manuskripteingang in TKP: 12. Dezember 2008

List of Symbols and Abbreviations

AZAZ-1C Weld designated to metallurgical characterisation according to condition "1" described in Table 4.10

AZAZ-2C Weld designated to metallurgical characterisation according to condition "2" described in Table 4.10

AZAZ-3C Weld designated to metallurgical characterisation according to condition "3" described in Table 4.10

AZAZ-06/12 Series of joints welded using 06 mm studs/holes (tip and bottom hole diameter respectively) and 12 mm upsetting

AZAZ-08/10 Series of joints welded using 08 mm studs/holes (tip and bottom hole diameter respectively) and 10 mm upsetting

AZAZ-08/20 Series of joints welded using 08 mm studs/holes (tip and bottom hole diameter respectively) and 20 mm upsetting

AEAZ Dissimilar joints using AE42 studs welded with AZ91D-T6 base plates (8 mm stud tip diameter / 10 mm and 20 mm upsetting)

AZAZ Similar joints using AZ91D-T6 studs welded with AZ91D-T6 base plates (8 mm stud tip diameter / 10 mm and 20 mm upsetting)

MRIAZ Dissimilar joints using MRI230D studs welded with AZ91D-T6 base plates (8 mm stud tip diameter / 10 mm and 20 mm upsetting)

AWS American Welding Society

BL Bonding Line

BP Base Plate - The lower stationary AZ91D-T6 workpiece

BLR Bolt Load Retention (Test)

BM Base Material

DAS Data Acquisition System

DRX Dynamic Recrystallisation

EDS Energy dispersive spectroscopy

FP Forging Pressure

HAZ	Heat Affected Zone
R	Radius of the workpiece/stud
RS	Rotational Speed
RZ	Recrystallised Zone
TMAZ	Thermo-mechanical Affected Zone
UPS	Upsetting
WP	Welding Pressure

1 INTRODUCTION

Since after the Second World War, when its consumption slumped from 228,000 to 10,000 tons per annum, magnesium again appears strongly placed among the new innovative materials [1]. In recent years, magnesium alloys have gained increasing interest in different branches of industry. This interest can be attributed to the fact that the material has overcome some of its old barriers, as the fairly high base material prices somehow limited to a few technical alloys and associated with some costly recycling possibilities [2,3]. Over recent years the industrial output of magnesium alloys has been rising almost 20 % per year [4]. This increasing application of lightweight alloys particularly matches the interests of the automotive industry, with its goal of reducing the weight of vehicles to make them more fuel efficient [5]. In this context, several new Mg alloys for different applications have been developed recently, with the intention of obtaining an adequate combination of various properties. Evidently, a perfect combination of creep resistance, castability, mechanical properties, corrosion resistance and affordable cost is rarely achieved and most of the alloys can only address some of the required properties and performance.

The shift from air-cooled to water-cooled engines in the 1970s dramatically reduced the use of magnesium alloys. The existing AZ and AM series are not suitable for manufacturing drive train parts, which operate at temperatures above 130 °C. Aluminium-silicon and aluminium-rare-earths based creep resistant alloys developed in the 1970s and 80s also have not found their place in powertrain applications, for various reasons such as poor castability and corrosion resistance, increased costs and low strength. However, the development of new creep resistant and cost effective die cast magnesium alloys, primarily based on the use of Al, RE, Mn, Ca, Sr, Zr as alloying elements, has emerged as an alternative to fulfil modern demands in other structurally relevant applications, such as engine blocks, gears and converter boxes [6]. Consequently, more and more components have been fabricated using magnesium and its alloys. Table 1.1 and Table 1.2 list the present situation concerning the application of magnesium within the automotive industry, whereas Table 1.3 estimates the foreseen consumption of magnesium in 2015.

Table 1.1: Current applications in the automotive industry.

INTERIOR	***EXTERIOR***	
Seat and components	Engine hood	
Instrument panel and beams	Roof panels	
Knee bolsters	Rear deck lid	
Pedal brackets	Radiator support [(1)]	
Air bag retainers	Grill opening support	
Sunroof components	***ENGINE***	***DRIVE TRAIN***
Mirror brackets	Cylinder head covers	Manual transmission housing
Headlight retainers	Intake manifold	4WD transfer case
Inner door frames	Engine block	Automatic transmission
Support pillars	Oil pan	
Steering column components	Starter-Alternator housing	

[(1)] Highlighted columns are under development

Table 1.2: Vehicle platforms with high magnesium content [4,7].

Vehicle Platform	***Content per vehicle***
Volvo LCP 2000	49kg
Ford PNGV P2000	38kg
GM full size vans (Savana/Express)	Up to 26.3kg
Daimler Benz SL	17 to 23kg
GM minivans (Safari e Astro)	Up to 16.7kg
Ford F-150 truck	14.9kg
VW Passat, Audi A6/A4	13.6kg to 14.5kg
Porsche Boxter Roadster	9.9kg
Buick Park Avenue	9.5kg
Alfa Romeo 156	9.3kg
Daimler Benz SLK Roadster	7.7kg
Chrysler minivans	5.8kg

Table 1.3: Magnesium use forecast in the automotive industry [8].

2000	***2005***	***2015***
140,000 tons	240,000 tons	600,000 tons

In most of the cases, magnesium alloys need to be mechanically fastened, not only in a similar, but sometimes in a dissimilar configuration, by means of screws of different materials. In consideration of the elevated operating temperatures experienced by engine blocks and powertrain components, the creep resistance of magnesium alloys remains a major issue for such applications. In the literature, it has been reported that the use of aluminium and steel screws in magnesium components lead the screwed joint to lose the preload force, due to relaxation [9,10]. This barrier thus limits the broad use of magnesium within this segment and needs somehow to find an adequate solution to help overcome this limitation.

Furthermore, together with alloy development and the addition of reinforcement (MMCs), local material engineering processes have been conceived and are considered a good method to improve the properties and therefore expand the number of potential applications for magnesium alloys. In this context, Friction Welding (FW) and particularly Friction Hydro Pillar Processing (FHPP), which can be described as a drill and fill process, appear to be an alternative to make the use of magnesium more widespread. Although specialised literature involving FW on magnesium alloys has not expressly contributed to the development of this work and no literature on FHPP of lightweight alloys has been found, FHPP is intended to be used to locally reinforce mechanical fastened magnesium components. With this approach, the regions submitted to the stresses imposed by the tightening forces can be compensated by the use of a material with superior properties. It is therefore not necessary to fabricate the whole structure from an expensive material, thereby saving costs and addressing the economic pressures of an increasingly competitive global market.

Due to the current problems involving Mg bolted joints, there is an evident need for research into alternative solutions. Hence the overall objective is to locally reinforce Mg components through the welding of high creep resistance inserts (studs) to be used in automotive applications. Within this overall objective, some specific aims can be defined as follows:

- To describe the bonding formation mechanisms in FHPP of Mg alloys, based on the behaviour of different material combinations and welding parameters, leading to an understanding of the microstructural changes during welding;

- To characterise the base materials (BMs) in terms of structures and properties, in order to compare and evaluate the local reinforcement properties based on the base material's mechanical behaviour. Further, a correlation of BM microstructure/process/final microstructure is also intended to be done;

- To determine the local mechanical properties in terms of microhardness, pull-out and transverse tensile tests, to provide an analysis of the joint performance, based on microstructural development and the joint's formation mechanism;

- To generate knowledge from process data, such as process stability, thermal cycle and microstructural evolution, not only to evaluate the general reliability of the process, but also to validate further modelling and simulations;

- To estimate component performance, based on testing of bolted joints.

By fulfilling the above mentioned objectives, it is intended to propose to the scientific community a joint formation mechanism based on FHPP of Mg alloys, discussing both the microstructural and the respective performance changes imposed by the process. As a result, it is also intended to provide the industry with an alternative reinforcement process, applicable to a wide range of materials, which may contribute to the widespread use of Mg and its alloys.

2 STATE OF THE ART

2.1 GENERAL METAL CHARACTERISTICS

Mg and its alloys, as engineering metals, have always attracted great interest from the industry. This attraction can be attributed not only to its high specific strength, good machinability, excellent castability and suitability for high pressure die casting, but also to its good weldability under a controlled atmosphere, high damping properties, the possibility of recycling and relatively good corrosion resistance with high purity alloys [1,2,11]. However, poor cold workabilities, low corrosion resistance, high solidification shrinkage (in casting alloys), low toughness and high notch sensitivity as well as their high thermal expansion coefficients are often used as an argument against the utilisation of Mg alloys. Nevertheless, attempts have been made not only to improve the characteristic profile of Mg alloys, by employing different alloying elements, but also to develop new manufacturing/engineering techniques, which would definitely assure its insertion into the market.

Mg alloys are available in different forms, including cast and wrought. Die casting provides a good balance between the quality and cost of Mg products and are in most cases incorporated into vehicles in the form of complex structures with few final fabrication steps. Wrought products are still expensive, exhibit poor cold workability at room temperature, due to the limited number of glide systems and the formation of twins, although some wrought alloys containing zinc or lithium have demonstrated a significant increase in both ductility and mechanical properties [12]. However, since Mg is envisaged for use in parts with high safety concerns, there has been a noticeable increase in interest in wrought alloys in the industry, where casting may not work as well or needs to be joined [13]. Furthermore, Mg alloys have a closely packed hexagonal crystalline structure that makes its formability very difficult. However, at slightly elevated temperatures (200 °C to 300 °C) these materials can be easily formed and severely worked. The most popular physical attribute of Mg and its alloys is certainly its light weight and its high strength-to-weight ratios. Its weight is significantly lower when compared with Al and steels. Additionally, Mg has a relatively low heat of fusion and a high coefficient of thermal expansion. Such properties aid in casting, but the distortion during welding can be high [14].

Various mechanical properties of Mg determine how it will perform in particular applications. Table 2.1 summarises its physical characteristics compared with other common structural materials, and Table 2.2 lists its mechanical properties. In the latter, the competitiveness of Mg and its alloys in comparison with Al and steel products is clearly demonstrated when the specific properties are considered.

Table 2.1: Physical properties of common structural materials and its alloys [15,16].

Alloy	Density [Kg/m^3]	Melting Point [ºC]	CTE [µm/m-ºC]	Thermal Conductivity [W/m-K]	Electrical Resistivity [x10^{-9}Ωm]	Elastic Modulus [GPa]
Mg	1740	649	26.1	159	43.9	44
Al	2700	660	24	210	26.5	68
Iron	7870	1535	12.2	76.2	96.1	200
Copper	8960	1083	16.4	385	16.8	110
AZ91D-T6	1810	Min. 421	26	72.7	129	44.8
AE42-F	1800	594 - 626	26	---	---	45
AZ31	1770	605 - 630	26	96	92	45
Al2024-T6	2780	502 - 638	23.2	151	34.9	72.4
Al6082-T6	2700	555	24	180	---	70
AISI1040(1)	7845	1520	12.5	51.5	221	200

(1) Annealed

In general, Mg alloys tend to undergo a severe reduction in strength at elevated temperatures. However, alloys containing relatively expensive elements have shown superior performance at higher service temperatures [17-20] and are therefore designated to applications where temperature should be considered. Examples of grades belonging to this group of high temperature resistant alloys are the sand or permanent mould casting alloys containing zirconium, silver (QE22), scandium (MgScMn), yttrium (WE43 and WE54), thorium (HZ32, ZH62) and even heavy elements like gadolinium and dysprosium. These alloys require heat treatment to the T6 condition. However, some high pressure die casting alloys containing Ca and a combination of other rare earth mixtures (AE42, AE44, AS+RE) are also suitable to high temperature applications, and in these cases a further heat treatment is not required or even not possible. Ductility of Mg alloys is comparable with that of Al and substantially lower than that of steel at room temperature, but at elevated temperatures its ductility increases significantly. On the other hand damping capacity is one of the great attributes of Mg alloys in automotive applications.

Table 2.2: Mechanical properties of common structural materials and its alloys [15,16].

Alloy	Density [Kg/m^3]	Elastic Modulus		Yield Strength		UTS	
		E [GPa]	$E_{spec.}$ [km]	Rp [MPa]	$Rp_{spec.}$ [km]	Rm [MPa]	$Rm_{spec.}$ [km]
Mg	1740	44	2.58×10^6	21	1.23×10^3	90	5.27×10^3
Al	2700	68	2.57×10^6	98	3.70×10^3	118	4.46×10^3
Iron	7870	200	2.59×10^6	130	1.68×10^3	262	3.39×10^3
Copper	8960	115	1.31×10^6	62	0.70×10^3	170	1.93×10^3
AZ91D-T6 (chill cast)	1800	45	2.55×10^6	110	6.23×10^3	160	9.06×10^3
AZ91D-T6 (die cast)	1800	45	2.55×10^6	160	***9.06×10^3***	230	***13.0×10^3***
AE42-F	1800	45	2.55×10^6	135	***7.65×10^3***	240	***13.6×10^3***
AlSi8Cu3 (chill cast)	2700	70	2.64×10^6	160	6.04×10^3	220	8.31×10^3
AlSi8Cu3 (die cast)	2700	70	2.64×10^6	240	***9.06×10^3***	310	***11.7×10^3***
AZ31	1800	45	2.55×10^6	155	***8.78×10^3***	240	***13.6×10^3***
Al2024-O	2780	72.4	2.65×10^6	75.8	2.78×10^3	186	6.82×10^3
Al2024-T6	2780	72:4	2.65×10^6	345	***12.7×10^3***	427	***15.7×10^3***
Al6082-T6	2700	72.4	2.73×10^6	255	***9.63×10^3***	300	***11.3×10^3***
AISI1020(2)	7870	200	2.59×10^6	295	3.82×10^3	395	5.12×10^3
AISI1040(2)	7845	200	2.60×10^6	350	4.55×10^3	515	6.69×10^3

(1) Specific properties are related to density and the gravitational constant

(2) Annealed

(3) Green and yellow highlighted fields are defined for cast and wrought alloys respectively

2.2 NOMENCLATURE AND ALLOYING ELEMENTS

Similar to other materials, pure Mg is rarely utilised in industrial applications. Usually, it is applied in combination with several others elements, which improve or give to an Mg-based product the desired property.

Although it is known worldwide and extensively reported in the literature, no international system for designating magnesium alloys exists. However, there has been a trend towards adopting the naming method used by the American Society for Testing and Materials (ASTM) for Mg alloys. Since the ASTM nomenclature is well-known, not much effort is going to be put in the present work to explain it. Basically, each alloy is assigned with letters indicating the main alloy elements, followed by

numbers that indicate their respective percentages by weight. The final letters indicates the stage of development of the alloy (A, B, C, etc.) and the heat treatment. This final heat treatment code has to be separated from the rest of the designation by a hyphen. Those codes, as well as ASTM standardisation for the nomenclature of Mg alloys, are listed in Table 2.3. Figure 2.1 illustrates a schematic of the most used grades with their most common alloying elements. The influence of each element on the final properties of a grade is well described in the literature and so will not be discussed within this review [2,8,14].

Table 2.3: ASTM codes for Mg's alloying and heat treatment designations [14].

ASTM CODES		**HEAT TREATMENT DESIGNATIONS**	
AL(1)	**AE(2)**	**Designation**	**Heat-Treatment**
A	aluminium	**F**	As fabricated.
B	bismuth	**O**	Annealed, recrystallised (wrought alloys only).
C	copper		
D	cadmium	**H3**	Strain hardened and then stabilised.
E	rare earths	**H10 / H11**	Slightly strain hardened.
F	iron	**H23 / H24 / H26**	Strain hardened and partially annealed.
H	thorium	**T**	Thermally treated to produce stable tempers.
J	strontium		
K	zirconium	**W**	Solution heat-treated (unstable temper).
L	lithium	**T1**	Cooled and naturally aged.
M	manganese	**T2**	Annealed (cast products only)
N	nickel	**T3**	Solution heat-treated and then cold worked.
P	lead	**T4**	Solution heat-treated.
Q	silver	**T5**	Cooled and artificially aged.
R	chromium	**T6**	Solution heat-treated and artificially aged.
S	silicon	**T7**	Solution heat-treated and stabilised.
T	tin	**T8**	Solution heat-treated, cold worked and artificially aged.
W	yttrium		
X	calcium	**T9**	Solution heat-treated, artificially aged and cold-worked.
Y	antimony		
Z	zinc	**T10**	Cooled, artificially aged and cold-worked.

(1) Abbreviation Letter

(2) Alloying Element

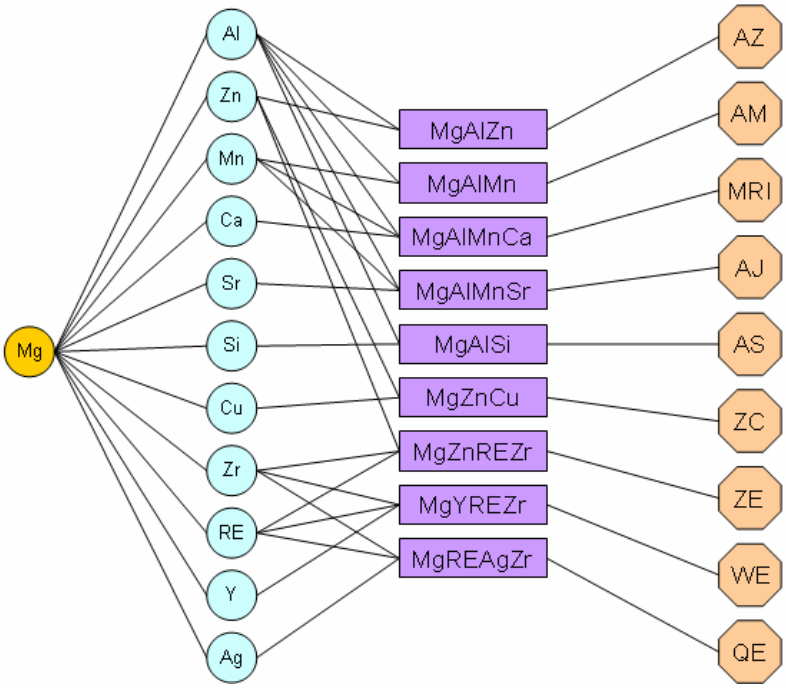

Figure 2.1: Most common Mg alloys with codes according to their ASTM classification.

2.3 GENERALITIES, PHASES AND STRUCTURES OF Mg AND ITS ALLOYS

2.3.1 Magnesium-Aluminium-Zinc (AZ) - Casting Alloys

Mg-Al alloys are among the most widely used industrial die casting applications. Such alloys present a good combination of castability, mechanical strength, ductility and excellent corrosion properties. Additions of Al improve mechanical strength and hardness, with the strengthening effect based on a solid-solution formation and an $Mg_{17}Al_{12}$ phase. As well as improving the mechanical properties, Al significantly enhances the castability of Mg (eutectic system T_E=437 °C). However, at high Al contents, an incoherent, interdendritic $Mg_{17}Al_{12}$ grain boundary phase is formed without the formation of Guinier-Preston zones or an intermediate metastable phase, which causes a rapid degradation in mechanical properties at temperatures beyond 120 °C [21-23]. Further, Mg-Al alloys present low heat and creep resistance with low ductility at room temperature. As reported on the literature [2,24], the presence of Al also contributes significantly to the formation of microporosity. The level of porosity increases with Al content up to 11 wt%, where a peak in porosity formation is observed, and decreases from there to the eutectic composition. In addition, it has been reported that the pore size increases with increasing Al content and porosity changes from a more distributed state to a concentrated small region.

Mg-Al alloys are often alloyed with Zn, to improve fluidity and room temperature strength by reducing the solid solubility of Al in Mg. This reduction increases in turn the amount of precipitated phase formed upon ageing, causing a moderate increase in strength [8,22]. It also assists in overcoming the harmful, corrosive effects of iron and nickel. By adding up to 3 % zinc, shrinkage can be compensated for and tensile strength increased. Additions of Zn in concentrations above 1.0 % – 1.5 % in Mg alloys containing 7 % to 10 % Al leads to a hot cracking effect [25]. Compared with phases present in binary Mg-Al alloys, no new phases occur in ternary Mg-Al-Zn alloys, if the Al to zinc ratio is greater than 3:1 and at no stage does AZ91 contain a ternary compound. Zinc can also change the eutectic morphology of a single casting from a completely granular to a fully divorced formation [25].

Manganese does not have much effect on tensile strength, but increases the yield strength slightly. Its most important function is in improving the saltwater resistance of Mg-Al and Mg-Al-Zn alloys by removing iron and other heavy metal elements into relatively harmless intermetallic compounds, some of which separate out during melting [14].

The microstructure and phase transformation taking place during solidification of Mg-Al-Zn-(Mn) shows, according to Figure 2.2, the following structural constituents: hypoeutectic Mg-Al solid solution, eutectic Mg-Al supersaturated solid solution and β-phase ($Mg_{17}Al_{12}$). Such phases result from non-equilibrium solidification conditions that determine the actual solidification process of real ingots and die castings. Under equilibrium, Mg-Al-Zn and certain Mg-Al-Mn alloys should solidify with the formation of only hypoeutectic Mg-Al solid solution. However, under non-equilibrium solidification conditions, the slow diffusion of Al leads to a coring effect in hypoeutectic Mg-Al solid solution and to the formation of a eutectic β-phase and an Al-rich eutectic Mg-Al solid solution. In addition to the eutectic precipitates, discontinuous precipitation can also take place in cast ingots, due to their slow cooling rate in solid state.

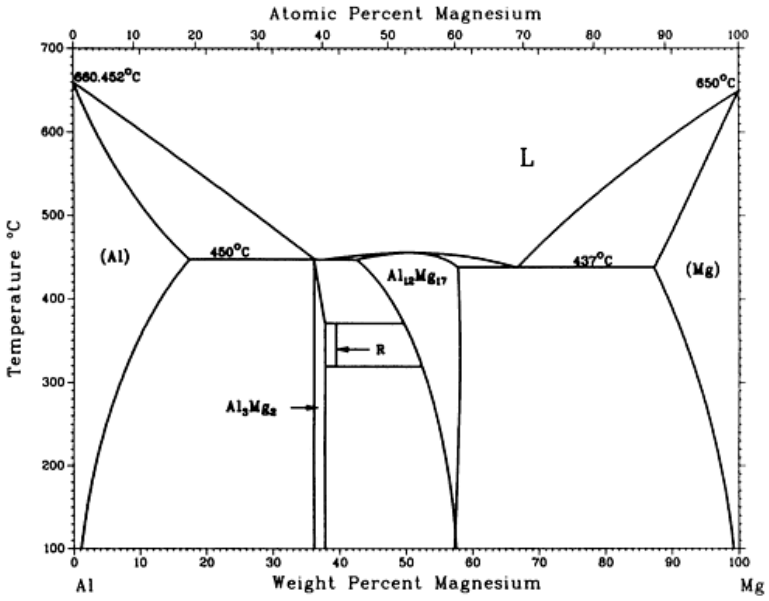

Figure 2.2: Al-Mg phase diagram [14].

2.3.2 Magnesium-Aluminium-Rare Earths (AE) - Casting Alloys

Due to the fact that Si leads to a deterioration of corrosion resistance and limits improvement of creep resistance in AS (Mg-Al-Mn-Si) alloys, a new Mg-Al-RE based variant was developed, which would enhance the creep properties of Mg alloys. These special alloying elements were added (RE stands for rare earth mixtures) and a new alloy designated AE42 was developed [8,26].

This alloy was developed from a non-aluminium Mg chemistry in which rare earths, under die-casting conditions, were shown to increase creep resistance by forming fine Mg_9RE second phase particles along the grain boundaries and some RE-containing precipitates. This interdendritic phase has been reported to be $Al_{11}RE_3$. Due to the formation of this phase, the formation of *β*-phase is suppressed and the corresponding creep properties of the AE42 alloy are largely improved. Rare Earth elements presented in commercially available AE alloys typically consist of Ce (>45 %), La (20–30 %), Ne (10–20 %) and Pr (4–10 %). Neither in “as cast” alloys nor in heat-treated specimens has the formation of Mg-Al-RE phases been reported [26]. Additionally, both Al-RE-Mn and other Al-RE based phases ($Al_{11}RE_3$ and Al_2RE) are also described in the literature as composing the microstructure of die cast AE42 and of the recently developed AE44 [8,14,27-29].

2.3.3 Magnesium-Aluminium-Calcium-Strontium (AXJ) - Casting Alloys

The addition of Ca to Mg-Al alloys has a positive effect on grain refining and aids creep resistance. However, Ca can lead the tool to sticking during casting, degrading corrosion resistance, castability, ductility and impact strength as well as increasing the tendency to hot cracking. Since calcium is a relatively inexpensive element and has an atomic weight, which is half of that of strontium and less than one-third of that of RE elements, it means that alloying with Ca results in a maximum increase of the above properties in terms of cost [2,8,14].

With the object of developing a new creep resistant and cost effective die casting Mg alloy, DSM, Volkswagen and the Technical University of Clausthal established a research program, resulting in a series of new alloys. MRI153M and MRI230, developed within this cooperation [30,31], contain around 1 % to 2 % Ca and up to 0.4 % Sr additions. Furthermore the alloy presents corrosion resistance and mechanical properties at room temperature, similar or better than those of AZ91D and other commercial alloys. Its elevated temperature strength and creep resistance are also significantly superior to those of commercial alloys, allowing its use at temperatures up to 190 °C. MRI alloys can be considered a further development of the AM alloy with additions of calcium and strontium. Ca produces an effective grain refinement and increases the creep resistance, as mentioned above, mainly due to the formation of many fine stable $Mg_{32}(Al,Zn,Ca,Sr)_{49}$ precipitates, among others. It has also been reported in the literature that MRI precipitates belong to the Mg-Al-Zn-Ca system and are expected to be predominantly $Al_2(Ca,Zn)$, which are more filigree than those of AZ91D [32]. Further, the addition of Sr generally causes an improvement of the mechanical properties and contributes to increases in creep resistance, since the free Al forms Al_4Sr instead of the prejudicial $Mg_{17}Al_{12}$ at the grain boundaries [33].

2.3.4 Combined Properties

Summarising the results found in the literature, one can conclude that it is very difficult to develop a new alloy that exhibits an adequate combination of castability, creep performance, corrosion resistance, ambient strength and affordable cost in order to meet the requirements, which are necessary to make the use of Mg widespread throughout the industry. Although AZ91 is the most widely used Mg die-casting alloy, presents excellent properties at room temperature and its costs seem

very reasonable, the dissemination of such material is restricted, under certain circumstances, mainly due to its inferior high temperature resistance. Conversely, Mg-Al-RE and Mg-Al-Ca-Sr maintain their high strength levels at higher temperatures. However, the field of application for such alloys is somewhat limited, principally due to their low castability and sometimes to the high costs involved in the fabrication of complex components. In Table 2.4, where mechanical properties versus projected costs for an application at 150 °C are considered, points were attributed to the different properties, assigning castability and creep resistance the highest importance. As a second stage, the products of each individual score by its weight were summed to calculate the total score for a given alloy. Correspondingly, Figure 2.3 draws a comparison between the most used alloys and their probable substitutes.

Table 2.4: Combined properties of Mg-alloys for applications at 150 °C [8].

		Cast ability	Creep Resistance	Yield Strength at 150°C	Fatigue Strength	Ductility	Corrosion Resistance	Total Score	% of maximum score
Alloy	**Weight**	**10**	**10**	**7**	**7**	**3**	**7**		
MRI153M	Score	9	8	8	10	5	10	381	100%
	WxS(1)	90	80	56	70	15	70		
MRI230D(2)	Score	6	10	10	9	3	8	358	94%
	WxS	60	100	70	63	9	56		
AX52J	Score	5	10	10	8	3	8	341	90%
	WxS	50	100	70	56	9	56		
ACM522	Score	4	10	9	8	3	9	331	87%
	WxS	40	100	63	56	9	63		
AJ52X	Score	6	9	6	6	5	8	305	80%
	WxS	60	90	42	42	15	56		
AS21X	Score	9	7	3	5	10	8	302	79%
	WxS	90	70	21	35	30	56		
AE42(2)	Score	7	8	4	5	9	8	296	78%
	WxS	70	80	28	35	27	56		
AZ91D(2)	Score	10	1	5	8	5	9	279	73%
	WxS	100	10	35	56	15	63		

(1) W x S = Weight x Score

(2) Highlighted rows are alloys considered within this work.

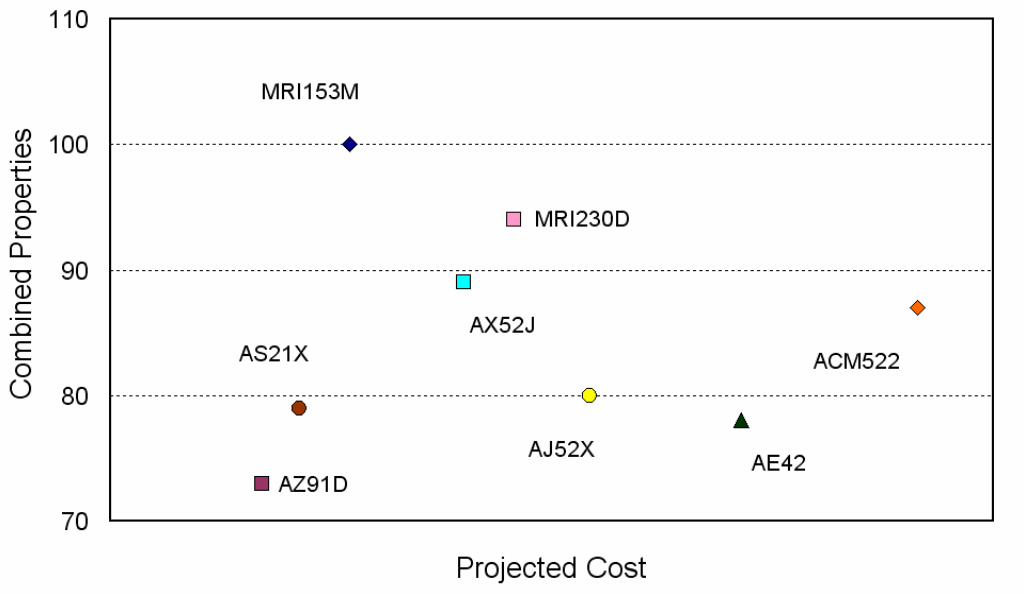

Figure 2.3: Combined properties rating vs. projected cost of new Mg alloys designated for applications at 150 °C [8].

2.4 BOLTED MAGNESIUM JOINTS

As briefly mentioned in the introduction, intensive lightweight design and the use of modern lightweight metals in the automotive industry are increasing the demand for new development of fasteners and the design of bolted joints. For many years, Al and steel components have been joined with high-tensile carbon steel fasteners without further problems. However, various challenges are experienced with the combination of both Al and high-tensile steel fasteners with Mg components.

According to the literature, the thermal cycles imposed by operating conditions can lead to significant loss of the preload force in bolted joints, due to relaxation. In some cases, losses of up to 95 % are reported in Mg AZ91D-T6 gearboxes fastened with steel bolts (see Figure 2.4) [9]. Loss of clamp is caused by relaxation of the joint due to the creep behaviour of Mg itself and the significant differences in the thermal expansion coefficients between the bolt and clamped material. Figure 2.5 shows the most used configuration, where the bolt is screwed into an extant thread directly into the member to be joined, which could be an Mg or Al component [34,35]. Some other variations involve thread grooving and through-all screws with nuts [36] are very often investigated and reported on the literature. Additionally, many investigations have been dedicated to the simulation of bolted Mg joints [37,38].

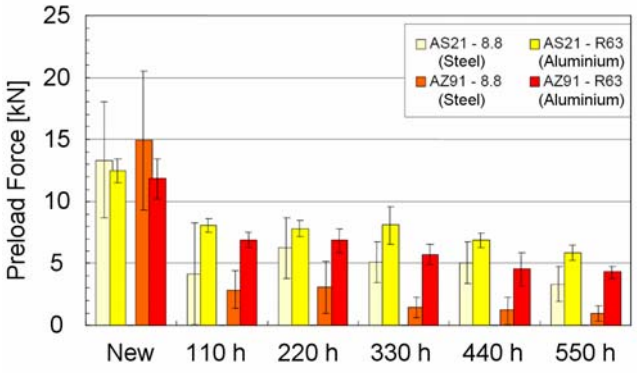

Figure 2.4: Load retained as a function of material combination and operating time [9].

Figure 2.5: Schematic of the most used Mg bolted joint [34,35].

Operating temperatures on modern powertrain units (e.g., engine and transmission) are in the range of 150 °C. According to Westphal *et al.* [34] Mg components joined by a steel fastener of a standard geometry (M8 flange bolt) experiments an additional load of 7 kN for a temperature difference of 130 °C (see Figure 2.6). This corresponds to 50 % of the assembly clamp load for this joint, which means that significant effects of relaxation due to creep are already observed during the increase in temperature. Experiments carried out by Westphal [35] using an Mg sample tightened against a threaded Al specimen of AlSi9Cu3 have shown a clearly higher remaining load for joints clamped with Al fasteners. Additionally, after 200 hours, clamp load change was negligible for Al, whereas for steel, losses after 200 hours were over 90 % and still declining (see Figure 2.7). The tendency to have higher residual clamping loads with Al fasteners seems to find consent between investigations [9,35]. According to the authors [9,35], Al fasteners are far more desirable on a cyclically loaded Mg component joint versus a similar steel fastener, due to the difference in stiffness ratio of the joint as well as a shorter full thread engagement (1.2 to 1.5D for Al and 2.5 to 3.0D for steel fasteners, where D is the diameter of the fastener). A fastener with a large bearing area to accommodate the compressive yield strength of Mg components would also be helpful, to significantly reduce clamp load losses.

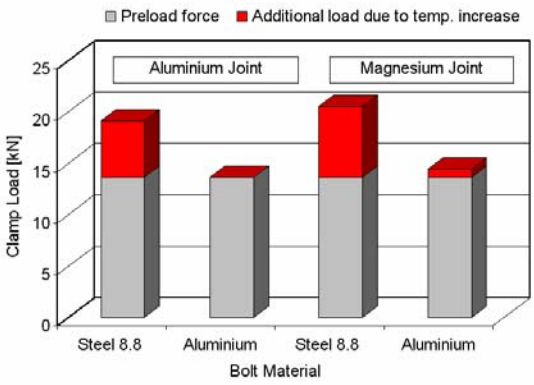

Figure 2.6: Theoretical additional clamping load due to different thermal expansion coefficients [34].

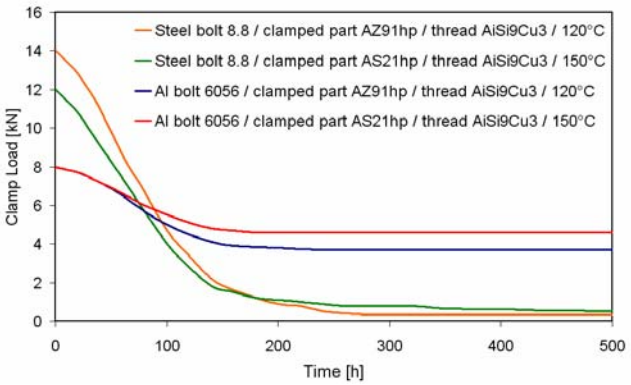

Figure 2.7: Loss of pre-load force as a function of time and temperature [34].

During bolt-joint tightening in a bolt-nut-washer experiment, the end of the bolt is assumed to experience uniform displacement when the bolt is in tension. The bolt head or washer applies pressure on the Mg joint surface through surface contact and the joint is under compression. Finite Element Analyses (FEA) show that stresses in Mg alloy bolt joints are highly non-uniform and the magnitude of stresses is sometimes close to yield or even above the yield strength. In a bolted joint loaded up to 72 kN, the stress in the larger part of the sample ranges from 20 MPa to 100 MPa (compressive stresses). The areas submitted to higher stresses close to contact corners experiments values up to 110 MPa, which in this case means that plastic deformation can occur in Mg alloy components under such loading conditions.

On the other hand studies have been directed to foresee the relaxation behaviour in Mg-sleeve/thread material with different bolt materials [39]. In these cases compressive stresses imposed by the bolt acting on the Mg-thread experiments show values near to the Mg yield strength, which is aggravated by high temperatures. According to the FEA presented in this study [37], the bolt material plays the most important role on the pretension losses in Mg bolted joints, being the clamping length the variable with the largest impact followed by the bolt head diameter (bearing area).

Since creep is the most important mechanism that influences the resistance of automotive Mg-bolted joints, many authors have investigated high temperature stable alloys to fulfil this gap, i.e. alloys which have a larger operational range in terms of temperature [40]. In this context, AJ, AS, ACM, MEZ, AE, WE, Ca-based (MRI) are examples of suitable alloys, which are being investigated to be used in high temperature applications [41-46]. Figure 2.8 summarises the tendency observed in most of the reports, where Mg-Al-Zn-Ca-Sr (MRI) alloys presented the highest creep resistance, and therefore the highest fraction of remaining load in bolt-load retention tests, followed by Mg-Al-RE (AE) and Mg-Al-Si (AS) alloys. Mg AZ91 clearly shows its high temperature limitations and appears as one of the most unsuitable materials for such applications. Performing a bolt-nut-washer bolt-load retention experiment Okechukwu [40] observed the alloy MRI230D as the one with the best bolt load retention properties. In his experiments at 150 °C, MRI230D retained about 32 % of its initial load, whereas MRI153 and AM50 retained 27 % and 11 % of their initial loads respectively. Under these conditions, AZ91D experienced permanent deformation.

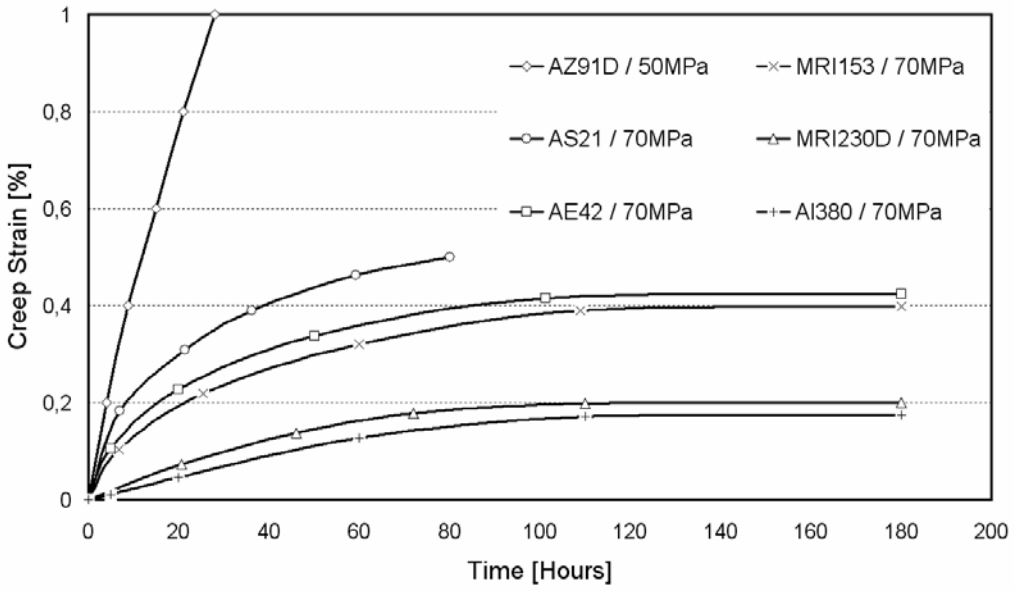

Figure 2.8: Creep curves from tensile creep tests of new Mg-Al-Ca-Sr alloys in comparison with commercial Mg and Al alloys at 150 °C [8].

2.5 FRICTION WELDING – A LITERATURE REVIEW

As reported by Crossland [47], the first patent related to friction welding was granted to Bevington in 1891 in the USA. According to his idea, heat would be generated between a fixed workpiece and a rotating high-speed steel die. In a further stage the workpiece would soften so that it could be easily extruded through the die. The next development occurred in Germany during the 1920s, culminating in a German patent in 1929. These efforts were followed by research in England, which resulted in a series of patents issued between 1941 and 1944. In September, 1941, Klopstock and Neelands [48] patented a friction welding process for seam welding. The heat generated between the rotating welding rod and the members being seam welded would cause the parent metal to become much more plastic, and induce melting of the rod. Again, the process apparently did not find wide acceptance. In spite of it being used for the first time in Germany, to weld thermoplastic piping during the Second World War, the real credit for the introduction of friction welding on a large scale is accorded to a Russian machinist A. I. Chudikov, who suggested the process and patented it in 1956. In 1957 and 1958, many research projects were carried out in the Soviet Union and other nations, such as Czechoslovakia and China, to develop and industrialise the process. During this time the first friction welding equipment were developed by VNIIESO (Scientific Research Institute for Welding Equipment) in the Soviet Union [47,49,50]. Although friction welding has been around for many years, the technology and its applications have broadened recently [51].

Friction related processes are versatile enough to join a wide range of part shapes, materials, and weld sizes. Therefore the technique has become widespread throughout the world and typical current applications include aircraft and aerospace components, cutting tools, agricultural machinery, automotive parts, waste canisters, military equipment and spindle blanks. Furthermore, due to its versatility, the process has been used to join bimetallic materials in a wide range of applications [52,53]. Figure 2.9 illustrates the actual importance of this subject, by means of the steeply increasing number of reports and research activities involving the topic of friction welding during recent years. In Europe, and particularly at GKSS-Forschungs-zentrum GmbH, Germany, various applied and fundamental R&D projects with extensive experience on optimisation and characterisation of microstructures of

friction welded joints have been conducted. The increasing number of publications highlights the importance of the topic “Friction Welding” and indicates that this subject is an actual issue and therefore needs further investigation.

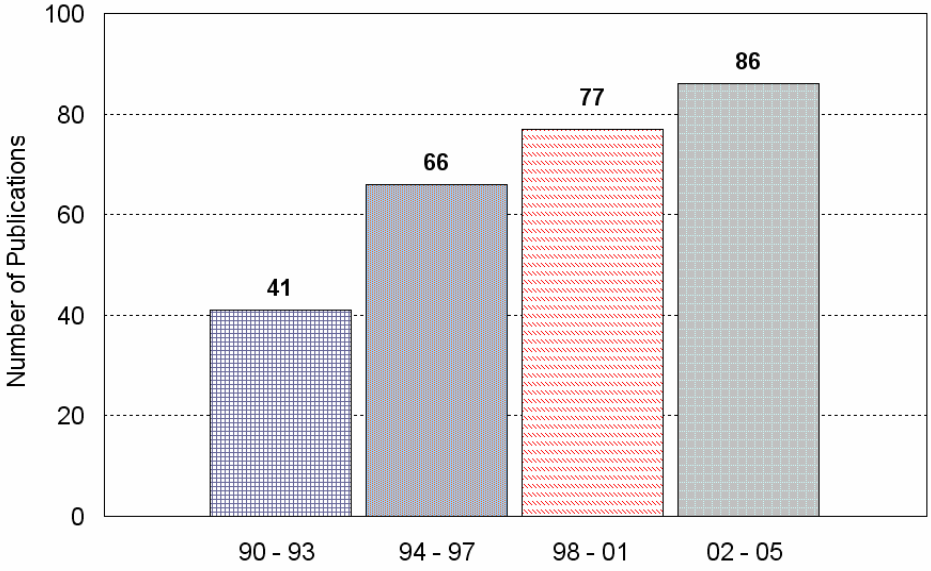

Figure 2.9: Number of ISI publications involving friction welding.

Friction welding is a group of solid-state welding processes, which use the heat generated through relative motion between two frictional interfaces to produce a joint. This method depends on the direct conversion of mechanical energy into thermal energy to form the weld. The fixed work piece is held stationary and is brought into contact with a rotating work piece, normally under a constant welding pressure. After the rotation stops, an increase in the pressure (upsetting force) can be applied to improve the mechanical properties [54-56].

Figure 2.10 shows an illustration of the typical friction welding process: In the first stage Figure 2.10(a) the rotating work piece is brought into movement while the fixed is held stationary. In Figure 2.10(b) both work pieces are brought in contact and an axial force is applied to begin the upsetting process (Figure 2.10(c)). In Figure 2.10(d), after the set upsetting is achieved, the rotation stops and the axial force is increased. The upsetting process continues, since the forging force is applied for some seconds. As reported by Elmer [55], during the last stage, atomic diffusion occurs while the interfaces are in contact, permitting a metallurgical bond to form between both materials, thereby consolidating the joint.

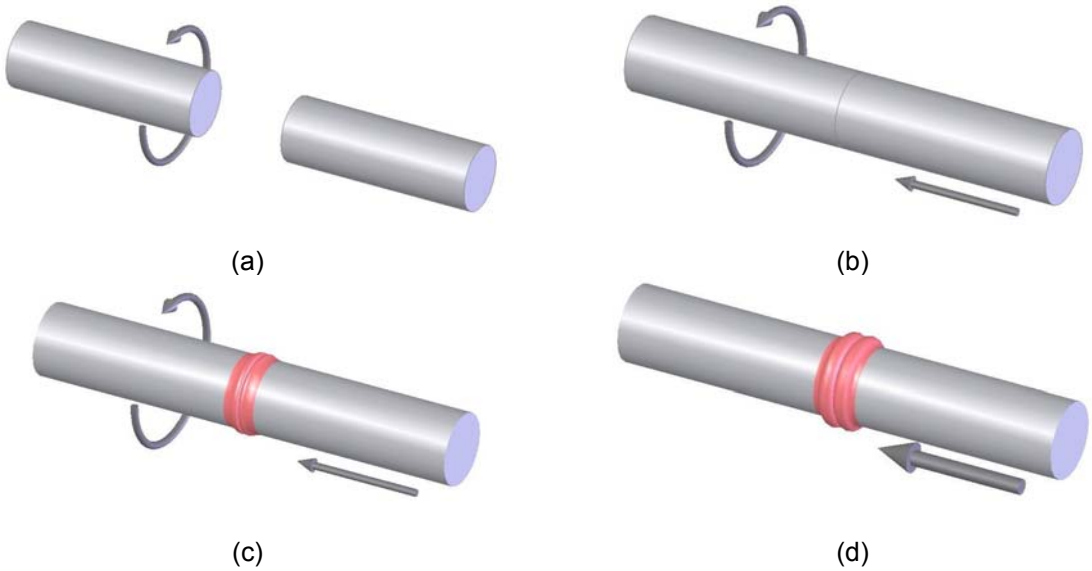

Figure 2.10: Schematic of basic rotational friction welding.

Friction welding involves heat generation through friction and abrasion, heat dissipation, plastic deformation, and atomic interdiffusion. The interdependency among these factors leads to complications when trying to develop predictive models of the friction welding process. The knowledge available is mostly based on empirical studies performed on a wide variety of materials. The quality of a weld is influenced by many qualitative factors (bulk material, surface condition, presence of surface films, etc.) as well as quantitative factors such as the rotational speed, welding pressure, upsetting/welding time and magnitude/duration of the forging force [50,56,57]. These variables should be controlled as accurately as possible, since they indirectly govern the mechanisms involved at the different temperature levels and therefore on the joint's formation [58,59].

2.5.1 Relevant Process Parameters

According to the literature [51,58,60-63], there are a number of important process parameters (related directly to the process) and variables (related to the material) in friction welding. Some of them are listed on Table 2.5. Although all the parameters are relevant and in some way influence the final quality of the weld, the first four are the most important and so will be considered in more details. Also, their influence on the joint quality and process performance will be discussed.

Table 2.5: Most important parameters in friction welding.

Process Parameters	Process Variables
1) Relative speed of the faying surfaces	1) Temperature of the friction surfaces
2) Normal force on the contact area	2) Nature of the material
3) Heating time	3) Presence of surface films
4) Upsetting and upsetting rate	4) Rigidity and elasticity of the friction surfaces
5) Time required to stop the spindle	
6) Duration and magnitude of the forging force	

Usually, welding parameters are developed and optimised through a series of trials for a given application. Dennin [64] presented the first attempt to establish welding parameters for new applications by numerical calculations without performing welding trials. The reduction of the of welding experiments needed prior to production is still a matter of research today [65].

2.5.1.1 Relative Speed of the Faying Surfaces

The relative rotational speed is the least sensitive process parameter. In practice, it may vary over a rather wide range without influencing the quality of the weld connection. The tendency to increase the rotational speed during friction welding to obtain better mechanical properties is erroneous, and there are certain optimum speeds for each individual material combination and application [50,58].

From the standpoint of an improvement of the quality of the welded connection (particularly for welding of metals sensitive to overheating), it is desirable to use relatively low rotational speeds. The process efficiency is improved as a result of reduced heat losses, which reduces the amount of energy used for welding. This, however, leads to a necessary increase in the power of the installation and, what is more important, to a much longer initial phase. The duration of this phase (and for low rotation speeds, throughout the entire welding process) depends to a large degree on the initial condition of the friction surfaces [50,64,66]. Keeping all the other parameters constant, Bethlehem [66] reported that when the welds are made with machined surfaces, the time necessary to complete the initial phase (when the point of maximum moment is achieved) is significantly shorter. On the other hand the maximum moment is achieved after a longer time if the surfaces are simply sawed. Other investigations observed a higher moment peak as the rotational speed

decreases [64,66,67]. Additionally, Sergin and Sababtsev [68] concluded that the difference in the distribution of temperatures along the length of steel bars at various speeds of rotation manifests itself mainly in the first, non-steady stage of the process. In this stage, at higher rates of rotation the metal along the length of the bar is heated to a greater depth, and faster, than at low rates.

At high rotational speeds, deep tearing at the friction surfaces is replaced by a polishing action [50,69]. As a result, to achieve the conditions for plasticisation at the faying surfaces, longer heating times are required. Longer heating times allow the propagation of thermal energy along the axial direction of the workpieces, and as a consequence a greater volume of material is heated. Therefore, in the case of mild steels, higher rotational speeds lead to lower cooling rates, wider heat affected zones (HAZ) and hence lower hardness at the vicinity of the bonding line (BL). On the other hand, lower speed of rotation produces a thinner HAZ, with a profile that is noticeably much more severely pinched, in comparison with similar welds produced at higher rotational speeds [60,61,70].

2.5.1.2 Normal Force (Axial Pressure)

Although this variable may vary in broad ranges in the heating and forging stage, it influences the temperature gradient in the weld zone, the required drive power, and the axial shortening [64,79]. The axial pressure must be high enough to hold the faying surfaces in intimate contact, to keep detrimental substances out of the welding zone and avoid oxidation. However, it should be noted that higher pressure causes local heating to high temperatures and rapid axial shortening (high upsetting rate), which might become uncontrollable. Hofmann and Thome [71] observed an increase in the temperature with pressure in welds performed in mild steel. For a given upsetting, some studies have shown that the time from the initial contact of the surfaces to the end of the weld process decreases as pressure increases. With higher pressures, the consumption of material is faster (higher upsetting rate), generating welds with shorter welding cycles [60,72,73].

Following the braking/stopping phase (phase where the rotational speed of the spindle goes from its maximum to zero), two different methods of varying the axial pressure are commonly used: maintaining the pressure or increasing it. For the latter a force called forging force is applied, which according to the American Welding Society (AWS) [58] improves the joint quality significantly. In general, the forging force can be applied while the spindle is decelerating during the stopping phase or after the spindle has stopped rotating at the end of the stopping phase. In both cases a terminal torque, influenced mainly by the axial pressure, by the rotational speed if the deceleration rate is high and by the deceleration rate itself, will be generated. As already mentioned, the second torque peak cannot be eliminated by reducing or removing the normal pressure before the end of the stopping phase [67,70].

The axial pressure also influences the width and character of the HAZ. Its overall shape changes from an almost parallel sided boundary at low pressures to a more ''pinched'' or double cone profile at the centre of the stud at higher pressures. In the second case, the heat liberated is totally used in plasticising the material and, thus, does not propagate in the axial direction. According to Ellis [60], welds made at higher pressures show a narrower region, where the hardness values are lower than the parent material. Figure 2.11 presents the tendency to increase the upsetting rate, thereby decreasing the welding time, with lower rotational speeds. Additionally a higher upsetting rate with welding pressure is also evidenced for mild steel.

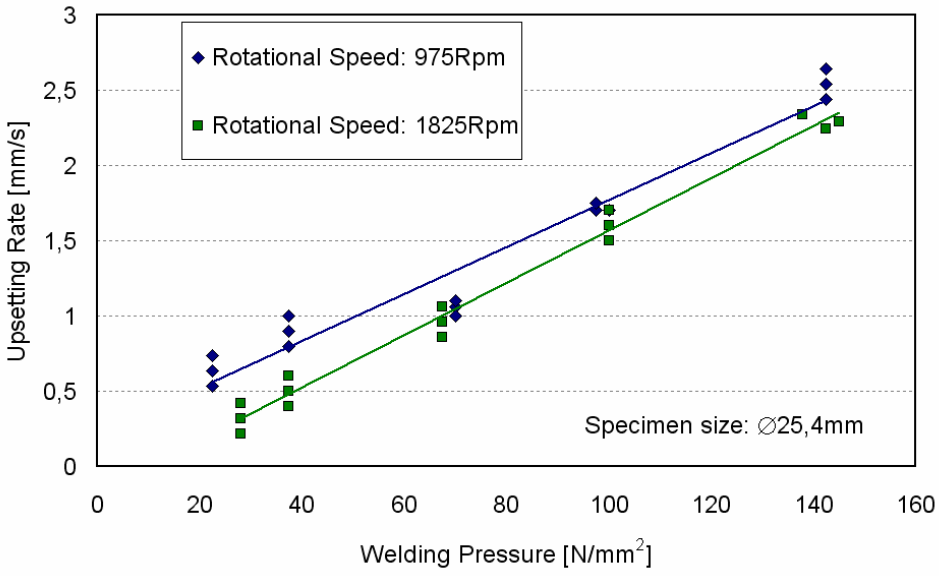

Figure 2.11: Relationship between welding pressure, speed and upsetting rate [60].

2.5.1.3 Heating Time (HT)

Vill [50] suggested that it would better to select the duration of the heating period rather than the upset as the third basic parameter of the friction welding process. Other authors [68,74,75] suggest the use of temperature in the joint as the third basic process controllable parameter. The first suggestion is based on the fact that for a given heat power of the process (speed and pressure are given) the duration fully determines the energy used in the welding operation. Thus for a given pair of materials and consequently to a certain extent, the HT determines the temperature conditions of the process, bearing in mind that the plastic deformation of the specimen is derived from the temperature conditions. However, the use of temperature is prompted by the fact that the energy spent in friction welding is used to create a suitable thermal profile in the interfacial region, which results in upsetting and bonding.

The HT is defined as the period from initial contact of the faying surfaces to the end of the braking phase. It is significantly influenced by the axial pressure and by the rotational speed. It is reduced as pressure is increased and increased with the rotational speed. For a given pressure, the HT increases with increasing rotational speed [50,58,60,61,76] and is normally controlled in two ways: the first is with a suitable timing device that stops rotation at the end of a pre-set time and the second is a special setting to stop rotation after a predetermined axial shortening (upsetting) is achieved. HT is also important, especially for low upsetting rate welds, because it not only defines the microstructure at the interface, but also affects the depth of heating in the workpieces by conduction and therefore the width of the HAZ. On the other hand the cooling rate is affected by the surrounding media and the welding time combined with the total amount of flash formed around the weld interface. If the flash has a large mass, then the heat stored within the flash will be conducted back into the weld thereby reducing the cooling rate of the metal within the HAZ. Short heating times naturally result in a higher heat generation rate. This also involves a relatively higher upsetting rate, forming a large flash where most of the heat is stored as sensible energy. By comparison, with longer heating times, not all of the heat generated at the weld interface is stored in the flash, and much of it has time to be conducted into the welded parts. Figure 2.12 shows the maximum temperature

recorded with an infrared camera (see snapshots in Figure 2.12) in the welding interface of similar rotational AE42 friction welds. This diagram evidences the direct dependence of peak temperature on the HT.

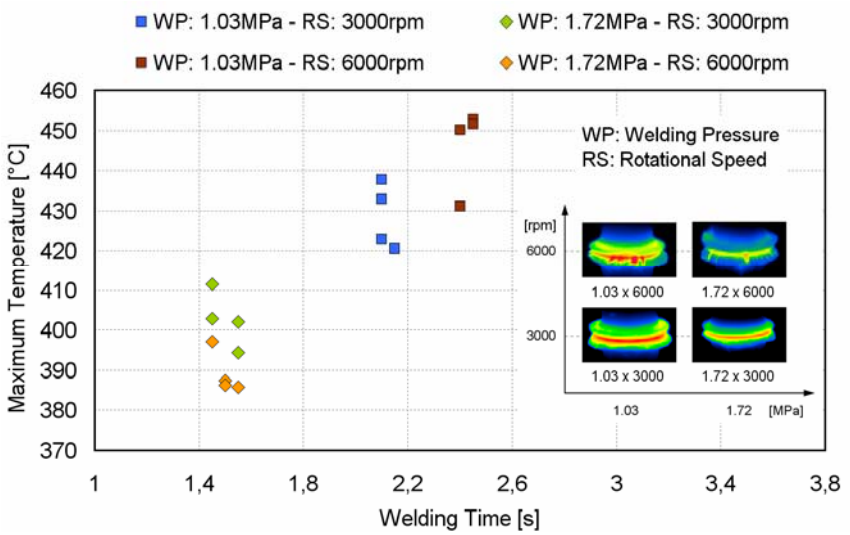

Figure 2.12: Relationship between welding time and maximum temperature [77].

In order to obtain an improvement in the quality of the welded connection, it is normally desirable to have short heating times, without flash formation. On the other hand, when it is desirable to preserve the toughness or not to have high hardness, for example, it is better to have longer heating times and consequently lower cooling rates.

2.5.1.4 Upsetting (Axial shortening)/Upsetting Rate

Generally, this variable is not only used to control the welding cycle, but it also has a significant influence on the joint properties. The applied pressure and speed of rotation will influence the time needed to reach a pre-set amount of upsetting. The time from initial contact of the surfaces to the end of upsetting becomes shorter as the pressure increases and rotational speed decreases. Drews and Schmidt [72] reported a sharp drop in the upsetting rate as the rotational speed increases (at lower speeds). On the other hand, at higher speeds (over 3000 rpm) no significant variation in the upsetting rate was observed with rotational speed. When the upsetting rate is increased, the total welding time is reduced and hence there is less time available for grain growth and homogenisation to take place. Figure 2.11 shows the upsetting rates as a function of the rotational speed and welding pressure.

Controlling the process by upsetting has disadvantages as well. It has been reported that large burrs ("collar"), central projections remaining on the surface of the workpieces, misalignment of the end cross sections (when the friction surfaces are not perpendicular to the rotation axis) and similar surface defects may have a negative influence if the process is controlled by upsetting. In these cases, the welding system considers the wear of these irregularities as the beginning of the upset process, although the surfaces at this point are not entirely in contact, i.e. are not yet making full contact. Hence, the control system would stop the weld before the preset necessary upsetting was achieved [50,78].

Drews and Schmidt [72] have developed a method to calculate the welding parameters in order to have a defined upsetting. With this method it was possible to foresee and pre-calculate the parameters to achieve a certain final length of a component after the welding operation. Generally, Figure 2.13 summarises the influence of process parameters on friction welding.

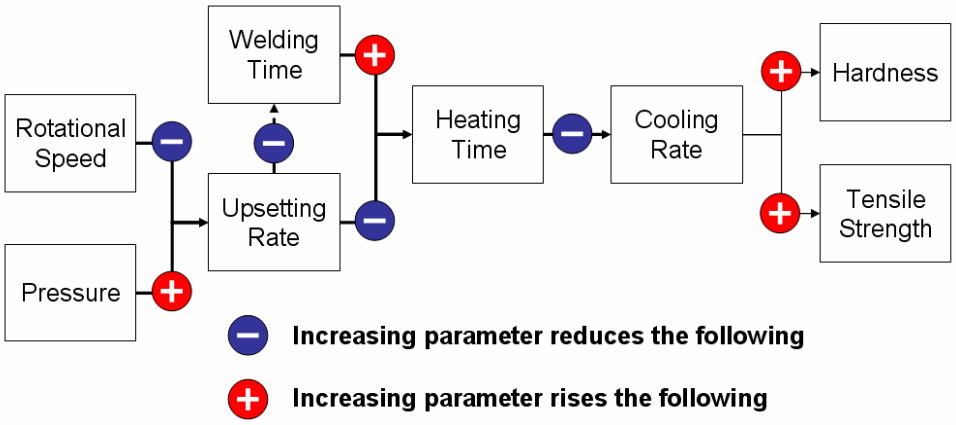

Figure 2.13: Parameter influence in Friction Welding.

2.5.2 Process Characterisation – Phases of the Process

The division of the process into different phases is a common way when explaining the weld cycle and the mechanisms related to the welding process. Various authors divide the cycle into different numbers of phases. Two [58], three [47,50,79], four [62,64,80-82] and even five [60] different phases are proposed in the literature to describe the process. The division in four phases is used by most of the authors and seems to be the most suitable to be presented in this review.

2.5.2.1 Phase 1 – Rubbing Phase

During the first part of phase 1 (see Figure 2.14) the initial contact of the faying surfaces mainly results in a smoothening effect of the surfaces. The remaining phase 1/2 can be briefly characterised by seizing and microbonding processes [47,50,83].

At the beginning of phase 1/1 only a limited amount of the nominal welding surface actually makes contact. Therefore, the surface pressure reaches extremely high values locally, promoting plastic deformation and hence, flattening of the faying surfaces. In addition to these relatively high stresses, the outer regions of the joint are subjected to the highest relative rotational speed between the faying surfaces. By rubbing, the surface roughness is partly smoothened by elastic and plastic deformation and local melting starts in the outer regions of the weld zone [47,50,84]. As the process progresses, isolated local bonding (microbondings) that eventually takes place across the contact surface are immediately sheared off. The shearing of those microbonds induces additional heating in the adjacent material since the energy used to deform them is liberated in form of heat [50,85]. Neumann and Schober [81] explain this shearing-off phenomenon by the fact that once the temperature has quickly, but only locally, reached the melting point or even higher values, the heat generation decreases substantially. The heat dissipation increases and melting cannot be maintained, leading the material to plasticisation. When the material has plasticised, the recrystallisation rate is smaller than the deformation rate, which results in shearing-off the local microbonding. The mechanism of the energy input and transformation is also presented by Bethlehem [86]. As the material reaches the melting point for a short period of time, followed by a sharp temperature drop caused by high thermal gradients, low transformation temperature products (e.g. martensite) might be formed in the weld zone. However, Bethlehem [86] reported that even with longer heating times, no molten film was observed. Kreye [87] reported in some cases a molten film may be formed locally, although it is not necessary to build the joint.

The main effect of phase 1/1 is the smoothening of the outer regions of the rubbing surfaces, which takes place during the first revolutions of the work piece within phase 1. When the smoothening in the outer regions is almost completed, it starts to develop towards the rotational centre of the joint (gradual transition from phase 1/1 to phase 1/2). In the outer regions, almost no heat is produced during this intermediate phase, because of the reduced frictional contact (the faying surfaces are now widely smoothened) and the presence of oxide layers generated in phase 1/1. Bethlehem [86] observed that the region between 0.3R and 0.7R, where R is the radius of the workpiece, is subjected to severe deformation and heating in the beginning of this second stage. According to his work, the heat losses in the outer regions and the lower heat generation in the inner part of the welding cause, at the beginning of the rubbing phase, this localised increase in the temperature. Eichhorn and Schaefer [70] observed that heating and plasticisation at the beginning of the process occurs more preferably in the rotating partner, which leads to an uneven HAZ and degree of deformation.

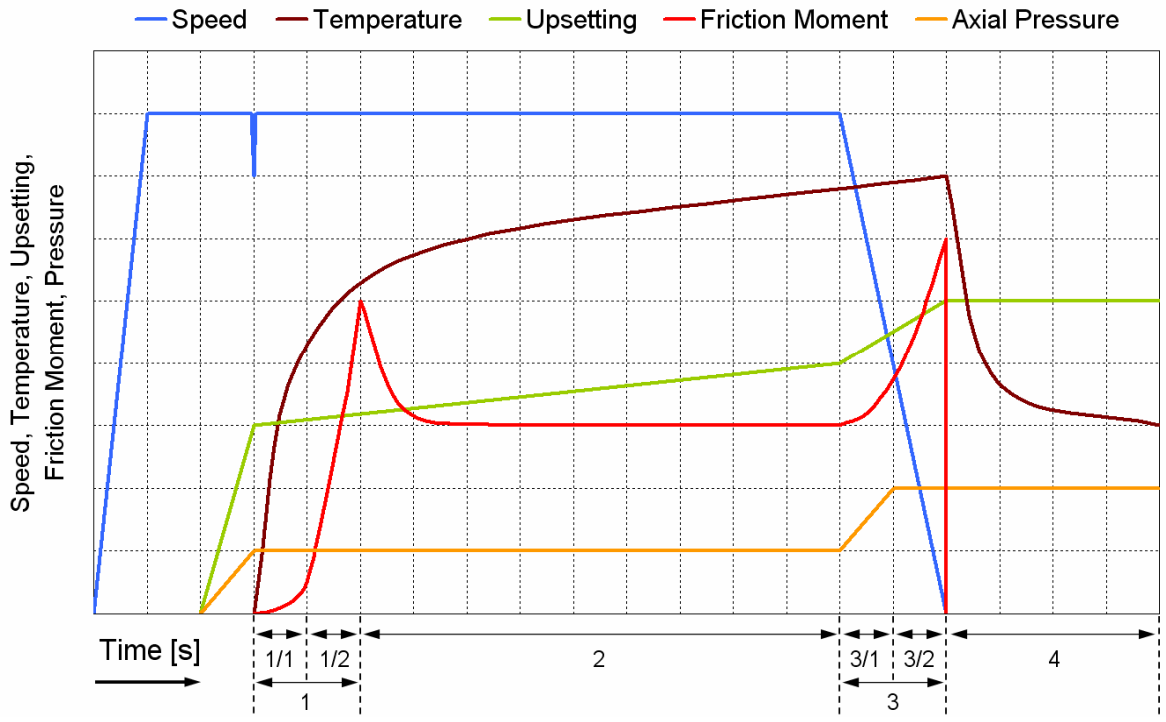

Figure 2.14: Phases of the process: 1) Rubbing phase; 2) Heating phase; 3) Braking phase and 4) Bonding phase.

Phase 1/2 is completed as soon as the friction moment reaches its maximum. This peak is caused by the removal of the contaminant film on the one hand and by a significant increase in the number of microbonds distributed along the faying surfaces on the other. The extraction of the contaminant film allows contact of fresh metal surfaces with a considerable increase in the coefficient of friction. On the other side, as a consequence of the increased number of microbonds formed, since a larger common area is brought into contact, the friction moment necessary to shear such regions off is also significantly higher. The temperature of the friction surfaces increases accordingly. Bethlehem [86] observed a considerable influence of the rotational speed on the maximum frictional moment. However, the axial pressure causes almost no change in the magnitude of such a parameter. Additionally, it was also reported the influence of innumerable external variables, such as the preparation of the faying surfaces, the presence of surface contaminants, oxidation, grease and oil also affect the magnitude of the maximum friction moment.

2.5.2.2 Phase 2 – Heating Phase

The hydro-extraction effect of surface contamination particles closer to the rotational centre is obstructed by lower radial forces and restricted material flow conditions. Therefore, a material concentration on a circular ring area can be observed between 0.5 and 0.7 of the friction surface radius. This concentration causes local heating forming a thin plasticised film of sheared-off material [62,84,86]. This ring area increases in size and causes the squeezing of highly plasticised material to the cooler zones of the friction area. The temperature in this area is comparatively low, because the radial deformation is quite small due to the low relative speed. In this case, particles encapsulated in the ring and not re-dissolved into the plasticised material are transported to the rotational centre of the welding zone. The widening of the ring area continues until it reaches the rotational centre, forming a circular area, now extending its diameter slowly towards the outer regions of the weld zone. When the faying surface is fully plasticised, temperature equilibrium is achieved, which is supported by a self-balancing effect and causes a decrease in the friction moment. This effect can be described as follows:

"*As the temperature rises, the metal becomes more plastic, the friction moment necessary to disrupt the microbonds decreases, due to the lower yield strength of the materials resulting in a reduced torque, which gives a lower heat generation with a resultant lower temperature. This in turn softens the material, resulting in less deformation work and in a local decrease of temperature. Owing to the axial shortening, fresh material comes to the frictional interface, which causes an increase in the coefficient of friction leading to an increase in the temperature*" [47,50,86,88-90]. Subsequently the temperature rises to a maximum during the first 10 seconds of frictional contact and remains at a somewhat steady state until the end of the heating phase. As the process stops, the generation of heat is reduced, causing the joint to cool down.

In the outer regions of the interface, the material is easily pressed out of the frictional surfaces, due to the high plasticisation and to low deformation constraints. As the temperature of the material and the height of the plasticised zone increase, the resistance to the axial pressure reduces and the material is pressed out of the friction area forming the flash. This process is maintained as long as the temperature and the height of the plasticised zone can be kept in balance. As a result more material is pressed into the flash. These balanced actions result in heat saturation of the friction area and the corresponding zones. From this point on, an almost constant upsetting (i.e. shortening of the workpieces) is established.

With increasing thermal saturation of the workpieces, the required energy for plasticisation reduces, leading to a lower frictional moment. However, the growing flash increases the frictional surface and hence the frictional moment. The common opinion is that these phenomena at some point balance each other, resulting in an almost constant friction moment. Phase 2 is concluded as soon as the process reaches the limiting control parameter, which means a predetermined temperature point, a certain amount of upsetting or a pre-set time.

2.5.2.3 Phase 3 – Braking Phase

The braking phase begins with a controlled (when using a continuous drive unit) decrease of rotational speed (Phase 3/1). Reduced rotational speeds increase the number of microbondings that simultaneously takes place along the frictional

surfaces. The shearing of those increased number of microbonds produces additional heating, which keeps the temperature raising. Additionally, the shear resistance increases due to the lower deformation rate and hence the friction moment reaches its second peak. It has been published some literature [91,92] investigating the deceleration time in friction welding of mild steels. A conventional friction welding machine was used with the brake pressure varying. In some tests, the brake was disconnected, allowing the friction at the rubbing surface to stop the component. It was found that the second peak of torque and the upsetting rate increases as the brake pressure decreases at the end of the heating phase. Furthermore, it has been found [70] that this terminal torque cannot be prevented by reducing or removing the axial force before the end of rotation. Duffin and Crossland [93] have indicated that in continuous drive welding it is not essential to use a brake to produce welds free of defects. The increase of the frictional moment causes additional deformation in the adjacent material, which had previously not been subjected to any deformation. It should be noted that the deformation resistance of these areas is comparatively low, since they have almost reached the friction surface temperature (due to thermal saturation in the axial direction) before they are actually subjected to deformation. At a critical point, the rotation is reduced to such a low level that the temperature at the faying surfaces can no longer be maintained. Therefore, the shear resistance of the material increases and torsional deformation takes place in a larger region along the workpieces. The spindle stops followed by the beginning of the recrystallisation process, which occurs during the end of this phase resulting in a microstructure with very fine grain size [62].

2.5.2.4 Phase 4 – Bonding Phase

The mechanism of bonding already begins in the final stage of the heating phase, although bonding is not homogeneous across the contact surface. A homogeneous bonding in the whole cross section is achieved by the so-termed forging pressure within the bonding phase. Although the most authors state that the use of forging pressure significantly improves the mechanical properties of the weld, some experiments show that good welds can be obtained without an increase of the force after rotation stops, which means without any forging force [60].

The change from the friction to the forging force should take place at the end of the braking phase. The increased axial force results in an abrupt increase of the upsetting rate, and consequently of the frictional moment. Oxide layers in the outer regions of the weld zone produced by insufficient frictional contact are now expelled. The welding surfaces make closer contact and particularly the materials in the outer regions are brought together within atomic distances to produce metallic bonding. After the rotation has stopped, the dynamic softening process continues, i.e. the deformation is complete, but the diffusion processes still remain. As the material begins to cool down, static recrystallisation, crystal regeneration and creeping processes occur. Internal stresses are widely eliminated - a determinant factor for the mechanical properties of a friction weld [62].

2.6 FRICTION HYDRO PILLAR PROCESSING

Friction Hydro Pillar Processing is, when compared with other conventional friction techniques, a very recent welding process. Patented by TWI [94], this variation on friction welding can be described as a drill and fill process, and since its invention has been investigated in many publications [78,95-108]. Although approximately 15 studies have been published on this topic, there are basically only two groups investigating the process worldwide. Furthermore, studies published in various conferences have fundamentally the same content, which significantly limits the information available and makes a sound literature review on the topic a difficult task. Bearing that in mind, the most comprehensive description was given by Thomas and Nicholas [101], while an illustration can be found in Figures 2.15 and 2.16.

"The FHPP technique involves rotating a consumable rod co-axially in an essentially circular hole whilst under an applied load, to generate continuously a localised plasticised layer. The plasticised layer coalesces and comprises a very fine series of adiabatic, helical rotational shear interfaces, partly spherical in shape. During FHPP the consumable member is fully plasticised across the bore of the hole and through the thickness of the work piece. The plasticised material develops at a rate faster than the axial feed rate of the consumable rod, which means that the frictional rubbing surface rises along the consumable to form the dynamically recrystallised deposit material. The plasticised material at the rotational interface is maintained in a sufficiently viscous condition for hydrostatic forces to be transmitted, both axially and radially, to the inside of the hole, enabling a metallurgical bond to be achieved."

Although filler metal, flux and shielding gas are not required, it has also been shown in the literature the use of a shielding gas as a method to reduce possible atmospheric contamination. In this action, the pillar, which in the present work will be responsible for the local component reinforcement, will undergo significant hot working when subjected to these severe deformations. Consequently, the formation of a refined heat-treated microstructure will result in a remarkable change of the static and dynamic properties of the consumable rod and the parent plate material. However, such microstructure changes can be modified by thermal treatment later on, thereby achieving the required properties.

Figure 2.15: Schematic of FHPP process.

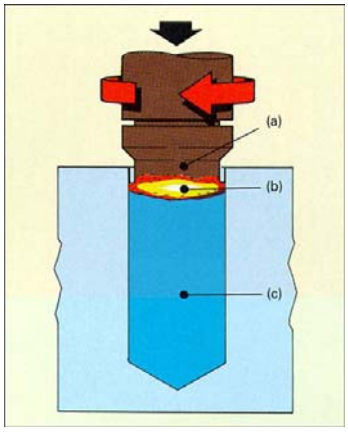

Figure 2.16: FHPP principle.
(a) Pillar
(b) Frictional Interface
(c) Extruded Material

The developments that lead to the invention of FHPP have been described by Andrews and Mitchell [109]. This report covers the development of the friction plug welding process for the repair of offshore structures. The friction taper plug welding (FTPW) process involves drilling a tapered hole through the full thickness of a plate at the location of a defect and forcing a rotating tapered plug with similar (but not necessarily identical) taper angle into the hole. The heat generated from the contact between the plug and the hole's wall causes the material to soften and flow, and the complete conical surface of the tapered plug is welded to the matching hole surface almost instantaneously [110]. The need to keep the equipment size down, but retain the possibility to repair thick sections, later led to the invention of FHPP [97]. Figure 2.17 depicts a macrograph of an FTP weld in Al AA6082-T6.

Cross sections of FTP welds (see Figure 2.17) showed that the consumable only plasticises in the contact area near to the surface [109,110], while in FHPP the consumable plasticises across the whole bore of the hole through the full thickness of the section [96,105,106] (see Figure 2.18).

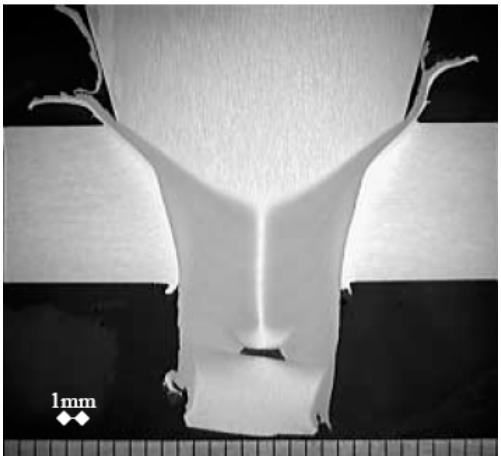

Figure 2.17: Macrograph of a FTP weld [110].

The first comprehensive report on FHPP, including microstructure and mechanical properties was compiled by Nicholas [97]. The first part of this report covers the process itself, where a parallel hole configuration is presented, as well as a tapered hole arrangement. Nicholas [97] found that those “materials which do not exhibit adequate plastic flow characteristics, often respond much better to a tapered joint design”. The bonding mechanism is described by metallurgical bonding, owing to a normal force on the interface between the plasticised material of the stud and the base material. The formation of a normal force at the sidewalls, although only an axial force is applied, is explained by hydrostatic behaviour of the plasticised material inside the hole [96]. Nicholas [97] assumes that a tapered hole configuration will assist the bond formation due to the additional forces on the tapered surfaces. Investigations into the influence of the taper angle on the bond quality have not been reported so far. Furthermore, as the consumable rod undergoes significant hot working during the welding process, a very refined, hot worked microstructure was reported. Owing to the superior static and dynamic properties of the extruded material, FHPP was suggested as a method of enhancing materials as well as for the production of monolithic materials and MMCs [95].

In the second part of his report, Nicholas [97] presented microstructural and mechanical results of a mild steel stud welded in a C-Mn steel substrate. Depending on the process parameters, either a very refined microstructure across the joint or some refined regions, which have not undergone layer shearing, could be found. These characteristics were attributed to the balance between thermal transfer and material displacement. If the balance results in a heat flow along the stud, a part of the stud will shear off due to thermal softening. Nevertheless, it was reported that both weld specimens had good bending and tensile test properties, while the exact values were not given. In addition, welding trials with aluminium alloys showed poor bonding quality with parallel hole configurations, while the change to a tapered hole and stud shape resulted in good bonding properties. This was explained by the extra welding force generated by the tapered surfaces and the reduced tendency to shear due to the increasing stud diameter [97].

The first investigations and welding trials with a portable FHPP welding head have been described by Pauly [98]. In this work it has been successfully demonstrated that sound FHPP welds could be produced with portable welding equipment. The main difference in the welding equipment used by Pauly [98] to the one used by Nicholas and Thomas [94-96,101,103] is the possibility to apply rotational speeds up to 7000 rpm. Pauly [98] studied a number of different stud and hole configurations with encouraging results, although still leaving some lack of bonding at the bottom area of the hole at the end of the investigation. Aiming to further develop the process and assess the joint properties, Meyer [78] investigated similar welds using API 5L X65 (a HSLA C-Mn steel) as the base material. In this case, the shear planes mentioned by Nicholas [97] could be perfectly visualised with nickel tracer rods experiments (see Figure 2.18) carried out by Meyer [78]. The only difference between both approaches is that Nicholas [97] used big, stationary workshop machines, limited to low rotational speeds and high axial pressures, while the system employed in Meyer's work makes use of high rotational speeds and low axial pressures.

The nickel tracer in Figure 2.18 shows that at the beginning of the weld a significant amount of stud material is plasticised and pressed into the gap between stud and hole. According to the author [78], in the bottom area the nickel tracer is moved out of the centre over a wider area. This happened another three times along the weld with reduced amounts of nickel material. Those three areas depict shear planes. Between the shear planes the plasticisation of the nickel is considerably less. This means that after a certain amount of plasticised material is produced at the beginning of the weld, it is pressed up the gap between stud and hole. Owing to the frictional heat the stud material is heated as well. The plasticised material in the gap cools down in contact with the cold plate and increases the torque on the stud. As reported by Nicholas [97], this results in shearing of a certain amount of stud material. After this the process continues on top of the sheared stud material, creating a new HAZ, which can be seen in Figure 2.18. Meyer [78] further suggests that the number of shear planes and the distances between depends on the process parameters and the material properties (i.e. tensile strength at elevated temperatures).

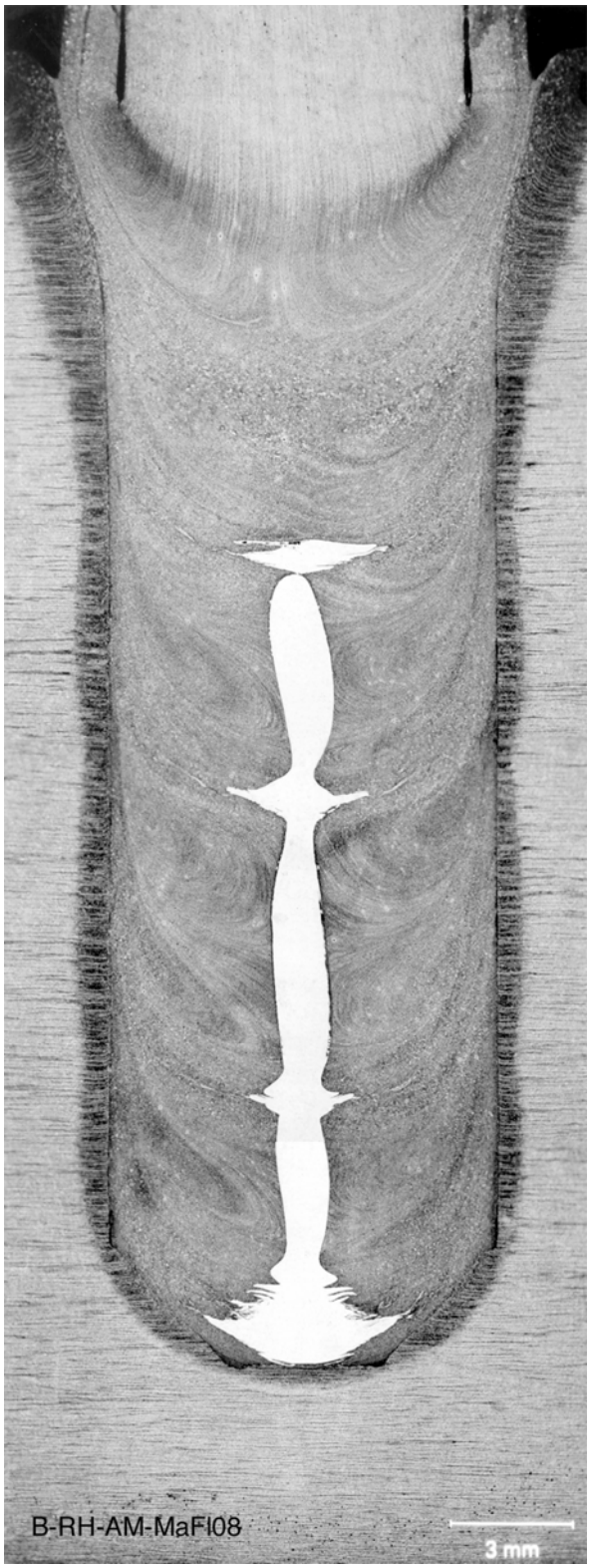

Figure 2.18: Macrograph of an API 5L X65 weld with a nickel tracer rod [78].

The patent on the process was granted to TWI in 1993 [94]. Thomas and Nicholas [95] presented further advantages of the process in the same year, focusing on its application in the heavy industry joining or repairing of thick steel structures. It was stated there are special advantages for FHPP with thick-walled structures, due to the fact that the amount of weld material needed is comparably low and, as in all friction welding processes, FHPP is readily mechanised and easy to automate.

The main application areas were indicated as the repair of steel structures in the construction as well as in the oil & gas industries, where some tests have already been done in order to use the process commercially. Single FHPP welds and Friction Stitch Welding (FStitchW - a series of successive FHPP welds) are being developed for sleeve welds and for hot-tapping saddles onto a large diameter pipeline or a substrate with gaps varying between zero and four millimetres. Recently, investigations have confirmed in both single FHPP (see Figure 2.19) and FStitchW (see Figure 2.20), the feasibility of the process to perform sound welds without a lack of bonding even in adverse conditions [100,111]. To date, any current investigations or research programs involving the application of FHPP in lightweight alloys have not been published.

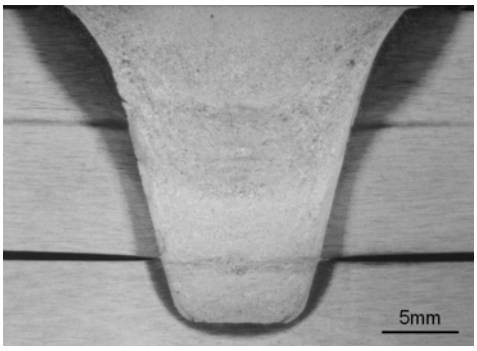

Figure 2.19: Macrograph of a single FHPP sleeve weld [100].

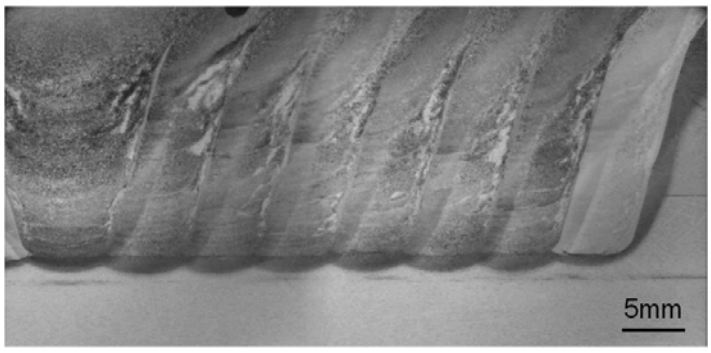

Figure 2.20: Macrograph of an FStitch weld conceived for the repair of large diameter pipelines [111].

The FHPP-related nomenclature is not fully defined so far, with a lot of similar names used for different process variations. The following list tries to define some of the terms related to FHPP. These phrases will only be used with these given meanings within this work.

Friction Hydro Pillar Processing (FHPP): Friction welding process where a rotational welding consumable is friction welded in a bore hole. The welding consumable and the bore hole can be of different geometries and shapes, including a tapered configuration. The welding consumable plasticises across the whole diameter and across the whole welding depth.

Friction Tapered Plug Welding (FTPW): Friction welding process where a through-thickness hole is closed by friction welding a rotational welding consumable to the sidewall of the hole. The welding consumable is only plasticised near the surfaces and not across the whole diameter. Usually, a tapered configuration for the consumables (plug) and hole is used.

2.7 FRICTION WELDING IN MAGNESIUM AND ITS ALLOYS

As presented in the earlier sections, Mg and its alloys play actually an increasing role mostly in the aeronautic and automotive industry. In order to further extend the number of applications where such alloys can be employed, the development of new manufacture procedures and an improvement of the available joining processes are necessary. Although its potential has already been demonstrated, Friction Welding of Mg alloys in Europe has been a lesser explored area, with no more than 7 publications [112-118]. However, most of those contributions deal very superficially with the subject, principally in terms of microstructural changes. Some other reports deal with dissimilar weldability of those alloys [119] while the rest show developments in the friction stir welding of Mg in similar and dissimilar configurations [120-124]. As a review, the main aspects presented in these publications will be discussed, however, keeping in mind the lack of specialised literature on the subject.

Most of the authors consider the friction weldability of Mg and its alloys as possible, although some references indicate it as not weldable [125] with direct drive welding systems (the motor remains attached to the workpiece during the whole welding cycle). According to Bowles *et al* [112], it is possible to join AE42 to AZ91 by friction tapered plug welding without considerable loss of hardness across the bonding line. On the AZ91 side of the weld, more significant microstructural changes are observed, since dynamic recrystallisation occurs from the weld line to approximately 500μm on this side of the weld. On the other hand very few changes in the microstructure are

evident on the AE42 side. Only a mechanical fragmentation of the intermetallic particles is observed. Such a process was used to improve local mechanical properties of an AZ91 cast component by joining AE42 studs. A series of investigations, involving not only the results reported by Bowles *et al* [112], but also many experiments on similar and dissimilar weldability using different friction welding processes (see Figures 2.21 to 2.24) were considered initial approaches, which have resulted in this study.

Figure 2.21: Picture of a similar FTP weld using AZ91D-T6 as base material [126].

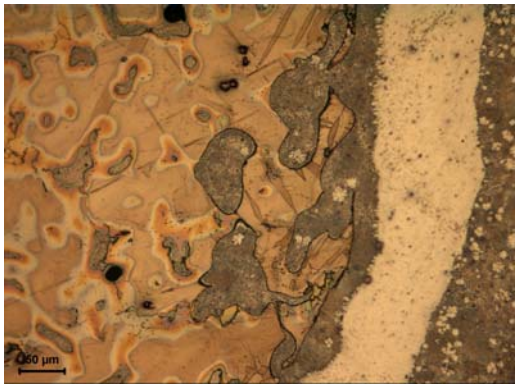

Figure 2.22: Macrograph of a dissimilar FHPP weld using an aluminium AA6082 stud and a magnesium AZ91D-T6 base plate [126].

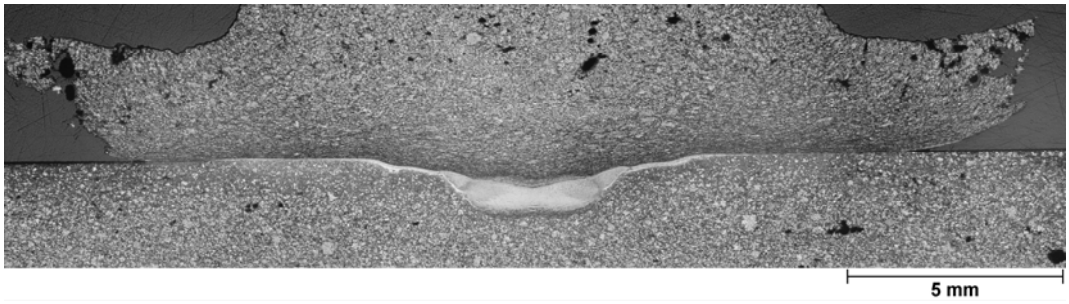

Figure 2.23: Macrograph of a dissimilar friction stud weld between a magnesium MRI153M and a magnesium AZ91D-T6 plate [127].

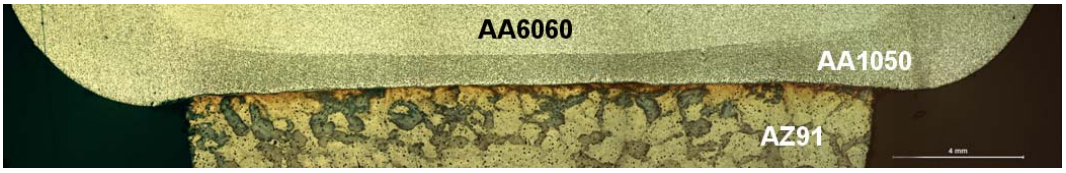

Figure 2.24: Macrograph of a dissimilar rotational friction weld between an AA6082 and an AZ91D-T6 stud. The presence of a pure aluminium AA1050 interlayer was also investigated [128].

Ogawa *et al.* [113] have shown, through several experiments in a wide variety of friction welding conditions with similar AZ31 welds, that the deformation heat input in the upset stage and upset loss can be used to evaluate the joint performance in terms of tensile strength. In this study, the minimum values of heat input and axial shortening to obtain sound joints are more than around 1500 J/sec and 17 mm respectively. Friction time, rotational speed and upset pressure must have expressive values for the welds to lie in the sound joints range. According to the author [113], in order to obtain an elongation and reduction of area equivalent to those of the base material, it is recommended to set a fairly high friction pressure and forging force without any excessively long friction time or high rotational speed.

Similar AZ31 joints were also studied by Kato and Tokisue [114]. According to the authors, the macrostructures in the vicinity of the weld interface are symmetrical in relation to the weld interface and joint axis regardless of the applied friction time. The fibrous structure running parallel to the extrusion direction, as observed in the base metal, shows a change of structural flow into the flash discharge direction, i.e. the circumferential direction. It was also reported that this fibrous structure disappears in the region very near to the weld interface. Concerning mechanical properties, the hardness is, in the weld interface, equivalent to that of the base material and seems not to significantly vary along the weld interface. Furthermore, the authors assure that tensile strength and elongation tend to be improved with an increase in the friction pressure and heating time.

Pinheiro *et al.* has demonstrated in a series of studies [73,77,126,127,129] the feasibility of the process to join Mg-Al-RE alloys. These investigations have demonstrated that sound welds can be obtained, with a weld region characterised by a thin layer of dynamically recrystallised grains without any unexpected particles or phases precipitated at the grain boundaries. Additionally, SEM analyses have indicated a complete disintegration of the typical lamellar BM structure along the recrystallised zone, extended partially to the thermo-mechanically affected zone. Fully satisfactory bonded joints, in terms of tensile strength, were obtained with no joint collapsing at the welding line.

Friction weldability of Mg alloys has also been investigated recently by Draugelates *et al.* [115,116,118]. According to these experiments, an increasing rotational speed reduces the upsetting rate up to a value where the speed has no further influence, i.e. the upsetting rate achieves, after a certain speed, a quasi-stationary value and cannot be further influenced by changes in the rotation. Similar to the investigations carried out by Kato e Tokisue [114], Draugelates *et al.* [118] observed that the microstructure in magnesium friction welded cast alloys is completely recrystallised along the welding area, with the grains reoriented to a direction parallel to the welding interface. Furthermore, in the AZ91 alloy, the $Mg_{17}Al_{12}$ phase, previously present in the grain boundaries, is dissolved along the bonding area due to the higher temperatures achieved during the process. In terms of mechanical properties, heating times of 20 s lead to the highest performance welds, with respective failures taking place always in the base material outside the welding area (see Figure 2.25).

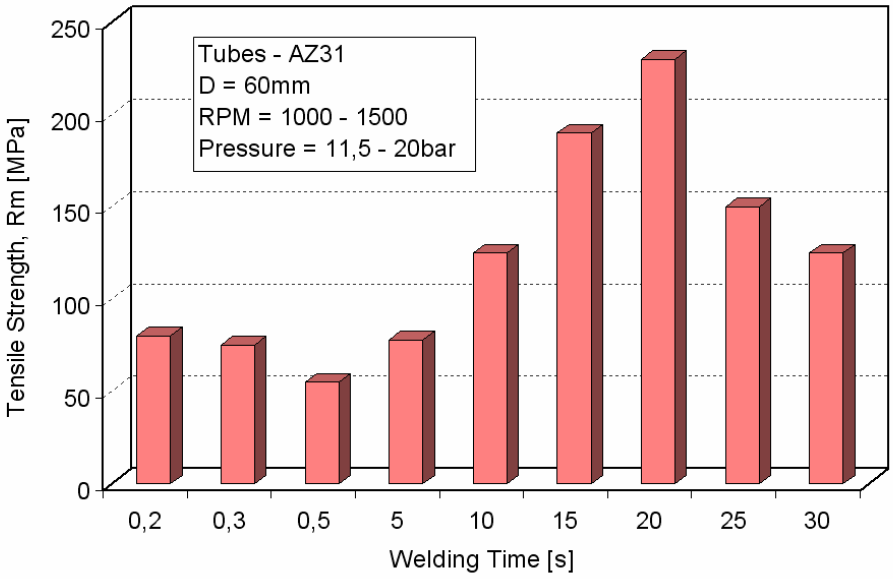

Figure 2.25: Tensile strength vs. heating time [118].

3 EXPERIMENTAL

As presented in Figure 3.1, the experimental strategy adopted in this study consisted of an initial exploratory development of the FHPP technique. In this initial phase, different materials and several geometries were investigated using a range of parameters, set in order to determine the outline of a suitable window in which this study would be further developed. After this initial stage, three materials were selected for the main experimental phase, based on the commercial importance associated with its use within the objectives proposed in this work.

The second experimental phase consisted of welding these materials, divided into two groups: In the first group, similar welds were produced while varying the welding pressure, considered the most influential welding parameter. As the effects of the welding pressure would be investigated by the first group, three material combinations were welded in a second group, using two upsetting variations with all other variables kept constant.

In the main experimental phase, the work was divided into four topics: *Process, Microstructural Development, Properties and Performance*. For each topic, suitable tests were proposed and performed. By coupling the single results of these individual topics, conclusions on the bonding mechanisms, structure/properties relationships and service behaviour were arrived at. Based on the information gained during the work, a design catalogue has been outlined, where the resultant properties are compiled, based on the process welding parameters.

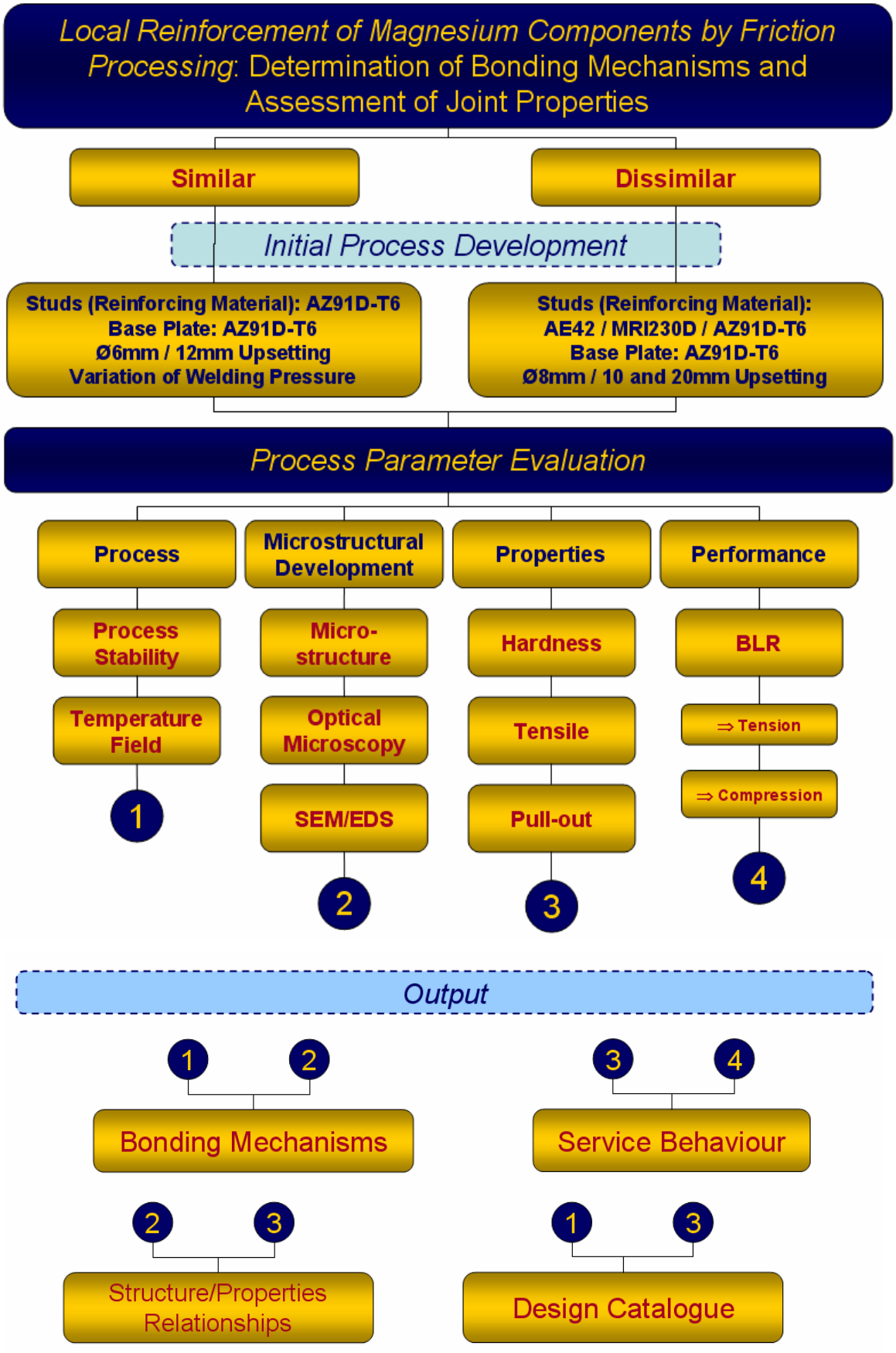

Figure 3.1: Summarised experimental strategy of the present work.

3.1 BASE MATERIALS

Three different Mg alloys have been used within this study. For all the experiments the alloy AZ91D-T6 was used as the base plate. The material was delivered in the form of cast ingots, heat treated (413 °C/20 hs) and artificially aged (168 °C/16 hs) to T6 condition according to DIN65582 [130] (ASTM B 661-03) [131] since the mechanical properties of AZ91-F, as fabricated, is shown to vary across a very wide range.

For welding studs, AZ91D-T6, MRI230D and AE42 cast ingots were used. Further heat treatment of MRI230D and AE42 ingots (see Figure 3.2) was empirically estimated, so as not to exert any positive influence on the performance of the alloys. Therefore, in both cases the material was used in the "as fabricated" condition. A detailed description of the microstructure and properties of the base materials is presented in Section 4.1. Cast ingots have a coarse microstructure with consequently limited mechanical properties. Despite this, the base materials were chosen in this form, since the changes imposed by the welding process would significantly enhance their properties.

3.2 STUDS AND HOLES CONFIGURATION

Based on previous studies carried out by Pauly [82] and Meyer [78], tapered studs (reinforcing material) with a 10° taper angle, 6 mm and 8 mm tip diameter studs were chosen. Similar and dissimilar configurations involving these two different stud geometries were tested. Figure 3.3 shows one of the stud configurations (8 mm tip diameter) used within this study.

Holes with 10° and 20° taper angles and with 6 mm and 8 mm bottom hole diameters were used. Figure 3.4 illustrates a hole with 20° taper angle and 8 mm bottom diameter. Lateral openings were drilled in the base plate with 0.5 mm distance to the borehole at 6 mm and 11 mm from the plate surface. Type K thermocouples with 1.0 mm diameter were then placed in these openings and connected to the thermocouple measuring system (described in detail in Section 3.4.2).

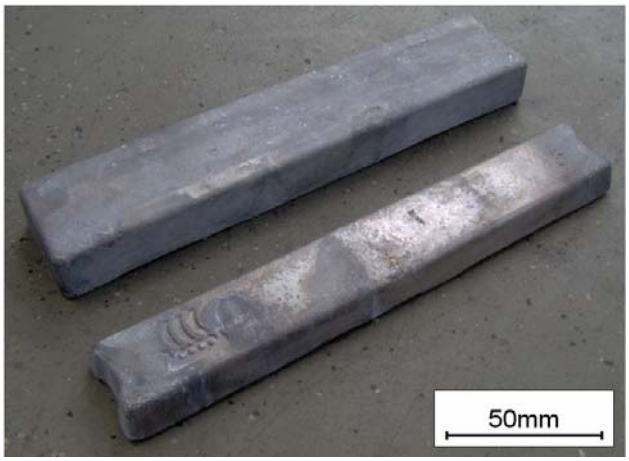

Figure 3.2: AE42 and MRI230D Ingots.

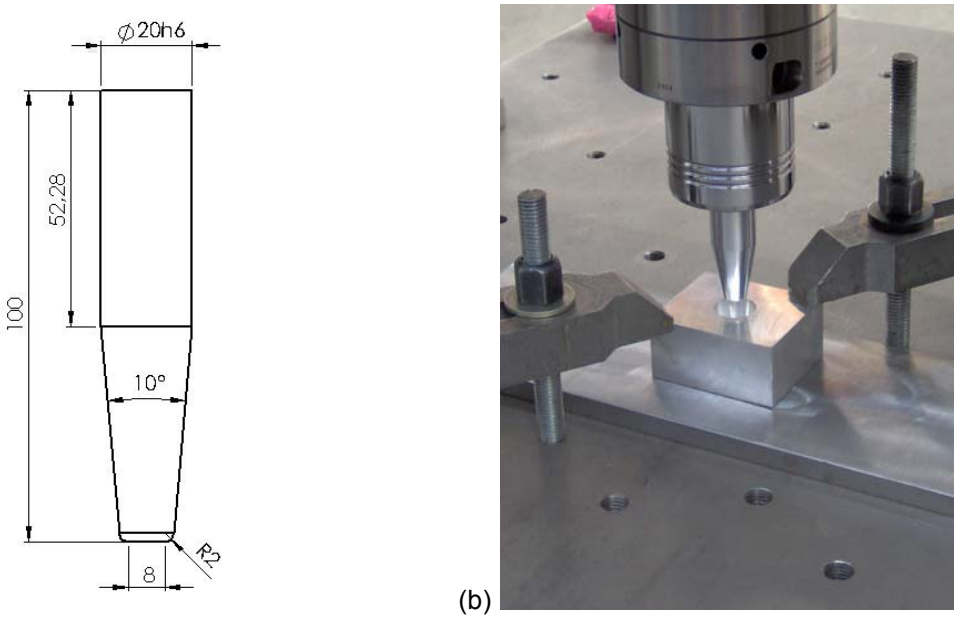

(a) (b)

Figure 3.3: In (a) the configuration of the tapered stud and in (b) the stud clamped on the welding head before the welding.

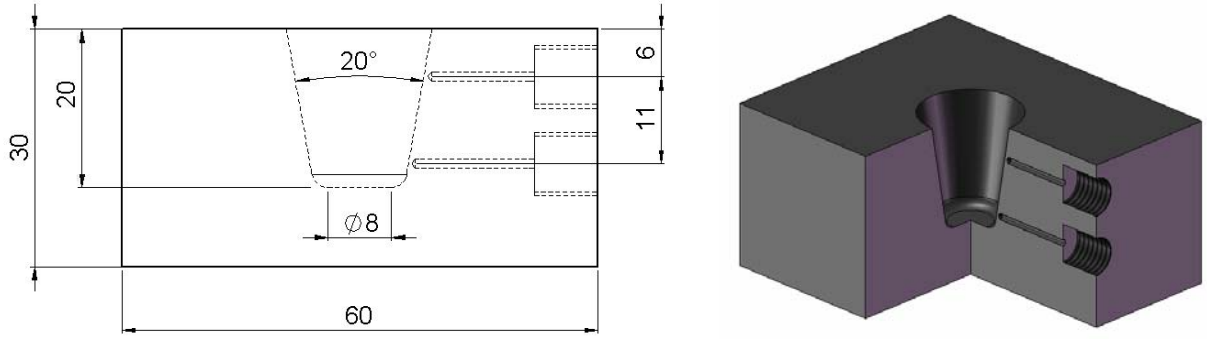

(a) (b)

Figure 3.4: Hole geometry combinations.

3.3 WELDING SYSTEM

The welding system used, whose components are briefly introduced below, can be described as a hydraulic powered friction welding machine, which was designed and built as a portable equipment for underwater use by Circle Technical Services Ltd. in Aberdeen. The system is capable of applying 40 kN axial load at speeds up to 8000 rpm (see Figure 3.5) and consists of four major components: Hydraulic Power Unit (HPU), valve block, welding head and control system. The weld cycle is electronically controlled, with the functions monitored and displayed on-line on a monitor. The welding can be classified as a direct drive system in which the friction welding process is controlled by the upsetting distance, which is the amount of plasticised material pressed out during the welding cycle (distance that the hydraulic ram moves out).

HPU: In the configuration used, the HPU's pump is driven by a hydraulic power pack with a 50kW electric motor, supplying up to 115 l/min at 315 bar. The maximum oil pressure is continuously adjustable, while the pump automatically adjusts the flow.

Valve block: The valve block regulates the oil flow and pressure supplied by the HPU. Electrically driven proportional valves on the valve block control all operations of the weld head. Besides additional safety valves, three pressure transducers are used to monitor the mainline pressure (supplied by the HPU) and the two sides of the piston in the welding head (axial force). Supplementary to this standard configuration, a number of additional sensors were installed, to allow a comprehensive monitoring of all system variables. Two pressure transducers are used to measure the pressure across the hydraulic motor of the welding head.

Welding head*:* The portable head itself is approximately 600 mm long and 160 mm in diameter. It consists mainly of a hydraulic fixed-displacement motor on the upper side and a hydraulic piston inside the lower cylinder. The piston can move the lower part of the shaft by a nominal 50 mm in the axial direction and applies the pre-set axial force. Welding studs (consumables) are fixed in the chuck at the lower end of the shaft. A metal proximity sensor on the shaft inside the housing monitors the rotational speed, while a linear proximity sensor (LPS) measures the axial movement inside the piston.

The weld head is attached to a welding rig and support structures by a bayonet connection on the housing. Figure 3.5 and Figure 3.6 show respectively the welding head itself and the complete welding equipment mounted on the rig.

Figure 3.5: Circle Technical Service's HMS 3000 Welding Head.

Figure 3.6: Welding equipment.

Control System: A PC-based control system acquires the sensor information (rotational speed, axial position and piston pressure) and controls according to the settings of the welding parameters. This control system regulates the welding process's force and rotational speed. The upsetting rate is a result of these parameters. The pre-set welding parameters (rotational speed and axial pressure) can be changed according to the actual upsetting a number of times during one weld. This gives a very flexible tool to respond to changes in the welding conditions during a single weld (i.e. changes in geometry). Process parameter sets are saved as "projects" by the control system. They have to be defined before the actual weld takes place. The welding parameters are displayed in real time during a weld and stored within the projects.

3.4 DATA ACQUISITION SYSTEM (DAS)

3.4.1 Data Recording System – DRS/Process Stability

As mentioned in Section 3.3, an additional measurement system was employed for acquisition and processing of process parameters and complementary data. This system, denominated the Data Recording System (DRS), was used to measure and store the welding parameters and additional signals for every weld (rotational speed, axial position of piston, hydraulic position on both sides of the piston, main line flow, the oil temperature in the main line, main line hydraulic pressure and hydraulic pressure to and from the weld motor). The system is based on a standard PC connected to National Instruments hardware for signal conditioning. The software was programmed in LabView and gives real-time diagrams from all signals generated during the welding. Data can be stored and exported into standard data processing software for further analysis and for complementary evaluation. Owing to the fact that all sensors are processed by a single unit, including signals generated by the welding control system, reference across all data (welding parameters and system variables) is possible. The DRS records data at 100 Hz per channel. Data files were stored for every weld produced in this study. These files were than evaluated and a precise analysis of the stability and consequent repeatability of the welding system within the welded range could be established.

3.4.2 Temperature Measurements

For experiments on thermal phenomena, a special measuring system based on signals generated by thermocouples was devised, programmed and assembled. This is a PC-based measuring and data acquisition unit. The PC is connected to National Instruments SCXI-hardware for signal conditioning. The software was programmed in LabView and generates real time diagrams during measurement. Data can be stored and exported for further evaluation and analysis. Up to 32 thermocouples can be recorded simultaneously, with a maximum of 50 Hz per channel. Temperature measurements were started simultaneously with the HMS control system and all recorded at 50 Hz. Calibration curves for the different types of thermocouples were already implemented in the LabView software package to convert the electromotive force (mV) into the appropriate temperature (°C).

As previously presented in Figure 3.4, FHPP welds were performed using 2 type K thermocouples with 1.0 mm diameter placed 0.5 mm away from the borehole at 6 mm and 16 mm from the top base plate surface and connected to the thermocouple measuring system. The main objectives of these measurements were to establish the influence of welding parameters and geometry combinations on the temperature cycle and therefore on mechanical properties of the welded joints.

3.5 TESTING EQUIPMENT AND PROCEDURES

3.5.1 Welding Procedure

The welding studs and plates were permanently marked, prior to preparation for a welding trial. Studs and plates were then degreased and cleaned with Acetone to avoid any influence of machining fluids. The stud was fixed in the weld-head chuck and aligned with the hole in the base plate. All welding parameters were previously typed into the control system and could then be loaded by reference number. The DRS system and the weld control are manually started and the weld is performed according to the given welding parameters. The rotational speed is started first and after the required speed is reached, the piston is moved down and the stud then moves into the hole and makes contact with the cavity bottom. From this point on, the axial movement is measured as upsetting and is used to control the welding process. When the full upsetting distance is reached, the rotational speed is stopped and the axial pressure is increased for a further six seconds. Afterwards, the pressure is released and the specimen can be taken out of the fixtures.

3.5.2 Metallurgical Characterisation

3.5.2.1 Optical Microscopy

Macro and microstructural characterisation has been conducted on both base materials and cross-sections of welded specimens. This assessment included different welding areas following the ASTM E3-95 [132] and ASTM E-340-95 [133] standards. Welded specimens were cut at the centre of the stud across the base plate, followed by grinding and polishing with diamond paste down to 0.05 μm using a Phoenix 4000 automatic polishing machine and based on standard metallographic techniques. Two different etching solutions were subsequently used for

characterising the joints; first an acetic glycol based solution, used to assess grain size, and another picric acid based solution, basically used to reveal details of the microstructure across the welded samples. Micro and macrographs were made using a LEICA DM IRM microscope equipped with the software LEICA Q550IW. Chemical composition was ascertained using inductively coupled plasma source mass spectrometry (ICP-MS), which is a very sensitive analytical method for rapid multi-element determination. The quantisation limit was in the worst cases 0.01 % for silicon followed by iron with 0.005 % inaccuracy.

3.5.2.2 Grain Size

Grain size measurements were also carried out, in order to firstly evaluate the changes imposed by the friction process on the stud material and secondly to investigate the influence of the welding parameters on the resultant microstructure, by scanning the grain size distribution across the joint. Consequently, a relation between microstructure and mechanical properties could be ascertained. The system used to assess grain size was a LEICA DMI 5000 microscope with an image analysis system (a4i-Analysis) interfaced to it. According to ASTM E-112-96 [134] grain size was measured in 9 different positions across the transversal section, as illustrated and indicated in Figure 3.7.

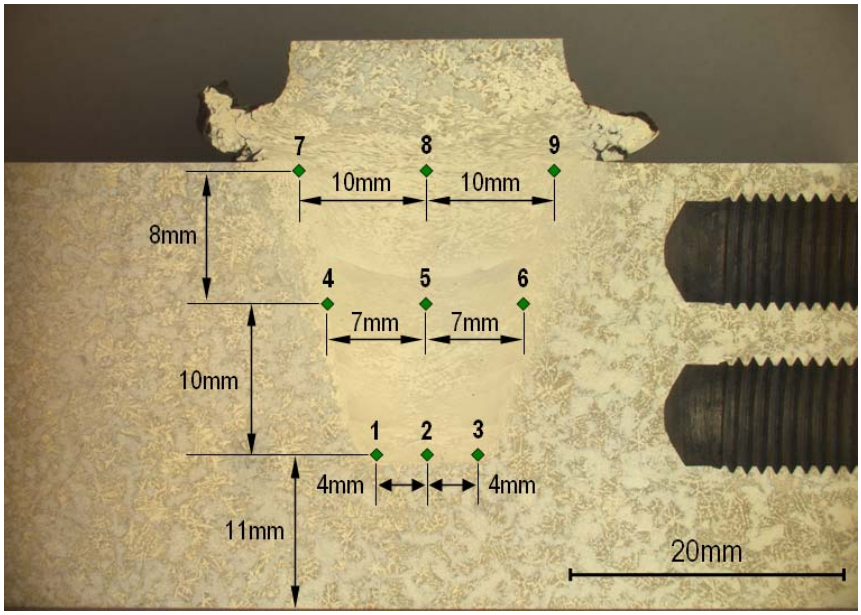

Figure 3.7: Position of grain size assessment across the welded joint.

3.5.2.3 Scanning Electron Microscopy/EDS

SEM/EDS was used in this investigation to characterise base materials and identify second phase particles as well as when high resolution and high depth of field images were necessary during the assessment of welded joints. The microstructural analysis was performed using two types of imaging signals – back-scattered electrons (BSE) and secondary electrons (SE).

Specimen preparation was identical to that used for macrostructural characterisation. A Zeiss DSM 962 SEM was used during the analysis and the welded specimens were not embedded, in order to have the appropriate electric contact between the sample (cathode) and the SEM table (anode).

Energy dispersive spectroscopy (EDS) was performed to assess local chemical composition along the joint line. Second phase particles were also investigated, in the lamellae particles originally from the BM as well as in fractured particles in the recrystallised zones of welded samples.

3.5.3 Hardness Testing

Microhardness testing using conventional Vickers hardness measurements was performed on base material and across the joints at specific locations according to DIN EN ISO 6507 [135] and DIN EN 1043-2 standards [136]. The measurements were taken in three rows at 2 mm, 10 mm and 18 mm from the top surface and three columns in the middle, at -4 mm and 4 mm from the stud central axle, as illustrated in Figure 3.8. A load of 200p was applied for 30 s (HV0.2) with a distance between indentations of 0.5 mm. The surfaces to be tested were polished with 4000 grit SiC paper, which is a polishing paper with 3 μm average particle diameter, and etched, in order to enable the correct identification of the different welding zones. Hardness tests were performed on an EMCOTEST M1C010 testing machine with computer controlled specimen positioning and indentation.

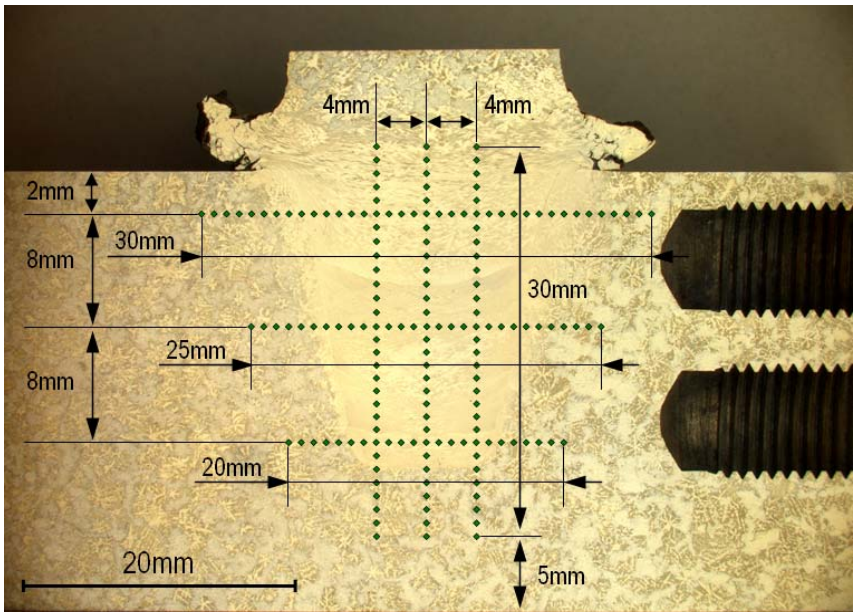

Figure 3.8: Position of hardness profiles on welded specimens.

3.5.4 Pull-out Testing

Pull-out tests were also performed in the welded joints based on the pull-out standards found on the literature [137,138]. Pull-out specimens were produced from welded samples with the rest of the stud machined similarly to the half of a “Form B” (see DIN 50125 [138]) round tensile sample. Figure 3.9 shows the pull-out specimen geometry and the position of the sample in relation to the joint. Figure 3.10 shows the clamping system developed for the test as well as the complete assembly prior to testing. Tests were performed with a deformation rate of 0.5 mm/min using a Schenck-Trebel RM100 with 100 kN load capacity.

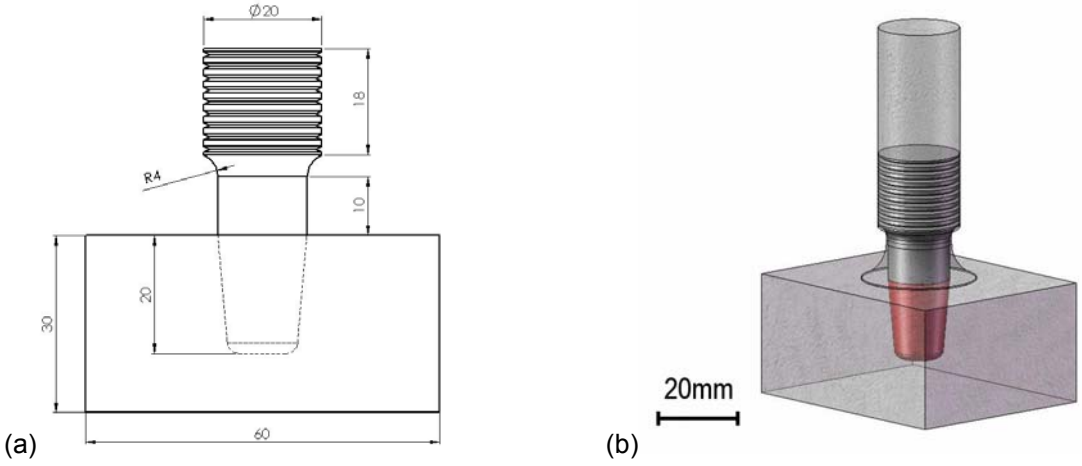

Figure 3.9: Pull-out specimen geometry (a) and position of the sample in relation to the joint (b).

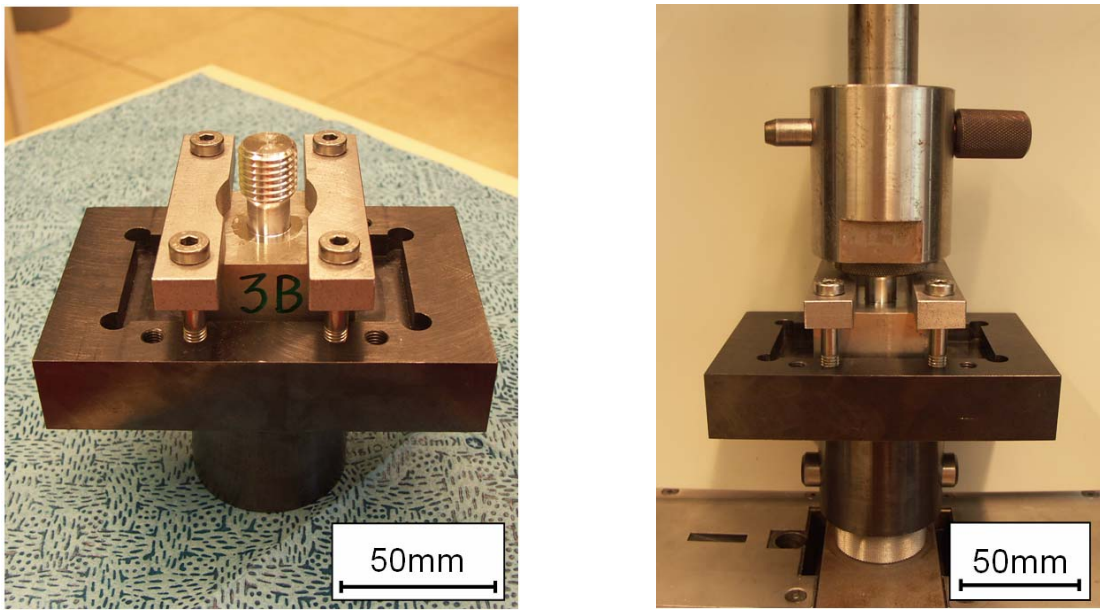

(a) (b)

Figure 3.10: Clamping system developed for the pull-out tests. In (a) the sample attached to the lower fixture and in (b) the joint completely mounted on the machine prior to testing.

Considering the welded area as a function of the hole's geometry, pull-out tests were performed to calculate the magnitude of stresses acting directly on the joint, as the samples were expected to collapse within the gauge length. Welded surface areas, as is highlighted in red in Figure 3.9, were calculated in both cases using the 3D mechanical design software SolidWorks and are presented below:

$A_{hole\ [6\ mm,\ 20°]} = 872.77\ mm^2$

$A_{hole\ [8\ mm,\ 20°]} = 1029.35\ mm^2$

3.5.5 Transversal Tensile Testing

Specimens for tensile testing were precision machined from the welded samples, as well as from the base material, by spark erosion (EDM – electric discharge method) with the welded interface stud/base plate located exactly in the centre of the tensile specimen (see Figure 3.11). Specimens were first spark eroded and after lathed according to DIN 50125 – B6 x 30 [138] (see Figure 3.11(a)).

Two specimens were machined from each joint and tested in laboratory air at room temperature, according to the DIN EN 10002 standard [139]. The equipment used for testing the samples was a screw-driven tensile testing machine Schenck-Trebel RM100 with 100 kN load capacity. The traverse speed of 0.5 mm/min and the displacement was recorded by a laser system coupled to the testing machine. Five specimens were tested for each welding condition. Figure 3.11(b) represents the position where the tensile specimen would theoretically intersect the stud and illustrates both bonding lines between the base plate and the stud material.

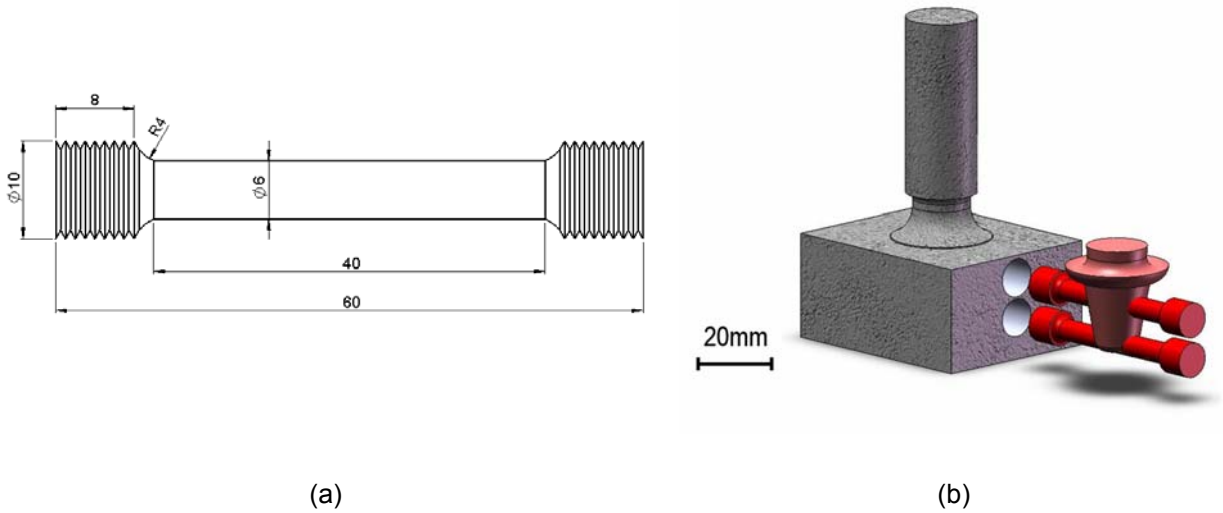

(a) (b)

Figure 3.11: Tensile specimen geometry (a) and position of specimens relative to the joint (b).

3.5.6 Bolt-Load Retention Testing (BLR)

Bolt-Load retention tests were carried out, in order to simulate and further investigate the loss of pre-load force used during the assembly of Mg transmission cases. Transmission cases, typically joined by pre-loaded bolts, suffer from stress relaxation, which could thus adversely impact the sealing of the joint. This issue has been extensively reported on the literature [44-46,140-142]. A through-bolt type of bolt joint configuration was used with a 30x30x30 mm hardened steel flange and a centred 10.5 mm diameter hole, according to DIN EN 20273 [143]. Figure 3.12 shows the geometry of the BLR specimen (Figure 3.12(a)) and the position of the case relative to the joint (Figure 3.12(b)). Furthermore, the threaded hole was positioned as centred on the reinforced area.

The case was a 50x60 mm block, 18 mm thick and with the threaded hole concentric with the block. The base materials and welded samples were tested for further comparison at 125 °C and 175 °C, in accordance with ASTM E 328-86 [144]. Specimens were torqued with 40/60 Nm and 25/35 Nm, for steel and Al bolts respectively, at room temperature and held one hour before being put in the oven. This waiting period minimises the effects of short-term relaxation following the tightening of bolted joints, as suggested by Bickford [145]. Tests were conducted over periods of 100 hours, using Al and steel bolts fabricated according to DIN EN ISO 7989 [146] and DIN EN ISO 4014 [147] standards respectively. Ultrasonic measurement equipment BoltMike III [148] was used to monitor the initial and remaining fraction of load. With this equipment, an ultrasonic pulse, generated in the transducer, is transmitted into the fastener. The pulse travels down the length of the fastener and is reflected back from the end. The BoltMike III measures the total pulse transit time, and based on the physical properties of the fastener material, calculates the tension and clamp load according to ASTM E1685-00 [149].

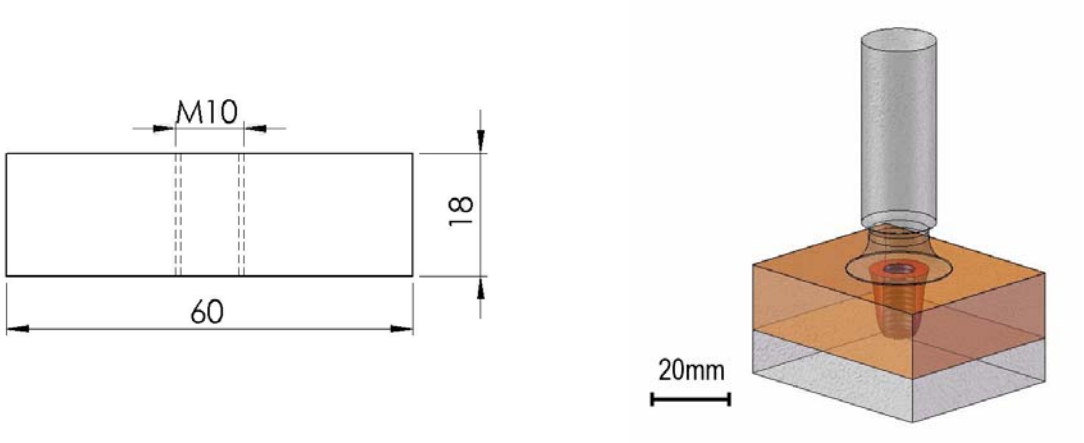

(a) (b)

Figure 3.12: Schematic of BLR sample for tension. In (a) the geometry of the case and in (b) the position of the case in relation to the welded sample.

In order to reproduce experiments carried out by Westphal [35], some insights were provided by the reinforced specimen being positioned in the upper part of the joint. This configuration would simulate the fastening of an Mg gearbox directly into an Al (AlSi9Cu3) engine block, as reported recently [6]. Figure 3.13 illustrates the configuration used, which was tested at different temperatures and with different bolt materials.

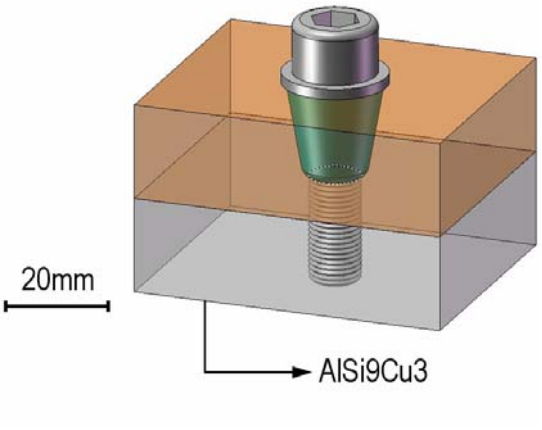

Figure 3.13: Schematic of BLR test with the reinforced component in the upper part.

3.5.7 Creep Testing

Bearing in mind the main technological application addressed in this work and knowing that joint performance is directly related to creep resistance, the creep behaviour of welded samples in all three different material combinations was evaluated. Welds were produced using the same procedure previously discussed. Creep test samples with ∅6x15 mm were extracted from the extruded material (denominated lower samples – see Figure 3.14) and from the upper stud area as a reference (denominated upper or reference samples). Three temperatures (125 °C, 150 °C and 175 °C) and a constant compression load of 80 MPa were used.

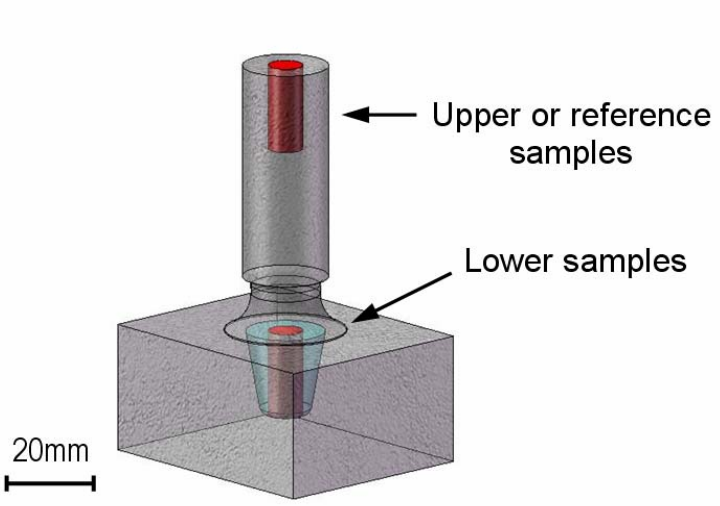

Figure 3.14: Positions where creep samples were machined.

Creep results are presented in terms of creep curves and activation energy. In general, the dependence of the minimum or steady state creep rate $d\varepsilon/dt_{min}$ on stress and temperature can be expressed for most metals as:

$$d\varepsilon/dt_{min} = A_0.\exp(-Q_c/RT)\sigma^n, \qquad \text{[Equation 3-1]}$$

where A_0 is a material constant, σ the applied stress, n the stress exponent, Q_c the activation energy for creep, R the gas constant and T the absolute temperature.

Based on Equation 3-1, in order to determine the activation energy, which represents the necessary energy to activate the creep process, the minimum creep rate $d\varepsilon/dt$ should first be calculated [27]. To calculate $d\varepsilon/dt_{min}$ one can define in the creep curves the region with the minimum creep rate, from which the slope of the curve in the selected interval gives the minimum creep rate directly. After $d\varepsilon/dt_{min}$ has been calculated, the activation energy can be determined by plotting $\ln(d\varepsilon/dt_{min})$ versus $[T^{-1}]$. The linear curve fitting these data has the slope $-Q_c/R$, from which the activation energy can subsequently be calculated. For all the combinations, the activation energy was calculated.

4 RESULTS

4.1 METALLURGICAL AND MECHANICAL CHARACTERISATION OF BASE MATERIALS

4.1.1 Base Material AZ91D-T6

Table 4.1 shows the chemical composition of heat treated AZ91D.

Table 4.1: Chemical composition of the AZ91D ingot (T6 condition).

	Chemical composition							
Element	**Al**	**Zn**	**Si**	**Cu**	**Mn**	**Fe**	**Others**	**Mg**
Actual Composition [wt.%]	8.5	0.63	0.04	0.005	0.22	0.013	---	Bal.
Nominal Composition [14] [wt.%]	8.5 9.5	0.45 0.90	0.05	0.015	0.17min	0.004	0.01 O.E.	Bal.

Micrographs of the heat treated base material, shown in Figure 4.1, expose the irregular structure dominated by the typical lamellae eutectic morphology surrounded by isolated islands of a divorced eutectic structure, as described by [14]. The microstructure is formed basically by a lamellar interdendritic $Mg_{17}Al_{12}$ precipitate (β-phase) produced throughout the grains of Mg solid solution (α-phase) by artificial aging. Particles of both Al-Mn (grey) and Mg_2Si (blue) are also reported to be typically found in Mg-Al-Zn alloys and this has been partially confirmed. Additionally, some isolated islands of massive $Mg_{17}Al_{12}$ compound (white) were also identified. EDS was performed to assess local chemical composition. Points are indicated in Figure 4.1(b), (c) and (d) and identified as points 1 through 11. The corresponding results are shown in Table 4.2. The average grain size varied from 200 µm up to 600 µm in both the central and the outer regions of the ingot.

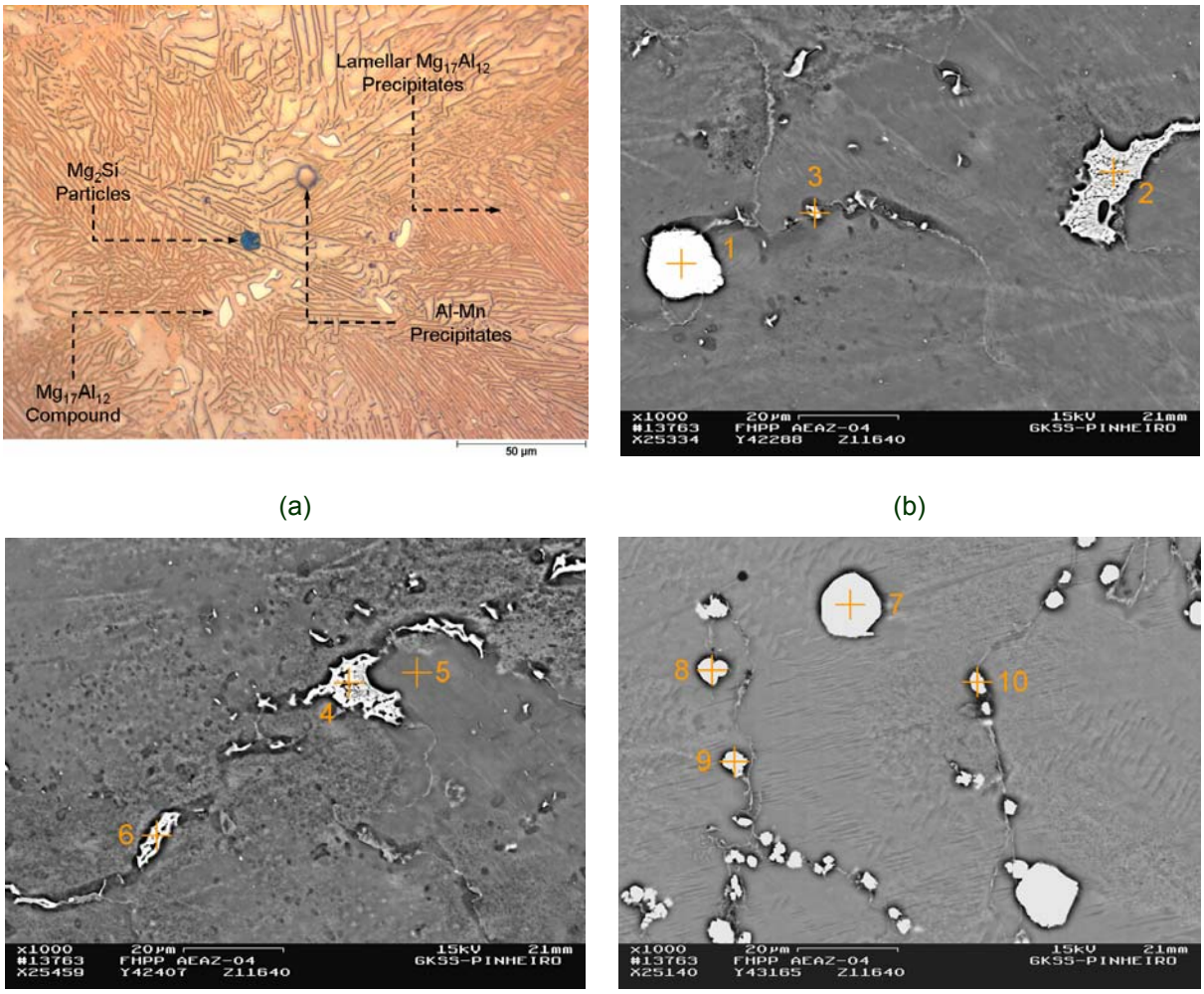

(a) (b)

(c) (d)

Figure 4.1: Micrographs of AZ91D-T6 after heat treatment in (a) light microscope and EDS analysis of the particles found in the base material (b), (c) and (d).

Table 4.2: Results of EDS analysis at 11 different points within the base material AZ91D-T6.

	Mg(wt.%)	Al(wt.%)	Mn(wt.%)	Zn(wt.%)	Si(wt.%)
Point 1	4.80	50.64	44.56	---	---
Point 2	62.89	31.48	---	5.63	---
Point 3	65.37	30.37	---	4.27	---
Point 4	61.68	32.42	---	5.90	---
Point 5	89.05	10.95	---	---	---
Point 6	61.45	32.44	---	6.11	---
Point 7	1.35	36.47	58.87	---	0.54
Point 8	2.10	40.1	55.37	---	0.50
Point 9	2.51	43.51	48.84	---	0.49
Point 10	2.30	40.44	56.59	---	0.68
Point 11	2.28	36.74	58.94	---	0.49

Table 4.3 lists some of the mechanical properties assessed during mechanical characterisation, while Figure 4.2 presents tensile curves obtained for the BM. Strength and elongation values ranging respectively from 140 MPa to 210 MPa and from 0.5 % to 3 % were obtained, with the upper samples clearly presenting higher strengths.

Table 4.3: Mechanical properties of the AZ91D ingot (T6 condition).

	Mechanical Properties			
	Rm [MPa]	**$Rp_{0,2}$ [MPa]**	**A[%]**	**Hardness**
AZ91D-T6 (Tested)	140 - 210	100 - 140	0.5 – 3	65 – 80 HV

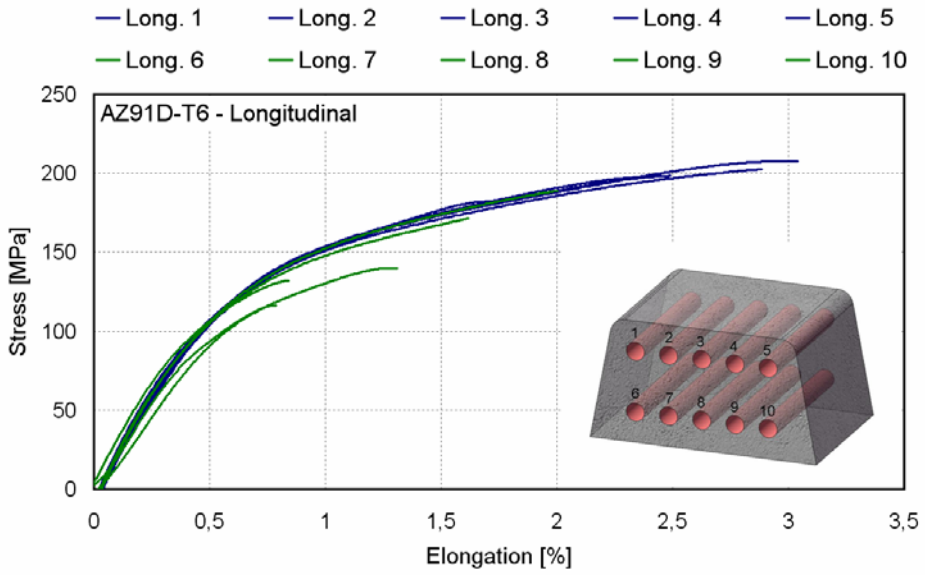

(a)

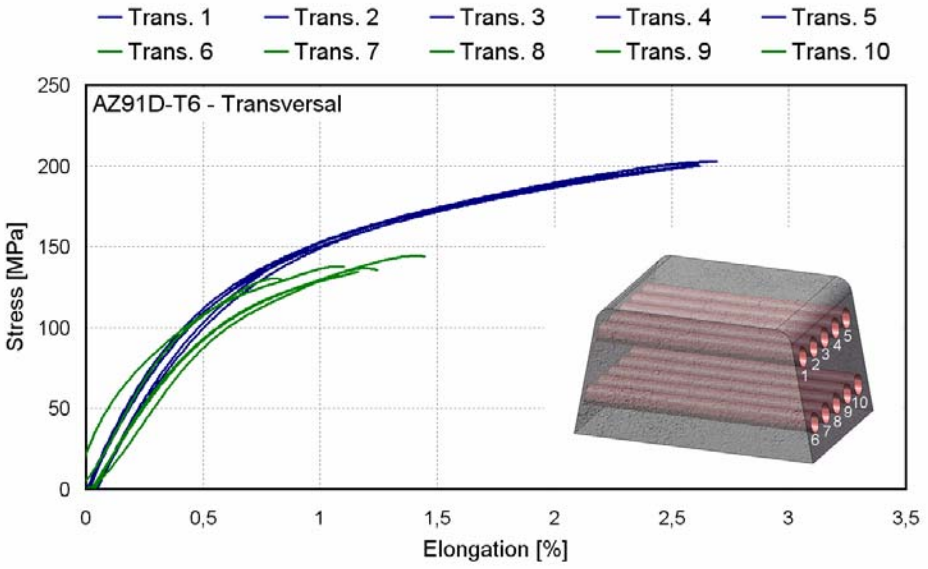

(b)

Figure 4.2: Stress-elongation curves for Mg AZ91D-T6 tensile samples. In detail, the longitudinal (a) and transversal (b) direction.

4.1.2 Base Material AE42

Table 4.4 lists the chemical composition of the base material AE42, while Figure 4.3 presents the typical base material (BM) morphology, with selected regions for EDS analysis.

Table 4.4: Chemical composition of the AE-42 ingot (cast condition).

	Chemical composition								
Element	**Al**	**Mn**	**Si**	**Ce**	**La**	**Ne**	**Pr**	**Others**	**Mg**
Actual Comp. [wt.%]	4.0 4.3	0.44 0.54	0.01	1.3	0.61 0.64	0.38 0.42	0.14	Zn 0.003	Bal.
Nominal Comp. [8] [wt.%]	3.6 4.4	≥ 0.27	≤ 0.01	2.0 – 3.0 RE				---	Bal.

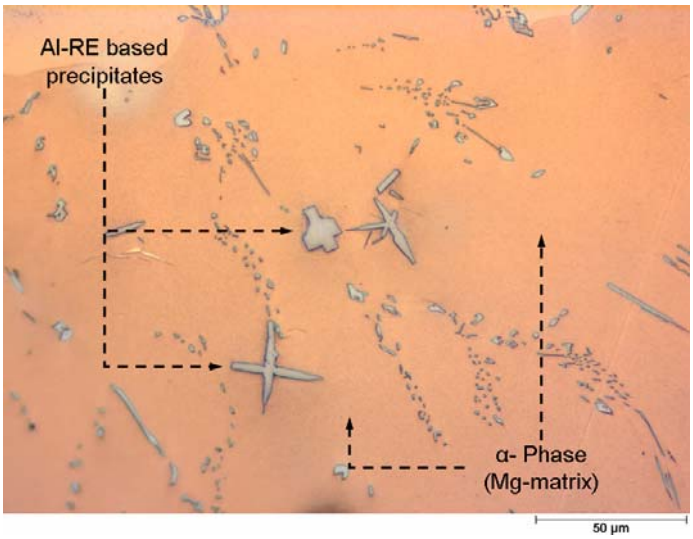

(a)

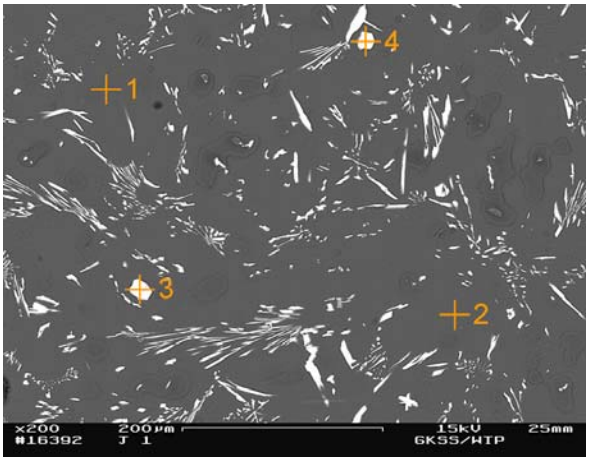

(b)

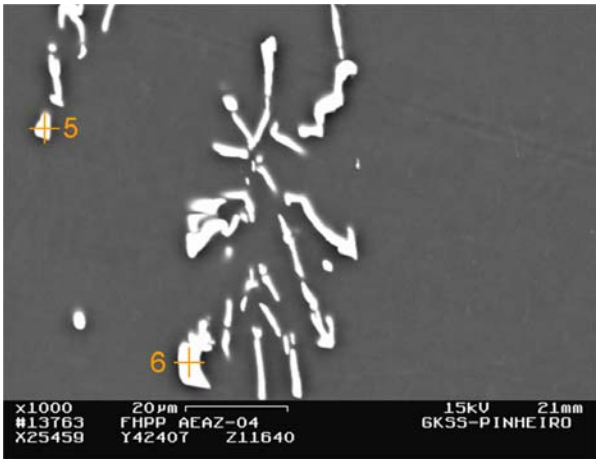

(c)

Figure 4.3: Micrographs of AE42 (a) and points for EDS analysis (b) and (c).

The ingot's material is generally characterised by a pronounced dendritic structure in the matrix, in combination with dispersed lamellae and particulate second phase particles of $Al_{11}RE_3$, preferentially located along the grain boundaries [29,150,151]. Figure 4.3(b) and (c) show backscattered electron images of the BM, evidencing second phase particles with different sizes, randomly distributed within the Mg matrix. Points subjected to EDS analysis are indicated and identified as points 1 through 6. The corresponding results are shown in Table 4.5.

Table 4.5: Results of EDS analysis at six different points within the base material AE42HP.

	Mg (wt.%)	**Al (wt.%)**	**Si (wt.%)**	**Mn (wt.%)**	**RE (wt.%)**
Point 1	98.80	1.20	---	---	---
Point 2	98.37	1.63	---	---	---
Point 3	0.32	34.47	---	41.25	23.96
Point 4	0.55	32.24	1.38	38.59	25.48
Point 5	4.45	33.32	---	0.60	59.63
Point 6	4.04	34.33	---	0.68	58.47

Table 4.6 presents some relevant mechanical properties of the base material AE42, while Figure 4.4 presents the tensile curves recorded during material characterisation. In the longitudinal direction, the samples investigated presented tensile strengths varying between 120 MPa and 130 MPa, with elongations values ranging from 5 % to 7 % in the upper part of the ingot. On the other hand, in the lower areas, similar strengths of around 90 MPa were observed, however with the elongation varying between 3 % and 6 %. In the transversal direction, tensile strength and elongation presented values varying between 85 MPa and 130 MPa and between 3 % and 7 % respectively, independent of the position in relation to the ingot.

Table 4.6: Mechanical properties of the AE-42 ingot (cast condition).

	Mechanical Properties			
	Rm [MPa]	**$Rp_{0,2}$ [MPa]**	**A[%]**	**Hardness**
AE-42 (Tested)	85 - 130	---	3 - 7	39 - 49

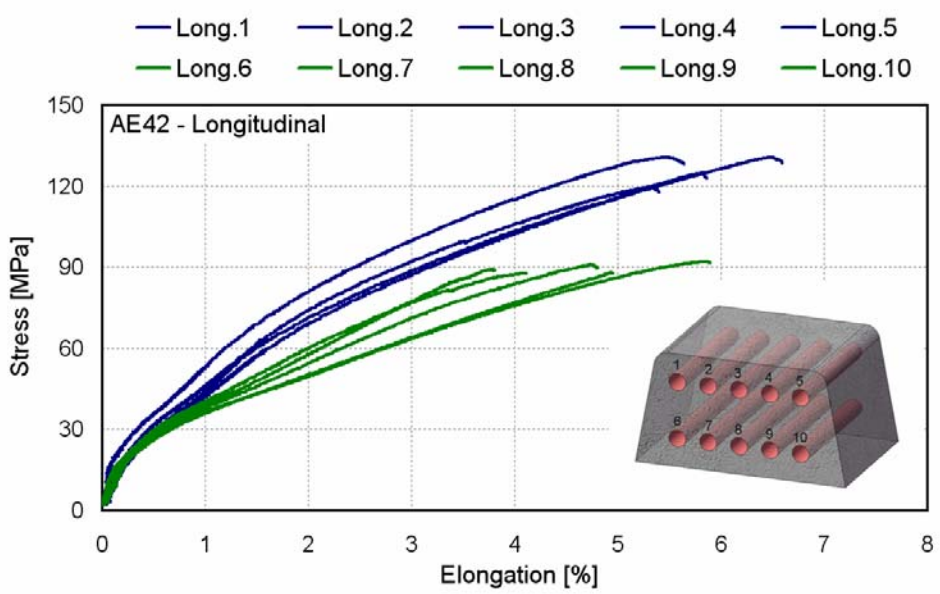

(a)

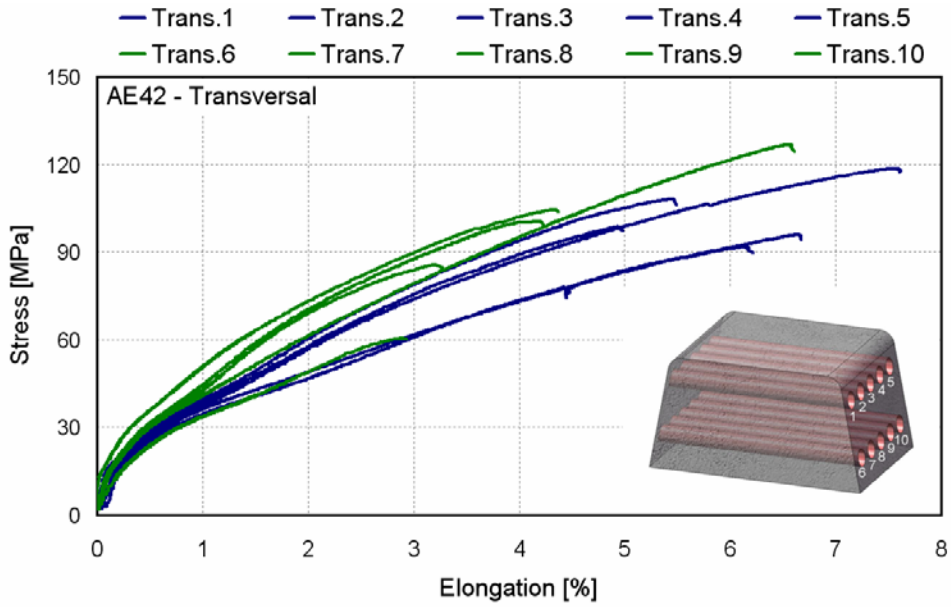

(b)

Figure 4.4: Base Material tensile curves for longitudinal (a) and transversal (b) round AE42 samples. Ingot detail indicates the position where the samples were machined from.

4.1.3 Base Material MRI230D

Table 4.7 lists the actual MRI230D chemical composition.

Table 4.7: Chemical composition of the MRI230D ingot (cast condition).

	Chemical composition							
Element	**Al**	**Zn**	**Si**	**Cu**	**Mn**	**Fe**	**Others**	**Mg**
Actual Composition [wt.%]	6.6 7.5	0.002	< 0.01	0.002	0.29 0.33	---	Ca: 2.1 – 2.4 Sr: 0.29 – 0.33 Sn: 0.71 – 0.89	Bal.
Nominal Composition [33] [wt.%]	6.4 7.2	≤ 0.08	≤ 0.03	≤ 0.005	0.17 0.40	≤ 0.004	Ca: 1.8 – 2.6 Sr: ≤ 0.4	Bal.

Micrographs of the MRI230D base material (see Figure 4.5) indicate microstructures consisting of the α-Mg matrix and intermetallic compounds that form an almost continuous network distributed at grain boundaries and interdendritic areas. The morphologies of the intermetallic compounds in these alloys have been revealed by backscattering electron SEM images.

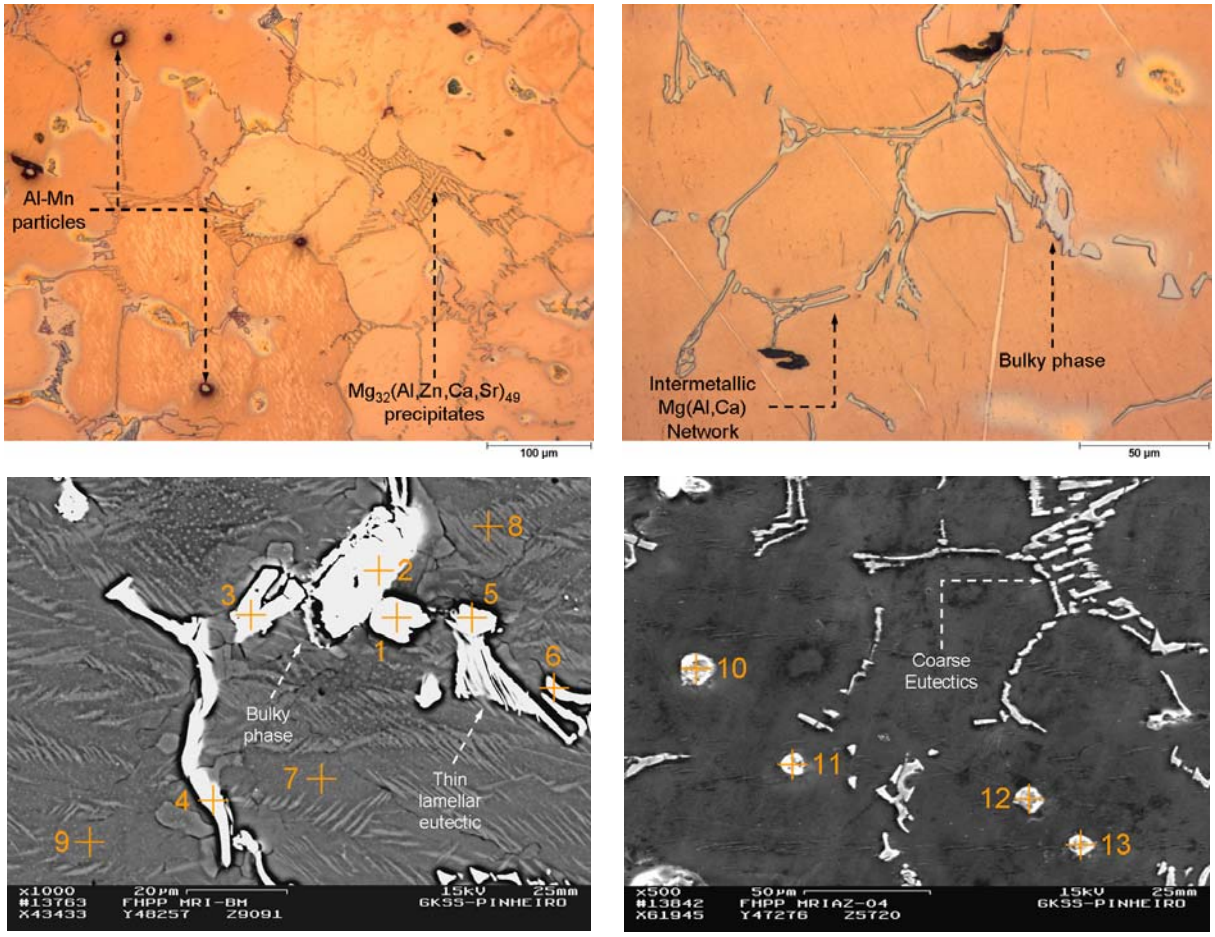

Figure 4.5: Micrographs of MRI230D (above) and backscattering electron SEM images (below) with points identified for further EDS analysis.

As shown in Figure 4.5, the interdendritic compounds show three morphologies: thin lamellar, a coarse irregular shaped eutectic and a bulky phase located at triple junction of grains. Stable, round Al-Mn based precipitates were also observed to compose the microstructure of such alloys. In order to identify the local chemical composition of these intermetallic compounds existing in the as-cast microstructure, EDS was performed. Points are indicated in Figure 4.5 and identified as 1 to 13. The corresponding results are shown in Table 4.8. Additional microscopic observations revealed an average grain size varying between 90 µm to 120 µm in the centre and in the periphery of the ingot.

Table 4.8: Results of EDS analysis at 13 different points within the base material MRI230D (in wt.%).

	Mg	Al	Ca	Mn	Zn	Sr	Sn
Point 1	---	27.15	---	42.18	15.75	---	7.67
Point 2	7.23	---	6.25	---	---	---	86.52
Point 3	16.61	---	11.51	---	---	2.14	69.73
Point 4	12.31	51.93	34.99	---	---	---	---
Point 5	---	19.74	---	43.40	24.09	---	10.13
Point 6	46.36	35.21	18.43	---	---	---	---
Point 7	96.35	3.65	---	---	---	---	---
Point 8	96.86	3.15	---	---	---	---	---
Point 9	96.57	3.43	---	---	---	---	---
Point 10	---	26.79	---	47.07	13.96	---	4.58
Point 11	---	27.59	---	43.47	14.45	---	5.59
Point 12	---	9.63	---	19.46	38.39	---	11.43
Point 13	---	22.70	---	39.18	21.29	---	5.68

Table 4.9 presents further mechanical properties, while Figure 4.6 shows stress-strain curves, plotted during tensile testing. In both cases, i.e. in the longitudinal and transversal directions, the upper samples (1 to 5) presented strength and elongation values varying between 100 MPa and 120 MPa and 1.5 % and 2 %, respectively. In the lower part of the ingot, elongation values were similar and ranged between 1 % and 1.5 % in both directions, while tensile strengths were around 90 MPa and varied between 60 MPa and 90 MPa for transversal and longitudinal directions respectively.

Table 4.9: Mechanical properties of the MRI230D ingot (cast condition).

	Mechanical Properties			
	Rm [MPa]	**$Rp_{0,2}$ [MPa]**	**A[%]**	**Hardness**
MRI230D (Tested)	60 - 120	50 - 100	0.5 – 2	46 – 54 HV

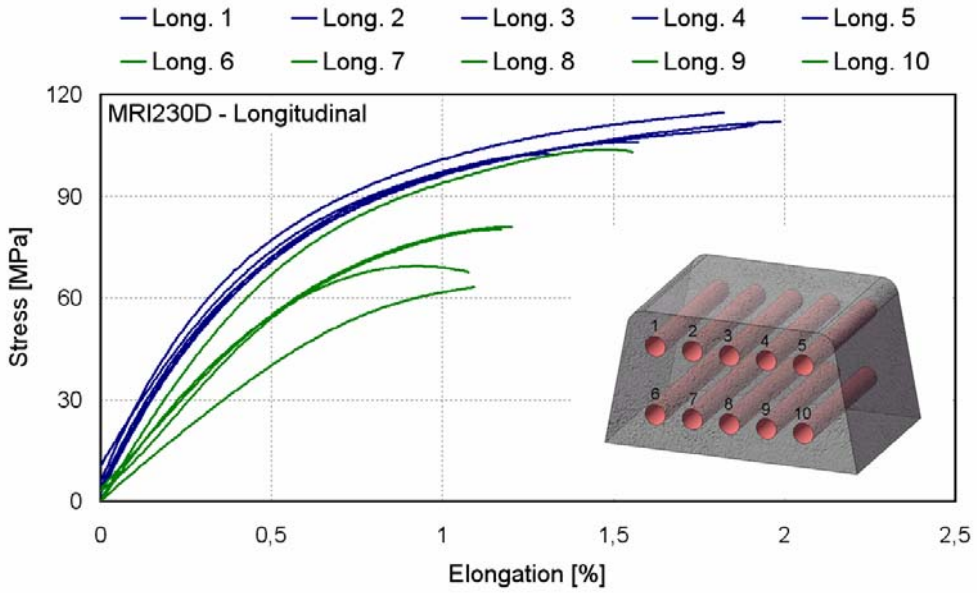

(a)

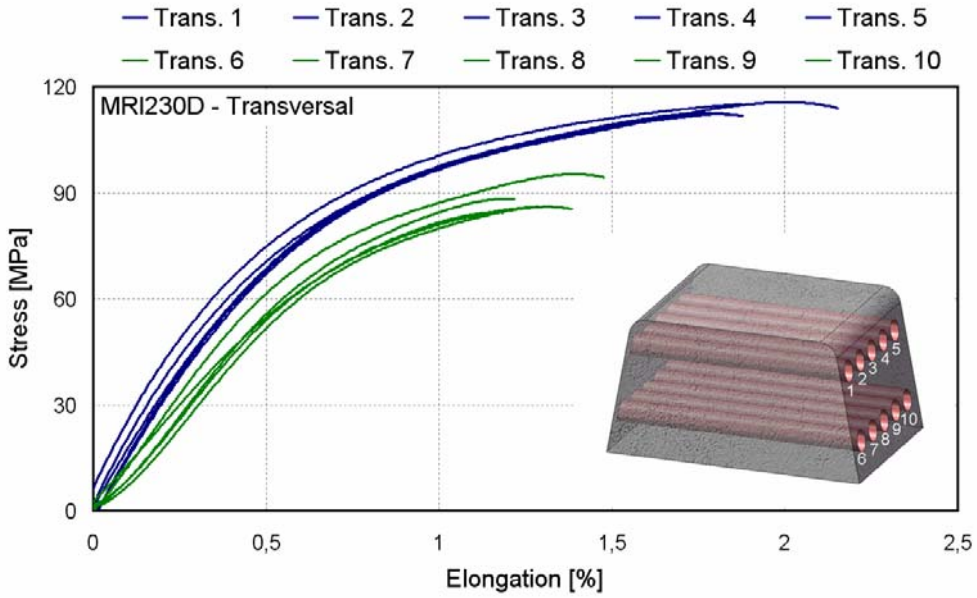

(b)

Figure 4.6: Base Material tensile curves for longitudinal (a) and transversal (b) round MRI230D samples. Positioning of samples in relation to the ingot is shown in the detail (right).

4.2 SIMILAR AZ91D-T6 JOINTS – 6 MM DIAMETER/12 MM UPSETTING

As the rotational speed has been demonstrated to be the least sensitive parameter in friction welding [73,118,152] and considering the experience acquired from previous trials, FHPP joints were performed in this section in a similar configuration, varying the welding pressure and forging force. On the other hand the upsetting, as one of the main welding parameters, has shown to play an important role in rotational friction welding. Therefore, its influence on FHPP is also investigated in this study with the respective results presented in Section 4.3. In FHPP, a certain amount of upsetting is required to fill the hole completely. If the upsetting is too small, the hole will not be filled up to the surface, while if it is too high, much stud material is plasticised on top of the weld, heating the consumable stud and the base plate excessively, and needlessly extending the welding time in most of cases. For the experiments performed within this section, all welding studs and base plates were machined from the base material AZ91D-T6. The chemical composition and mechanical properties of this base material have been reported previously (see Section 4.1.1). Based on previous studies carried out by the author and on some prior investigations on FHPP [78,82,99,100], a combination involving 10° tapered studs with 6 mm tip diameter and base plates with 20° tapered holes and 6 mm bottom diameter was chosen. Within this configuration, even minor bonding defects, especially at the wall of the holes, would not be expected, due to the horizontal component of the forces created by the taper angle. A parameter matrix was devised and extended to the operational limits of the system on one side and to the mechanical properties of the materials on the other. The rotational speed was kept constant at 4000 rpm while the axial pressure was changed from 6.90 to 13.79 bar in 3.45 bar steps. The upsetting was set to 12 mm, based on early trials, and the forging pressure was always 13.79 bar higher than the welding pressure. Nine welds for each parameter combination were produced and designed for a certain test, as listed in Table 4.10. In this context, welds “F” to “I”, for example, were used only for transversal tensile testing. Throughout this section the welds will be referred to as 1,2 or 3, according to the set of parameters used.

Table 4.10: Designation of welded samples (AZAZ-06/12 series) according to the testing program.

Weld	Welding Parameters (bar x rpm)	Process Stability	Temperature	Met. Analysis	Hardness	Pull-out Test	Transversal Tensile Test
AZAZ 1A ⇒ 1I	6.90 x 4000 12 mm Ups. FP: 20.69 bar	1A ⇒ 1E	1A ⇒ 1E	1C	1C	1A, 1B 1C, 1E	1F⇒ 1I
AZAZ 2A ⇒ 2I	10.34 x 4000 12 mm Ups. FP: 24.13 bar	2A ⇒ 2E	2A ⇒ 2E	2C	2C	2A, 2B 2C, 2E	2F ⇒ 2I
AZAZ 3A ⇒ 3I	13.79 x 4000 12 mm Ups. FP: 27.58	3A ⇒ 3E	3A ⇒ 3E	3C	3C	3A, 3B 3C, 3E	3F ⇒ 3I

Figure 4.7 presents the process diagram, including the most important parameters and additional information about the process, such as welding duration and holding time (6 s for every weld). As can be seen, the rotational speed is started first and after the set speed is reached (in this case 4000 rpm), the stud is moved down, making contact with the bottom of the cavity. From this point the axial downward movement is measured as upsetting. As soon as both faying surfaces are brought in contact, the rotational speed falls briefly, due to the first initial friction being corrected by the control system almost instantaneously. Simultaneously the welding pressure reaches its preset value and the welding stud starts to be deposited. When the predetermined upsetting distance is reached (the welding time is finished), the rotational speed is stopped and the pressure increased to the preset value. Finally, the forging force is held constant for 6 s (forging time) to consolidate the joint.

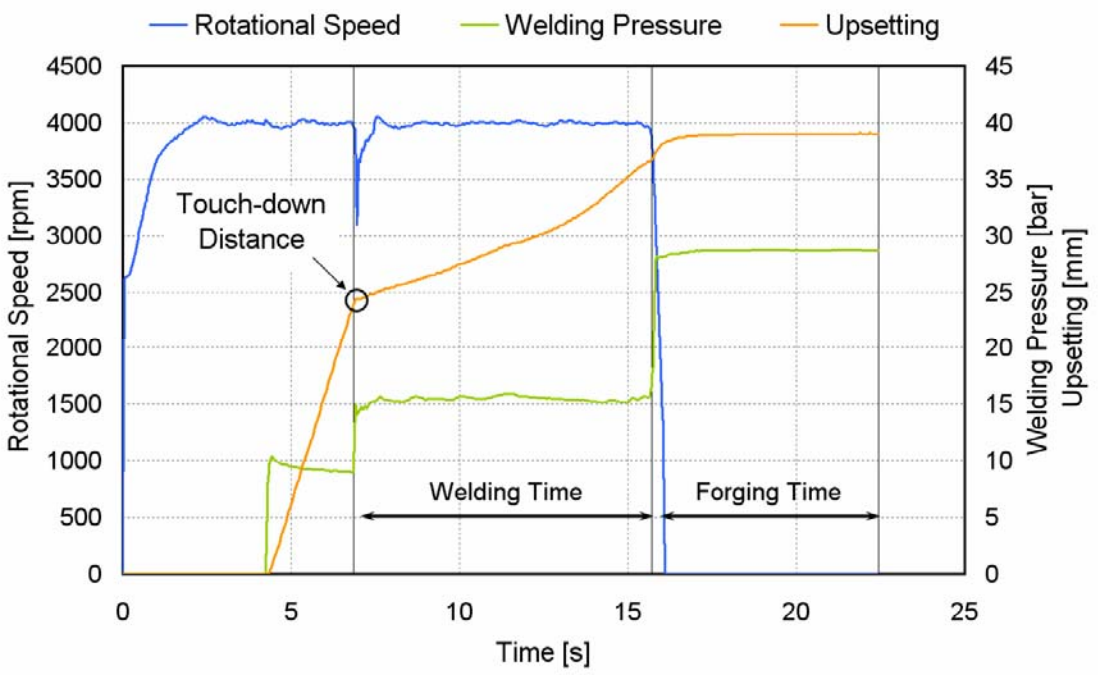

Figure 4.7: Welding progress diagram (welding pressure 13.79 bar, forging pressure 27.6 bar, rotational speed 4000 rpm and 12 mm upsetting).

4.2.1 Process Monitoring

As mentioned on the experimental procedure, data files were stored for every weld produced in this study. These files were then transferred to a standard data processing software (EXCEL) for further processing and complementary evaluation. Figure 4.8 presents the upsetting curves generated by the data acquisition system. Based on this and on the calculated upsetting rate (see in Figure 4.8, *UR* values for the different welding conditions), the influence of the welding pressure on the welding time can be clearly observed. Welds performed with low pressures present on average a welding time (*WT*) of 24.4 seconds (s), whereas high pressure joints are consolidated in around 9.5 s. Furthermore, the total upsetting (*TU*), which mirrors the total shortening of the welded pair, increases from 15.5 mm to 16.3 mm with increasing forging pressure.

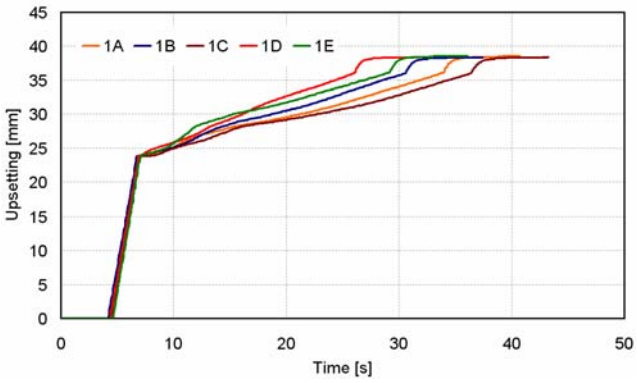

Spec.	WT	ST	TWT	UWT	UST	TU
1A	27.2	0.8	28.0	13.0	2.4	15.4
1B	23.9	0.9	24.8	13.6	2.3	15.9
1C	29.5	0.9	30.4	13.7	2.4	16.1
1D	19.1	1.0	20.1	12.8	2.4	15.2
1E	22.0	1.0	23.0	12.7	2.4	15.1
AV	24.4	0.9	25.3	13.2	2.4	15.5
SD	4.1	0.1	4.0	0.5	0	0.4

(a) 6.90 bar x 4000 rpm - UR: 0.541 mm/s.

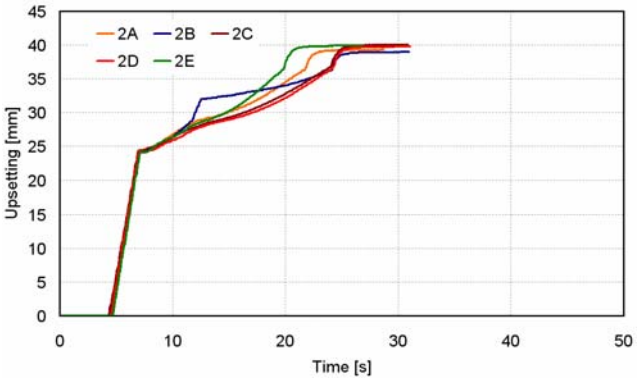

Spec.	WT	ST	TWT	UWT	UST	TU
2A	14.9	0.9	15.8	13.0	3.0	16.0
2B	17.2	0.9	18.1	13.4	2.7	16.1
2C	17.0	1.0	18.0	12.8	3.3	16.1
2D	17.2	0.9	18.1	12.7	3.3	16.0
2E	12.8	1.0	13.8	13.1	3.5	16.6
AV	15.8	0.9	16.7	13.0	3.2	16.2
SD	2.0	0.0	1.9	0.3	0.3	0.2

(b) 10.34 bar x 4000 rpm - UR: 0.823 mm/s.

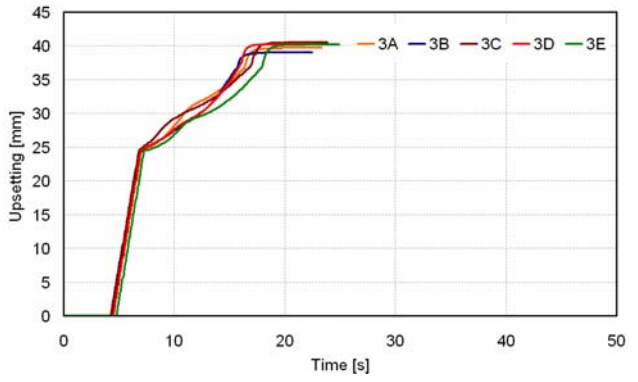

Spec.	WT	ST	TWT	UWT	UST	TU
3A	9.4	1.0	10.4	12.7	3.0	15.7
3B	8.8	0.9	9.7	12.7	3.4	16.1
3C	9.9	1.3	11.2	12.9	3.6	16.5
3D	9.0	1.0	10.0	13.0	3.2	16.2
3E	10.7	1.1	11.8	12.9	3.5	16.4
AV	9.5	1.0	10.6	12.8	3.3	16.3
SD	0.8	0.1	0.9	0.1	0.5	0.6

(c) 13.79 bar x 4000 rpm - UR: 1.347 mm/s.

Figure 4.8: Process stability and the influence of axial pressure on the upsetting rate **(WT: welding time; ST: stopping time; TWT: total welding time; UWT: upsetting during the welding time; UST: upsetting during the stopping time; TU: total upsetting and UR: upsetting rate)**.

4.2.2 Thermal Cycle

Figure 4.9 shows the measurements of three sets of joints, consisting of five samples per set, welded with different axial pressures and monitored in two different positions. Although the axial pressure significantly influences the welding time (see Section 4.2.1), this tendency cannot be directly transferred to the maximum temperature. While welding time showed a significant variation by duplicating the pressure, the peak temperatures presented a variation of 16 °C (≈4 %) in T1 and 33 °C (9 %) in T2 under similar conditions, i.e. between samples AZAZ-1 and AZAZ-3.

For low pressure welds (AZAZ-1), average peak temperatures of 427 °C and 361 °C respectively were measured in upper (T1) and lower (T2) weld areas. For high pressure welds, however, average peak temperatures of 411 °C and 328 °C respectively were observed in upper and lower weld areas. Extending the analysis and considering the cooling rates demonstrated in Figure 4.9, one can observe a longer cooling time for welds produced within the AZAZ-1 series. After 40 seconds, the upper thermocouples indicated temperatures around 195 °C and 95 °C respectively for AZAZ-1 and AZAZ-3 series.

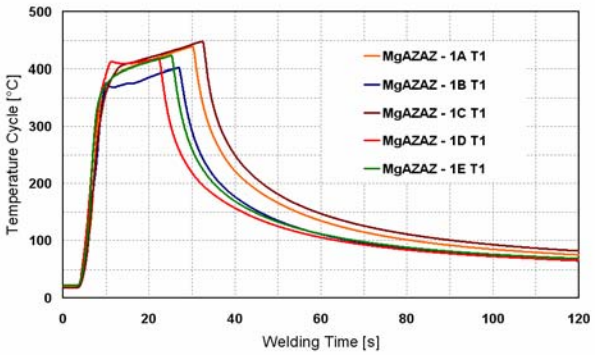

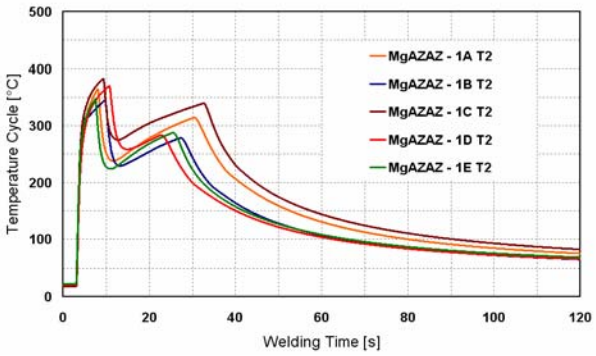

(a)	Peak Temperature	Cooling Rate (°C)		
		40s	50s	60s
Average	427 °C	194	148	121
AZAZ-1C	448 °C	249	181	147

(b)	Peak Temperature	Cooling Rate (°C)		
		40s	50s	60s
Average	361 °C	182	142	119
AZAZ-1C	383 °C	231	175	144

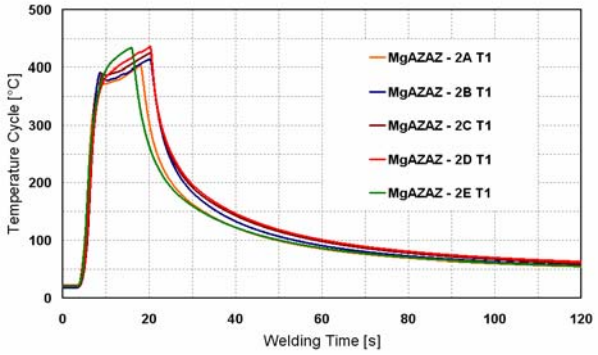

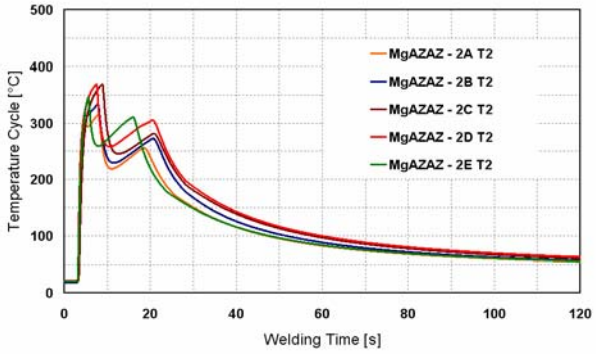

(c)	Peak Temperature	Cooling Rate (°C)		
		40s	50s	60s
Average	422 °C	133	108	92
AZAZ-2C	389 °C	142	115	97

(d)	Peak Temperature	Cooling Rate (°C)		
		40s	50s	60s
Average	347 °C	128	105	90
AZAZ-2C	368 °C	139	113	97

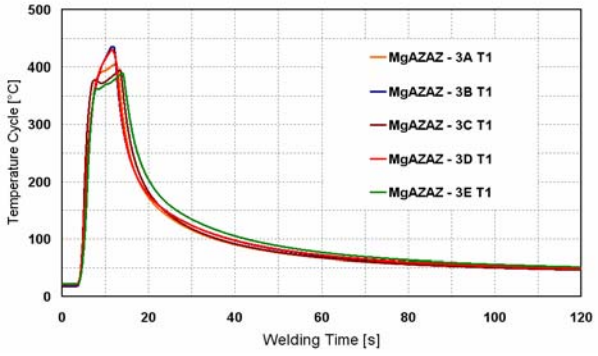

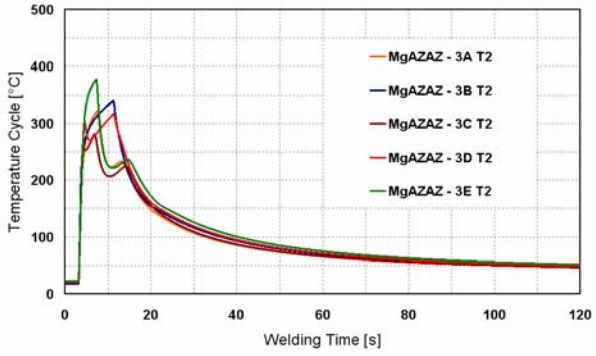

(d)	Peak Temperature	Cooling Rate (°C)		
		40s	50s	60s
Average	411 °C	96	81	71
AZAZ-3C	395 °C	91	77	67

(e)	Peak Temperature	Cooling Rate (°C)		
		40s	50s	60s
Average	328 °C	92	78	69
AZAZ-3C	281 °C	87	74	66

Figure 4.9: Thermometric results for similar AZAZ welds. Measurements respectively at 6 mm (T1) and 17 mm (T2) from top surface for 6.90 bar x 4000 rpm (a) and (b), 10.34 bar x 4000 rpm (c) and (d) and 13.79 bar x 4000 rpm (d) and (e) welds.

4.2.3 Metallurgical Characterisation

Weld-zone cross-sections indicate joints with no porosity and without any lack of bonding along the welding line in all the investigated conditions. At the bottom of the stud, under higher magnification, no clearly visible transition zone (bonding line) was identified, suggesting an intimate contact between the stud/base plate pair, imposed mostly by the forging pressure. A clear bonding line could only be observed in the sidewall interface, since the forces acting in those areas are not directly applied by the process, but are transferred by a combination of solid and hydrostatic conditions via the plasticised material. The influence of the welding parameters on the material flow is shown in Figure 4.10. Based on a visual analysis, it can be clearly seen that joint 1C, welded with lower pressure, and therefore with a longer welding time, presented a larger heat affected zone (HAZ) when compared with weld 3C.

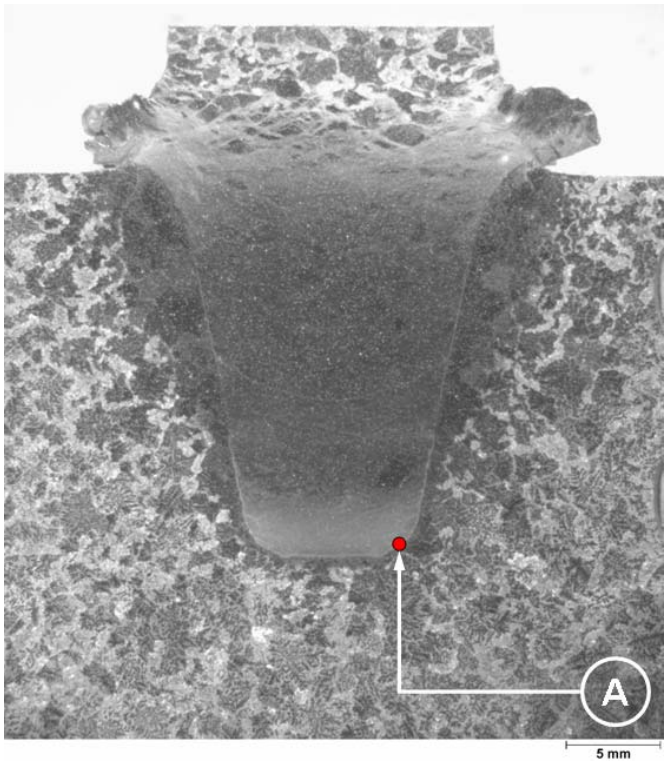

(a) AZAZ-1C (6.90x4000).

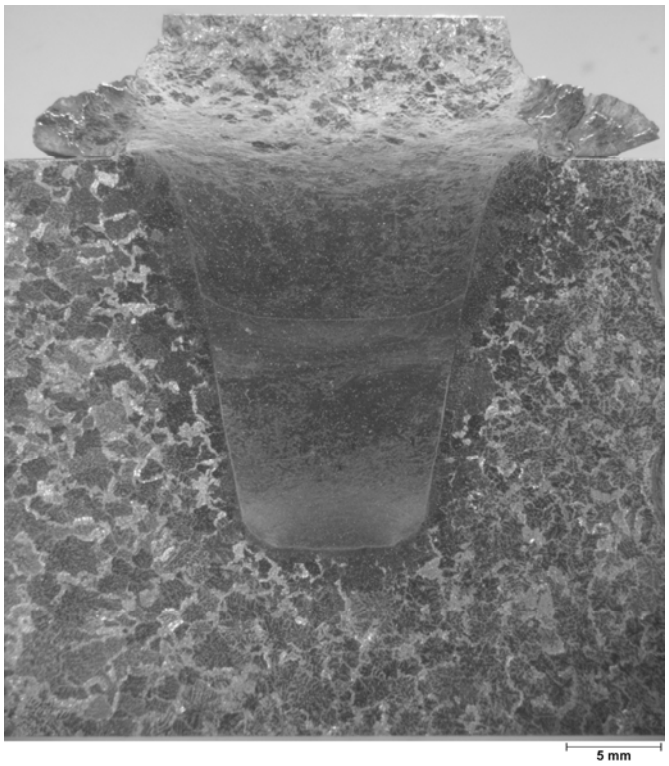

(b) AZAZ-2C (10.34x4000).

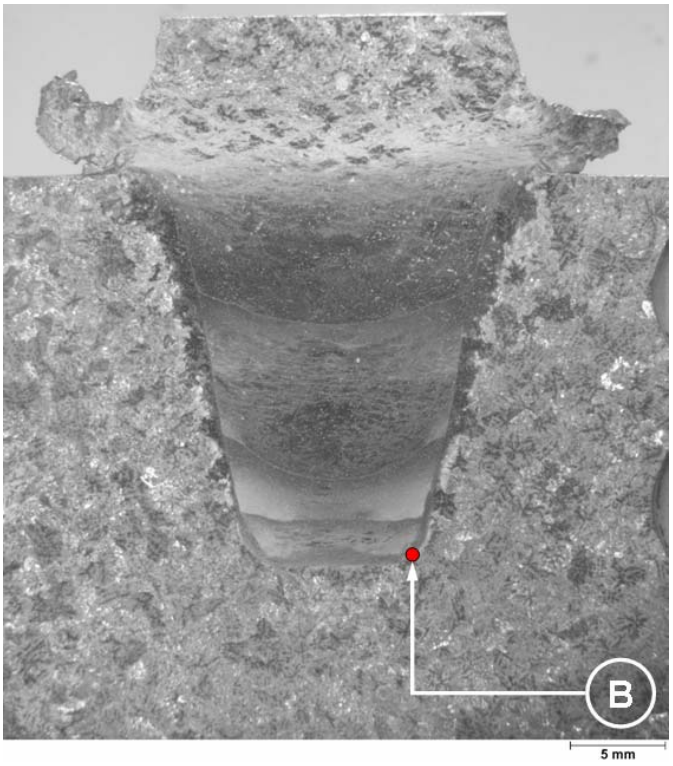

(c) AZAZ-3C (13.74x4000).

Figure 4.10: Friction welding macrostructures of similar AZ91D-T6 x AZ91D-T6 joints.

Figure 4.11 evidences, in terms of microstructural changes, the difference in the global heat generation. While in sample 1C the microstructure in regions adjacent to the welding area is completely recrystallised, with most of the eutectic phases disrupted and entirely dissolved into the Mg-Al solid solution (see Figure 4.11(a), in sample 3C the typical lamellar eutectic morphology, formed during the ingot casting process, is observed in an extension very close to the BL (see Figure 4.11(b).

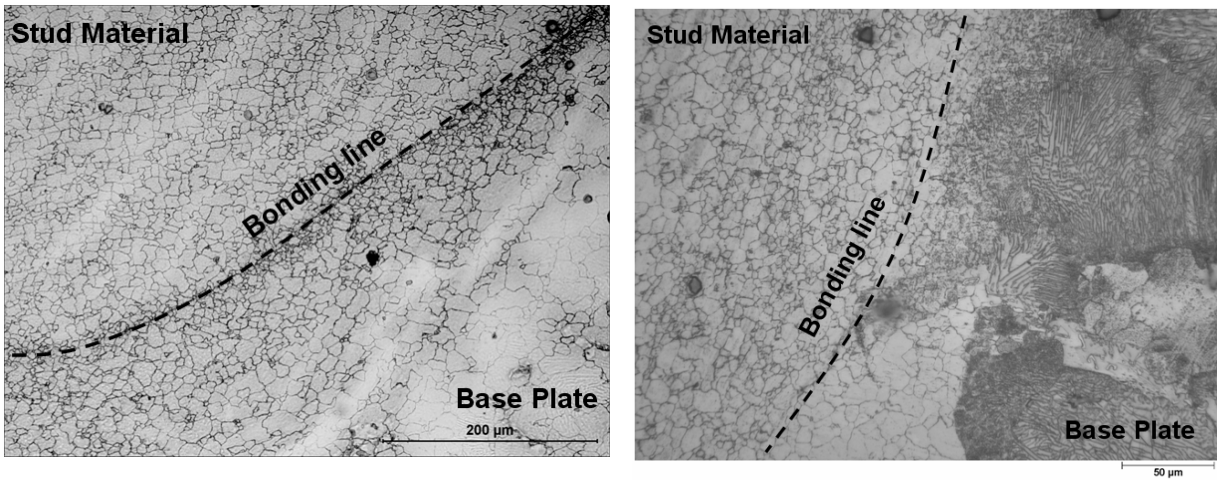

(a) Microstructure in region A – see Figure 4.10a. (b) Microstructure in region B – see Figure 4.10c.

Figure 4.11: Comparison of microstructures at the same position between samples 1C and 3C.

As shown in Figure 4.12, the microstructure of FHPP welded specimens generally consists of a homogenised area in the lower part of the consumable and a region of plastically deformed stud material in the upper part. Figure 4.12(a) and (b) comprise the microstructures around the side bonding line, which is identified by means of a dashed line. The grain size can be seen to decrease in the vicinity of the joint in an extension varying between 50 µm and 150 µm. Even under higher magnification it can be observed that the lateral interface presents a smooth transition between stud and base plate material (Figure 4.12(b)). The recrystallised Mg grains in a region immediately adjacent to the bonding line (see Figure 4.12(c)) can be seen to be fine, homogeneous and equiaxed. The frictional heat created by the rubbing of both faying surfaces and the mechanical working imposed by the process provided the driving force for dynamical recrystallisation of the materials within the weld zone. Figure 4.12(d) shows the transition area at the bottom of the cavity on the right side, indicating no visible discontinuity on the interface.

The lamellar eutectic phases $Mg_{17}Al_{12}$ seem to be dissolved and re-precipitated as large particles with various shapes around the primary-grown Mg-Al solid solution. However, the coarse second phase particles, even those exactly over the bonding line, are not mechanically fragmented and remain in the composition of the microstructure (see indications in Figure 4.12(a) and (d). Three main weld zones, in agreement with the literature [129,153-155], can be pointed out according to the type and intensity of the supplied energy (heat input) and deformation they were subjected to during the welding cycle:

- ***HAZ – heat affected zone***, where the microstructure and respective mechanical properties only suffer the influence of the heat generated during the welding process. At lower magnifications, such regions did not show any significant microstructural change in comparison with the base material (BM), but grain growth can still be observed, depending on the energy input used to perform the weld;

- ***TMAZ – thermo-mechanical affected zone***, where the amount of heat is higher than in the HAZ and grains experience a substantial deformation, essentially resulting in recovery of the highly strained grains. In this region, the pancake grains from the BM are deformed and can be observed easily in the micrographs surrounding the joint line (see Figure 4.12(c)), as a transitional interface between HAZ and the recrystallised zone, where grains are equiaxed and refined. Furthermore, a rearrangement of dislocation and formation of sub-grain interfaces is expected in this region, since recovery takes place;

- ***RZ – recrystallised zone*** is distinctly characterised by the formation of a fine grain microstructure with equiaxed morphology as a result of the dynamic recrystallisation phenomenon. The refined microstructure of the recrystallised zone is the core of the joining among the two workpieces and corresponds to the microstructure resulting from the highest levels of deformation and temperature during the friction welding process. In FHPP, as the consumable rod undergoes significant hot working and is therefore fully plasticised across the entire diameter, the total filled up area can considered to be the recrystallised zone.

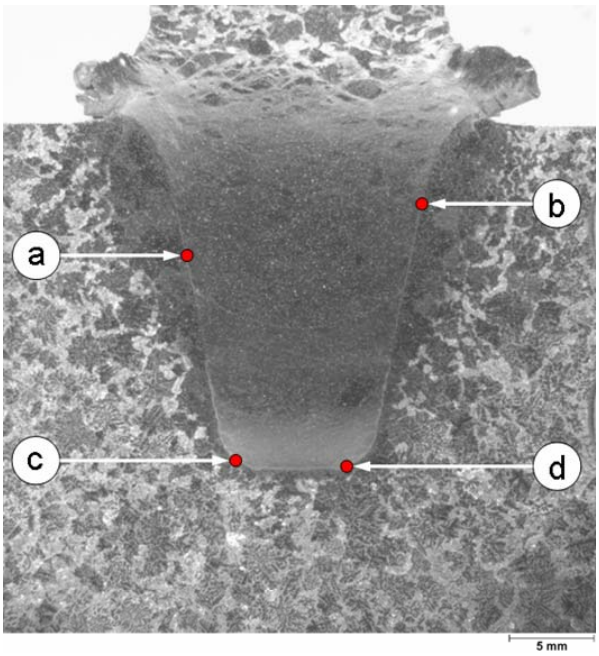

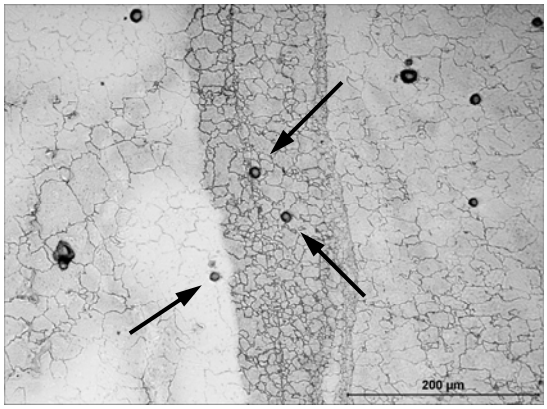

(a) Sidewall recrystallised zone.

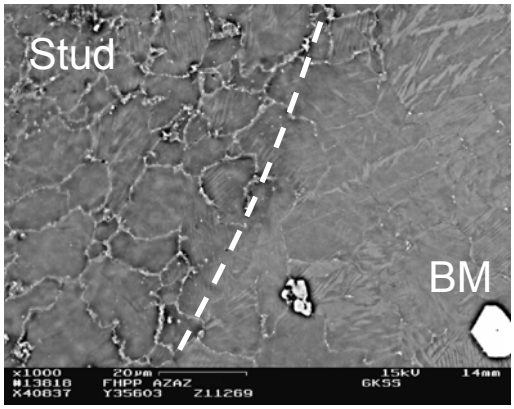

(b) Lateral transition area without apparent discontinuity.

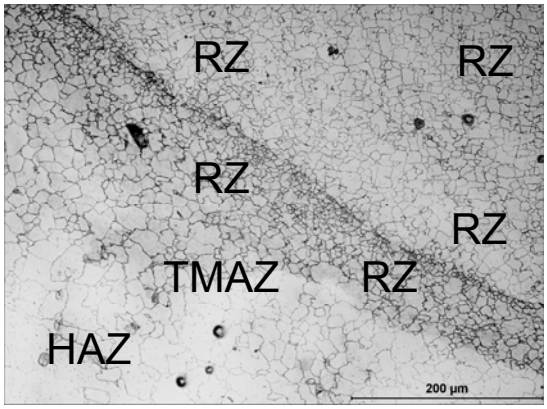

(c) Microstructural development at the lower stud areas with indication of welding zones.

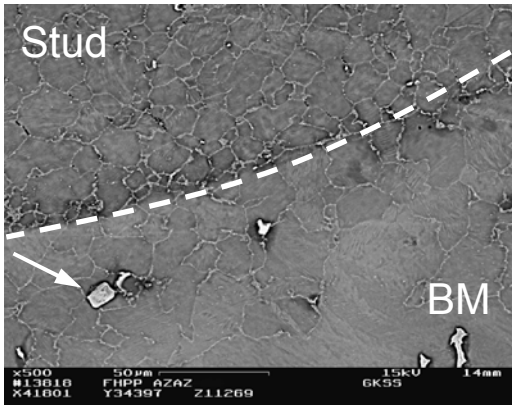

(d) Transition area.

Figure 4.12: Macro and micrographs of the AZAZ-1C joint.

The average grain size within the deposited (stud) material varies between 7 µm in the lower regions of the joint to 17 µm in the upper parts. Three measurements were performed in each position, for each sample, i.e. the results presented in Figure 4.13 are the average of three scans. Base material has, on the other hand, a grain size varying between 200 µm and 600 µm.

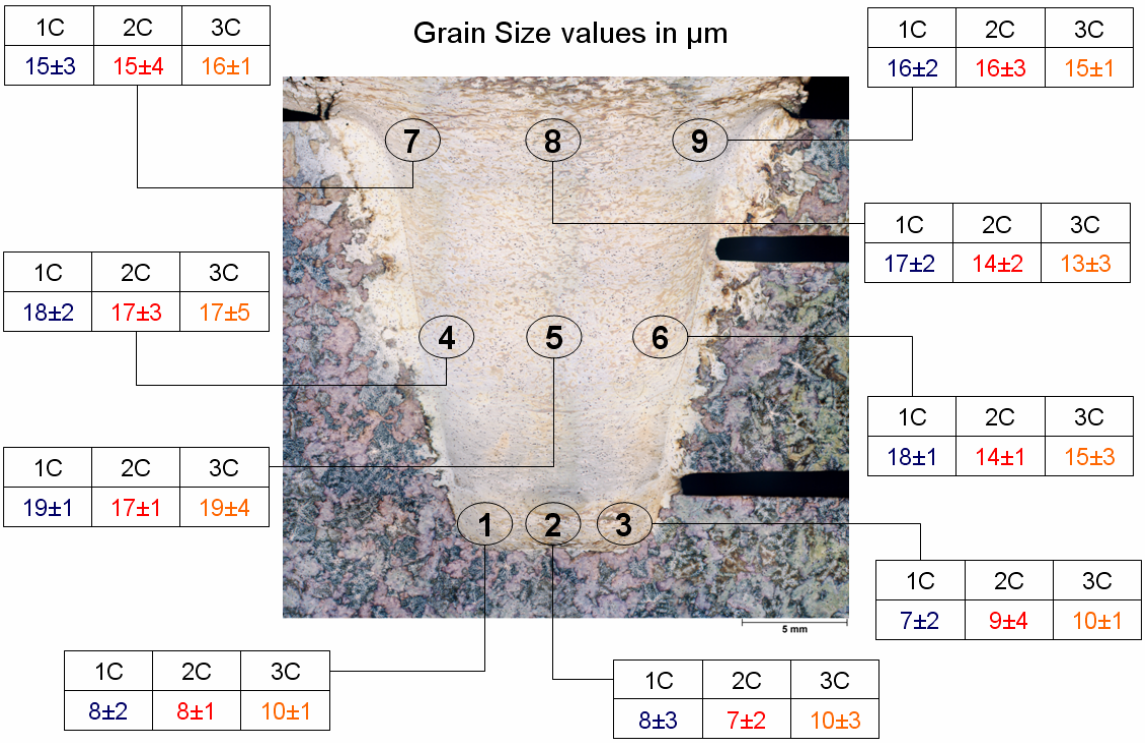

Figure 4.13: Grain size distribution within the deposited material (values in µm).

As mentioned above and demonstrated in Figure 4.14(a) and (b), AZ91D-T6 cast ingots have a grain size varying between 200 µm and 600 µm. Their typical microstructure is basically formed by an α-Mg matrix, a lamellar interdendritic α-Mg-$Mg_{17}Al_{12}$ precipitate (β-phase) and some isolated islands of $Mg_{17}Al_{12}$ compound. Similar to the bonding line, the microstructure within the deposited material is basically characterised by the complete dissolution of the typical base material phases, followed by the formation of a very fine, equiaxed and dynamically recrystallised structure. The previous Mg(Al,Zn) phases are either dissolved into the α-Mg matrix or precipitate at the grain boundaries, according to Figure 4.14(c) and (d). Several EDS analysis were performed in this region, in order to identify the resultant phase compositions after welding. Figure 4.14 and Table 4.11 indicate and show respectively the 10 different points where such EDS analyses were performed.

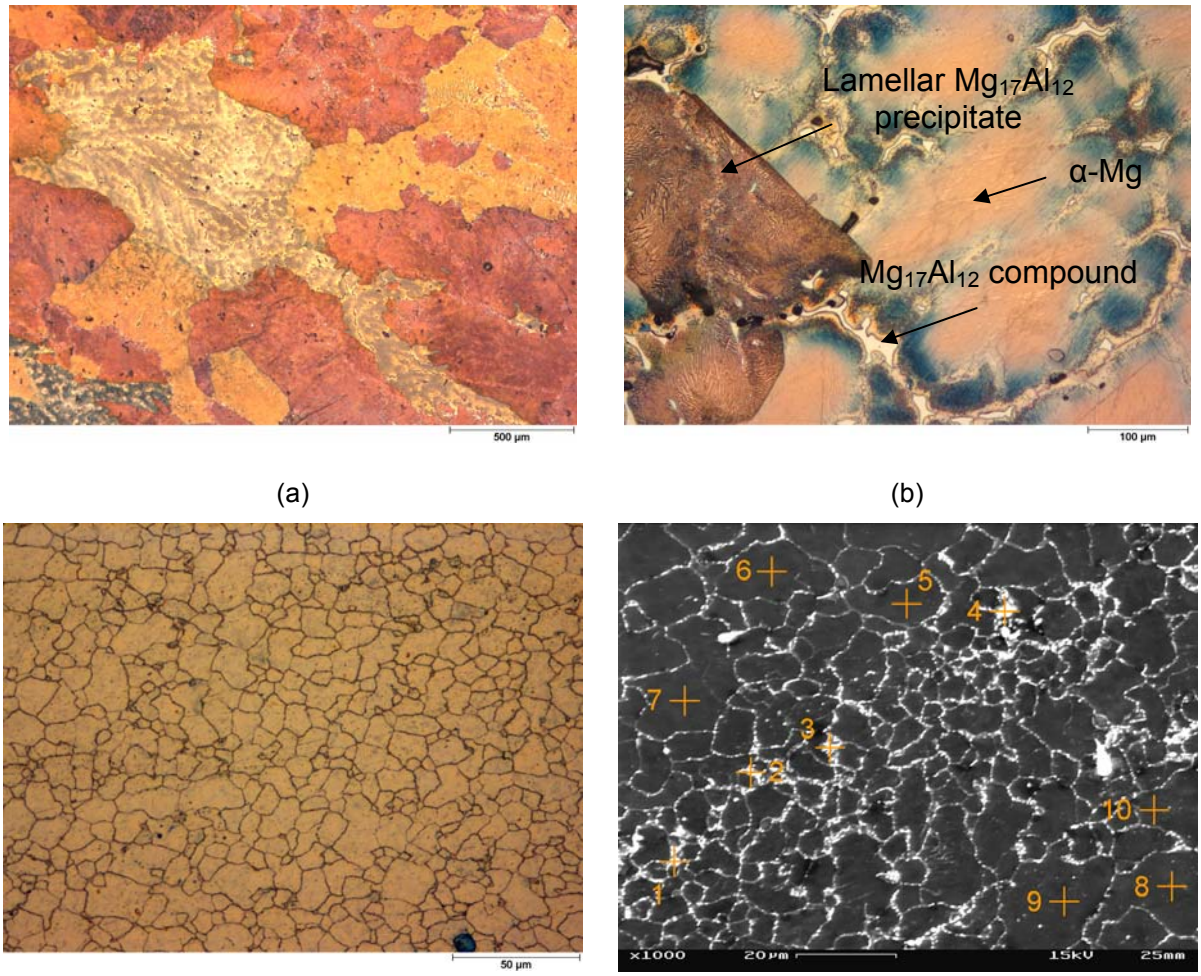

(a) (b)

(c) (d)

Figure 4.14: Microstructural characteristics of the AZ91D-T6 BM (a) and (b) and of the extruded material within the welding zone (c) and (d).

Table 4.11: Results of EDS analysis in 10 different points within the extruded material.

	Mg(wt.%)	Al(wt.%)	Mn(wt.%)	Zn(wt.%)
Point 1	87.67	10.97	---	1.36
Point 2	85.19	12.98	---	1.34
Point 3	87.16	11.62	0.12	0.42
Point 4	87.18	11.77	0.12	0.93
Point 5	87.19	11.25	0.13	1.04
Point 6	90.68	8.59	---	0.88
Point 7	87.39	11.18	0.14	1.28
Point 8	92.35	6.56	---	---
Point 9	93.70	6.03	---	---
Point 10	93.56	6.14	---	---

4.2.4 Mechanical Characterisation

4.2.4.1 Hardness Tests

In the case of similar AZ91D-T6 joints, microhardness profiles were performed along the transversal cross section surfaces for the three different conditions, using the procedures listed in Section 3.5.3. Figure 4.15 presents the microhardness profiles in welds produced with low (1C), intermediate (2C) and high (3C) pressures at 2 mm, 10 mm and 18 mm from the top plate surface. Hardness values in the BM were shown to vary from 60 HV to 120 HV in cases where the indenter hit a harder phase or precipitate. In contrast to the BM scans, hardness profiles within the extruded material point out similar values of approximately 80 HV for all three welded conditions at 2 mm and 10 mm from the top surface. At 18 mm, however, a slight increase in the average hardness values was observed. Microhardness profiles indicated in those areas values over 80 HV for the three welding conditions.

Further analysing Figure 4.15(a) to (c), a significant decrease in the scattering within the extruded material was observed in comparison with the BM. Furthermore, profiles performed 2 mm away from the top surface presented a wider region outside the extruded zone, where a reduced dispersion in hardness was observed. On the other hand, measurement of scattering in the lower stud areas (see Figure 4.15(c)) increases significantly, as soon as the scan crosses the bonding line and reaches the BM, inside of the TMAZ/HAZ.

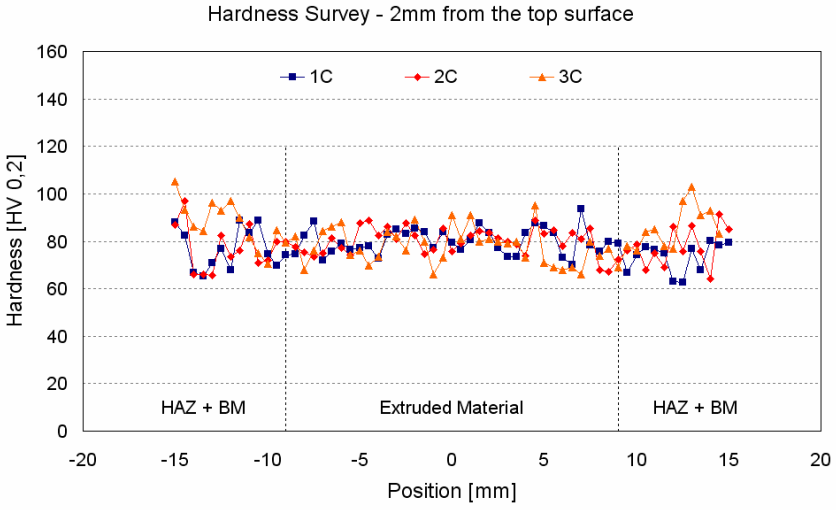

(a)

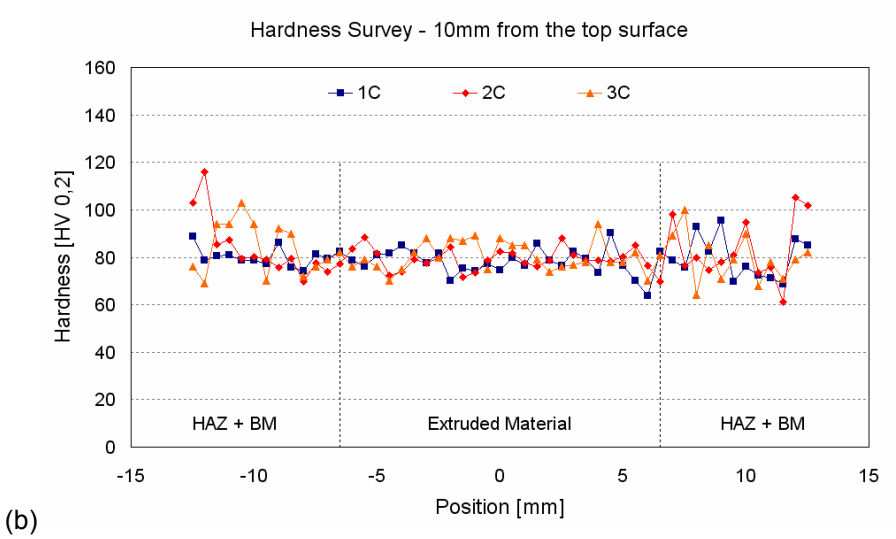

(b)

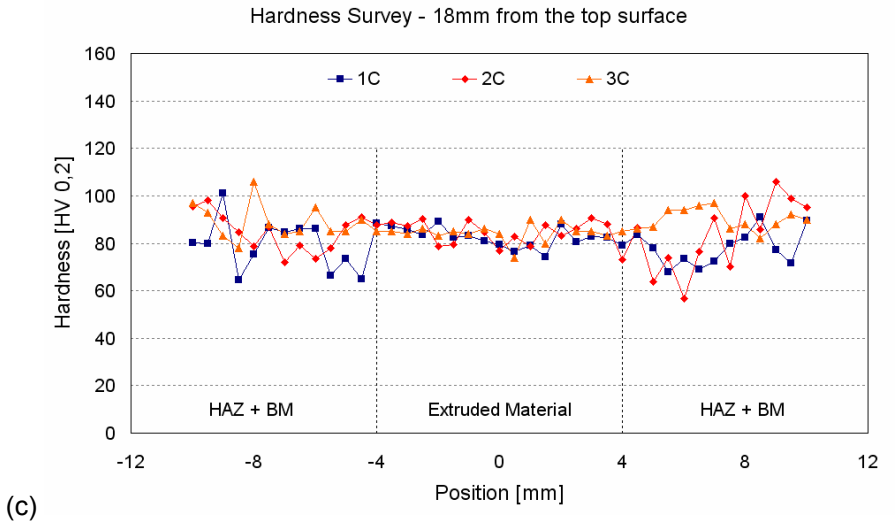

(c)

Figure 4.15: Hardness survey of welded samples, transversal to the consumable at 2 mm (a), 10 mm (b) and 18 mm (c) from the top surface, according to Figure 3.8.

4.2.4.2 Pull-out Tests

Pull-out properties were determined at room temperature for the AZ91D-T6 alloy for the three different welding conditions. Based on Figure 4.16, pull-out tests confirm the suitability of the process to perform high strength welds. Generally, similar joints achieved BM strength values of 35 kN for low (AZAZ-1 series), intermediate (AZAZ-2 series) and high (AZAZ-3 series) pressures with no failure observed within the welded area (see corresponding detail in Figure 4.16).

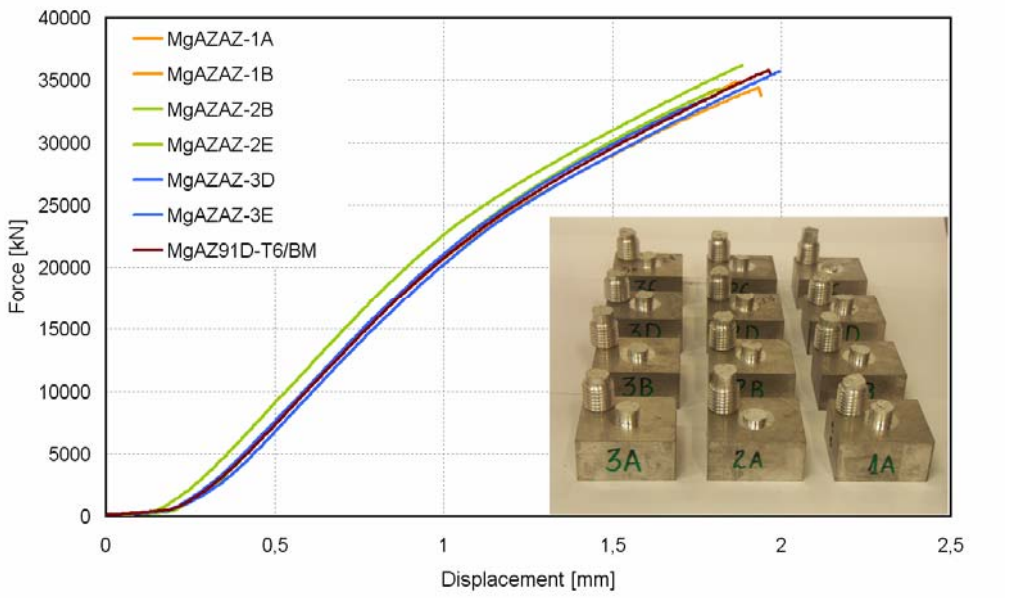

Figure 4.16: Pull-out test results for similar MgAZAZ-06/12 welds.

4.2.4.3 Transversal Tensile Tests

According to Table 4.10, four samples were welded in the same condition to evaluate the bonding strength at the sidewall. Two tensile samples were machined from each specimen (see Figure 3.11). Figure 4.17 presents the tensile strength results, considering the average strength obtained from four specimens tested at the same location. According to this, joints performed under different welding conditions generally show similar mechanical properties to those of the base material. Low pressure joints (AZAZ-1 series) achieved strength values ranging from 150 MPa up to 167 MPa, for lower and upper weld regions respectively. High pressure welds (AZAZ-3 series), however, presented strength values comparable to those from the BM, achieving 100 % joint efficiency in lower and upper weld areas. A significant decrease in the elongation was observed for low and high pressure welds, reaching values inferior to 1 %. BM elongation, on the other hand, presented values ranging from 0.5 % to 3 % according to Table 4.3. Low, intermediate and high pressure welds also showed equivalent yield strengths, indicating values of 90 % to 100 %, 86 % to 100 % and 97 % to 100 % of the BM properties for lower and upper weld areas respectively.

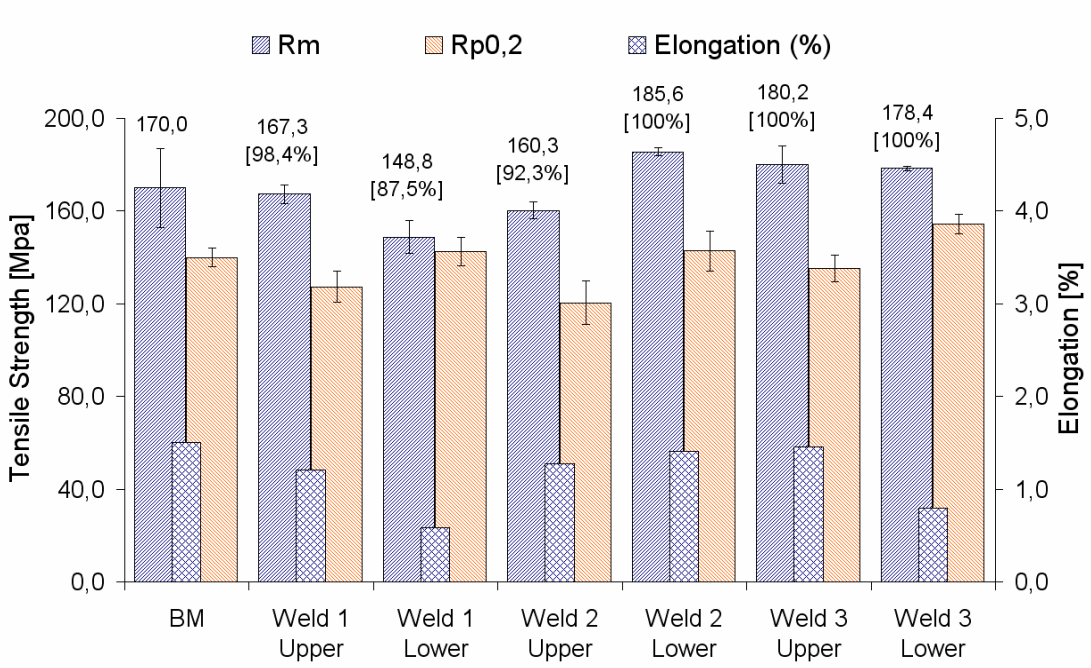

Figure 4.17: Transversal tensile test results. Values in brackets indicate the weld efficiency with reference to the base material (BM) for low AZAZ-1, intermediate AZAZ-2 and high AZAZ-3 welding pressures (see Figure 3.11 and Table 4.10 for details).

4.3 DISSIMILAR JOINTS – 8 MM DIAMETER/10 MM AND 20 MM UPSETTING

In Section 4.2, similar AZ91D-T6 welds with 6 mm diameter and 12 mm upsetting (AZAZ-06/12 series) were presented. By this approach, the influence of the welding pressure on the process as well as mechanical properties and the joint formation mechanism for similar welds (see Section 5.2.2) were established. As a further stage, dissimilar welds, using higher temperature resistant consumable materials were performed and will be assessed in this section. Further, similar joints, using the same geometry utilised for the dissimilar welds, were also performed for comparison purposes. Hence, all the results of the so-termed *"8 mm diameter/10 mm and 20 mm upsetting"* welds will be presented in this section.

For the following experiments studs were machined from base material AE42, MRI230D and AZ91D-T6, while base plates were produced from base material AZ91D-T6. Chemical composition and mechanical properties of these base materials have been previously reported (see Section 4.1). A geometry combination was chosen of an 8 mm tip diameter 10° tapered stud and an 8 mm bottom diameter 20° tapered hole. With this configuration, larger bolts could be used to perform the small-scale component tests. After some initial trials, one parameter set (i.e. rotational speed and pressure), was selected as the basis to perform the welds. Rotational speed and welding pressure were kept constant at 4000 rpm and 13.79 bar respectively, while 10 mm and 20 mm upsetting were used. Forging pressure was always set to 17.24 bar. As in the previous case, nine welds for each parameter combination were produced and devised for a specific test, as listed in Table 4.12.

Table 4.12: Designation and allocation of welded samples.

Weld	Welding Parameters	Process Stability	Tempe rature	Met. Analysis	Hard ness	Pull-out Test	Transversal Tensile Test
AE, MRI, AZ with AZ (1, 2, 3…, 9)	4000 rpm WP: 13.79 bar FP: 17.24 bar 10 mm Ups.	1 – 5	1 – 5	4	4	1, 2, 3, 5	6, 7, 8, 9
AE, MRI, AZ with AZ (a, b, c…, h)	4000 rpm WP: 13.79 bar FP: 17.24 bar 20 mm Ups.	a – d	a – d	a	a	b, c, d	e, f, g

4.3.1 Process / Temperature Monitoring

Similar to the analyses previously performed, the welding process was monitored for five joints within this investigation. Based on data delivered by the DAS it could be observed that the weld progress follows its particular deposition path for each material combination, however, with some instability within the same group. Welding process curves, in terms of upsetting/upsetting rate, were obtained and kept for further evaluation. Figure 4.18 presents the total welding time versus the achieved temperatures in upper (Figure 4.18(a)) and lower (Figure 4.18(b)) weld areas. Average peak temperatures with a respective scattering of results are summarised in Figure 4.19.

The peak temperatures measured for the AEAZ joints ranged between 453 °C to 470 °C and 492 °C to 524 °C in upper and between 406 °C to 442 °C and 462 °C to 476 °C in lower weld areas for 10 mm and 20 mm welds respectively. Welding times varied from 9.65 s to 15.72 s and from 31.9 s to 46.53 s for 10 mm and 20 mm upsetting welds respectively. For MRIAZ 10 mm upsetting joints, temperature indications ranging from 453.8 °C to 484.4 °C and from 398.8 °C to 421.8 °C in upper (T1) and lower (T2) weld areas were observed, with corresponding welding times varying between 19.08 s and 23.31 s. For higher upsetting, values from 485 °C to 495 °C and 389 °C to 446 °C were measured for T1 and T2 respectively. Welding times varied in these cases between 19.1 s and 23.3 s, and between 44.6 s and 65.2 s respectively for 10 mm and 20 mm upsetting. Moreover, the AZAZ joints experienced temperatures ranging between 430 °C to 464 °C and 467 °C to 497 °C in the upper and between 361 °C to 381 °C and 390 °C to 414 °C in the lower weld areas, for 10 mm and 20 mm welds respectively. Welding times varied from 20.4 s to 28.5 s and from 30.1 s to 51 s, for 10 mm and 20 mm upsetting welds respectively.

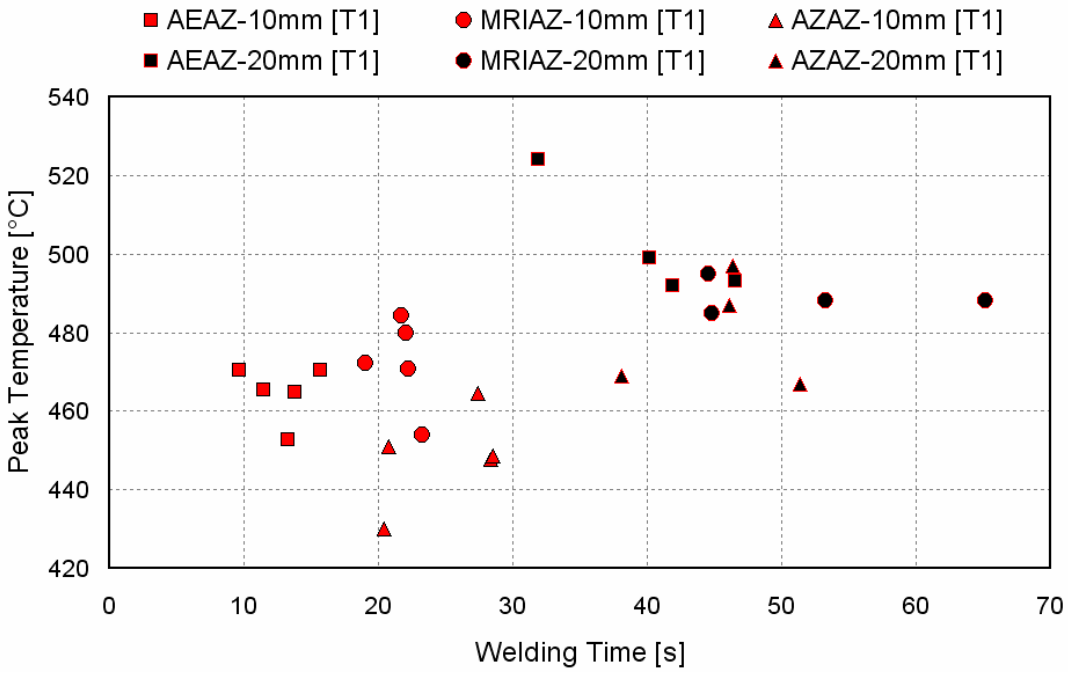

(a)

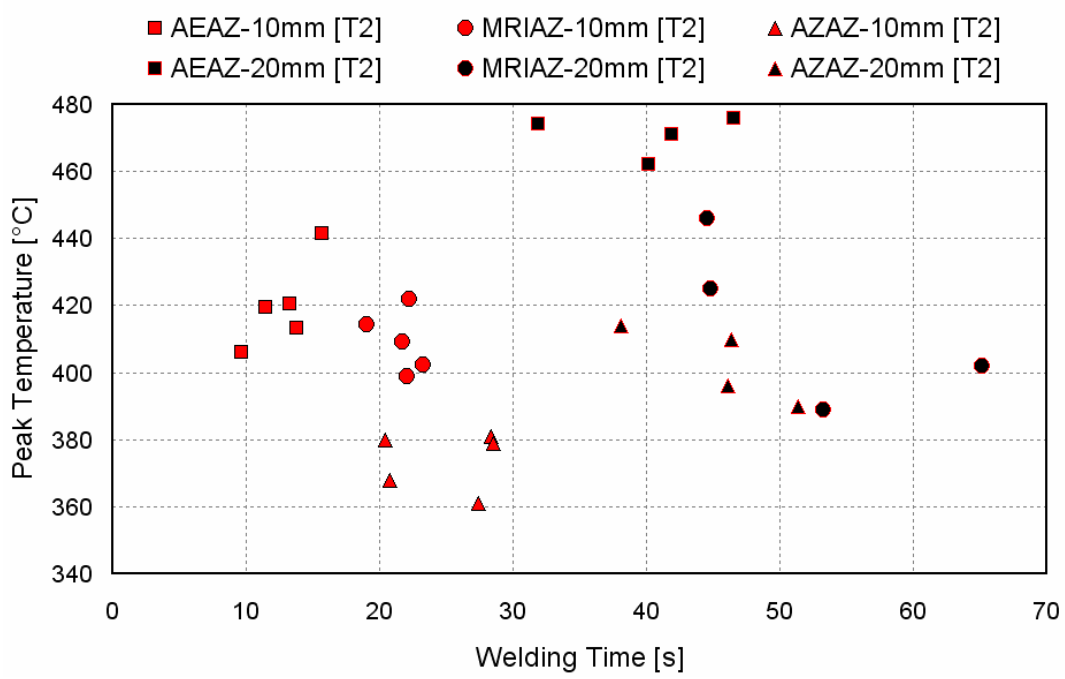

(b)

Figure 4.18: Peak temperatures in upper (a) and lower (b) thermocouples for similar and dissimilar welds, 10 mm and 20 mm upsetting.

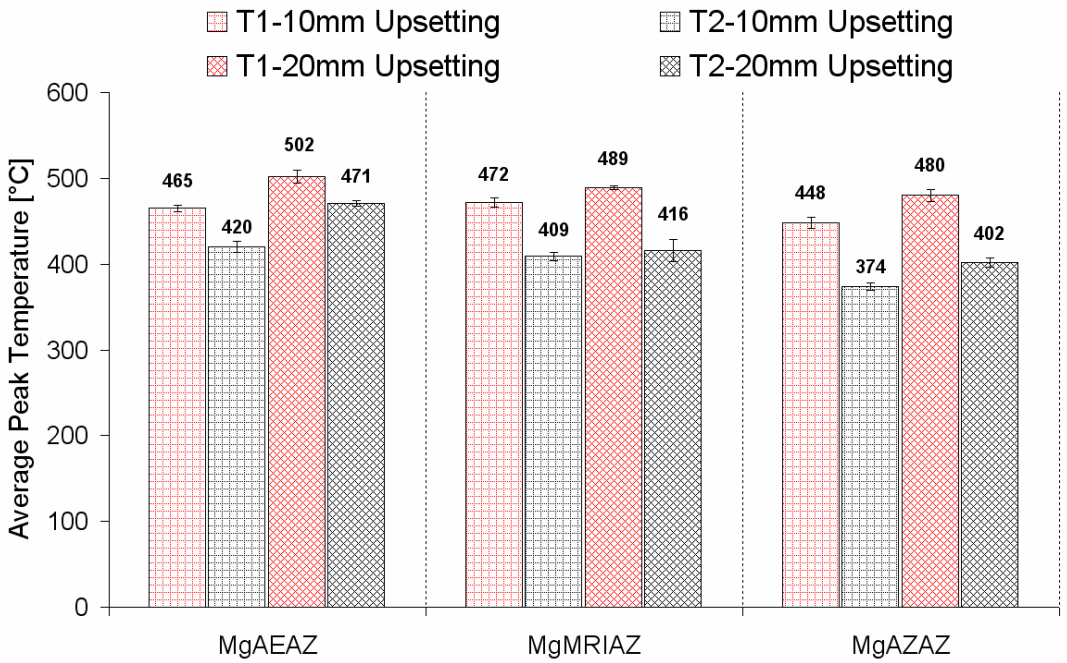

Figure 4.19: Average peak temperature in upper (T1) and lower (T2) weld areas for AEAZ, MRIAZ and AZAZ, 10 mm and 20 mm upsetting welds.

4.3.2 Metallurgical Characterisation

4.3.2.1 AEAZ Joints

Macrostructural investigations of the dissimilar AEAZ joints indicate that sound welds with no defects, such as porosity or lack of bonding, can be produced using FHPP (see Figure 4.20). Since both materials are composed of different alloying elements and therefore have different microstructural features, in most of the cases the bonding line could be clearly identified suggesting an intimate contact between consumable and base plate. As a consequence of the higher heat generation, which can be estimated through the width of the heat affected zone, in the upper joint regions (see Figure 4.20(a) and (e)) a smooth transition between stud and base material can be seen. However, in the lower parts of the joint, where the heat is almost instantaneously conducted out of the weld region, the border between consumable and base plate is well defined. On the AZ91 side of the weld, a thin layer of dynamically recrystallised grains presenting a non-uniform thickness extending up to 150 µm from the welding line followed by an almost unmodified base material was observed (see Figure 4.20(b) and (d)). In the central region at the bottom of the cavity, where a higher amount of plasticised material is usually concentrated (see Figure 4.20(c)), it seems that the consumable is mixed with the base material.

EDS was performed to assess the local chemical composition along the joint line. Second phase particles were also investigated within the RZ. Points chosen for EDS analysis are shown in Figure 4.21, and the corresponding results are presented in Table 4.13.

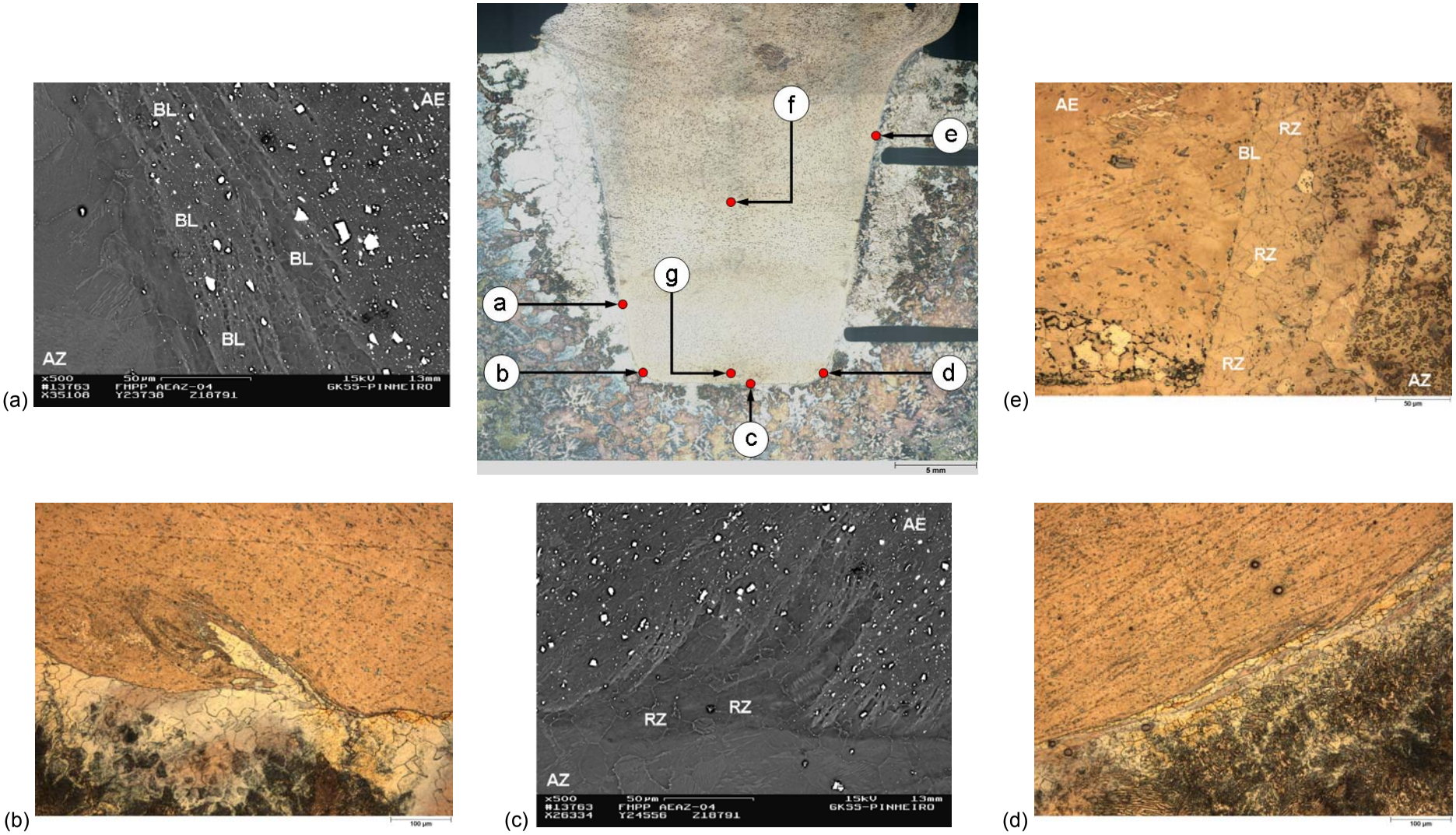

Figure 4.20: Microstructural details of the dissimilar AE42/AZ91D-T6 joint after etching in a solution with 20 ml distilled water, 100 ml ethanol, 6 ml glacial acetic acid and 12 g Picric Acid. In the centre on the left side an overview of the joint cross section; In (b), (d) and (e) micrographs taken with OM; In (a) and (c) BSE scans detailing the bonding line.

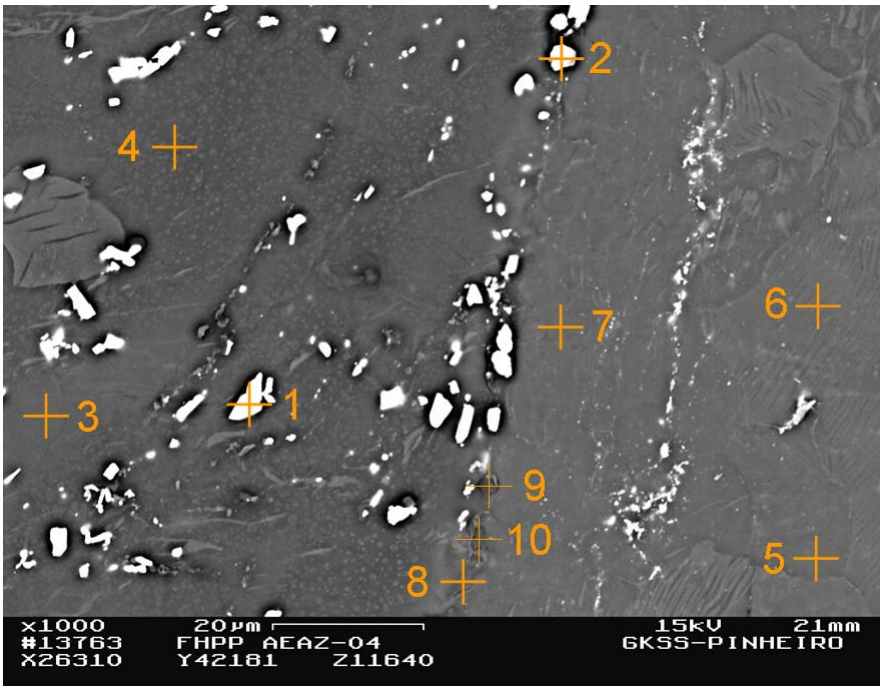

Figure 4.21: Weld interface of the dissimilar AE42/AZ91D-T6 FHPP welded joint. Backscattered electron micrograph showing points for EDS analysis in particles distributed along the joint line.

Table 4.13: Results of the EDS analysis in ten different points along the BL (wt.%).

Point	Mg	Al	Zn	Mn	Ce	Nd	Pr	La
1	8.94	34.89	---	---	31.81	7.35	---	17.01
2	4.51	34.33	---	0.68	31.81	8.76	4.06	13.84
3	96.27	3.73	---	---	---	---	---	---
4	98.16	1.84	---	---	---	---	---	---
5	92.97	7.03	---	---	---	---	---	---
6	92.86	7.14	---	---	---	---	---	---
7	93.06	6.94	---	---	---	---	---	---
8	92.82	7.18	---	---	---	---	---	---
9	88.51	10.68	0.81	---	---	---	---	---
10	88.40	10.59	1.01	---	---	---	---	---

4.3.2.2 MRIAZ Joints

As for the previously investigated AEAZ joints, micrographs of dissimilar MRIAZ welds suggest that sound joints can be produced using FHPP. Joints were characterised by longer welding times (see Figure 4.18), which led the microstructures to present wider HAZs (see overview in Figure 4.22). Figure 4.22(a) details, in upper weld areas on the left-hand side, the transition between the AZ91 base material, where a narrow region with grain growth can be observed, and the MRI consumable with a significantly refined microstructure. Macrographs from the bottom regions of the joint, i.e. Figure 4.22(b), (c) and (d), show a severely deformed area in the vicinity of the joint on the AZ91 side of the weld, where dynamically recrystallised grains appear in an extension from 100 μm to 400 μm from the weld line without, however, the presence of the eutectic structure. In those regions no voids or discontinuities along the joint line, referred to as lack of bonding, were observed. On the MRI side of the weld, a full degradation of the typical base material's second phase Mg(Al,Ca) particles was observed. Figure 4.22(e) presents a micrograph obtained from the upper joint parts, where a smooth transition can be observed, probably due to the role played by the forging force. In those areas an exact determination of the bonding line was also not possible.

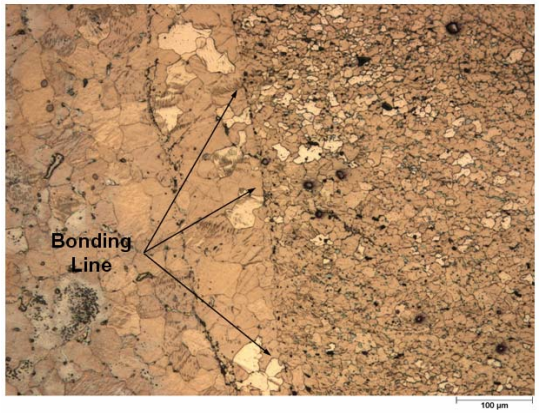

(a)

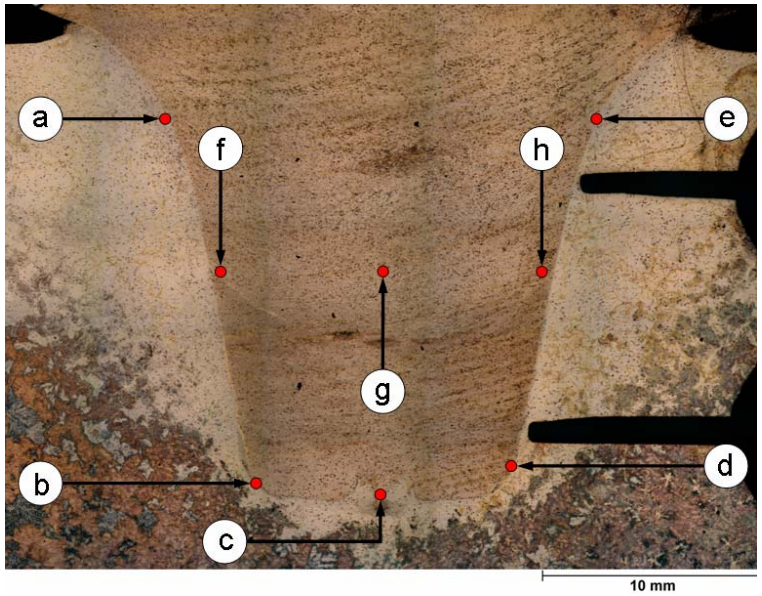

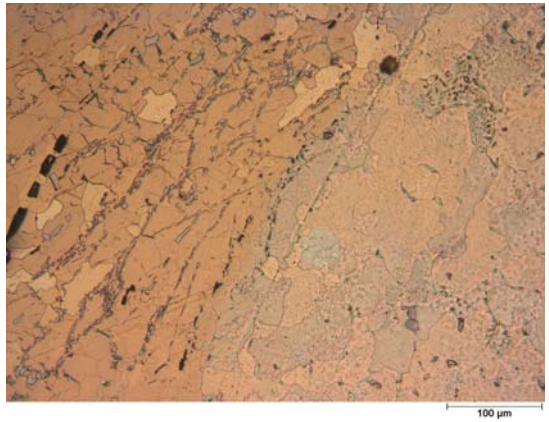

(e)

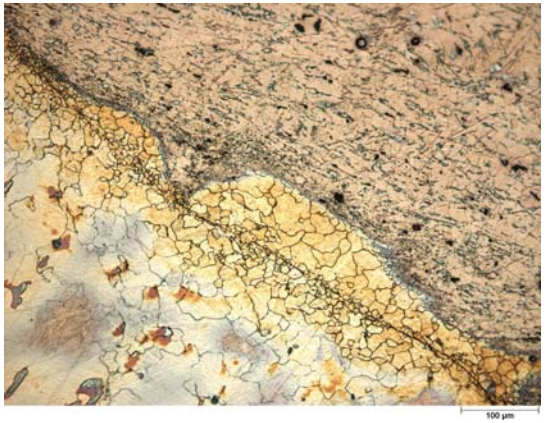

(b)

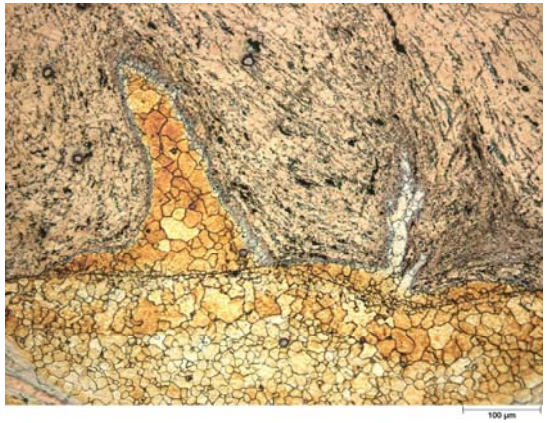

(c)

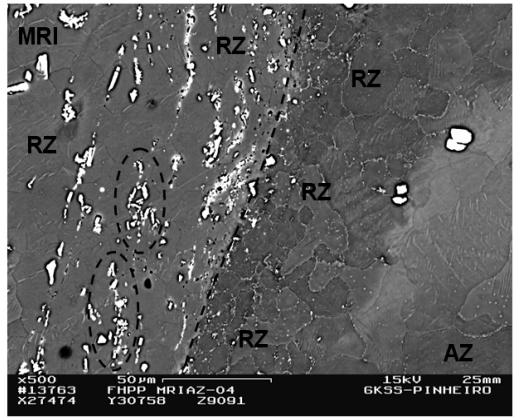

(d)

Figure 4.22: Microstructural details along the bonding line of the dissimilar MRI230D/AZ91D-T6 weld (a), (b), (c) and (e). In (d) a SEM micrograph showing clusters of particles in regions adjacent to the BL as well as different weld zones.

EDS analyses along the welding line indicate the presence of diverse eutectics with a chemical composition varying in a fairly large range. Points for EDS analyses are shown in Figure 4.23, and the corresponding results are presented in Table 4.14.

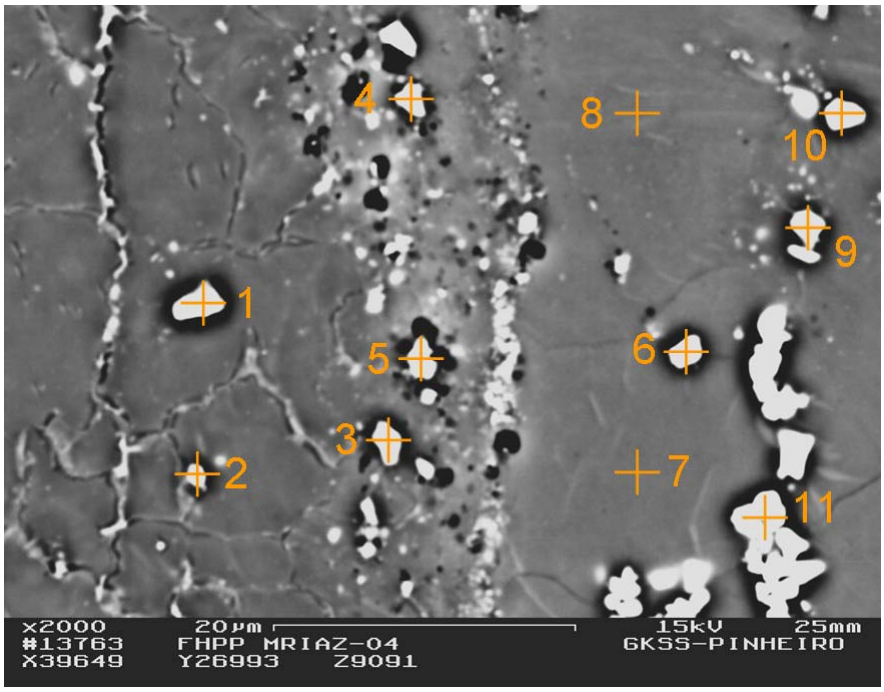

Figure 4.23: Points for EDS analysis - MRI230D/AZ91D-T6 weld (see Figure 4.22, position “a” for reference).

Table 4.14: Results of the EDS analysis over the bonding line (wt.%).

Point	Mg	Al	Zn	Mn	Ca	Sr
1	10.32	45.85	---	43.83	---	---
2	33.76	35.67	0.99	26.39	1.96	0.40
3	34.33	41.97	---	---	22.62	1.07
4	36.68	39.91	---	---	22.74	0.67
5	65.06	25.46	---	---	9.12	0.36
6	83.29	13.06	---	---	3.01	0.45
7	93.99	6.01	---	---	---	---
8	93.51	6.49	---	---	---	---
9	73.19	19.62	---	---	7.19	---
10	83.31	14.11	---	---	2.59	---
11	57.98	17.92	---	---	1.18	10.04

4.3.2.3 AZAZ Joints

Also within this geometry, since the process has shown to be suitable for performing similar defect-free welds with 6 mm diameter consumables, Friction Hydro Pillar Processing demonstrates its feasibility to produce visually high quality welds without apparent discontinuities along the joint line with 8 mm diameter consumables. Figure 4.24 comprises not only an overview of the MgAZAZ-4 weld, but also some micrographs taken along the bonding line. Figure 4.24(a) and (e) show, on the consumable side, the typical refined, equiaxed and homogeneous microstructure resultant from the dynamic recrystallisation (DRX) processes, which take place during welding. The base plate, however, is seen to have grains of unequal size and distribution intercalated with islands of non-recrystallised material in regions near to the bonding line. On the other hand, micrographs from the bottom of the weld (see Figure 4.24(b), (c) and (d)) show a broad range on both sides, where a dynamically recrystallised structure is observed. Figure 4.24 shows also within the recrystallised zone at the bottom, intercalated microstructures with lamellar-like shear bands. Additionally, in the lower consumable stud areas, where the most severe hot working is imposed, AlMn and MgSi (assumed to be Al_8Mn_5 and Mg_2Si respectively) second phase particles are not split and remain still composing the microstructure. Figure 4.25 shows the presence of AlMn (dark grey precipitates with black indications) and MgSi (green compounds with white indications) phases over the bonding line.

Welds with higher upsetting generally show larger grain sizes within the extruded area, larger recrystallised and heat affected zones with a much reduced grain size gradient along the transitioning zone and an apparently much more homogeneous structure in the deposited material. Grain size measurements in 10 mm upsetting welds indicate average diameter values ranging from 9 µm in the lower to 20 µm in the upper weld areas respectively, whereas the 20 mm welds show indications varying between 8 µm in the lower and 28 µm in the upper areas. EDS was performed to assess the local chemical composition. Points are indicated in Figure 4.26, taken in different areas along the welding line. The corresponding results are shown in Table 4.15.

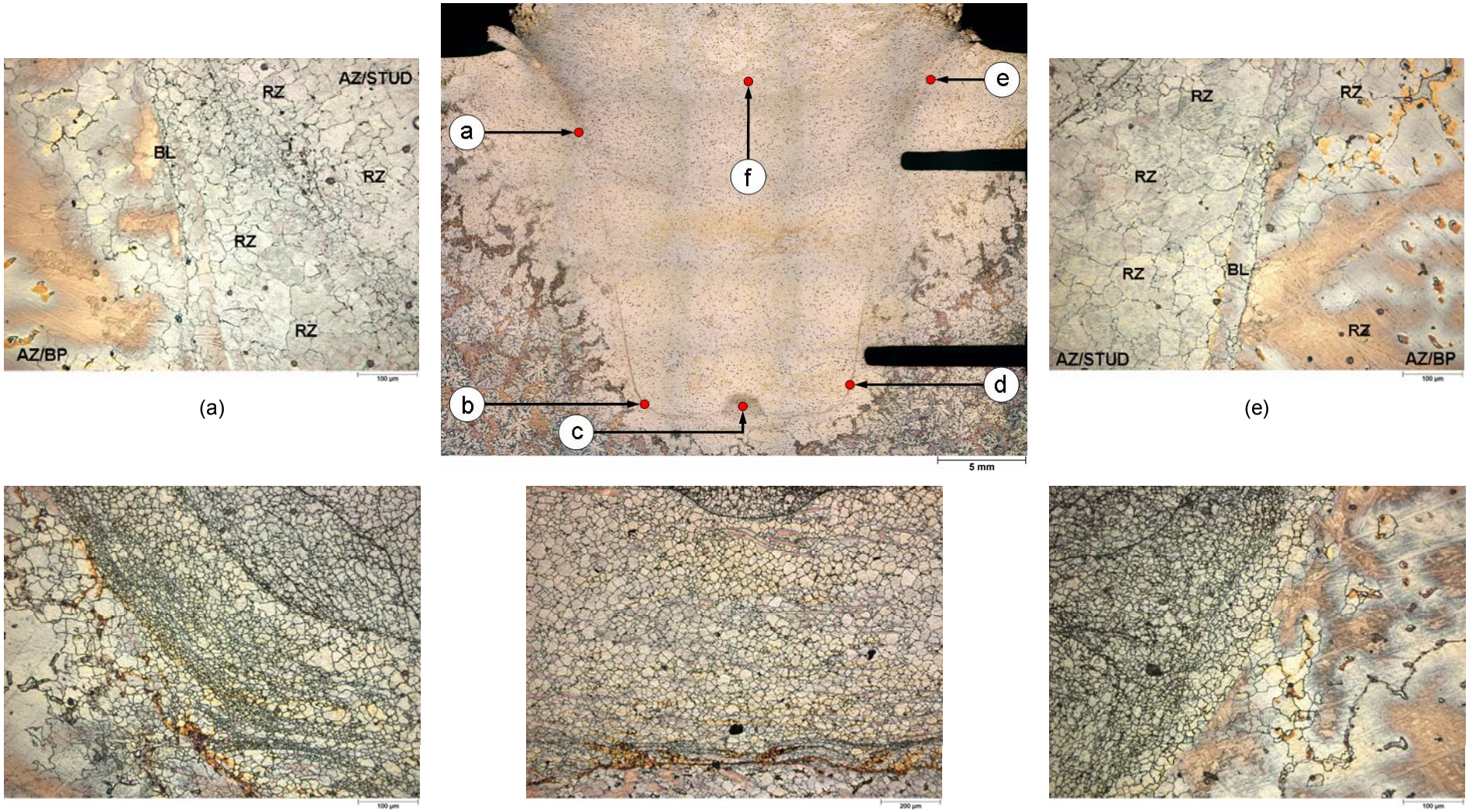

(a) (e)

(b) (c) (d)

Figure 4.24: Microstructural details along the bonding line of a similar AZ91D-T6/AZ91D-T6 weld. Defined bonding line in the upper regions (a) and (e) with a very refined transition zone in the lower stud areas (b), (c) and (d).

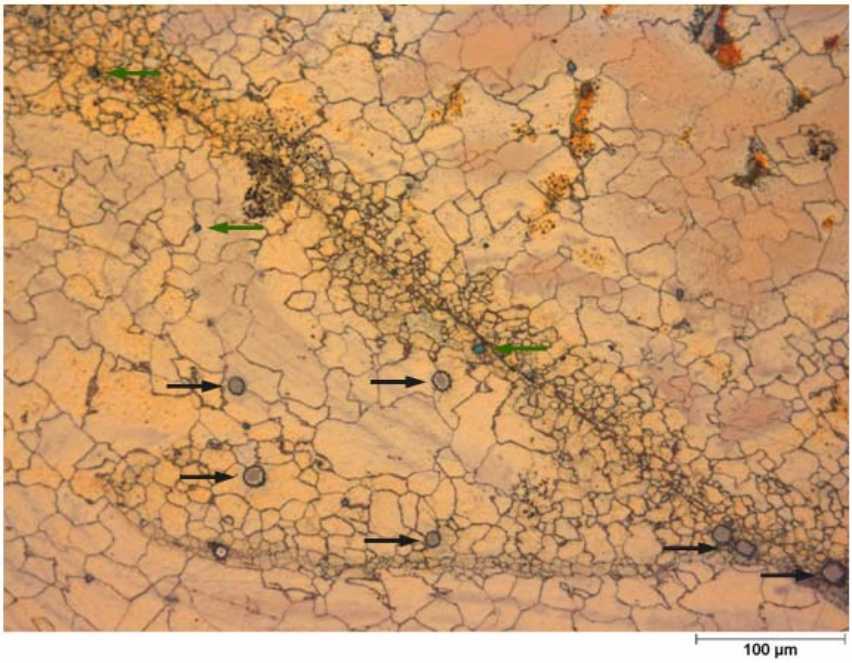

Figure 4.25: Second phase particles in regions highly plasticised within the welding zone.

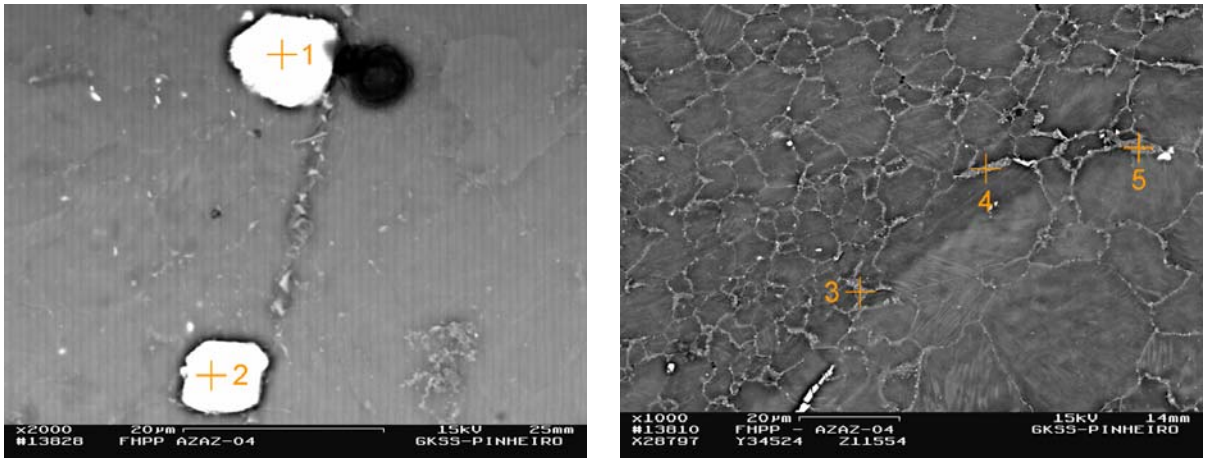

(a) (b)

Figure 4.26: SEM micrographs taken over the BL with points for EDS analysis. In (a) particles stacked along the BL and in (b) intermetallic compounds concentrated along grain boundaries.

Table 4.15: Results of the EDS analysis over the bonding line in similar AZAZ welds (wt.%).

Point	Mg	Al	Zn	Mn	Si
1	2.23	39.64	---	57.45	0.68
2	1.37	39.39	---	58.71	0.56
3	60.86	32.91	3.88	2.36	---
4	66.56	29.21	4.23	---	---
5	67.14	28.74	4.12	---	---

4.3.3 Mechanical Characterisation

4.3.3.1 Hardness Tests

As presented in Section 3.5.3, several microhardness profiles were obtained vertically and horizontally along the welded area. Figure 4.27(a) to (f) show horizontal profiles at 2 mm and 18 mm from the top base plate surface for different weld combinations. In AEAZ joints, the welding process seems to have a positive influence on the resultant microstructure of the consumable. While hardness values were shown to vary between 40 HV and 50 HV in the BM, in the extruded area these values range from 50 HV to 60 HV and from 60 HV to 70 HV in the upper and lower weld areas respectively (see Figure 4.27(a) and (b). However, hardness values in the RZ were practically unaltered with an increase in upsetting. On the AZ side of the weld, one can note an increase in the hardness in comparison to the RZ, which to some degree agrees with values found for the BM.

For MRI joints, material hardening in comparison with BM is easily observed from start to finish of the extruded zone, resulting from the weld thermal cycle. Hardness of the BM was shown to range between 46 HV and 54 HV, whereas in the extruded area values varied generally between 60 HV and 70 HV in the upper and 60 HV and 80 HV in the lower weld areas (see Figure 4.27(c) and (d). Scans performed near the top surface are very smooth and present a significantly lower scattering, even in regions of the HAZ far away from the joint line on the AZ side of the weld. However, in the lower stud areas, the 20 mm upsetting weld presented slightly superior hardness values.

According to Figure 4.27(e) and (f), in AZAZ joints the hardness profiles also indicate no apparent loss of hardness along the welding area. For 20 mm upsetting welds, the hardness values varied randomly around 70 HV in the upper and between 75 HV and 80 HV in the lower weld areas. For the 10 mm upsetting welds, a significant increase in hardness was observed in the lower region relative to the upper. Upper surveys indicated values between 60 HV and 70 HV, while in lower scans values ranging from 80 HV to 90 HV were obtained. Similar to the previous analyses, hardness scattering in the upper survey was clearly reduced in relation to the lower measurements.

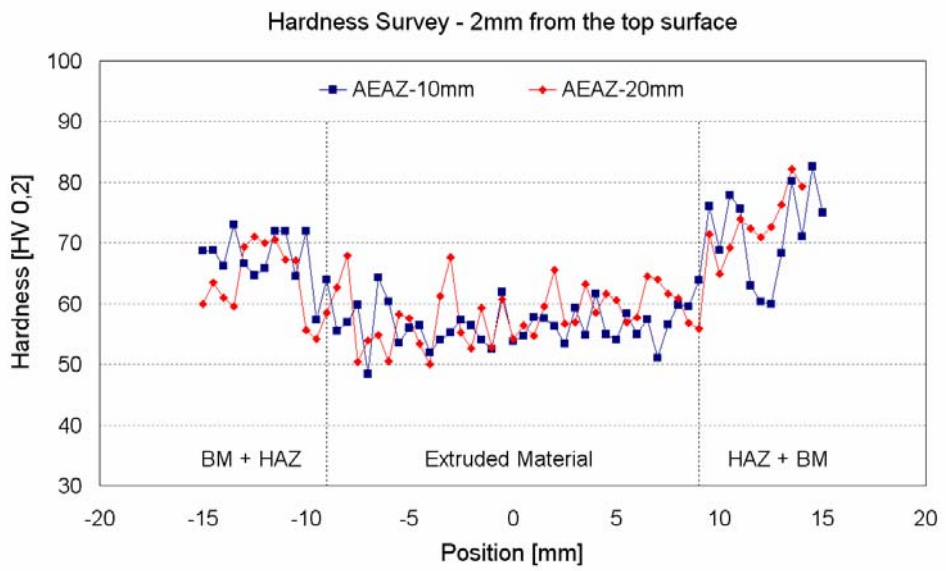
Hardness Survey - 2mm from the top surface
AEAZ-10mm
AEAZ-20mm
Hardness [HV 0,2]
BM + HAZ
Extruded Material
HAZ + BM
Position [mm]

(a)

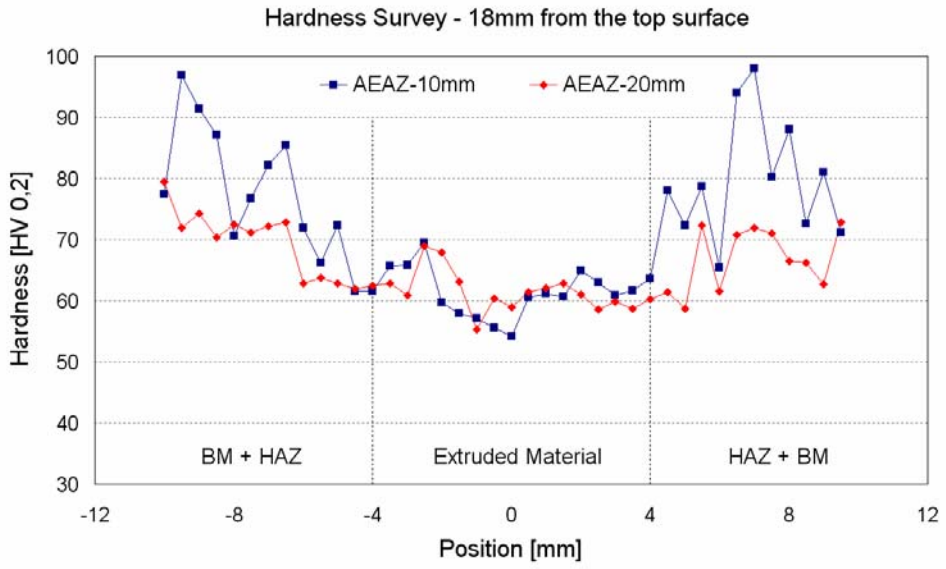
Hardness Survey - 18mm from the top surface
AEAZ-10mm
AEAZ-20mm
Hardness [HV 0,2]
BM + HAZ
Extruded Material
HAZ + BM
Position [mm]

(b)

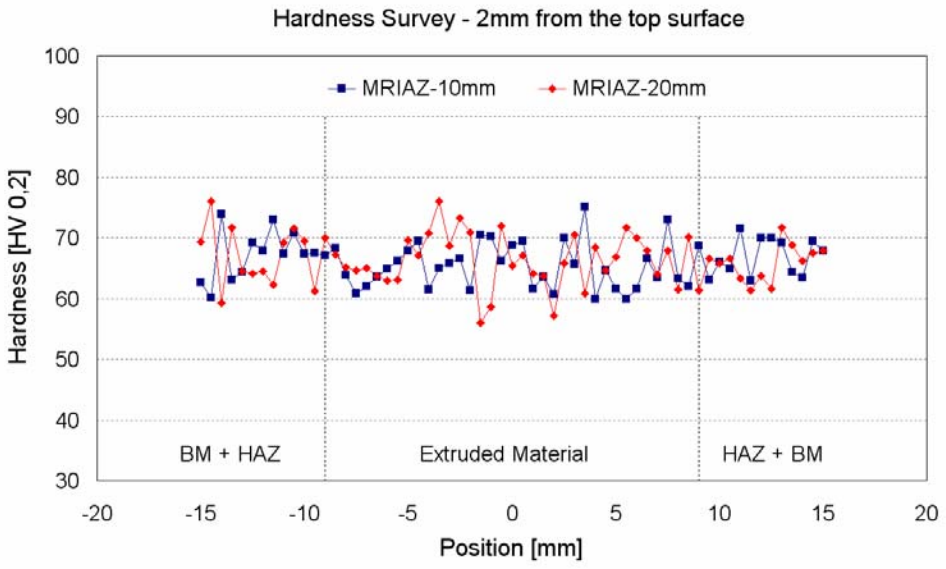
Hardness Survey - 2mm from the top surface
MRIAZ-10mm
MRIAZ-20mm
Hardness [HV 0,2]
BM + HAZ
Extruded Material
HAZ + BM
Position [mm]

(c)

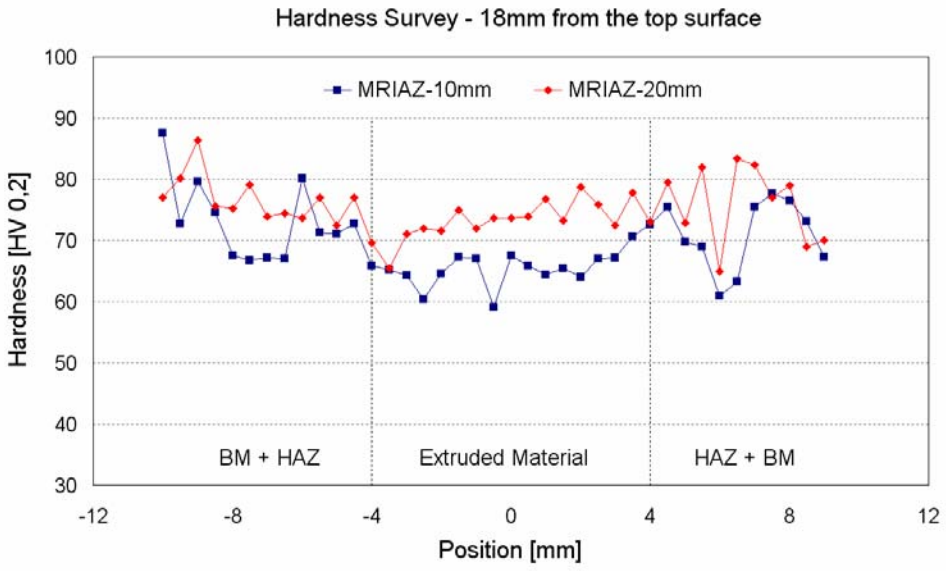

(d)

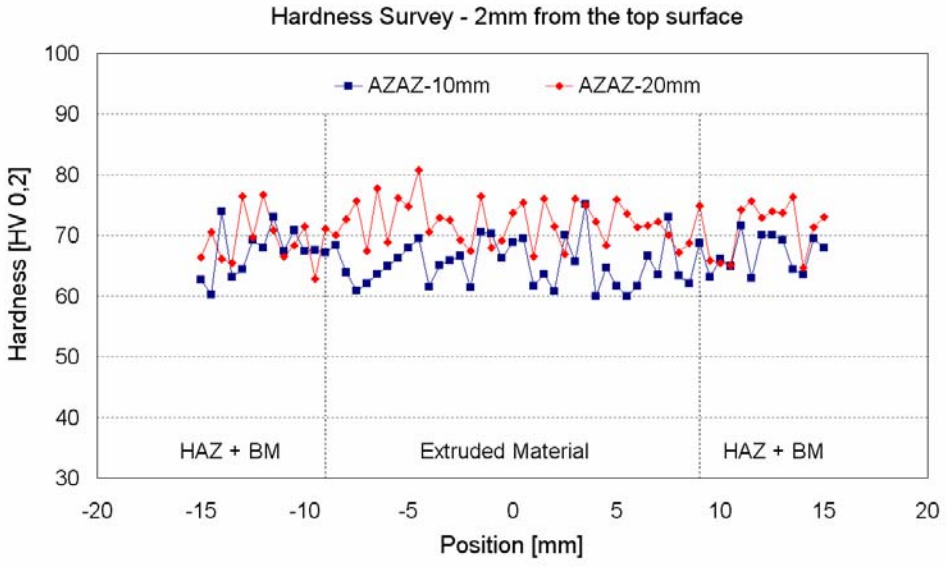

(e)

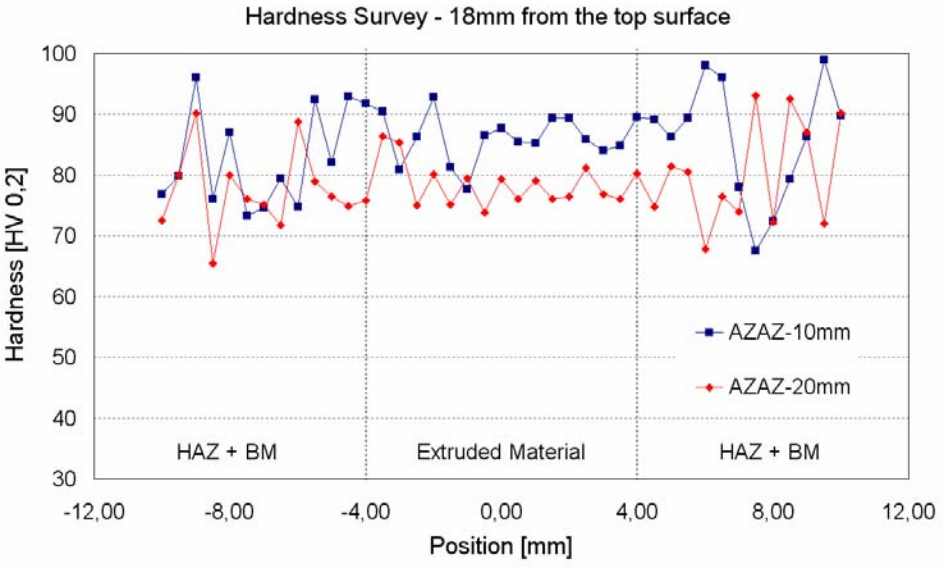

(f)

Figure 4.27: Horizontal hardness profiles along the joints at 2 mm and 18 mm from the top surface.

4.3.3.2 Pull-out Tests

Similar to the results obtained in Section 4.2.4.2 for similar AZAZ-6/12 joints, AEAZ, MRI and AZAZ welds within these welding parameters also always collapsed in the stud material outside the deposit area. Since the failures occurred in the stud material, very similar curves for 10 mm and 20 mm upsetting welds could be observed, as demonstrated in Figure 4.28. As may be observed, up to approximately 10 kN all the curves are almost coincident. After this load is achieved, yielding begins. Pull-out strength values were observed to vary from 25 kN to 30 kN for AEAZ and from 30 kN to 35 kN for AZAZ joints. MRIAZ welds presented similar results, indicating a maximum of 20 kN independent of the upsetting used.

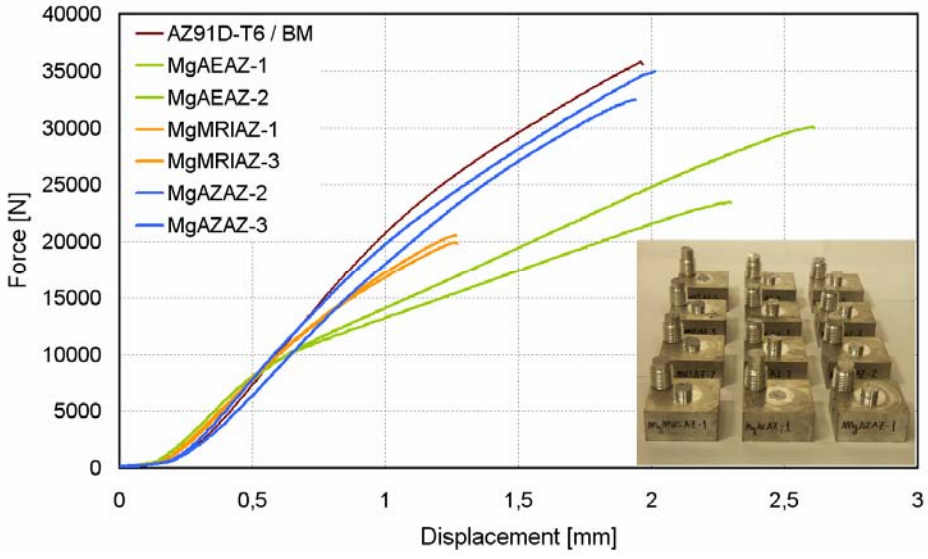

(a)

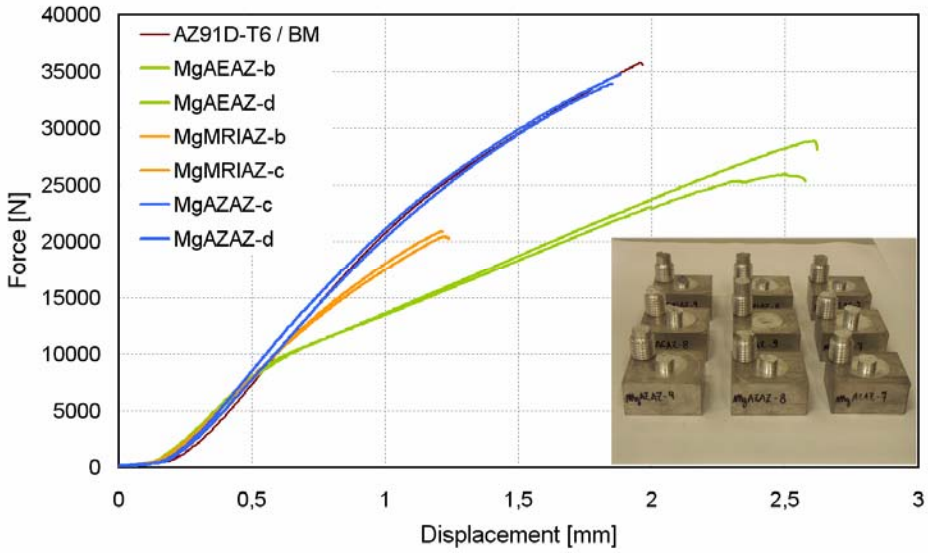

(b)

Figure 4.28: Pull-out test results for ∅8 mm/10 mm upsetting welds.

4.3.3.3 Transversal Tensile Tests

Tensile properties were determined at room temperature for the base materials and for the different welding combinations/parameters. Following the same procedure presented in Section 3.5.5, two tensile specimens were obtained from each welded sample, with the weld area placed in the middle of the gauge length. Tensile strengths for dissimilar AEAZ welds are presented in Table 4.16 and summarised in Figure 4.29. According to these results, AEAZ welds presented high strengths even comparable with those of the AZ91D-T6 BM. For 20 mm upsetting samples, specimens from the upper weld areas presented the higher average strength values (166 MPa) in relation to those machined from lower areas (150.5 MPa). The converse occurred for 10 mm upsetting samples, where the lower areas showed higher average strengths (166.1 MPa) compared with the upper weld areas (151.7 MPa). In terms of elongation, values ranging from 0.8 MPa to 1.8 MPa and 2.7 MPa to 1.6 MPa were observed for lower and upper samples in 10 mm and 20 mm upsetting welds respectively.

Table 4.16: AEAZ - Tensile testing results.

Sample		Rm [MPa]	$Rp_{0,2}$ [MPa]	A [%]
AEAZ-10 mm	*Upper*	151 ± 14	123 ± 6	0.8 ± 0.5
	Lower	166 ± 8	118 ± 6	1.8 ± 0.3
AEAZ-20 mm	*Upper*	166 ± 6	103 ± 3	2.7 ± 1.6
	Lower	150 ± 3	105 ± 4	1.6 ± 0.1
AE42	*Base Material*	104 ± 8	90 ± 2	4.5 ± 1
AZ91D-T6	*Base Material*	171.5 ± 16	140 ± 4	1.3 ± 0.7

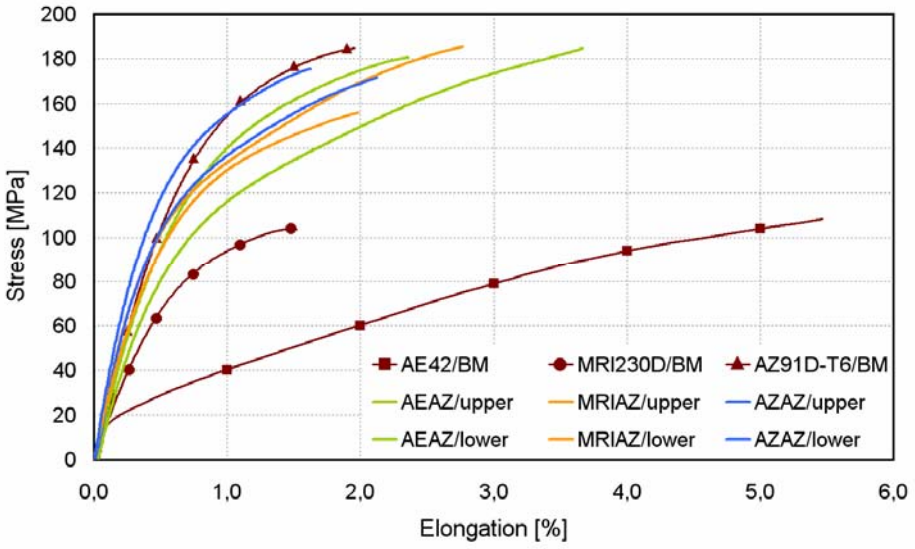

Figure 4.29: Tensile test curves for ∅8 mm/10 mm upsetting welds in association with BM values.

MRIAZ welds also presented satisfactory strengths. As demonstrated in Table 4.17, average values in the upper and lower weld areas respectively of 173 MPa and 150 MPa were obtained for MRIAZ-10 mm welds, whereas slightly lower values of 159 MPa and 147 MPa were found for MRIAZ-20 mm joints. Elongations were observed also to match the BM values and varied between 1.0 % and 1.6 % and between 0.8 % and 2.0 % respectively for 10 mm and 20 mm upsetting welds in the lower and upper weld areas.

Table 4.17: MRIAZ - Tensile testing results.

Sample		Rm [MPa]	$Rp_{0,2}$ [MPa]	A [%]
MRIAZ-10 mm	*Upper*	173 ± 8	129 ± 5	1.6 ± 0.1
	Lower	150 ± 2	124 ± 2	1.0 ± 0.1
MRIAZ-20 mm	*Upper*	159 ± 4	103 ± 6	2.0 ± 0.3
	Lower	147 ± 9	123 ± 4	0.8 ± 0.1
MRI230D	*Base Material*	94 ± 8	90.1 ± 2	0.8 ± 0.2
AZ91D-T6	*Base Material*	171.5 ± 16	140 ± 4	1.3 ± 0.7

According to Table 4.18, AZAZ-08/10-20 welds presented values that to some extent were similar to those of the BM. Specimens welded with 20 mm upsetting present average strength values of 184 MPa and 159 MPa respectively for upper and lower stud areas. Following the same tendency, tensile strengths of 10 mm upsetting welds showed average values varying from 156 MPa to 175 MPa respectively for lower and upper samples. On the other hand, yield strengths seem to differ widely from BM values, particularly in the upper weld areas. Values around 116 MPa and 118 MPa were obtained for 10 mm and 20 mm upsetting welds respectively.

Table 4.18: AZAZ - Tensile testing results.

Sample		Rm [MPa]	$Rp_{0,2}$ [MPa]	A [%]
AZAZ-10 mm	*Upper*	175 ± 3	116 ± 4	2.1 ± 0.3
	Lower	156 ± 7	141 ± 7	1.0 ± 0.5
AZAZ-20 mm	*Upper*	184 ± 3	118 ± 4	2.1 ± 0.1
	Lower	159 ± 6	123 ± 13	1.2 ± 0.5
AZ91D-T6	*Base Material*	171.5 ± 16	140 ± 4	1.3 ± 0.7

4.4 JOINT PERFORMANCE

4.4.1 Creep Tests

4.4.1.1 AE42 Studs (Reinforcement)

Creep tests conducted in AEAZ welds, according to the procedures presented in Section 3.5.7, presented a very similar behaviour between lower and upper samples (see Figure 4.30). At 125 °C the extruded material (lower sample) demonstrated a slightly better performance, while at 150 °C the upper (ref.) sample showed a superior creep resistance after 100 hours. Creep compression indicated values of 1.42 % and 1.79 % respectively for lower (weld) and upper (ref.) samples at 125 °C after 100 hours. At 150 °C compression values of 4.1 % and 5 % for upper and lower samples respectively were observed. In this case, the reference sample presented a higher deformation within the first stage of the test. However, after approximately 65 hours the strain observed in the reference sample was surpassed by that of the lower sample, which demonstrated a higher creep rate in the secondary region. At 175 °C the AE42 material suffers an expressive creep strain in both cases.

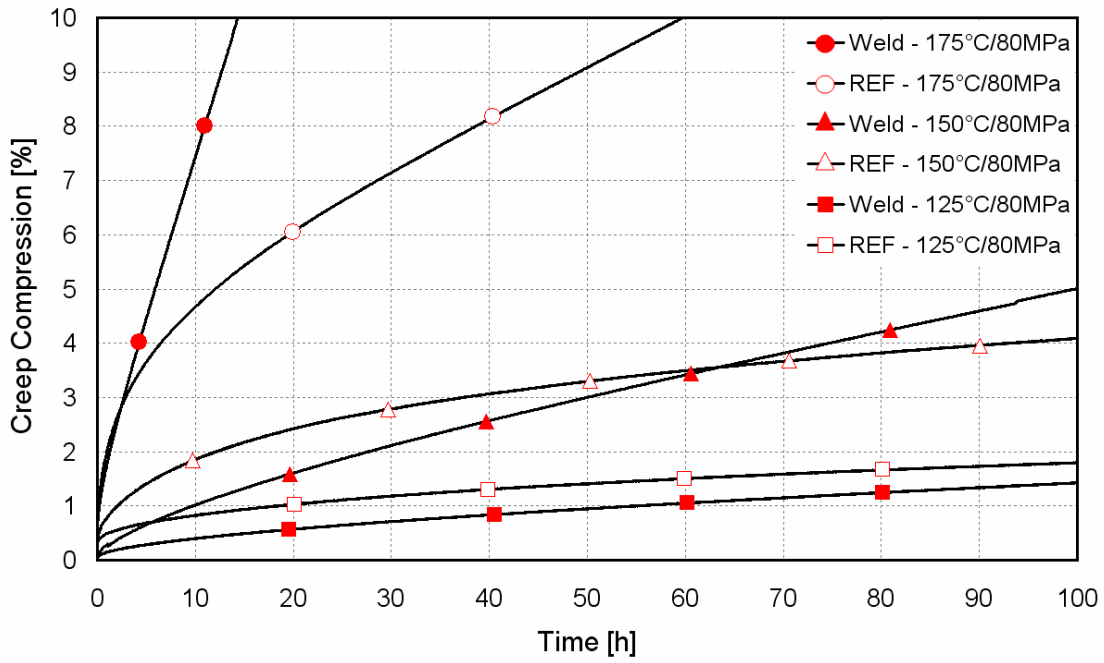

Figure 4.30: Creep curves of dissimilar AEAZ welds in compression at 125 °C, 150 °C and 175 °C with 80 MPa.

4.4.1.2 MRI230D Studs (Reinforcement)

As expected, MRIAZ welds presented a very high performance among the tested combinations. Lower and upper samples demonstrated very similar creep behaviour at lower temperatures (see Figure 4.31) with creep compression values around 0.3 % after 100 hours. At 150 °C, the reference sample creeps at a higher rate during the first stage being, however, overtaken by the lower sample somewhere in the middle of the test, as observed for AE42 Studs. After 100 hours, creep compression values of 1.4 % and 2 % were obtained for upper and lower samples respectively. At 175 °C the upper reference sample creeps around 3 %, while the lower sample creeps between 9 % and 10 % after 100 hours at 80 MPa.

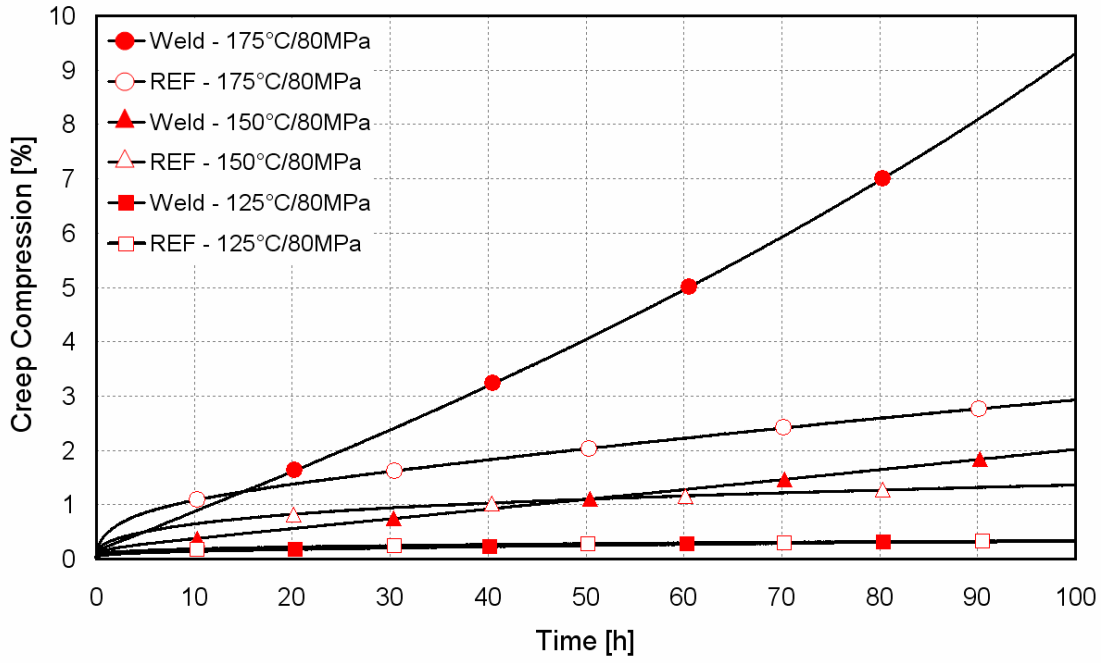

Figure 4.31: Creep curves of dissimilar MRIAZ welds in compression at 125 °C, 150 °C and 175 °C with 80 MPa.

4.4.1.3 AZ91D-T6 Studs (Reinforcement)

According to Figure 4.32, in similar AZAZ welds, the samples extracted from the lower stud areas presented in all three cases a reduced creep resistance compared with the upper samples (ref.). Primary creep regions are relatively short and exhibit a sharp transition to steady state creep in tests performed at lower temperatures. Under these temperatures, creep compression around 0.6 % and 1.3 % were observed after 100 hours for upper and lower samples respectively. However, a clear

transition from stage II to III was not observed, independent of the temperature. At 125 °C and 150 °C (only for the reference sample) an evident steady creep stage, characterised by the minimum creep rate extending to the end of the experiment, was observed. At 150 °C the reference sample presented 2 % creep compression, while the lower one experienced values around 10 % after 83 hours. At 175 °C the unsuitability of AZ alloys for high temperature applications became clear, with creep compression values of 10 % after 10 and 14 hours for lower and upper samples respectively.

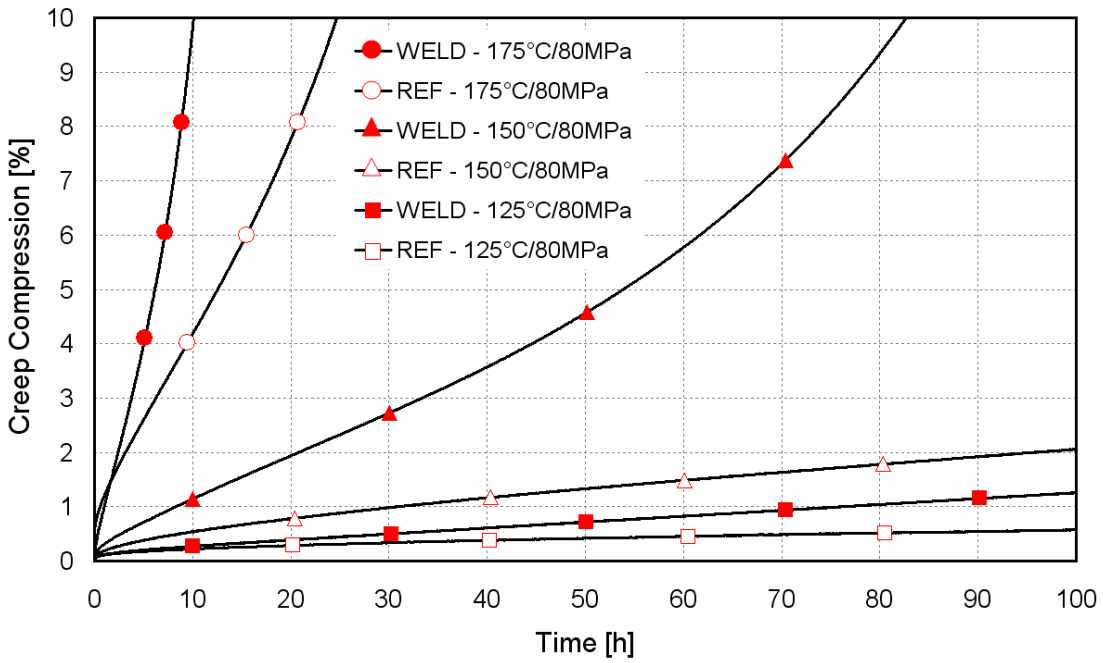

Figure 4.32: Creep curves of similar AZAZ welds in compression at 125 °C, 150 °C and 175 °C with 80 MPa.

4.4.2 Bolt Load Retention Tests

As presented in the experimental procedure (see Section 3.5.6), bolt load retention (BLR) tests were performed for the different configurations. In the first case, as presented in Figure 3.12, welded joints would be subjected to tensile stresses, whereas in the second case the reinforced area would be subjected to retention tests in compression (see Figure 3.13). Both nomenclatures, i.e. BLR in tension and BLR in compression, are used only within this study and make reference to the position of the reinforced component in relation to the couple.

4.4.2.1 BLR Tests – In Tension

Bolt load retention tests (in tension) within this study were performed in a variety of samples welded with different parameters and subjected to different testing conditions. In order to keep the scope of this work within reasonable limits, only the most relevant results are reported in this section.

Figures 4.33 and 4.34 show the remaining load in tests carried out at 175 °C after 100 hours. Figure 4.33 shows AZ91D-T6/BM bolted with steel screws having after 100 hours at 175 °C remaining load values of around 30 % and 1 % of the preload force for joints tightened with 40 Nm and 60 Nm respectively. In comparison, under the same circumstances the MRI230D base material presented retaining loads of 75 % and 35 % in relation to the initial preload force for respectively 40 Nm and 60 Nm tightening torque. BLR in reinforced joints, in this context, presented an intermediate behaviour between AZ91D and MRI230D. Joints produced with larger diameter studs show a better performance than those produced with 6 mm studs. After 100 hours, welds produced with 6 mm studs retained 36 % and 11 % of the initial load for joints tightened with 40 Nm and 60 Nm respectively. For 8 mm stud welds, however, higher values of around 41 % and 20 % were observed under the same conditions. It was also clear to see that higher tightening torques lead the couple to inferior remaining loads. Joints tightened with 60 Nm retained 11 % and 20 % for 6 mm and 8 mm geometries respectively, while 40 Nm screwed couples presented 36 % and 41 % remaining loads, also for 6 mm and 8 mm geometries. Furthermore, welds produced with 8 mm studs retained higher loads (41 % and 20 % for 40 Nm and 60 Nm tightening torques) than those retained by 6 mm stud welds, which presented 36 % and 11 % for 40 Nm and 60 Nm tightening torques respectively.

Welded joints tightened with aluminium fasteners (see Figure 4.34) presented clearly higher remaining load values, varying from 63 % to 69 % of the initial preload force. Also in this case, the load remaining in welded joints were higher than those observed for the AZ91D-T6 BM, but lower than those verified for the MRI230D BM. For 6 mm stud welds, an uncommon trend was observed, in which samples tightened with 35 Nm showed a slightly higher remaining load (64 %) in relation to those torqued with 25 Nm (63 %). However, as in the previous case, joints produced with

larger diameter studs showed a better performance than those produced with 6 mm studs and welds produced with 8 mm studs retained higher loads (69 % and 66 % for 25 Nm and 35 Nm tightening torques) than those retained by 6 mm stud welds, which presented 63 % and 64 % for 25 Nm and 35 Nm tightening torques respectively.

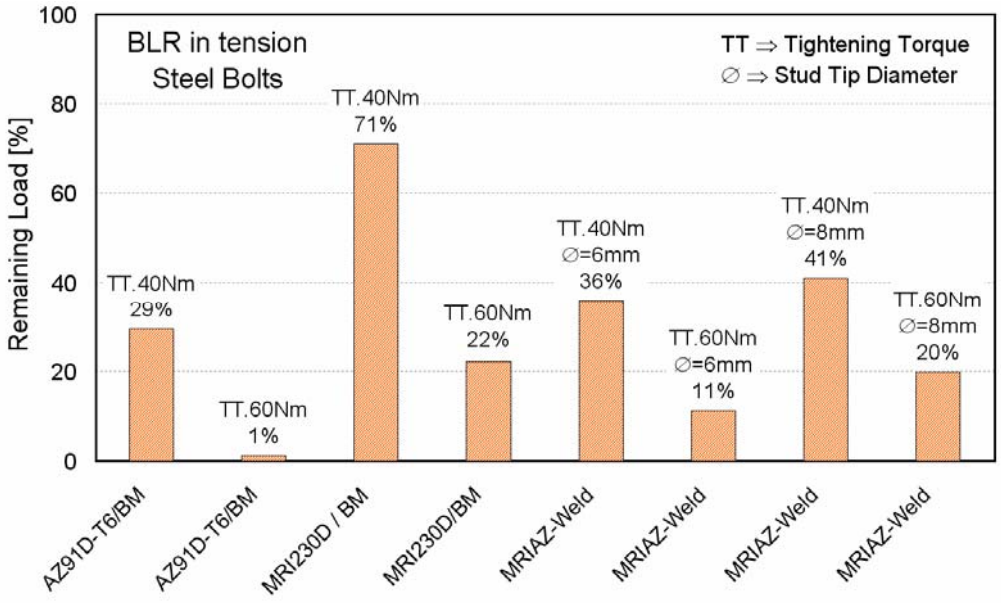

Figure 4.33: Remaining load in tensile stress retention tests at 175 °C for dissimilar MRIAZ joints with steel fasteners. MRI230D and AZ91D-T6 base material results are also presented for comparison.

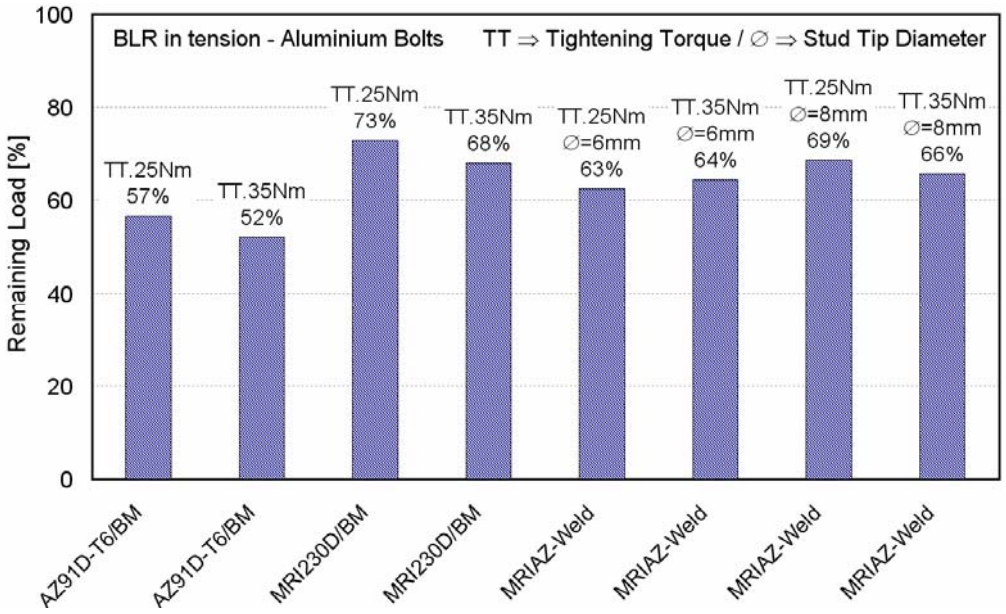

Figure 4.34: Remaining load in tensile stress retention tests at 175 °C for dissimilar MRIAZ joints with aluminium fasteners. BM results are also presented for comparison.

4.4.2.2 BLR Tests – In Compression

In order to investigate BLR also in compression, welded samples were tested under different conditions. In experiments carried out at 175 °C using steel bolts of strength grade 8.8, Mg samples (AZ91D-BM, AEAZ, MRIAZ and AZAZ welds) were tightened with a pretensioning force of 20 kN against a threaded Al AlSi9Cu3 specimen (see Figure 3.13). Labelled points P_I (= initial load at room temperature), P_k (= highest load attained by the couple during heating at test temperature), P_R (=retained load at test temperature) and P_F (= final load retained by the couple after returning to room temperature) indicate the critical loads, which define the bolt load behaviour of the investigated alloys. In terms of the overall BLR behaviour and its effect on engine performance, the two most significant loads are the initial load P_I and the load at the completion of the test after returning to ambient temperature P_F. The important ratio is therefore P_F/P_I as the engine is cycled from room to operating temperature and back again. The ratio P_R/P_K represents the fraction retained at test temperature, whereas P_F/P_I the fraction retained after the joint returns to ambient temperature. The overall relaxation behaviour (P_I - P_F) is made up of two major components: the compressive creep component (P_K - P_R) and a component due to yielding, which is obtained from the difference. These important factors are presented in the following table for the different materials and joints under investigation.

Based on Figure 4.35 and Table 4.19, Mg AZ91D-T6 seems not to be suitable for applications at 175 °C, even if reinforced with high-temperature resistant materials. This is because the BLR test P_F values, which gives the final load retained by the couple after returning to room temperature, dropped below the zero level in all the investigated cases. The ratio P_F/P_I presented values around zero, which means that no load is retained by the couple after returning to room temperature. The similar AZ91D-T6 welded joint followed the same behaviour revealed by creep tests and clearly presented the lowest remaining load.

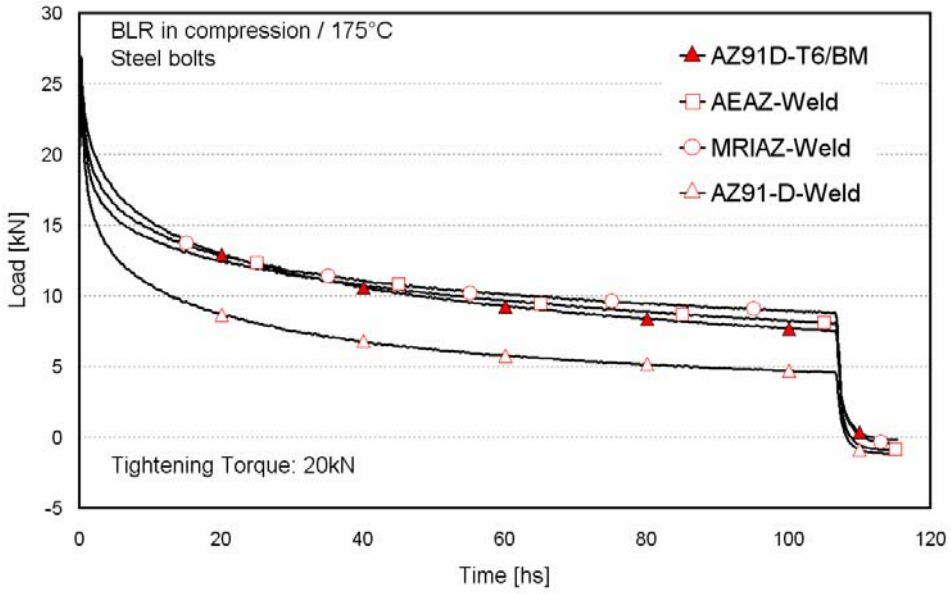

Figure 4.35: Typical bolt load compressive stress retention curves at 175 °C for AZ91D-T6 similar and AEAZ, MRIAZ dissimilar welds covering the entire test. Base material behaviour is also presented for comparison.

Table 4.19: Critical loads in (kN) for Mg welds tested at 175 °C.

Temp.	Alloy	P_I	P_K	P_R	P_F	P_R / P_K	P_F / P_I	$P_I - P_F$	Creep	Yield
175 °C	AEAZ - Weld	20.6	26.9	8.06	-0.9	0.30	-0.04	21.50	18.84	2.66
	MRIAZ - Weld	20.3	26.2	8.86	-0.5	0.34	-0.02	20.80	17.34	3.46
	AZ91D - Weld	19.7	24.9	4.59	-1.15	0.18	-0.06	20.85	20.31	0.54
	AZ91D - BM	19.7	26.4	7.53	-0.2	0.29	-0.01	19.90	18.87	1.03

Since BLR tests at 175 °C demonstrated that AZ91D-T6 alloys, even reinforced, were not suitable to be used under these conditions, tests at 150 °C were performed in AZ91D-T6/BM, MRI230D/BM and MRIAZ welds with steel and Al bolts. Figure 4.36 illustrates the plots depicting bolt load retained after 50 hours at 150 °C for 15 kN and 10 kN. As expected, from Figure 4.36 and Table 4.20 one can clearly observe the higher P_F/P_I ratio (the retained load after joint returns to room temperature) for the MRI230D/BM, confirming the superior high temperature properties of this alloy. MRI/BM sustained a P_F value of 6.81 kN, which is approximately 44 % of the initial load (P_I), after being subjected to the temperature cycle. MRIAZ welds tested under the same loading condition records a P_F value of 6.49 kN, which is approximately 41 % of P_I. AZ91D BM, on the other hand, retains only 24 % of the initial load. The joint bolted with an Al fastener presented an untypically low remaining load of only 27 %, which was to some extent unexpected.

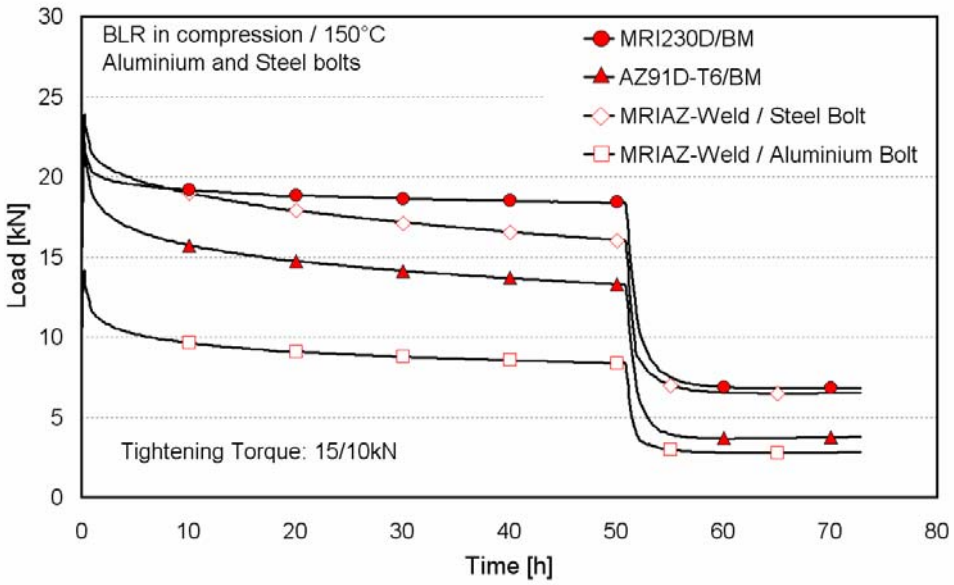

Figure 4.36: Typical bolt load compressive stress retention curves at 150 °C for MRIAZ dissimilar welds with steel and aluminium bolts covering the entire test. MRI230D and AZ91D-T6 base materials' behaviour is also presented for comparison.

Table 4.20: Critical loads in (kN) for Mg welds tested at 150 °C.

Temp.	Alloy	P_I	P_K	P_R	P_F	P_R / P_K	P_F / P_I	$P_I - P_F$	Creep	Yield
150 °C	MRI230D/BM	15.4	22	18.4	6.81	0.84	0.44	8.59	3.60	4.99
	AZ91D-T6/BM	15.6	22.1	13.3	3.68	0.60	0.24	11.92	8.80	3.12
	MRIAZ - Weld Steel Bolt	16	23.9	16	6.49	0.67	0.41	9.51	7.90	1.61
	MRIAZ - Weld Aluminium Bolt	10.3	14.2	8.36	2.77	0.59	0.27	7.53	5.84	1.69

5 DISCUSSION OF RESULTS

5.1 BASE MATERIAL CHARACTERISATION

5.1.1 Mg-Al-Zn [AZ] – Ingot (heat treated to T6 condition)

According to the EDS results listed in Table 4.2, round particles within the Mg-matrix corresponding to points 1 and 7 to 11 showed a high concentration of Al and Mn with a minor presence of Si. Such compounds are suggested to be AlMn based phases, commonly present in AZ alloys. Points 2 to 4 and 6 indicate a high concentration of Mg and Al with some significant evidence of Zn. Such Mg containing phases (Mg-(Al-Zn)) have been reported in the literature [14] to be present in Mg-Al-Zn alloys and are suggested to be $Mg_{17}(Al, Zn)_{12}$ second phase products. Point 5 reveals the average composition of the Mg-matrix. No clear presence of Mg_2Si particles was observed within the investigated points, although its presence has also been reported in AZ Mg alloys. Since the lamellae structure covered most of the material's macrostructure, to count the average grain diameter was difficult. However, microscopic observations with higher magnification revealed the traces of grain boundaries delineated by undissolved particles.

Table 4.1 shows the AZ91D chemical composition, which contains no drastic differences when compared with values stated in the literature. However, although the AZ91 ingots were heat treated to homogenise the microstructure, mechanical testing also indicates significant differences between properties in the lower and the upper part of the ingot. Furthermore, values ranging from 50 % to 75 % of the strength stated in the literature [14,16,156] were obtained during the mechanical characterisation.

5.1.2 Mg-Al-Rare Earths [AE] – Ingot (cast condition)

AE42 cast alloys, under die cast conditions, are shown in the literature [27,150,151,157] to form an eutectic phase near the grain boundaries. According to Figure 4.3 and in agreement with prior investigations [29], SEM analysis revealed that grain boundaries of AE42 base material present widespread precipitation of second phase particles

with lamellar morphology across the interdendritic microstructure. In Table 4.5, points 1 and 2 reveal the average composition of the Mg-matrix. Although the chemical analysis indicates 4 % Al in weight, the matrix has rarely over 2 % Al. This characteristic may be explained by the fact that the interdendritic phases are mostly composed by Al-based compounds. Furthermore, the Al content in solid solution is somehow limited, firstly because of the stability of the Al-RE phases and secondly due to the limited solubility of Al in Mg at room temperature. Points 3 and 4 indicate a high concentration of Al and Mn with some significant amount of RE, indicating possibly the presence of the classical Mn-(Al-RE) phase formation. Such Mn-containing phases (Mn-(Al-RE)) have been reported in the literature [112] to be present in minor amounts in the "as-cast" condition and are suggested to be $Al_{10}RE_2Mn_7$ particles. Scans corresponding to points 5 and 6 showed a high content of Al and RE with minor traces of Mn. Such compounds are suggested to be Al-RE based phases, possibly $Al_{11}La_3$, Al_4La or Al_2Nd, commonly present in AE Mg alloys. Evidence of Si has been observed, but considered an impurity, although it is known that Mg_2Si can be formed in some other Mg-alloys.

Mechanical characterisation of the AE42 BM, as demonstrated in Table 4.6 and Figure 4.4, has pointed out a significant difference between the lower and the upper part of the ingot in the longitudinal direction. Furthermore, mechanical properties obtained during the course of this study differ from those available in the literature [8,14,16]. In the transverse direction, however, tensile strength results presented a large scattering, independent of their position in relation to the ingot.

5.1.3 Mg-Al-Ca-Sr [AXJ (MRI)] – Ingot (cast condition)

Similar to the AE42 alloy, chemical composition and mechanical properties were analysed and indicated significant differences between the obtained values and those found on the literature [33]. According to Table 4.7, a significant Sn content was identified in the actual composition, which is in disagreement with the literature. Furthermore, tensile strength values, shown in Table 4.9 and Figure 4.6, were found to strongly vary, not only in relation to the literature, but also between the lower and the upper portion of the ingot. Strength values (i.e., Rp and Rm) were significantly lower than those indicated in the literature [8,33], as expected for an ingot, which was chilled cast.

Additions of Ca and Sr in the MRI230D alloys increase their creep resistance, due to the formation of stable Al-based precipitates instead of the detrimental $Mg_{17}Al_{12}$ in the grain boundaries [33]. The rest of free Al is reported to form Al-Ca precipitates (specifically Al_2Ca). EDS analysis (see Figure 4.5 and Table 4.8), corresponding to points 1 to 6, showed at grain boundaries intermetallic compounds with compositions varying in a broad range. Points 1 and 5 indicate a high concentration of Al, Mn and Zn with some significant traces of Sn. Such compounds are suggested to be former AlMn-based phases, commonly present in AZ alloys that apparently incorporated some Zn and Sn during the casting process. According to the chemical analysis (see Table 4.7) Zn was found in very low percentages while Sn, although it does not compose the alloy [33], was present in a high content. Points 2 and 3 evidence a substantially high Sn concentration with a minor presence of Mg and Ca, whereas points 4 and 6 indicate the fine distributed Mg-Al-Ca precipitates with a large variation in chemical composition. From this analysis, it is evident that the formation of eutectic $Mg_{17}Al_{12}$ phase was completely suppressed in the presence of Ca and Zn, as reported in the literature [43]. Points 7, 8 and 9 reveal the average composition of the α-matrix, which seems to be very homogeneous. No clear presence of Al_4Sr was identified in the investigated points, although its presence has been reported in MRI Mg alloys [40]. Round particles within the Mg-matrix, corresponding to points 10 to 13, showed a similar concentration as revealed by points 1 and 5. However, in this last case, the particles are randomly distributed inside the α-Mg matrix and not grouped along the grain boundaries, as observed in the previous case.

Summarising the base material characterisation generally, significant differences were observed concerning not only chemical composition, but also mechanical properties in the selected BMs. In relation to chemical composition, the presence of Sn and some indication of Zn in the EDS analysis of MRI230D alloys can be considered the most prominent changes in comparison with values found in the literature [33]. Additions of Sn serve to increase ductility, to reduce the tendency of cracking while being hot worked and increase high temperature properties due to the high temperature stability of the Mg_2Sn phase formed [14,23]. On the other hand, Zn is often used in combination with Al to produce an improvement in the room temperature strength of Mg alloys. A further evaluation or discussion involving this material is difficult draw, since not very much information on this alloy is available in

the literature. Furthermore, a significant difference concerning mechanical properties was observed, not only between the lower and the upper part of the ingots, but also between the values obtained and those reported in the literature. A sensible reason for such differences could be attributed to the fact that typical mechanical properties and characteristics found in the literature are normally assessed using thin cast plates. In those cases, a refined microstructure is formed on the outer regions (skin) of the plate, due to the faster cooling gradients imposed at these locations. This refined microstructure contributes to enhance the mechanical properties, therefore achieving the high strength values reported in the literature. However, in this investigation tensile samples and later studs were extracted from the middle of the ingots avoiding the beneficial influence of the skin microstructure and consequently generating lower strengths. Additionally, chilled casting rather than die casting samples were used in this work, which also contributes to the inferior strengths observed during mechanical testing. Finally, the fact that the specimens machined from positions 1 to 5 (see Figure 4.2) indicated higher strengths than those from 6 to 10 can be directly related to the casting process. Regions 1 to 5 are in contact with the mould, and so experience higher cooling rates and probably present a refined microstructure and consequently generating samples with higher strengths.

5.2 SIMILAR AZ91D-T6 JOINTS – 6 MM DIAMETER/12 MM UPSETTING

5.2.1 Process and Thermal History

Based on the results presented in Figure 4.8, the equipment showed a sufficient repeatability with a relatively low standard deviation within the investigated range of parameters. One can also observe a considerable decrease in the standard deviation values as soon as welds with higher pressures are performed, i.e. towards the middle of the control range of the system. However, in some particular cases welds performed with the same parameters showed a large variation in welding time (see Figure 4.8(a) – welds 1C and 1D). Since the welding system has been assessed in previous studies and demonstrated to have a high repeatability, the possible source, which could cause such deviations on the welding cycles in welds carried out under the same conditions, was directed to the material itself. As presented in section 4.1.1, the upper and lower side of the ingots have significant differences with regards to their mechanical properties. Furthermore, as a high Al content gravity casting alloy,

AZ91D may present some regions with grouped pores, which maybe was the cause for the early collapse observed in some samples during mechanical characterisation (see Figure 4.2). Considering the present study, studs from different parts of the ingots, machined in different directions (longitudinal and transversal, depending on the dimensions of the ingots) were welded within the same group. In this context, a region with fine grouped pores could have been present inside the stud, which would influence the upsetting rate during the welding (see as an example Figure 4.8, specimen 2B). As soon as this region achieves the frictional interface during the welding, the upsetting rate increases instantaneously, causing interference to the welding progress. Both intrinsic characteristics of the material have to be considered in a future approach and these have possibly influenced and contributed to increase the dispersion of the process stability results.

Figure 4.8 also highlights a significant influence of the welding pressure on the welding time. By duplicating the pressure, the welding time is reduced by more than 60 %, from 24.4 to 9.5 seconds on average. Moreover, although the motor is electronically stopped by proportional valves, the total upsetting (*TU*) was observed to be significantly higher than the preset value. As observed in Figure 4.8, the upsetting during the stopping time (see *UST* values), which is a non-controlled event, increases significantly the *TU*. Generally, a higher forging force tends to increase the axial shortening during the stopping time (*UST*) leading the remaining length of the welded pair to be substantially smaller. Figure 4.8 indicates on average a *UST* value of 2.4 mm for low pressure welds, while 3.3 mm upsetting values were observed for higher pressure welds. In this context, if the welding system is upsetting controlled, the welding parameters should be accurately monitored and controlled if the final length of components plays an important role.

The accepted opinion is that the use of a forging force significantly improves the mechanical properties of the weld [158] by breaking up the coarse inclusions, which are adversely reoriented during frictional heating, and by refining the coarse grains by hot-working [47,60]. However, some experiments show that good welds can be obtained without an increase of the force after rotation stops, which means, without any forging force [61].

Both tendencies discussed above are summarised in Figures 5.1 and 5.2. Figure 5.1 shows the *UR* dependency on the welding pressure, while the variation of the upsetting during the stopping time (*UST*) with the forging pressure is presented in Figure 5.2.

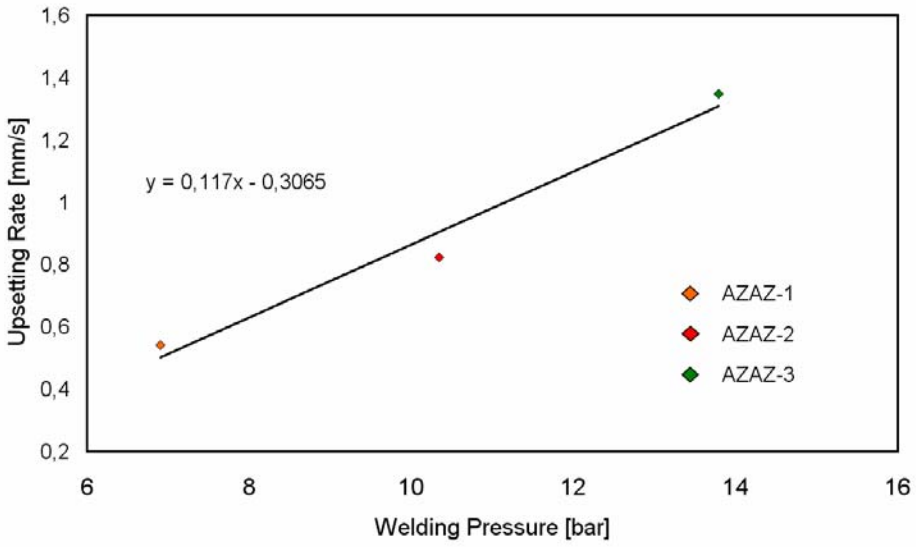

Figure 5.1: Upsetting rate (UR) dependency as a function of welding pressure.

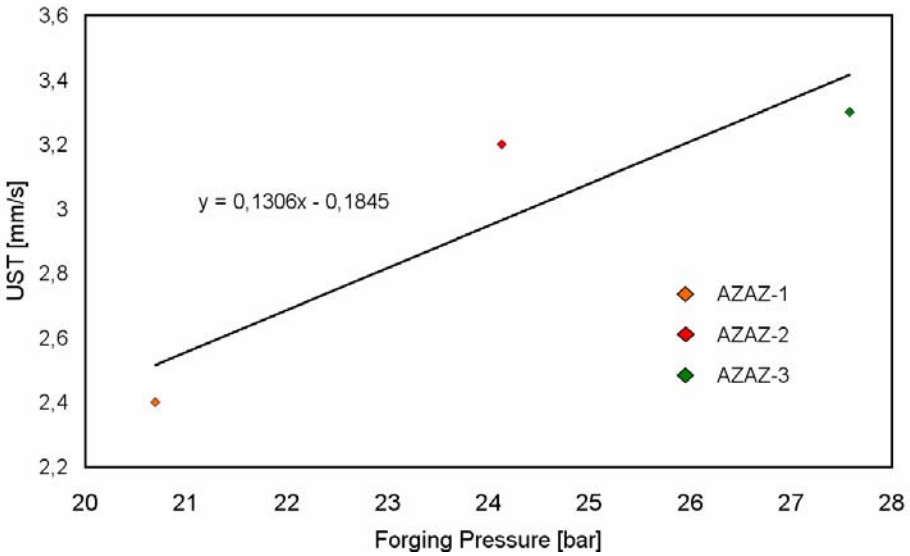

Figure 5.2: Variation of the upsetting during the stopping time (UST) in relation to the forging pressure.

According to Figure 3.4 (see Section 3.2), temperature monitoring was performed with two thermocouples along the bonding interface with the upwards moving frictional plane considered the heat source. It should be also emphasised that with

this experimental set-up only the temperature within the heat affected zone (HAZ) on the sides of the holes were measured. Additionally, it has been observed that, owing to the difficult procedure during the spark erosion of the thermocouple holes, the actual distance between the tip of the holes and the bonding line varied significantly, although 500 µm was specified. Although Mg materials have a high thermal conductivity, which could compensate for small variations in thermocouple hole depth, these variations complicate the analysis and the direct comparison of results. Hence, the measurements presented should only be considered as general indications and not as an absolute thermal analysis.

In all the records, the maximum temperature was reached at the end of the weld, as demonstrated in Figure 5.3. Some milliseconds after the stud has touched the cavity bottom, the lower thermocouple (T2) starts to record the temperature. Once the process reaches a steady state, i.e. the temperature and height of the plasticised zone is kept in equilibrium, the frictional interface starts to move upwards. Temperature indication T2 increases rapidly within the first seconds due to its proximity to the heat source. As soon as the frictional interface reaches a position parallel to thermocouple T2 (see Figure 5.3) the first peak temperature is observed, since the heat source has its closest position in relation to T2. As the process continues, the frictional interface moves further upwards, causing a drop in the T2 measurements due to conduction losses on the way between the heat source and the thermocouple. However, with increasing thermal saturation of the base plate, at a certain point temperature T2 reaches a minimum and starts to increase again up to the end of the welding process. On the other hand in T1, positioned 6 mm from the top surface, a slight rise in the temperature field is observed after the first steep increase at the beginning of the process, due to the increasing thermal saturation of the base plate. Contrary to T2, T1 does not show any peak during the welding progress. This phenomenon can be explained by the fact that when the frictional interface (in the form of an elliptic paraboloid) achieves T1 level, the process reaches the limiting control parameter, i.e. the last frictional interface coincides with the position where the upper thermocouple is placed. At this stage, the maximum temperature is achieved after the deposition process has finished.

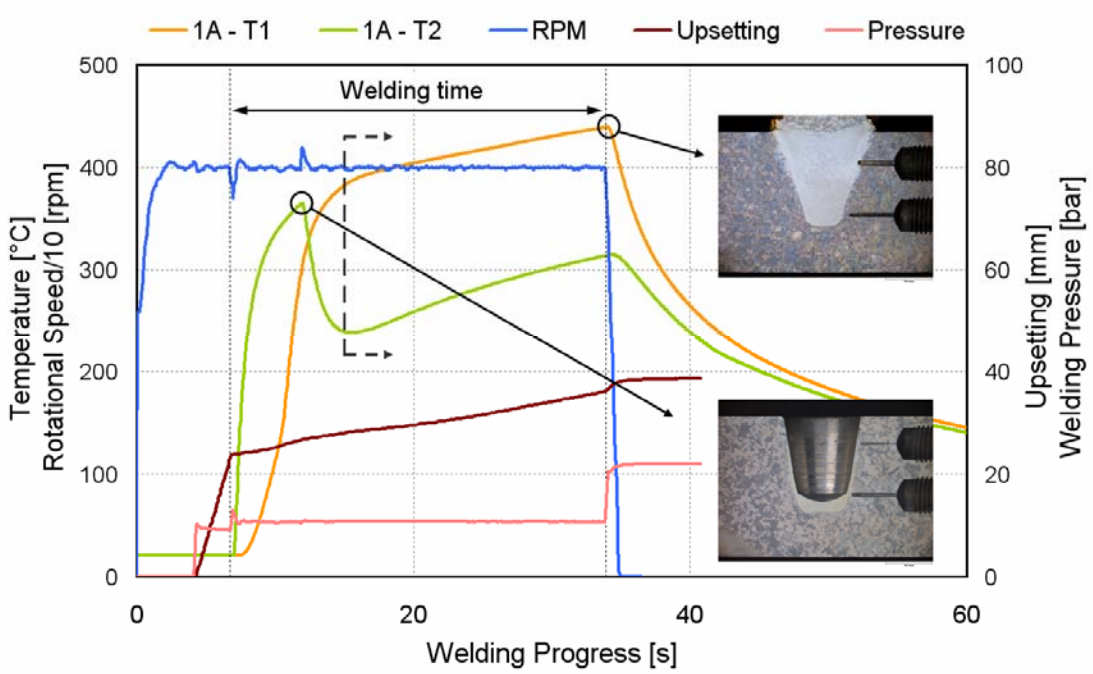

Figure 5.3: Welding progress diagram combined with temperature measurements (welding pressure 6.90 bar, forging pressure 20.7 bar, rotational speed 4000 rpm and 12 mm upsetting).

Bearing in mind the different frictional interfaces at the beginning and at later stages of the process (see Figure 5.4), the different temperatures measured along the hole depth (as demonstrated in Figure 5.3) can be better understood. The temperature development changes due to the different heat generation and due to the different cooling conditions at initial and final welding stages. On the one hand the frictional interface, i.e. the area between the stud tip and the deposited material in direct contact and relative movement (see Figure 5.4), changes from the basic stud diameter at the beginning of the weld (see Figure 5.4(a)) to an elliptic-paraboloid shaped surface in later stages (see Figure 5.4(b)). Owing to the increased contact area, since the stud is tapered, the heat production is higher, thereby generating the higher temperatures at the final stages of the weld. On the other hand before the touch-down distance is achieved, the base plate is situated in air at room temperature, which explains the steep temperature increase at initial stages of around 130 °C/s. As the process advances, a thermal saturation seems to occur in the base plate, leading the temperature to show a reluctant increase during the final stages. From this point (see grey dashed arrows indications in Figure 5.3) the temperature experiences an increase of around 2.28 °C/s up to the final stage of the process.

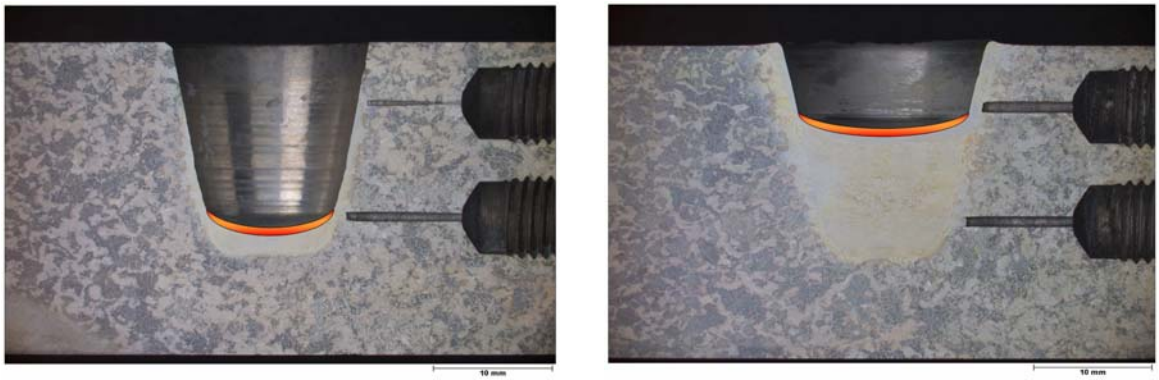

(a) Ups: 4 mm. (b) Ups: 10 mm.

Figure 5.4: Frictional interface after 4 mm (a) and 10 mm (b) upsetting.

While welding times showed a variation of more than 60 % by duplicating the pressure, peak temperatures presented a variation of around 4 % and 9 % for T1 and T2 respectively under similar conditions, i.e. by duplicating the pressure (see Figure 4.9). Moreover, although the peak temperature is not substantially affected, the dwell time (time at maximum temperature) and cooling rate are substantially affected. As an example, for low pressure welds the temperature remains for more than 20 s over 400 °C in some cases in the upper weld areas (see Figure 4.9(a)). On the other hand, for higher pressure welds, the time at peak temperature decreases and in some cases does not even achieve the same level (see Figure 4.9(e)). By approximately equal average peak temperatures, for some alloys the dwell time and cooling rate might be of substantial importance for precipitation/transformation phenomena. Moreover, the extension of the heat affected zone can be directly related to the temperature curves presented in Figure 4.9.

The mean values of peak temperatures (see Figure 4.9) revealed that temperatures very close to the melting point were achieved. Figure 2.2 shows the Al-Mg phase diagram, which points out a solidus temperature of approximately 440 °C for Al-Mg based alloys. Considering that the measurements were carried out some micrometers away from the bonding line, the solidus temperature was perhaps overcome in regions very close to those rubbing areas. As determined by Bowden *et al.* [159,160] there is an extremely steep temperature gradient close to the frictional interface, i.e. the temperature decreases remarkably over an extremely small distance from the interface. This statement supports the theory of achieving

temperatures above the solidus line in regions close to the frictional interface. Experimental evidence supporting local melting during friction based processes in Mg-alloys has been provided by a number of investigators [161-163]. As reported in the literature [164,165], once the solidus temperature has been overcome, local melting occurs and the viscosity of plasticised material decreases, so that the rate of heat generation suddenly decreases. However, when the material's temperature falls, the local molten films at the interface solidify, causing their viscosity and consequently the heat generation rate and temperature to increase. This process occurs repeatedly, so that the peak temperature at the bonding line (BL) attained during friction welding is the solidus temperature of the materials involved [166]. Figure 5.5 shows a micrograph taken over the BL, indicating that low melting point intermetallic eutetics, concentrated on the grain boundaries, could be segregated and molten during the welding process. Furthermore, the micrograph in Figure 5.5 seems to show epitaxial grain growth, which would suggest (or even confirm) the presence of incipient melting at the stud/BM interface. Considering local changes and dissolution of the second phase particles (see Section 4.2.3), the microstructure around the BL is very different from that observed in the cast material. Many publications in the literature [164-166] support the theory that microstructural features in friction welds are determined by a combination of grain boundary sliding and the limitation of cavity interlinkages when transient local molten films are formed, based on the relationships between strain rate/resultant microstructure.

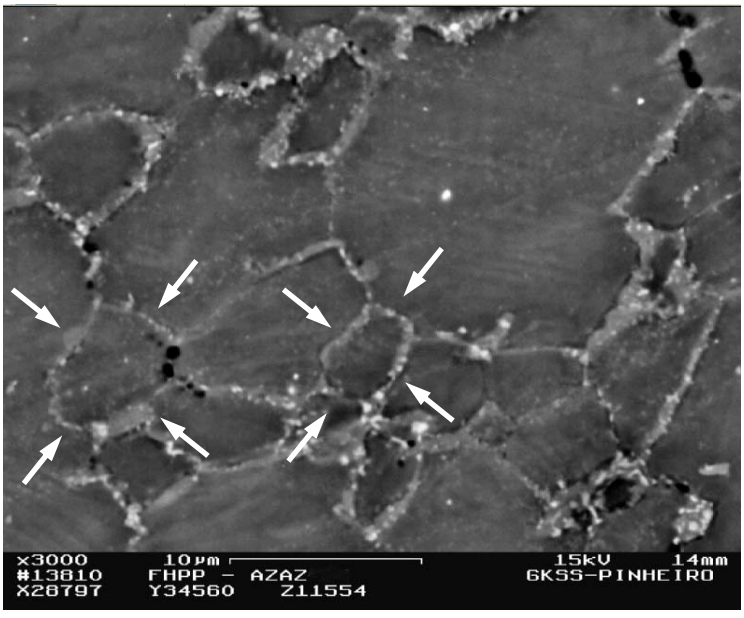

Figure 5.5: SEM micrography taken from the welding zone with indications of transient local melting.

In terms of heat input, Vill [50] proposed that the heat generation N during friction welding can be determined based on the following relation:

$$N \approx 2\pi p \frac{K}{n} r \cdot 10^{-6} \quad \text{[kW]} \qquad \text{[Equation 5-1]}$$

Where,

p – Axial pressure [kg/mm^2] K – Material dependent constant [mm^2/min^2]

n – Rotational Speed [1/min] r – Radius of the cross section [mm]

Considering Equation 5-1 and extrapolating its use for FHPP, one can observe that heat generation increases proportionally with welding pressure. Since the parameters *n*, *K* and *r* were constant, welds from group 3 would be expected to generate the higher amount of energy per time. In fact, Figure 5.9 showed that with higher axial pressure (group AZAZ-3) the temperature rises with about 180 °C/s, while lower axial pressures result in a heating rate of 120 °C/s (group AZAZ-2) and 80 °C/s (group AZAZ-1). However, the global heat generation is time-dependent and therefore strongly influenced by the welding time. Table 5.1 lists the heat generation per time and the consequent global heat generation. Comparing samples "C", selected to further metallurgical analysis, it can be seen that lower pressures (sample AZAZ-1C) have generated the higher amount of heat. However, sample AZAZ-3C produced approximately 65 % of the heat generated under lower pressures.

Table 5.1: Global heat generation for AZAZ welds.

Sample	Welding Pressure	Heat Generation N (1) [W]	Welding Time [s]	Global Heat Generation N' (2) [J]
1C	6.90 bar (1.0)	$1.0*(^{2\pi Kr}/_{n})$	29.5	$29.5*(^{2\pi Kr}/_{n})$
2C	10.34 bar (1.5)	$1.5*(^{2\pi Kr}/_{n})$	17	$25.5*(^{2\pi Kr}/_{n})$
3C	13.79 bar (2.0)	$2.0*(^{2\pi Kr}/_{n})$	9.9	$19.8*(^{2\pi Kr}/_{n})$

(1) Heat generation N (in J/s), considering the welding pressure;

(2) Global heat generation N' (in J), considering the welding pressure and the welding time.

5.2.2 Metallurgical Characterisation / Joint Formation Mechanisms

Metallurgical characterisation, as presented in Section 4.2.3, shows significant microstructural changes in the lower weld areas, resulting from different welding parameters. Considering that temperatures at the bonding line may have achieved even higher values than the maximum indications pointed out by thermocouples T1 and T2 (respectively 448 °C and 395 °C, 383 °C and 281 °C for samples 1C and 3C, see Figure 4.9), it seems that the axial pressure definitely plays an important role in the final structure around the welding area. Not only the different dwell times, but also the different cooling rates (see Figure 4.9) imposed by the process influence the joint formation in a decisive manner. Such different thermal cycles possibly allow solubilisation, precipitation and diffusion mechanisms to take place, establishing the changes in the microstructure after welding. However, to some extent the average grain size inside the extruded material remains similar for samples welded under different conditions. In this case, it seems that the different welding times and their consequent different cooling times (see Figure 4.9) have a minor influence and therefore do not change the microstructure drastically in this particular region. Furthermore, lower weld areas indicated smaller grain sizes compared to the upper part. The higher temperatures measured in the upper weld areas seem to be a reasonable cause of the unequal structure along the weld depth. The larger contact area in the upper regions, with a correspondingly higher heat generation, causes a greater volume of material to be heated, leading to wider affected regions.

Welds performed at lower pressures tend to result in a joint with a very homogeneous microstructure, associated with a smooth deposition process. On the other hand higher axial pressure tends to cause a more irregular deformation of the stud and consequently a very inhomogeneous microstructure along the hole's depth. Figure 5.6 shows the macrograph of the weld AZAZ-3C, where some areas with non-plasticised stud material were observed. Points "A", "B" and "C" indicate points where the stud shears off during the deposition process (welding).

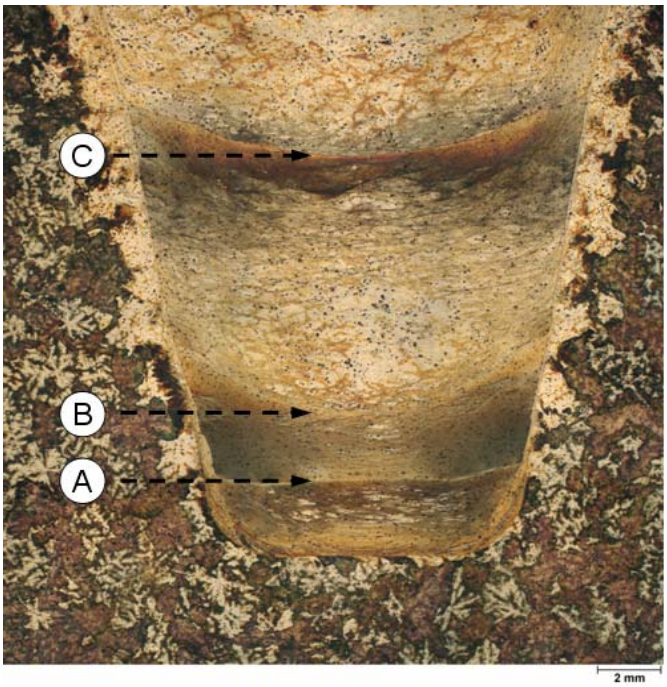

Figure 5.6: Macrograph of the AZAZ-3C joint.

Since the weld progress was monitored by a data acquisition system, based on that the mechanism of joint formation and its particularities can be outlined for each specific case. In joint 3C, presented in Figure 5.6, as soon as the stud touches the bottom of the cavity, heat is produced, generating a local plasticised layer in this region. Due to the very high axial pressure, the plasticised material develops at a rate slower then the axial feed of the consumable rod. In turn, it means that the frictional rubbing surface (frictional interface) does not have, under these conditions, enough time to rise along the consumable rod to form the dynamically recrystallised deposit material. Instead of being gradually consumed, lower stud areas rub against the cavity bottom and are, due to the heat generated, deformed and assume the positive form of the hole. With the increasing contact area, the torque increases correspondingly, up to a point where the frictional moment becomes larger than the stud's internal shear resistance. At this point, indicated as point "A" in Figure 5.6, the stud shears off and starts a new frictional plane on the top of this deposited material. The shearing-off of the stud can be also followed on the DAS measurements (see Figure 5.7). After the stud has sheared-off the frictional torque reduces abruptly, as a result of the significantly smaller frictional interface. This smaller frictional interface causes, in turn, a sudden increase on the rotational speed. After some milliseconds, the monitoring system brings the motor again to the preset rotational speed. Further

analysis can also be made in terms of temperature progress (see Figure 5.7). After the process has been initiated, the temperature T2 increases steeply. However, after the first stud shearing-off phenomenon, the heat generation reduces accordingly, as a consequence of the smaller frictional interface. The temperature drops for a while and starts to rise again at a lower rate as the process continues. Two further shearing phenomena can be identified in Figure 5.7, in agreement with the macrograph shown in Figure 5.6. At those locations the process “jumps” over a certain stud distance without the stud material being plasticised in between (see Figure 5.6 between indications “B” and “C”) and starts again with a new frictional plane on top of this sheared material. This irregular microstructure can lead the joints to an unexpected collapse and should therefore be avoided by means of optimal process parameters. The main outcome of Figure 5.7 can be related to the monitoring of the process. In other words, a sequence of welds could be monitored and, after a statistical treatment of welding data, an optimal range could be established where homogeneous welds are produced. Such control would be meaningful for mass production and could be used as on-line monitoring for quality control purposes.

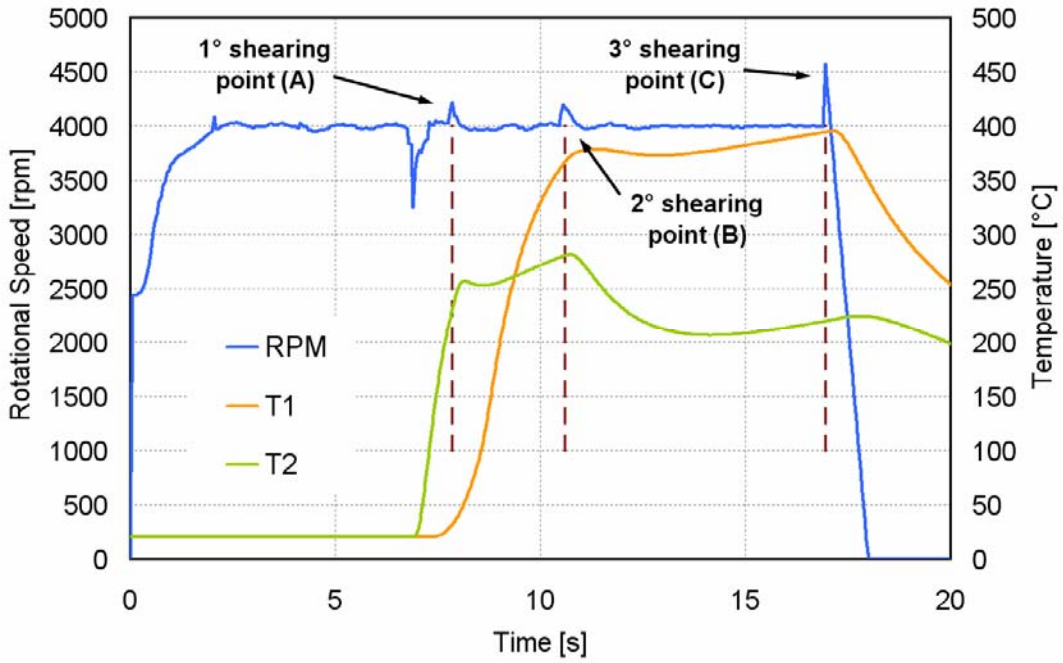

Figure 5.7: Welding parameter measurements of weld AZAZ-3C. The shearing phenomena observed on the macrograph could be clearly identified.

The results from the EDS analyses within the recrystallised zone, as presented in Table 4.11, suggest some changes in comparison with the cast microstructure. The grain boundaries in the extruded material within the RZ, corresponding to points 1 to 4 (see Figure 4.14), show in the first case a high concentration of Mg and Al with a minor presence of Zn. Despite the unfavourable stoichiometry shown by the EDS, such an analysis possibly indicates the formation of $Mg_{17}Al_{12}$ compounds around the primary growing Mg-Al solid solution, as a result of a non-equilibrium local solidification under rapid freezing conditions. Points 5 to 7 indicate an exceptionally high concentration of Al in the α-Mg phase inside the fine recrystallised grains. It seems that the absence of Al observed in the formation of the grain boundary structure was partially transferred and dissolved into the matrix, thereby elevating the Al content in those regions. Compared with EDS in the base material distant from the weld, points 8 to 10, one can clearly observe the enrichment of the α-Mg phase with Al in the above mentioned regions. Such points show the real composition of the matrix with around 7 % Al. Although the chemical analysis indicates around 9 % Al by weight, the matrix has rarely over 7 % Al. This characteristic may be explained by the fact that the interdendritic phases are mostly composed of Al-based compounds, i.e. the Al content in solid solution is somehow limited, due to the restricted solubility of Al in Mg at room temperature, which is compensated by the formation of high Al content second phase particles.

In order to monitor the joint formation, a sequence of welds were produced with an increasing upsetting from 2 mm to 12 mm (the full upsetting for such welds) in 2 mm increments. After the set upsetting was achieved the weld was interrupted and the rotating consumable was pulled out of the cavity. Figure 5.8 shows the gradual filling of the hole with increasing upsetting. Bearing in mind that in friction welding heat is produced due to friction, which transforms the kinetic energy into heat, as soon as both faying surfaces are in contact, heat begins to be produced. At the very first process stages the heat produced is only used to smooth both surfaces and to plastically deform the consumable. Due to the high heat generation, the consumable becomes the positive form of the cavity up to a certain length (see scratches in the sidewall in the white detail in Figure 5.8(a)) before it starts to be deposited. This initial phase is characterised by seizing and microbonding processes, where the surfaces reach locally an extremely high temperature, promoting plastic deformation and

hence flattening the faying surfaces, particularly in the outer regions where the surfaces are subjected to the highest relative rotational speed. Isolated local bonding that eventually takes place across the contact surface is almost instantaneously sheared off. The shearing of those microbonds induces additional heat in the surrounding material, contributing to an increase in the instantaneous temperature.

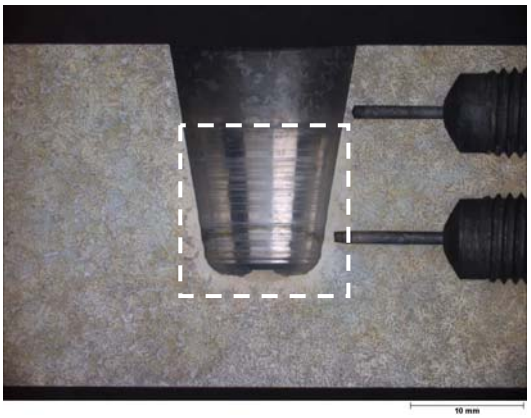

(a) 2 mm.

(b) 4 mm.

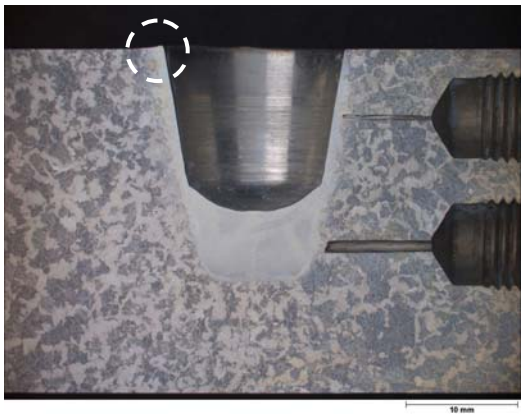

(c) 6 mm.

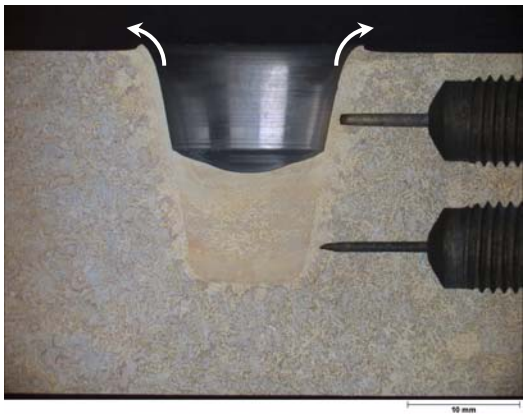

(d) 8 mm.

(e) 10 mm.

(f) 12 mm.

Figure 5.8: Sequence of tapered FHPP macrographs. Welds with increasing upsetting illustrate the development of plasticised material and the change in shape of the frictional plane.

When the smoothening of the outer regions is almost complete, the plasticised material produced in those regions starts to move towards the rotational centre. In the outer regions almost no heat is produced during this intermediate phase, because of the reduced frictional contact (the faying surfaces are now widely smoothened in these regions). Lower radial forces and restricted material flow conditions closer to the rotational centre combined with the constant generation of plasticised material in the outer regions causes a material concentration on a circular ring area around the rotational centre. Such a material concentration occurs after the first 2 mm upsetting and can therefore be observed in the Figure 5.8(a). With increasing saturation of plasticised material in the rotational centre, the ring area starts to extend its diameter slowly towards the outer regions of the weld zone. Temperature equilibrium is achieved, which is supported by a self-balancing effect. These effects have been discussed by many authors [47,77,81,83-87] and can be summarised as follows: As the temperature rises, the metal becomes more plastic and the torque is reduced, leading to a lower heat generation with a resultant lower temperature. This in turn softens the material, resulting in less deformation work and in an instantaneous decrease of the temperature. The height of the plasticised zone decreases and cooler areas now make frictional contact, heat up and become highly plasticised. At this stage the consumable is fully plasticised across the bore of the hole. The plasticised material develops at a rate faster than the axial feed rate of the consumable rod, which means that the frictional rubbing surface (frictional interface) rises along the consumable to form the dynamically recrystallised deposit material with an almost constant upsetting rate, as demonstrated in Figure 5.8(b) to (e). The plasticised material at the interface is maintained in a sufficiently viscous condition for hydrostatic forces to be transmitted and therefore consolidate the joint at the sidewalls. This process is maintained as long as the process control parameter (i.e. upsetting) is not achieved, which stops the motor and allows the system to apply the forging force to conclude the welding process (see Figure 5.8(f)). In Figure 5.8(c) and (d) it can also be observed that although the frictional plane has not yet achieved the middle depth of the hole, the consumable has deformed and already occupies the cavity entirely at this point. During this stage, the stud material starts to be pressed out of the friction area forming the flash. The white circular detail (see Figure 5.8(c)) and the arrows (Figure 5.8(d)) shows the top hole edge warped due to the further upsetting imposed by the process after the filling of the hole.

Due to the intensive high temperature mechanical working undergone by the consumable, the microstructure in the extruded material changes drastically. Figure 4.13 presents the grain size distribution after welding and clearly shows a reduction in average grain size in those dynamically recrystallised areas. Generally, the main advantage of a fine grain size is its enhanced mechanical properties, such as tensile and yield strength. This relationship can be explained by the Hall-Petch equation ($\sigma_y = \sigma_o + kd^{-1/2}$, where σ_o is the yield stress of a single crystal, k is constant and d is the grain size). The grain size effect on mechanical properties is more significant in alloys that have an HCP structure, such as Mg and Ti, than in many other alloys with a different crystalline structure (FCC or BCC), since there are fewer slip systems in the HCP structure [167]. Other advantages of a fine grain size include the reduction in hot tearing tendency and in the size of defects such as porosity, the improvement of corrosion resistance and the machinability of cast products.

5.3 DISSIMILAR JOINTS – 8 MM DIAMETER/10 MM AND 20 MM UPSETTING

5.3.1 Process and Thermal History

Considering the results obtained from DAS combined with temperature data, some conclusions can be drawn. Firstly, the upper part of the joint is generally 10 % to 15 % hotter than the lower, due to the higher frictional area and its corresponding higher heat generation. Secondly, welds with higher upsetting and consequently with longer welding times, presented the higher temperatures in both positions on average. It suggests that longer welding times generate higher peak temperatures, which could be associated with the heat input into the joint. Thirdly, one can observe that in some cases joints with much longer welding times present lower temperatures than joints performed within a shorter time. This statement contradicts the previous, i.e. the heat input and its consequent peak temperature might not be directly derived from welding time. An example of that, presented in Figures 5.9 and 5.10, is related to samples AZAZ-a and d, which presents welding times of 51 s and 38 s respectively, with correspondent peak temperatures of 467 °C and 469 °C, 390 °C and 414 °C for upper (T1) and lower (T2) weld areas.

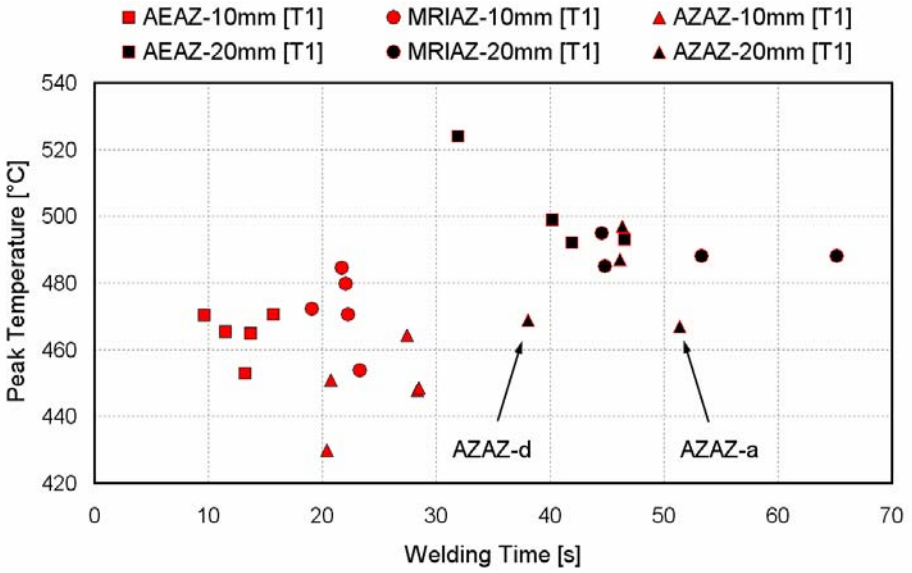

Figure 5.9: Peak temperature in upper thermocouple for similar and dissimilar welds, 10 mm and 20 mm upsetting.

In terms of material combinations, dissimilar welds always presented higher peak temperatures when compared with those of similar welds. This fact may not be directly related to the different thermal conductivity of the particular alloys, since the AE42 and the MRI230D present higher thermal conductivity than that of AZ91 [168]. The fact that AE42 and MRI230D have a superior high temperature resistant microstructure, and are consequently more stable, associated with the fragmentation of the stable second phase precipitates in the case of MRI230D, which could increase the heat generation rate, can be considered a reasonable explanation for the higher temperatures observed during dissimilar welds. According to Figure 4.19, MRIAZ and AEAZ have respectively achieved on average the highest temperatures in the upper (472 °C) and lower (420 °C) weld areas for 10 mm upsetting joints. For 20 mm upsetting, the AEAZ joints reached the highest temperatures, with 502 °C and 471 °C respectively for the upper and lower weld areas. Thermocouple T1 shows a variation of around 5 % between the highest (472 °C) and the lowest temperature (448 °C), while T2 indicates a larger difference of around 11 % between both values (420 °C for AEAZ and 374 °C for similar AZAZ welds) when 10 mm upsetting welds are considered. For 20 mm upsetting, T1 shows values differing 4 % between the highest (502 °C) and the lowest temperature (480 °C), while T2 points out a larger difference of around 15 % between both values (471 °C for AEAZ and 402 °C for similar AZAZ welds).

Samples of MRIAZ welded with 20 mm upsetting presented a particular feature in relation to both the welding time and the peak temperature. According to Figure 5.10, under the same welding conditions the preset upsetting is achieved in some cases after 44 s (MRIAZ-d), whereas in another cases after 65 s (MRIAZ-b). On the other hand, T2 indicates temperatures above 445 °C in some welds (MRIAZ-c) and around 390 °C in other cases (MRIAZ-a), which contribute to enlarge the scattering of temperature measurement results. Based on these results, temperature variations up to 55 °C within the same material combination were observed.

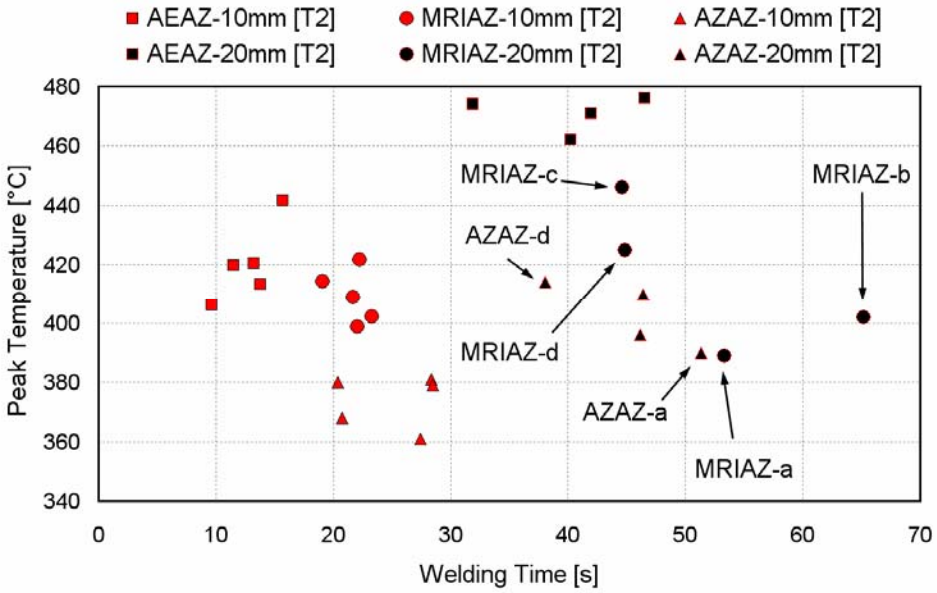

Figure 5.10: Peak temperature in lower thermocouple for similar and dissimilar welds, 10 mm and 20 mm upsetting.

As stated earlier, the difference in peak temperature indications may be correlated to slightly different deposition mechanisms, but could also be attributed to the positioning and type of the thermocouples as well as to the material itself. The first problem that arises, when temperature measurement procedures are questioned, is related to the accuracy of the depth of the thermocouple holes. It has been observed that owing to the difficult procedure during the spark erosion of the thermocouple holes, the actual distance between the tip of the holes and the bonding line varied significantly. This variation, according to the literature, might vary the temperature over a wider range [73,77,129,164,165], possibly causing an increased scattering in temperature indications. Another possible source of uncertainty that has been

discussed recently is directly related to the type of thermocouple utilised. Thermoelectric wires can undergo changes in their structure, because of sharp bending, folding and stretching, which causes an error associated with the inhomogeneities. In general, the hot junction – meaning the sensitive part of the thermocouple – has to be located in the zone of the object where the temperature is being measured. If this is not the case, the temperature is not measured correctly, leading the readings to an error known as “errors because of wrong measuring location” [169]. Further, errors associated with drift and with a wrong use of the compensation cable are often reported and so should be also considered. According to the manufacturer [169], acceptable deviations are around ± 2.5 °C up to 333 °C. In this context, an error associated with the measurements should be considered and the readings should not be taken as true absolute values. Furthermore, if joints performed with the same parameters generate welds with time and temperature values varying over a broad range, the deposition rate should be also investigated. This variable, which can be monitored through the DAS, has shown differences within the same group of welds. Such differences can be attributed either to oil flow fluctuations, which would indicate a problem related to the welding system, or to material imperfections. Figure 5.11 presents data recorded from welds MRIAZ-b and d. As observed, both variables delivered by the welding system, i.e. rotational speed and welding pressure, superimpose each other, indicating any interference of the hardware on the joint formation is implausible. On the other hand, the deposition (upsetting) rate, which is largely dependent on the material properties, seems to be strongly affected by a microstructural imperfection related to the material. Figure 5.12 shows a micrograph of the MRI230D base material. As observed, even with lower magnifications, dark regions representing grouped pores can be identified. As soon as this region reaches the frictional interface during welding, the upsetting rate (upsetting per time) increases instantaneously (see Figure 5.11/detail A). In addition, the frictional torque reduces and the axial resistance decreases due to void spaces within the material. Before the monitoring system adjusts the machine to keep to the preset parameters, this occurrence causes a peak in the rotational speed (see Figure 5.11/detail B) and a momentaneous decrease in the welding pressure (see Figure 5.11/detail C). As demonstrated, a material imperfection may generate a series of events, causing or contributing in some particular case to a great increase in the measurement dispersion.

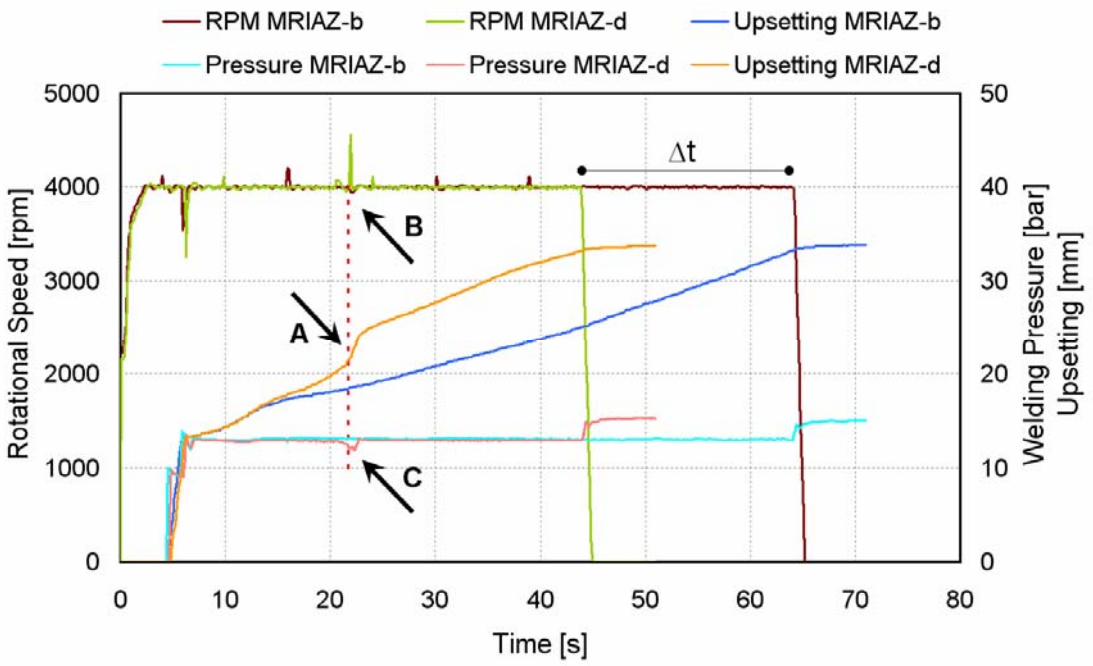

Figure 5.11: Weld plots of MRIAZ joints. Welds MRIAZ-b and MRIAZ-d present different upsetting rates despite identically selected welding conditions.

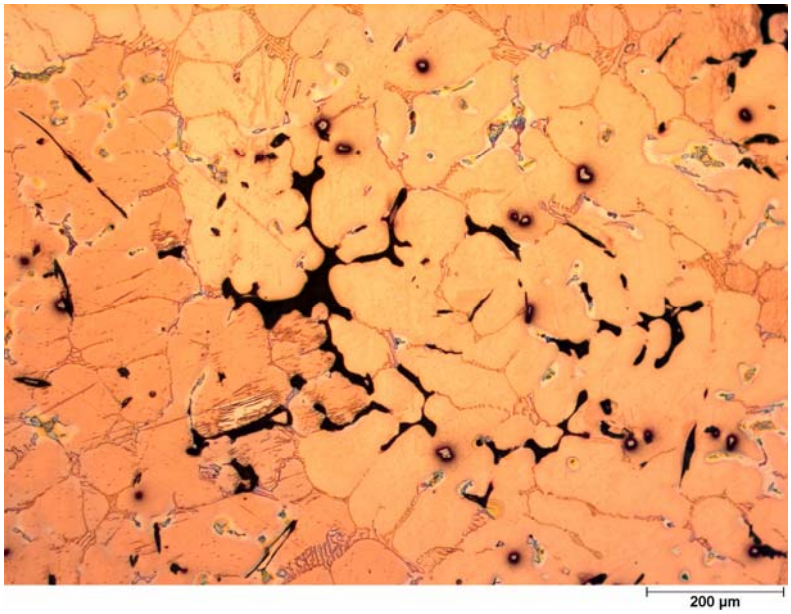

Figure 5.12: Microstructure of the MRI230D base material. Black regions are voids, resulting from chilled casting processes.

5.3.2 Metallurgical Characterisation / Joint Formation Mechanisms

5.3.2.1 AEAZ Joints

As described in the base material characterisation (see Section 4.1.2), the “as cast” parent material is characterised by a pronounced dendritic structure in the matrix, in combination with dispersed lamellar and particulate second phase particles of $Al_{11}RE_3$, preferentially located along the grain boundaries [29,150,151]. Figure 5.13 demonstrates the microstructure across the interdendritic microstructure (in (a)) and a complete rupture of the typical as-cast lamellar structure within the RZ in regions at the vicinity of the BL on the AE42 side of the weld after welding (in (b)). Such a rupture is to be expected, since the high level of strain produced in the weld interface, generated by the relative movement between consumable and base plate, associated to the welding pressure during the joining process, results in mechanical fragmentation of the intermetallic Mn- and AlRE-based phases. However, in regions towards the consumable centre, the microstructure seems to be to some extent unaffected by the welding process. In those regions, the typical dendritic structure with its lamellar second phase compounds remains almost unaltered, which suggests that the consumable was not fully plasticised through its diameter. Micrographs of the upper, unaffected BM in the middle of the RZ and of the second phase particles fragmented in regions at the vicinity of the joint are shown in Figure 5.13 (see indications “f” and “g” in Figure 4.20 for upper and lower stud areas respectively).

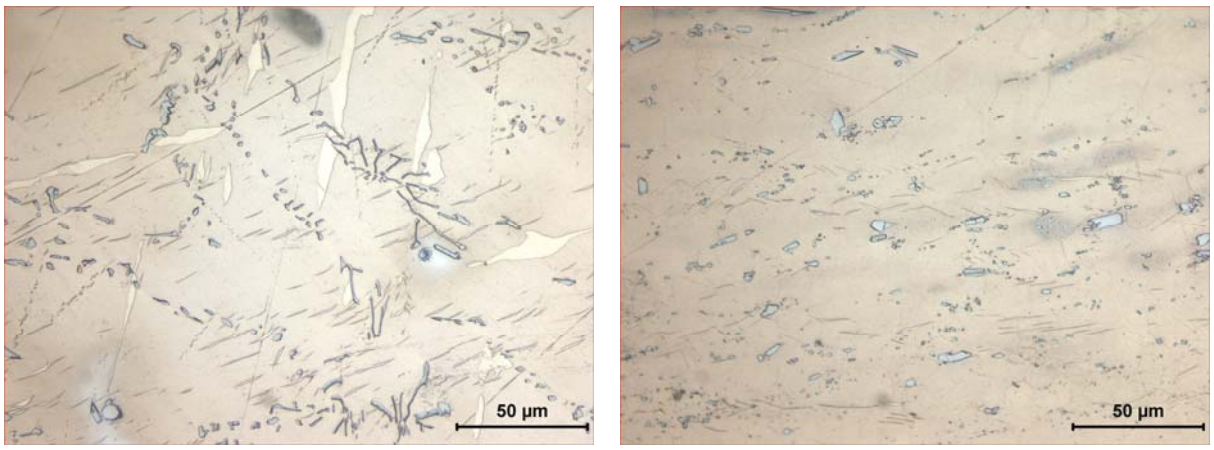

(a) (b)

Figure 5.13: Comparison of typical second phase particles across the interdendritic microstructure in the upper unaffected BM (a) and in lower stud areas near the bottom bonding line (b).

According to the metallurgical characterisation (see Section 4.3.2.1), fragmented particles have different sizes and are randomly distributed in the RZ along the joint line. In particular, in regions along this line, mostly in the upper joint areas, clusters of particles were observed as detailed by Figure 5.14. This particle concentration over the bonding line appears probably due to the higher hardness of the intermetallic compounds compared to the Mg matrix. The mechanical work and peak temperatures are not enough to mechanically dissolve such particles and the hydro-extraction effect, characteristic of friction processes, was not effective enough to expel them from the welding interface. The particles are pressed together and coalesce, due to the high temperatures/mechanical work imposed by the process. Further, the thermal cycle undergone during the process is very short to promote substantial diffusion and dissolution of the stable (Al-RE) intermetallic lamellar compounds originally present in the BM.

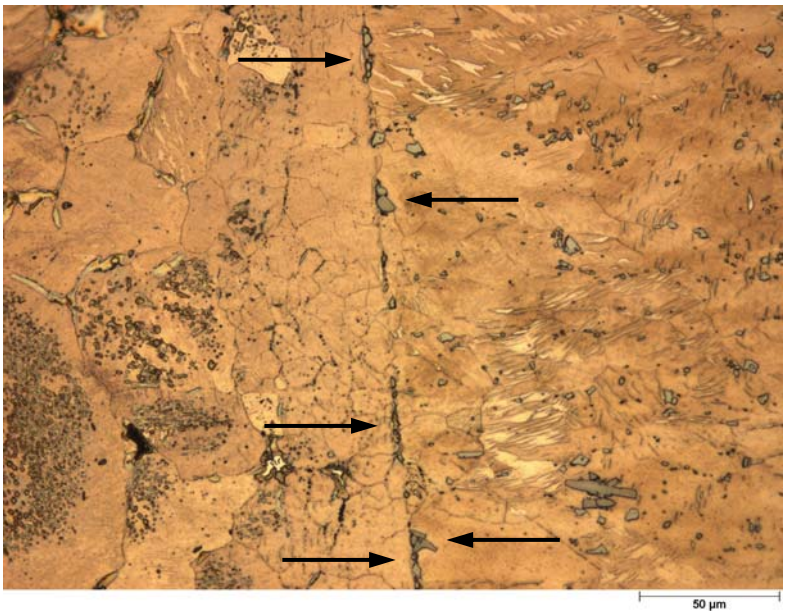

Figure 5.14: Second phase particles concentrated along the bonding line of the dissimilar AE42/AZ91D-T6 joint.

EDS analyses (see Figure 4.21 and Table 4.13) show lamellar particles within the RZ, corresponding to points 1 and 2, having a high concentration of Al and RE with a minor presence of Mg. Such compounds are suggested to be Al-RE based phases, possibly $Al_{11}La_3$, Al_4La or Al_2Nd, all commonly present in Al-rare earth Mg alloys. Although point 3 presents untypical Al content, points 3 and 4 reveal the average

composition of the AE42 α-Mg phase. Points 5 to 8 indicate the typical concentration of the Mg-matrix in AZ91 alloys. Point 8, placed somewhere inside of the RZ, gives a chemical composition very similar to that from the AZ91 matrix, indicating that a transitional region with an increasing Al content was not formed. On the other side, EDS analyses in points 9 and 10 recognise some dark grey regions with an abnormal Al content in the base matrix. Since the typical as cast lamellae AE42 base material structure was ruptured, associated with significantly higher temperatures, some Al-based second phase particles possibly became locally molten and therefore partially dissolved into the matrix. Due to the unstable solidification conditions imposed by the rapid cooling rate, the free Al, previously dissolved in the Mg-matrix, might not have had enough time to recombine and form stable intermetallic compounds. Hence some higher Al-content regions were presumably formed.

Just as with the analysis done for the similar AZAZ welds, this section proposes the mechanisms of joint formation for dissimilar welds, based on data from DAS, temperature measurements and *post-mortem* microstructural analysis. As previously mentioned, due to the differing material properties and structures within the ingots, to some extent the formation of the joint may vary slightly, even under the same welding conditions. Nevertheless, an attempt to describe the mechanisms involved in joint formation is made in this section.

For the AEAZ welds, although Figure 4.18 demonstrated the welding time varying over a relatively broad range, one can observe that the temperature remains at the same level to some extent. Figure 5.15 shows the temperature cycles for identical AEAZ welds with different upsetting rates, achieving, however, similar peak temperatures. Vertical dashed lines indicate the end of the welding. Comparing Figure 5.3, which shows the temperature progress for similar AZAZ welds, with Figure 5.15 and keeping in mind the microstructural differences at the vicinity of the joint and in the centre of the consumable, one can observe that the deposition mechanisms and therefore the bonding formation are perhaps different in both cases. Similar to that observed on the AZAZ welds, in the AEAZ joints the peak temperature was always reached at the end of the weld. However, in these curves a smooth and continuous temperature increase, without peaks or bends, was observed in both thermocouple positions (T1 and T2).

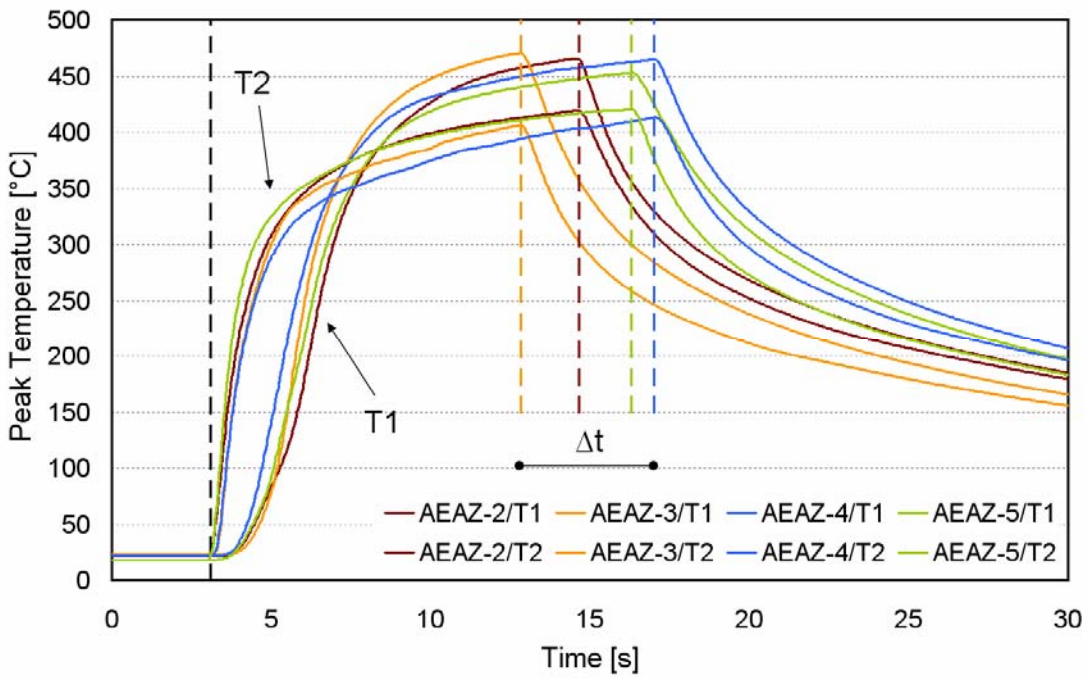

Figure 5.15: Temperature monitoring in AE42/AZ91D-T6 welds performed with identical parameters.

Although AE alloys presented similar or even higher strengths to those of MRI or AZ, AE studs have shown, unlike MRI and AZ, to be highly deformed during the welding test under the same conditions. Considering the stress-strain curves presented in Section 4.1, one can observe that the ductility of the AE alloys is clearly higher than that of the MRI ones, which explains why the former material presents a higher deformation under the same load. Bearing the high ductility of AE alloys in mind and examining the temperature curves presented in Figure 5.15, it seems that the filling mechanism observed in the similar welds, where the consumable member is fully plasticised across the bore of the hole and through the thickness of the workpiece, does not take place for this combination under these welding conditions. Instead, the stud yields and occupies the cavity before a plasticised layer is created in this case (see illustrations in Figure 5.16(a) and (b)), i.e. the consumable is inserted into the cavity at a faster rate than the one at which the plasticised material develops. Since the consumable is not plasticised, shear planes do not move up, generating a constant temperature increase without peaks or breaks. After the hole has been integrally occupied and the preset upsetting has not yet been achieved, the exceeding material is pressed into the flash, as demonstrated in Figure 5.16(c). At the final stages, the forging force is applied to consolidate the joint, which causes the detachment of the flash material from the base plate (see Figure 5.16(d)).

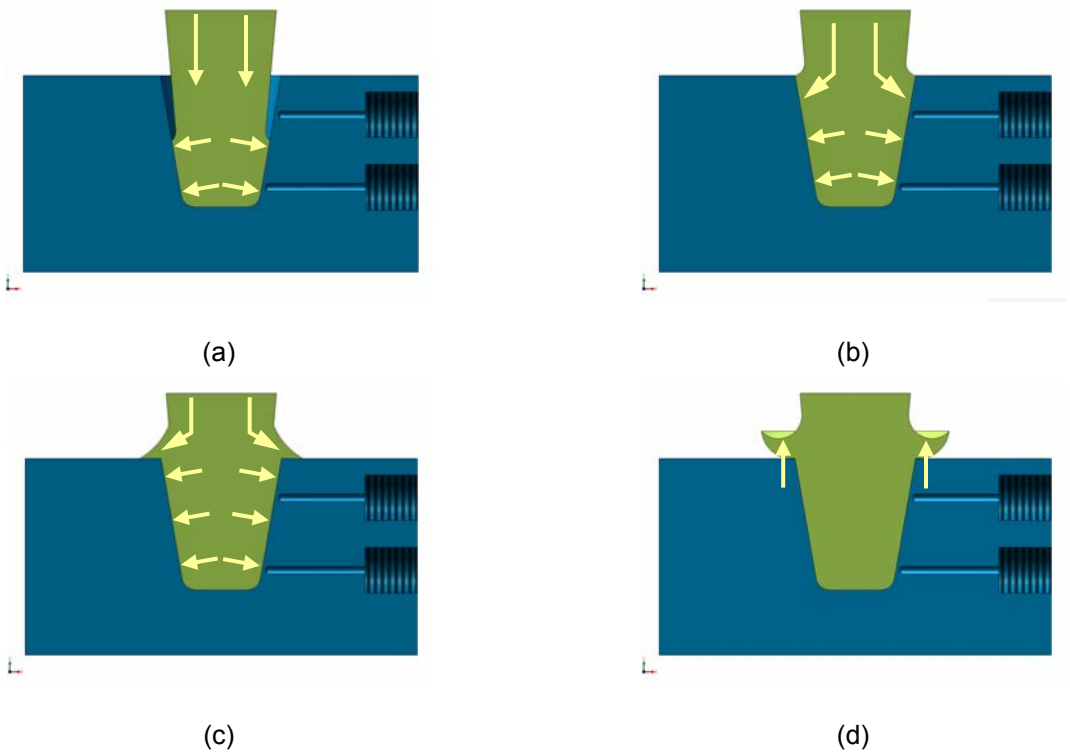

Figure 5.16: Proposed bond formation mechanism of AE42/AZ91D-T6 welds.

The fact that the consumable is neither plasticised across the bore of the hole nor through the height of the cavity perhaps causes the highest average peak temperatures observed in Figure 4.19. Since the consumable is not plasticised, the frictional area can be associated with the area of a conical frustum, which through its larger surface area generates a higher amount of heat and consequently the highest temperatures.

The bonding mechanism discussed above can be defined as a variation of friction taper plug welding (FTPW), formerly developed as an alternative repair technique for filling through the thickness of holes in offshore structures [110], however with a bottom, i.e. as if the FTPW process would be performed inside a hole. In this process, the heat generated from the contact between the consumable and the side wall causes the material to soften and flow through the hole. At a subsequent stage, the complete conical surface of the tapered plug is welded to the matching hole almost instantaneously.

5.3.2.2 MRIAZ Joints

As demonstrated in Figure 4.22, for this configuration defect-free welds were also produced, without visible discontinuities along the weld, for 10 mm and 20 mm upsetting. The bonding line could be easily identified most of the time, not only because of the different base material microstructures, but also due to the fine, dynamically recrystallised microstructure in the MRI230D consumable, resulting from the mechanical working imposed by the process. Figure 4.22(c) and (d) identified a narrow region on the AZ91 side of the weld (TMAZ) where dynamically recrystallised grains appear without the presence of the typical BM eutectic structure, which is also dissolved in regions extending towards the HAZ (see overview Figure 4.22). The absence of a eutectic structure in those regions can be explained as follows: The Al-Mg phase diagram (see Figure 2.2) shows that a heating temperature higher than 390 °C causes the partial dissolution of the $Mg_{17}Al_{12}$ into the Mg-matrix of AZ91 alloys. Sufficient frictional heating introduced during the process causes the dissolution of the eutectic phase in the transitional region (RZ). This free-eutectic zone is extended to the HAZ in the upper joint regions, which suggests that these regions are probably heated to temperatures higher than 390 °C during the process.

As also observed for the AEAZ joints, in regions close to the side walls, at the vicinity of the joint line in the upper weld areas (see details in Figure 4.22(d)), detailed metallographic investigations indicate the presence of grouped particles located along the joint line. Such elongated particles are formed by the grouping of smaller second phase particles, apparently fragmented during the welding process, which could not be pushed out of the interface. Such Mg(Al,Ca) based particles maybe have a superior strength than that of the matrix, in an intermediate stage of the process being anchored and promoting subsequently a kind of stacking process, which evolves and forms clusters of second phase particles in particular regions along the joint line.

The “as cast” MRI230D ingot material is generally characterised by an α-Mg matrix, some needlelike and polygonal type precipitates, described in the literature as being Al_8Mn_5, Al_2Ca and Al_4Sr, dispersed within the matrix and by the Mg(Al,Ca) eutectics with different morphologies located preferentially along the grain boundaries [33,40]. However, the microstructure on the MRI side of the weld is dominated by equiaxed

dynamically recrystallised grains, formed by deformation and the thermal cycle imposed by the process. In particular regions, at both the vicinity of the joint and at the middle of the consumable, a complete degradation of the typical base material second phase particles Mg(Al,Ca) was observed. Under the same magnification, Figure 5.17 highlights the common BM Mg(Al,Ca) intermetallic compounds, which form an almost continuous network, distributed at grain boundaries and interdendritic areas, and the resultant MRI microstructure after the welding. Fine Al, Ca, Sr and other round and polygonal precipitates dispersed among the α-matrix seem not to be strongly influenced by the process to any large extent, since they are present in the deposit with approximately the same form and size as commonly found in the matrix. Additionally, it should be mentioned that the morphology, i.e. size and form of the final precipitates in the deposit, can be roughly controlled by the welding parameters.

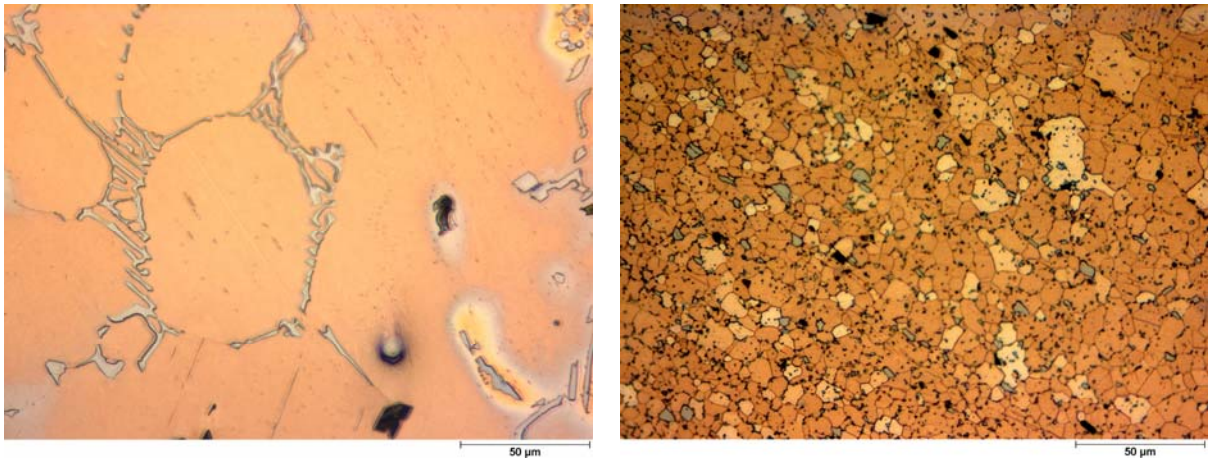

(a) (b)

Figure 5.17: Microstructural changes in the consumable in dissimilar MRI230D/AZ91D-T6 welds. In (a) the typical Mg(Al,Ca) eutectics along the grain boundaries and in (b) the same material after welding at mid-thickness at the rotational centre (see position “G” Figure 4.22).

As observed during the metallographic analysis, the extruded region presents an inhomogeneous microstructure along the deposit height in both welding conditions (10 mm and 20 mm upsetting). In comparison with the MRI base material, where grain size analyses indicate values ranging from 80 µm to 120 µm, the deposit’s grain size generally varies from a finer structure at the bottom, with an average grain diameter ranging from 5 µm to 13 µm, to a coarser structure at the top, where values varying from 18 µm to 22 µm were identified. Generally, the welds performed with 20 mm upsetting presented a more expressive grain growth in the upper regions of

the extruded area, probably as a consequence of the slightly higher temperatures and also the longer welding times, which allows not only recrystallisation, but also grain growth processes to take place subsequently. Further, Figure 5.18 evidences grain size differences in regions diametrically opposed (see Figure 4.22 indications “f” and “h”), theoretically where the welding conditions imposed were similar and therefore similar final structures should be obtained.

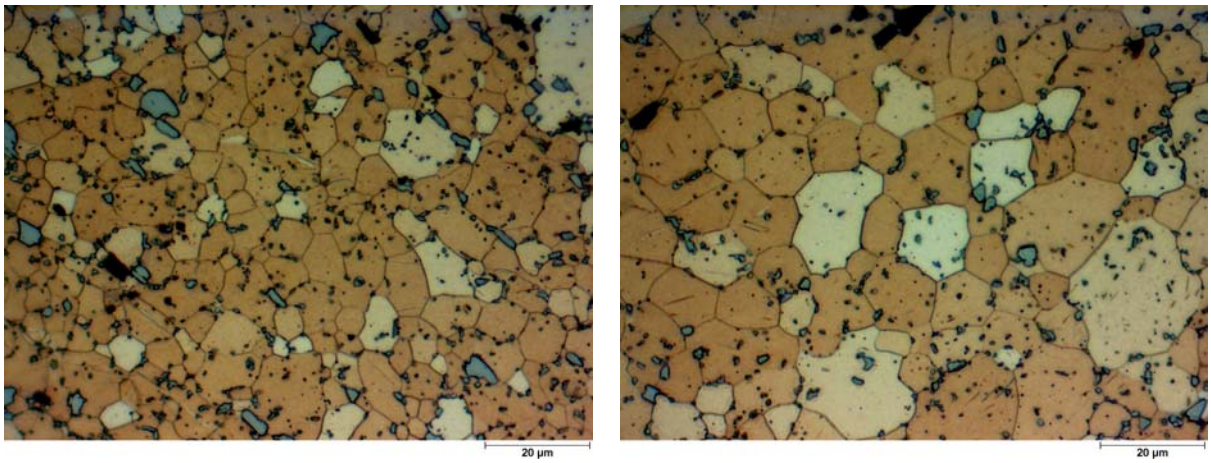

(a) (b)

Figure 5.18: Grain size assessment within the extruded material. In (a) the microstructure in the “f” (average diameter: 7.3 µm) and (b) in the “h” (average diameter: 11.8 µm) position.

North *et al.* [164] reported that transient local melting occurs sufficiently often during Al7075-T6 spot welding and directly affects the stir zone formation. Bearing this in mind, the high strain rates imposed by the process, associated with local liquid phase formation, in particular regions provide the conditions for grain boundary sliding, which influence the RZ’s formation, by reducing or increasing the local heat generation. The above mentioned mechanism varies from region to region, dependent on the base material’s homogeneity and maybe dictates and generates the resultant microstructure inside the extruded area.

EDS analyses (see Figure 4.23 and Table 4.14) along the welding line indicate the presence of different intermetallic compounds. Round particles within the AZ91 side of the weld, corresponding to point 1, showed a high concentration of Al and Mn with a minor presence of Mg. Such compounds are suggested to be AlMn based phases, commonly present in AZ alloys and described in the literature as being the Al_8Mn_5 phase. Point 2 indicates a high concentration of Mg, Al and Mn with some evidence

of Ca, Zn and Sr. In AZ, as well as in the MRI base material, some binary, e.g. AlCa (MRI) and AlMn (AZ and MRI), ternary, e.g. MgAlCa and even quaternary, e.g. MgCaAlSb, MgCaZnSn and MgCaCuSn (MRI) phases are often identified. However, phases with Mg, Al and Mn with some other minor presences seem to be created by the conditions generated in the welding process. A further and precise investigation, also involving an XRD analysis, would be helpful in determining and identifying such phases. Points 3 to 6 basically reveal Mg(Al,Ca) second phase particles, possibly originated from the mechanical fragmentation of the eutectics located previously along the grain boundaries of MRI BM, however, with main element contents varying over a broad range. Scans corresponding to points 7 and 8 show the composition of the MRI matrix in regions near to the bonding line, whereas points 9 to 11 identifies further fragmented precipitates on the MRI side, suggesting that such phases vary, not only in terms of content, but also in relation to the presence or absence of a specific element.

Conversely, joints performed with MRI studs seem not to follow the same joint formation mechanisms determined for AEAZ welds. According to the evidence presented in the metallographic analysis (see Figures 4.22, 5.17 and 5.18) and based on the temperature profiles recorded during 10 mm (MRIAZ-2) and 20 mm (MRIAZ-d) upsettings of MRIAZ welds (see Figure 5.19), one can affirm that, within this combination, the joint formation follows the same sequence discussed in Section 5.2.2 for similar AZAZ welds. Due to the matching correlation material/welding conditions, the plasticised layer is generated through the consumable's diameter, and rises along the hole, leaving beneath a fine dynamically recrystallised deposited material. Similar to that observed for the AZAZ joints, at T2 the temperature increases, experiencing a short drop as the frictional interface achieves the level of the thermocouple hole and slightly rises again towards the end of the process. At T1 the temperature increases continuously, achieving the maximum value and remaining practically constant up to the end of the process. In this case the self-regulating peak temperature mechanism proposed by North *et al.* [166] and detailed in Section 5.2.1, probably took place and forced the temperature not to overcome the solidus line. A temperature drop was not observed at T1, since the peak temperature is achieved somewhere before the frictional interface reaches the upper thermocouple level.

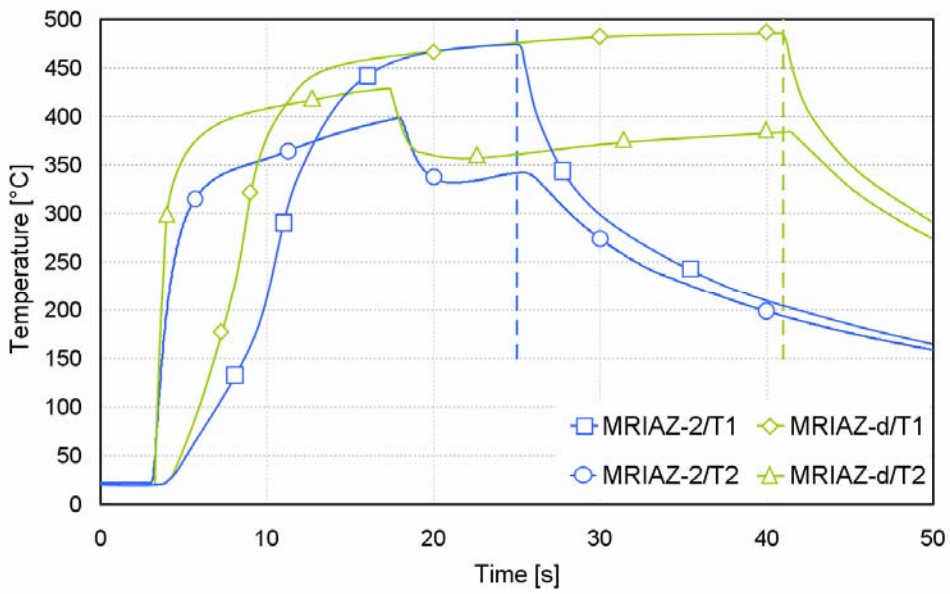

Figure 5.19: Temperature monitoring in MRI230D/AZ91D-T6 welds.

5.3.2.3 AZAZ Joints

As also observed with the other combinations, after some preliminary trials sound welds were obtained with no bonding defects along the welding line and without porosity. In conventional fusion welding of AZ cast alloys, porosity is always an important issue to be considered, since the gases entrapped during the casting process are liberated and remain in the welding seam under certain conditions [170].

Micrographs from the bottom of the weld (see Figure 4.24(b), (c) and (d)) show a broad range on both sides, where a dynamically recrystallised structure is observed, which enables the severe plastic deformation in the weld zone to be accommodated by the flow of the material in the solid state. Hence, DRX facilitates the solid-state flow and enables a suitable joint to be produced by FHPP. Also to be considered is the heat arising from the deformation-induced DRX that contributes to the higher temperatures achieved in the weld zone, and consequently to the formation and consolidation of the joint. Further, the intercalated microstructures at the bottom, seen in Figure 4.24(b) and (d), with its lamellar-like shear bands have been previously reported in other studies involving friction stir welding of Mg alloys [171]. In such regions one cannot observe a sharp demarcation, where it passes from base plate to rod material. Instead, there is a gradual transitioning into the weld zone dictated by DRX mechanisms implemented throughout the friction process.

The microstructure of AZAZ samples in regions around the final frictional plane in the upper welding area (see Figure 5.20) is characterised by complex intercalated flow patterns. In these areas, part of the former base material is recrystallised, while α-matrix islands, without the characteristic lamellar $Mg_{17}Al_{12}$ eutectics, can be observed in between. In such regions, it seems that the energy supplied by the process was not sufficient to cause a complete plasticisation with subsequent recrystallisation. Instead, the heat input provides enough energy to dissolve the β-phase and to nucleate new grains, generating a network, however in islands within the matrix.

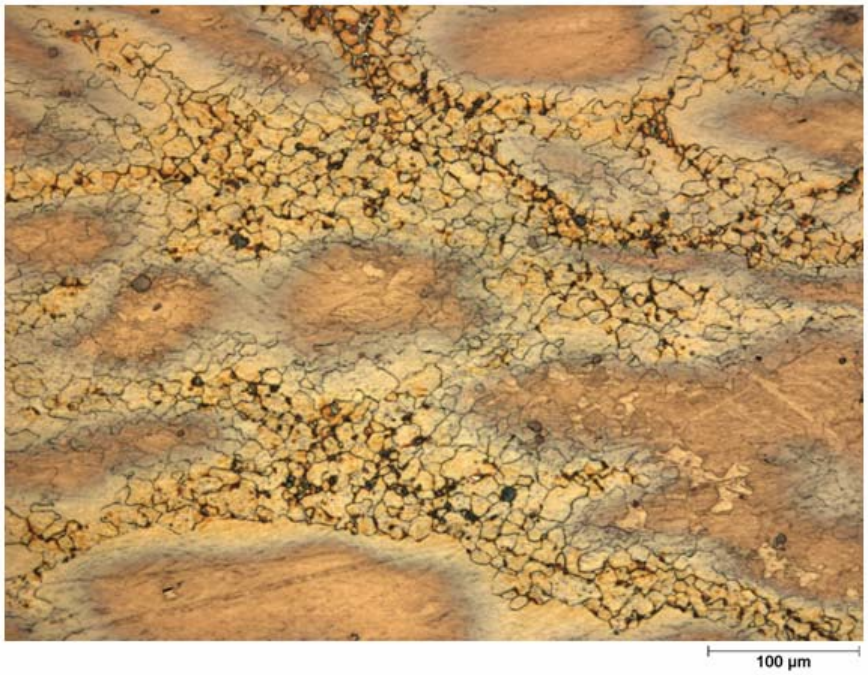

Figure 5.20: Microstructure around the final frictional plane (see point “F” in Figure 4.24).

Welds with higher upsetting generally showed a larger grain size within the extruded area. Higher upsetting and the consequent longer welding/cooling times certainly play the most important role in determining the final weld properties. However, in terms of joint quality, both conditions visually seem to produce welds with adequate joint strength.

EDS was performed, with the investigated points indicated in Figure 4.26 and the corresponding results shown in Table 4.15. Figure 4.26(a) shows round particles stacking at the sidewall interface, corresponding to points 1 and 2. EDS analysis of these particles indicates a high concentration of Al and Mn with a minor presence of Mg and Si. Such compounds are suggested to be AlMn based phases, commonly

present in AZ alloys and described in the literature as being Al_8Mn_5. The concentration of such particles over the bonding line should be controlled by welding conditions, in order to fragment such phases and so avoiding areas with low ductility in the final component. Points 3 to 5 (see Figure 4.26(b)) show a high concentration of Mg and Al with some evidence of Zn in scans over the grain boundaries. Such regions, probably formed by $Mg_{17}Al_{12}$ phase, are a strong indication of local melting, which causes low melting-point intermetallic eutectics, concentrated on the grain boundaries, to be segregated, molten and re-precipitated during the cooling phase. Temperature profiles and investigations involving the mechanisms of bonding formation led to results very similar to those presented at Section 5.2.2. Therefore such mechanisms will not be further discussed.

5.4 MECHANICAL CHARACTERISATION

5.4.1 Hardness Tests

As shown in Figure 4.15, AZAZ-06/12 (series of welds performed with 6 mm diameter studs and 12 mm upsetting) welded joints have resulted in generally similar hardness profiles along the transversal cross-sections, with no softening or hardening effects independent of the welding parameters. Although dwell times and cooling rates are seen to be different, peak temperatures experienced by the welds were to some extent similar. Therefore, and based on the metallurgical analysis, the resultant microstructures within the extruded area were similar, which would consequently generate similar properties within the RZ. Compared to the BM, the possible increase in hardness as a consequence of the fine dynamically recrystallised microstructure, resulting from the plastic deformation imposed by the process, is to some extent compensated by the dissolution of the second phase particles, which are produced to increase the strength of such alloys. Both phenomena influence one another and probably culminate in forming a weld deposit with an analogue of the hardness level of base material. Johnson *et al.* [5] and Kato *et al.* [114] have reported similar results, working respectively with friction stir welding and friction welding of Mg-Zn-Al-Mn alloys. According to their work, there did not appear to be any significant hardening, which can also be seen in the scans performed across the welded regions.

For AZAZ-06/12 and for AZAZ-08/10-20 (series of welds performed with 8 mm diameter studs and 10/20 mm upsetting), scans performed in the lower weld areas presented a tendency to produce higher hardness values than those from the upper weld areas (see Figures 4.15 and 4.27(e) and (f)). The slightly higher hardness in those regions can be attributed to the smaller grains (see Figure 4.13 and Section 4.3.2.3), generated due to the faster cooling rates imposed at the initial stages of the process. Draugelates and Schram [118] reported higher hardness values along the bonding line in rotational friction welding of AZ alloys. According to their work, the significant grain refinement imposed by the process suppresses the effect caused by the $Mg_{17}Al_{12}$ phase dissolution, thereby generating hardness values approximately 20 % higher in the welding area. Working with an Mg-Al-Zn friction welded alloy, Ogawa *et al.* [113] also reported an increase in hardness along the welding line, as a consequence of the work-hardening effect sustained under a fairly high forging pressure. Friction stir welds using the same alloys (AZ31) have indicated either higher hardness values across the welding zone, due to the refining mechanism imposed by the process [172], or lower hardness, due to the softening effect caused by the thermal cycle during the process [173]. According to the latter work, since AZ31 derives much of its strength from being rolled as a wrought product, the temperature adversely affects its properties, thereby causing such a softening effect [173].

In the AEAZ joints, material hardening in comparison to the BM is clearly observed from start to finish within the deposit (see Figure 4.27(a) and (b)), resulting from the welding thermal cycle imposed by the process. Although in this particular case the stud material was not fully plasticised across the bore of the hole, grain refinement, as a consequence of the mechanical working, has occurred and seems to elevate the average hardness. Pinheiro *et al.* [73] observed for similar AE42 rotational friction welds, a bonding line characterised by a thin layer of dynamically recrystallised grains with slightly higher hardness values. However, hardness values in the RZ were practically unaltered by an upsetting increase, suggesting that thermal cycles, although slightly different, affect the microstructure in a similar way. Bowles *et al.* [112] reported without further discussion the feasibility of friction welding to produce good quality dissimilar AEAZ joints with no significant loss in hardness across the welding area.

Similar to the previous case, the welding process and the consequent production of a very refined microstructure seems to influence the hardness values in the RZ of the MRIAZ welds. Scans performed near the top surface (see Figure 4.27(c) and (d)) are very smooth and present a lower scattering, probably due to the higher heat generated in those locations. Since the formation of these areas and the resultant microstructure in 10 mm and 20 mm-upsetting welds are to some extent similar, a hardening mechanism, probably involving fine precipitate dissolution or re-precipitation during cooling, took place under these conditions.

Generally, the scans performed at 2 mm from the top surface presented a much smaller scattering when compared with those carried out across the lower stud areas. This behaviour can be attributed to the partial dissolution/fragmentation of the eutectic phases within the extruded material and to the dissolution of the lamellar β-phase in the HAZ on the AZ91 side of the weld, due to the high temperatures achieved in those locations. Within the extruded area (RZ) the scatter is reduced, obviously due to a much more homogenised microstructure, generated by the hot working imposed by the welding process. Since such high hardness products are dissolved, the scatter is reduced. However, in scans performed across the bottom weld area, the decrease in dispersion is easily observed as soon as the extruded area is reached. In fact, as observed in the metallurgical characterisation (see overviews in Figures 4.20, 4.22 and 4.24), in the bottom areas on the AZ91 side of the weld, the BM is not modified in regions very close to the BL into a deep extension. Since the workpieces are at room temperature at the beginning of the process, the generated heat is almost instantaneously conducted out of the welding region. Hence the achieved temperatures, as well as the dwell times in these locations, are not high enough to partially homogenise the microstructure, causing the profiles to show a significantly increased scattering.

5.4.2 Pull-out Tests

According to the results shown in Sections 4.2.4.2 and 4.3.3.2, pull-out tests in the joints that were produced using a broad range of parameters have confirmed the ability of the process to deliver high-strength welds. After 10 kN is achieved, which is equivalent to a stress of about 32 MPa at the cross section of the stud, yielding begins. From that point, the pull-out test can be compared with a standard tensile

test, in which the sample has half of the gauge length. Based on that, the maximum achieved load seems to match the BM properties and small variations can be considered acceptable, due to the broad range in which BM properties vary. Converting pull-out values to strength, AE, MRI and AZ studs were loaded up to 170 MPa, 113 MPa and 198 MPa respectively, which to some extent matches the values found for the BMs (see Section 4.1).

Bearing in mind the application, in which the process is planned to be used, pull-out tests confirm the suitability of the proposed concept for locally reinforcing Mg components with high quality welds. According to the VDI-Handbuch Konstruktion [174], shank bolts are maximally loaded at their minimum yield point. Based on that and on the results delivered by pull-out tests (see Sections 4.2.4.2 and 4.3.3.2), for AZAZ-06/12 welds, steel bolts with a minimum of 10 mm, 12 mm and 14 mm nominal diameters respectively from 12.9, 10.9 and 8.8 strength grades could be used at room temperature without collapsing the joint, i.e. without pulling the welded stud out of the base plate. If 08/10-20 welds are considered, the results delivered by pull-out tests indicate that steel bolts with a minimum of 10 mm, 12 mm and 14 mm nominal diameters from 8.8 strength grade could be used with MRIAZ, AEAZ and AZAZ joints respectively at room temperatures without causing the joint to fail. Since an M8 screw strength of grade 8.8 is the largest bolt actually in use in the automotive industry [9,10], within the spectrum of applications delineated for the present study, it can be affirmed that these joints would be able to carry the load with some margin of safety.

5.4.3 Transversal Tensile Tests

Tensile tests from AZAZ-06/12 welds demonstrated joints with good performance, particularly those performed with higher pressures. Figure 4.17 shows that joints performed under different welding conditions have generally similar mechanical properties to those of the base material. Although joints welded with the highest pressure presented a very inhomogeneous microstructure in the metallographic analysis, in the transversal tensile test these samples presented the highest average strength. Low pressure joints achieved strength values in the range of 87 % to 98 % of the BM tensile properties for lower and upper weld regions respectively. However, high pressure welds presented values even superior to those of the BM values. It seems that in the former, the magnitude of both the welding pressure and

subsequently the forging force was not high enough to bring stud and base material into the intimate contact necessary to produce a strong bond. In his experiments, Meyer [78] demonstrated a decreasing influence of the welding pressure and of the forging force on the joint formation at the bottom of the cavity during the last stages of the welding cycle. Especially in welds performed at lower pressures, during the final stages of the welding process the microstructure, and consequently the bond formation at the bottom area, are to some extent already consolidated and therefore do not suffer a significant influence over the events occurring in the upper region of the joint. This fact could explain, as demonstrated in Table 5.2, why most of the samples welded with lower pressures collapsed at the bonding line, particularly in trials carried out on the lower part of the joint. However, with increasing welding pressures, the nominal set value is totally transferred to the lower joint parts, as long as the limiting control parameter is not reached. Table 5.2 mirrors this tendency, since at higher pressures (samples 2 and 3) most of the joints failed in the base material, outside the extruded area.

Table 5.2: Position and frequency of failure after tensile testing of AZAZ-06/12 joints.

		Failures at the BL	Failures in the BM
MgAZAZ - 1	Upper	37.5%	62.5%
	Lower	75%	25%
MgAZAZ – 2	Upper	12.5%	87.5%
	Lower	12.5%	87.5%
MgAZAZ – 3	Upper	0%	100%
	Lower	0%	100%

Tensile properties of dissimilar welds also indicated that high performance joints can be obtained using FHPP. The average strength of samples from upper and lower stud areas is shown in Figures 5.21 and 5.22 respectively. Based on these results, and on the curves presented in Figure 4.29, one can observe that the tensile behaviour tends to match the AZ91 BM curve, since this material composes the largest extension of the tensile specimen. Furthermore, grain refinement associated with particle fragmentation and a porosity-free microstructure, due to the hot working imposed by the process, seems to contribute to the enhancement of tensile properties. Table 5.3 indicates joints welded with AE/MRI inserts having up to 90 % superior strength of the BM in some cases. The failure location varied randomly, but in most cases occurred in the BM, outside the extruded area.

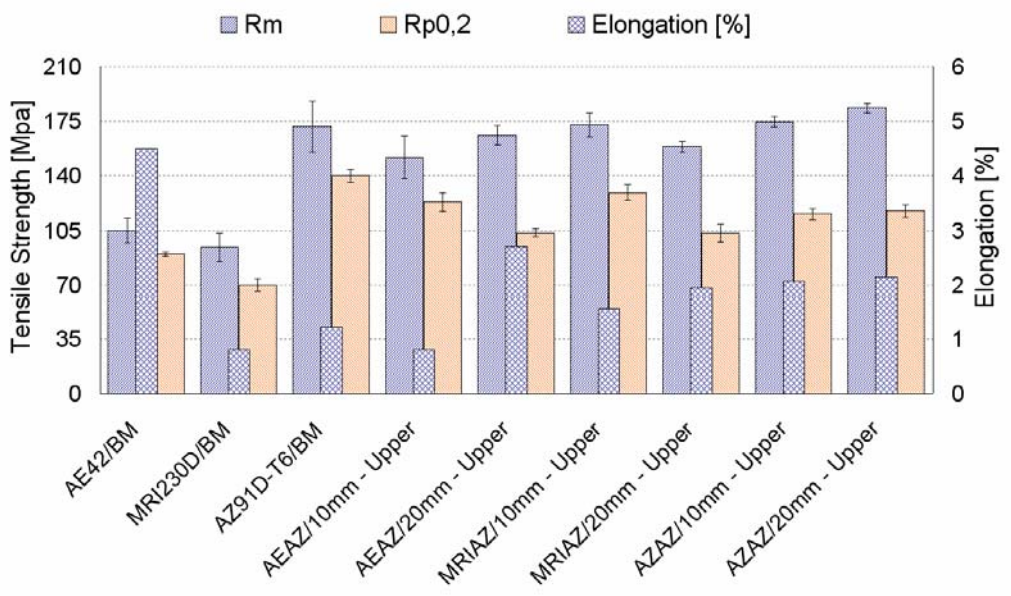

Figure 5.21: Effects of upsetting on the yield strength, tensile strength and elongation at rupture in ∅8 mm/10-20 mm welds (upper samples) in comparison with results from the base material.

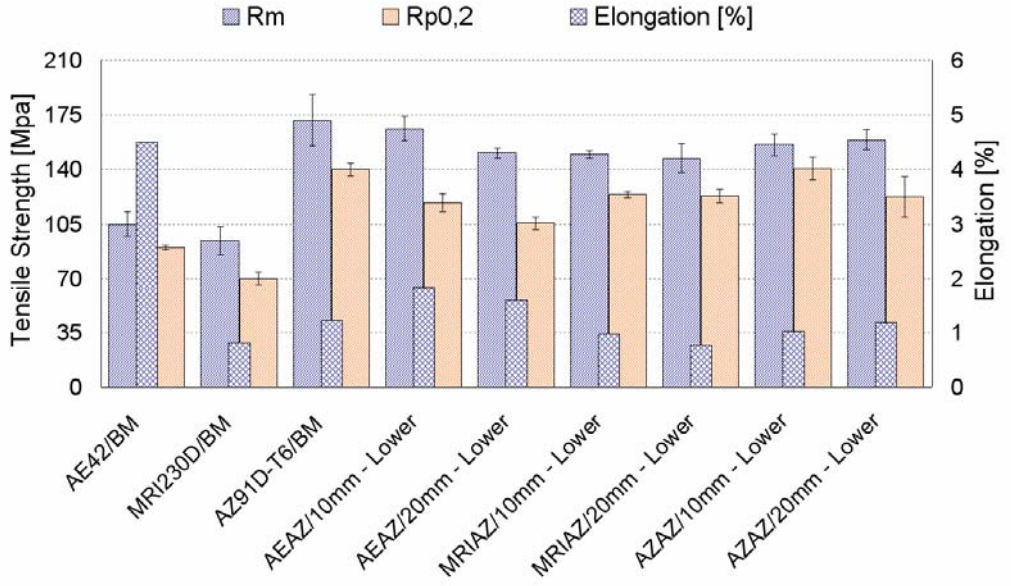

Figure 5.22: Effects of upsetting on the yield strength, tensile strength and elongation at rupture in ∅8 mm/10-20 mm welds (lower samples) in comparison with results from the base material.

According to Figures 5.21, 5.22 and Table 5.3, AEAZ welds presented generally the highest elongation, probably due to the AE42 base material's properties. However, in some cases, as demonstrated for welds AEAZ-10 mm, in the upper weld areas the concentration of second phase particles along the BL (see Figure 5.14) seems to decrease the elongation abruptly and often causes the fracture to take place in these regions. As reported on the literature [175] and observed in some initial SEM analysis,

such clusters of particles along the bonding line may have increased the notch sensitivity in these particular areas, leading the joint to collapse with lower elongation, but with significantly higher strength values. Tensile strength values varied arbitrarily, without a defined relation to both the specimen location (upper and lower samples) and the upsetting.

MRIAZ welds also presented satisfactory strengths and the resultant refined microstructure seems to contribute in producing such a high performance. In this case, the forging force seems to play an important role, since upper weld area specimens presented clearly higher strengths when compared with lower specimens. As discussed by Meyer [78], during the final stages of the FHPP welding process the microstructure of the bottom area is to some extent already consolidated and therefore suffers a marginal influence of the forging force. Furthermore, MRIAZ welds with 20 mm upsetting presented a more expressive grain growth in the upper weld regions (see Section 5.3.2.2), which probably contributed to generating the observed inferior tensile strengths in these locations. In the MRIAZ-10 mm upsetting welds, the failure was mainly located in the BM, in a region outside the RZ. On the other hand, the failure location moved towards the RZ with higher upsetting welds, which can be attributed to some extent to the different BM properties. Table 5.3 lists the highest absolute values and shows the feasibility of the process to perform high-strength dissimilar MRIAZ welds.

Transversal tensile samples from AZAZ-08/10-20 welds seem generally to present a higher elongation in relation to base material, probably due to the formation of a refined DRX microstructure in the extruded area. In most of the cases the failure location occurred in the BM outside the RZ. Generally, 20 mm upsetting specimens seem to present slightly higher strengths, although in the lower stud areas there is a global tendency (observed in all the combinations) to equalise the tensile strength for 10 mm and 20 mm upsetting values. The elongation, as observed also for AEAZ and for MRIAZ combinations, was significantly higher in samples from the upper weld areas. This characteristic can be attributed to the larger specimen gauge length occupied by the refined microstructure produced by the welding process. Moreover, AZAZ joints tested within this group demonstrated a similar behaviour to the AZAZ-06/12 welds (see Section 4.2.4.3).

Table 5.3: Maximum tensile strength experienced by 08/10-20 mm joints.

Sample		Rm [MPa]	$Rp_{0,2}$ [MPa]	A [%]
AEAZ-10 mm	*Upper*	184	132	1.32
	Lower	183	132	1.32
AEAZ-20 mm	*Upper*	175	100	3.83
	Lower	155	111	1.73
MRIAZ-10 mm	*Upper*	186	127	1.76
	Lower	155	128	1.01
MRIAZ-20 mm	*Upper*	167	106	2.48
	Lower	160	129	0.96
AZAZ-10 mm	*Upper*	182	111	2.70
	Lower	175	161	0.61
AZAZ-20 mm	*Upper*	188	112	2.29
	Lower	168	104	1.86
AE42	*Base Material*	104 ± 8	90 ± 2	4.5 ± 1
MRI230D	*Base Material*	94 ± 8	90.1 ± 2	0.8 ± 0.2
AZ91D-T6	*Base Material*	171.5 ± 16	140 ± 4	1.3 ± 0.7

5.5 JOINT PERFORMANCE

5.5.1 Creep Tests

Following the procedure presented in Section 3.5.7, the creep resistance of the materials used within this study was determined (see Section 4.4.1). Although MRI alloys have confirmed their superior performance, some results were to some extent unexpected and widely differed from values reported in the literature. As demonstrated in Figure 5.23, Mg-Al-RE (AE) alloys presented at 125 °C and 150 °C a significantly lower creep resistance when compared with Mg-Al-Zn (AZ) alloys. While AE alloys show strain values of 1.8 % and 4.1 % for 125 °C and 150 °C respectively, the latter indicates values of 0.6 % and 2.0 % under the same testing conditions, i.e. at 80 MPa and after 100 testing hours. As presented in Section 3.1, Mg AZ91D was heat treated and artificially aged to the T6 condition. The standard T6 heat treatment causes partial homogenisation of the microstructure and at the same time prevents, at least to some extent, precipitation of the intergranular β-phase particles. After solid solution treatment, most of the β-phase is dissolved in the matrix, but during aging treatment a trace amount of β-phase precipitates, again along the grain boundaries (see Figure 4.1(c)). Due to the subsequent aging, AZ

alloys presented at 125 °C a higher stability with a consequently better performance by comparison with AE42 alloys. At 150 °C, however, the coarsening of the $Mg_{17}Al_{12}$ phase precipitated along the grain boundaries seems to decrease the creep resistance of AZ alloys. Therefore, at this temperature, the differences between the performance of AZ and AE alloys are reduced. Bearing in mind that magnesium alloys undergo creep mainly by grain-boundary sliding, at 175 °C the coarsened $Mg_{17}Al_{12}$ phase, which has a melting point of approximately 460 °C and is comparatively soft at lower temperatures, does not serve to pin the grain boundaries in AZ alloys. As a consequence, Mg-Al-Zn alloys creeps very early under those testing conditions.

In AE alloys, it is estimated that the presence of one or more stable Al-RE and Mg-RE phases contributes greatly to its superior behaviour at elevated temperatures, through intergranular and transgranular strengthening. However, as demonstrated in Figure 4.3(a), the intermetallic Al-RE phase in the ingot material is inhomogeneously distributed within the matrix. Furthermore, the matrix is composed of bulky precipitates with a large relative distance to each other, which may contribute to the lower creep resistance observed in AE alloys. Working with a die-cast Mg-Al-RE (AE) alloy, Bakke *et al.* [140] reported a tensile creep strain of 0.1 % after 100 hours at 175 °C/75 MPa, whereas Dieringa [27], working with squeeze casting materials found compressive creep strain values of around 3 % under similar conditions. In both cases, as may be expected, their reported BM creep strain values are clearly lower than those determined within this study.

MRI alloys demonstrated the highest performance among the BMs. As reported in the literature [43], the formation of eutectic $Mg_{17}Al_{12}$ is suppressed by the presence of Ca and Zn. The resultant Mg-Al-Zn-Ca phases are evenly distributed along the grain boundaries and impede grain boundary sliding. Thus, superior behaviours of AXJ and MRI alloys were observed.

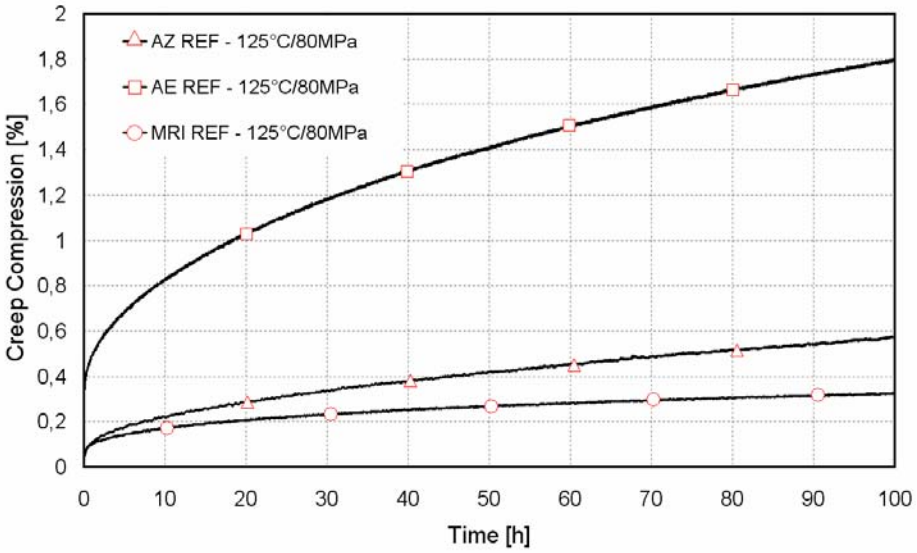

(a)

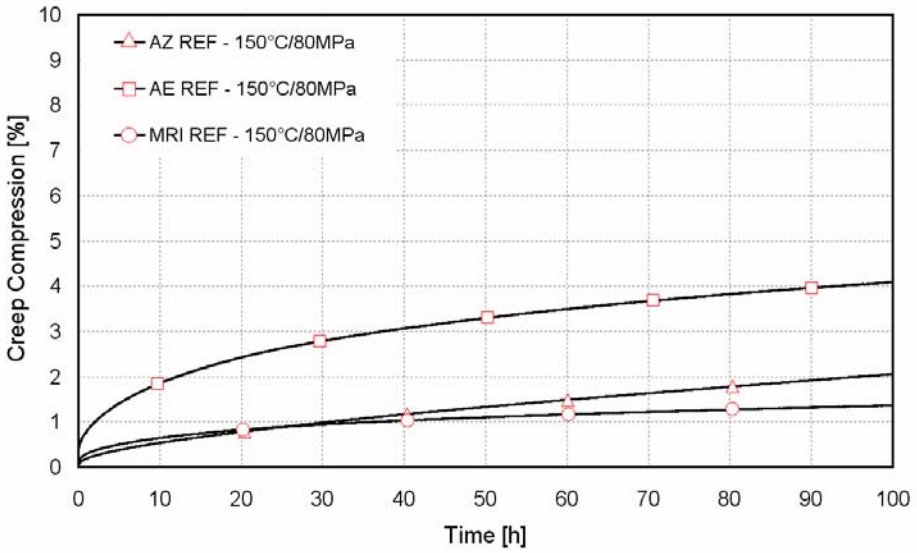

(b)

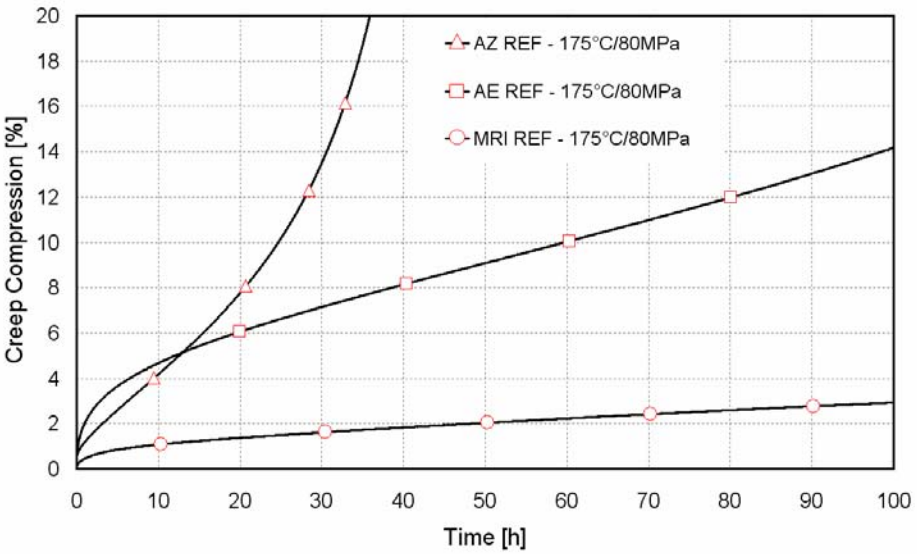

(c)

Figure 5.23: BM compression creep curves at testing temperatures.

For AEAZ joints, creep resistance of the welded area indicated at 125 °C and 150 °C similar strain values to those determined for the upper (ref.) area (see Figure 4.30). However, at higher temperatures, where testing conditions become very severe for Mg alloys, the upper (ref.) specimen showed a clearly superior creep resistance. Based on the mechanism of joint formation identified for AEAZ welds, one could observe that minor differences occur between microstructures of deposited and base material, because the stud is not fully plasticised across the bore of the hole. According to Moreno [44], a relatively refined microstructure, resulting from the hot working imposed by the process, would be detrimental to high temperature properties, since the creep of metals is driven by grain boundary sliding mechanisms. However, since no expressive grain refinement was observed for AEAZ joints, mechanical fragmentation of the second phase particles in regions close to the bonding line seems to be a more reasonable explanation for the lower creep resistance of the welded areas. Figure 5.24 demonstrates lower (A) and upper (B) samples after testing at 150 °C/80 MPa. As evidenced in the picture, the deformation of the welded sample (A) is concentrated in a small area, while in the reference sample it is distributed along the whole specimen length. Knowing that the deformed area coincides with the bottom weld area, it seems that mechanical fragmentation somehow influences the creep mechanisms, decreasing the resistance of the material locally. Figure 5.13 shows a comparison of typical second phase particles in position 1 (upper weld areas – see Figure 5.13(a)) and position 2 (lower stud areas near the bottom bonding line – see Figure 5.13(b)) of sample (A) in Figure 5.24.

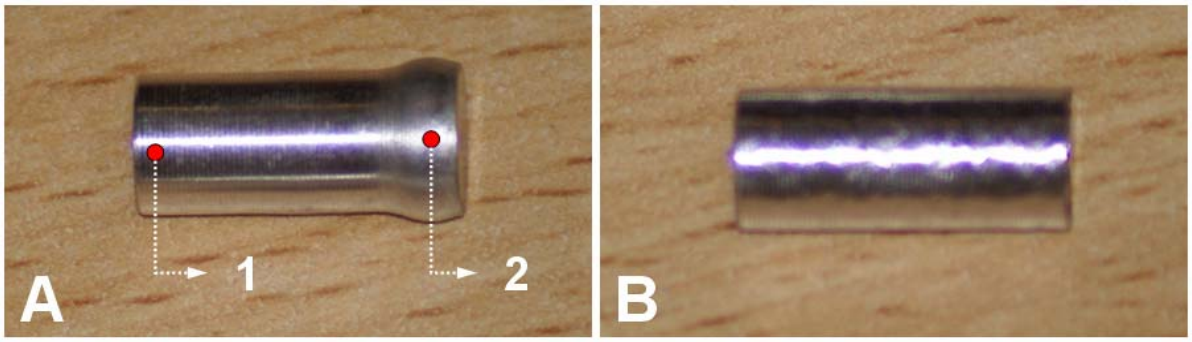

Figure 5.24: AE lower (left - A) and reference (right - B) samples after creep test at 150 °C/80 MPa.

Bearing in mind that AE42 alloys have their high temperature strength attributed to the formation of stable AlRE precipitates, which suppress the formation of β-phase, it could be that the mechanical fragmentation caused by the process liberates some Al within the matrix. This free Al would hence increase the probability of $Mg_{17}Al_{12}$ phase formation, which would consequently contribute to a decrease in high temperature properties. EDS analyses performed during metallurgical characterisation of AEAZ joints identified some dark-grey regions with an abnormal Al content (see Figure 4.21 and Table 4.13, points 9 and 10).

In addition, the calculated activation energy of 121.9 kJ/mol and 78.2 kJ/mol respectively, for lower and upper (ref.) samples (see Figure 5.25), are to some extent in agreement with results published by Dieringa [27] for AE42 and AE42+saffil reinforced alloys. The lower activation energy determined for upper reference samples may be related to the limited number of experiments performed. Furthermore, the activation energy estimated from the plot is lower than that for lattice self-diffusion in Mg (135 kJ/mol) or activation energy for diffusion of Al in Mg (143 kJ/mol). Since these values give an estimation of the predominant creep modus, one can conjecture that both samples present different deformation mechanisms. In order to calculate the stress exponent *"n"* and determine accurately the deformation mechanisms acting, tests under different stresses should be performed, which are outside the scope of the present work.

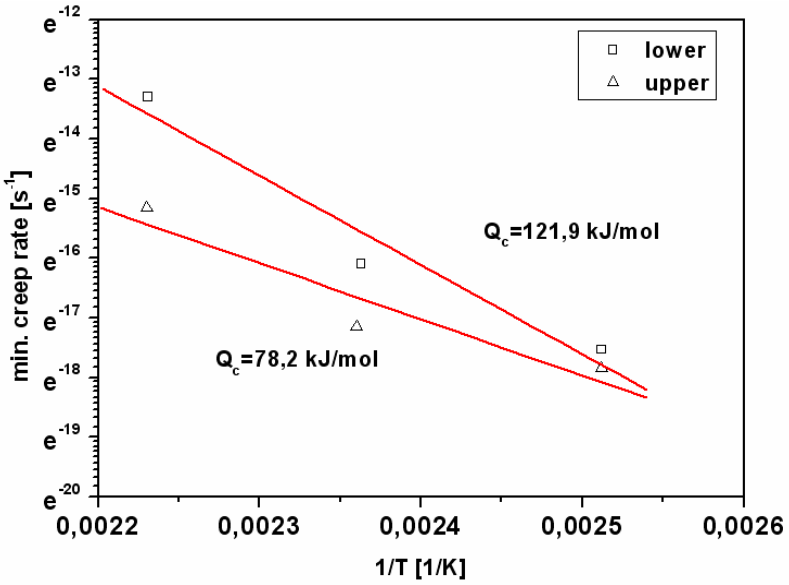

Figure 5.25: Plots of ln(dε/dt) against 1/T for AE42 reinforcements in order to determine the activation energy for creep. Test conditions: 125 °C, 150 °C and 175 °C, under 80 MPa.

As indicated in Section 4.4.1.2, MRI alloys presented a very good creep performance. Despite this, the creep values ascertained within this study are far removed from those reported in the literature [176,177]. At 175 °C, for example, the upper reference sample creeps at around 3 %, while the lower sample creeps between 9 % and 10 % after 100 hours at 80 MPa. In the literature, creep strains varying between 0.02 % and 0.15 % for Mg-Al-Sr-Ca alloys [176] and around 0.25 % for MRI230D alloys [177] have been reported after 100 and 200 hours respectively at 175 °C/70 MPa. Considering that the MRI230D is a fairly newly developed alloy, there are a limited number of publications involving its high temperature properties and the microstructural changes related to it. This lack of information in the literature makes a relevant analysis of the mechanisms acting during creep tests of Mg-Al-Ca-Sr alloys a relatively difficult task.

According to Hirai [178], additions of Ca and Sr, up to 1wt% and 0.5wt% respectively, in AZ alloys decrease the grain size substantially, consequently improving the creep properties. Bearing that in mind and considering the expressive grain size refinement within the extruded material, a higher creep resistance would be expected in those areas when compared with the reference samples. However, similar to that observed in regions surrounding the bonding line in AEAZ welds, the process imposes a complete disrupture of the second phase precipitates (see Figure 5.17, Section 5.3.2.2), which apparently liberates Al into the α-matrix (compare Table 4.8, EDS points 7,8 and 9 with Table 4.14, EDS points 7 and 8). Although the free Al inside the matrix is reported to form stable Al_4Sr and Al_2Ca [33], its excess probably aids the β-phase formation, but which perhaps justifies the reduction of creep properties inside the extruded material, as demonstrated in Figure 4.31. This effect seems to exceed the positive contribution of grain refinement. Another possible reason for the reduced resistance within the deposit was reported by Bai *et al* [176]. According to their study, the improvement of creep resistance caused by Sr and Ca additions may be attributed to the formation of an intermetallic network at grain boundaries. Considering grain boundary sliding the most common creep mechanism in alloys based on Mg-Al containing Ca and Sr, the intermetallic network constitutes a restriction, thereby improving the overall creep resistance over different temperature and stress conditions. According to this theory, the network fragmentation imposed by the process would have a detrimental influence on creep properties within the

deposit, which is to some extent confirmed by Figure 4.31. Additionally, it has also been reported [176] that intermetallic particles present in Mg-Al-Sr-Ca quaternary systems are larger than 1 µm and are therefore not effective on inhibiting dislocation motions. Metallurgical characterisation (see Section 4.3.2.2) shows that fine polygonal Al, Ca and Sr precipitates remain apparently unchanged after the weld operation and consequently were not related to changes in the creep properties. Further TEM microscopic analysis would be helpful, perhaps to comprehend the changes on fine precipitates and their probable relationships with creep properties after the welding operation.

Moreover, the activation energy for creep was calculated and reaches 110.1 kJ/mol and 109.9 kJ/mol respectively for lower and upper (ref.) samples (see Figure 5.26). Compared with the activation energy found in the literature [27,179], the observed values seem to be of the same order of magnitude, indicating that on average the same energy is necessary to initiate the creep process in both, the upper and lower samples.

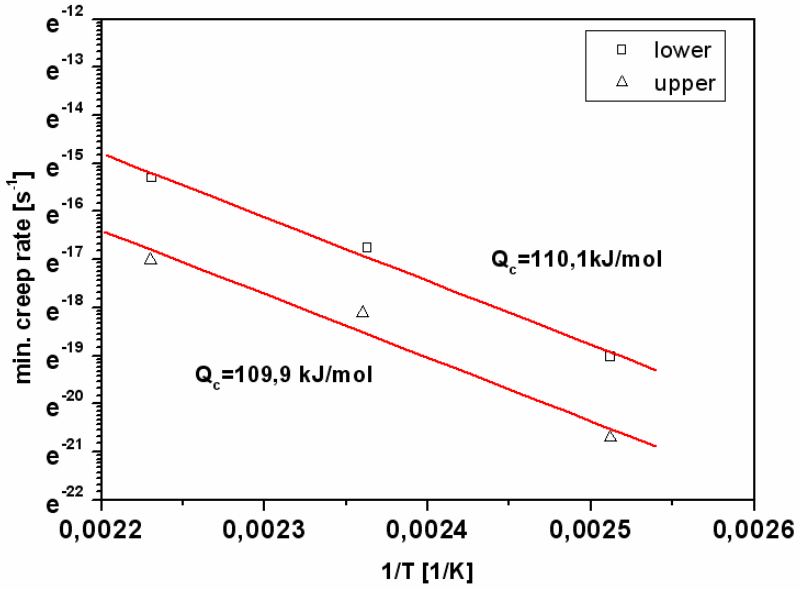

Figure 5.26: Plots of ln(dε/dt) against 1/T for MRI230D reinforcements, in order to determine the activation energy for creep. Test conditions: 125 °C, 150 °C and 175 °C, under 80 MPa.

Since AZ91 is one of the most used Mg alloys, many authors have been investigating its high temperature properties [179-181] recently. According to Figure 4.32, samples extracted from the lower stud areas of similar AZAZ joints presented, in all three cases, a reduced creep resistance when compared with the upper (ref.) samples. As demonstrated in Sections 4.2.3 and 4.3.2.3, in similar AZAZ welds, the extruded material shows a very refined dynamically recrystallised microstructure with a complete rupture of the intragranular lamellae β-phase and a further re-precipitation of these phases at grain boundaries, which can explain its poor creep properties. On the one hand, grain refinement associated with the presence of intragranular lamellae β-phase has been reported to result in improved creep resistance for alloys that contain a hard divorced eutectic, since the fully grain-refined state with a hard divorced eutectic helps to lock grain boundaries and reduce grain boundary sliding [182]. On the other hand, discontinuous precipitation of $Mg_{17}Al_{12}$ at grain boundaries allow grain boundary sliding at elevated temperatures, increasing creep susceptibility [180]. In creep tests of AZAZ welds, the effect of grain refinement seems to be suppressed by the rupture of the intragranular lamellae β-phase associated with its precipitation along grain boundaries. As a consequence the welded region presents a reduced creep resistance.

As observed within this section, the authors have different opinions concerning the influence of grain size and the presence of second phase particles in the creep properties of Mg alloys. At temperatures above half the melting point, deformation can occur in different ways. A rough way of distinguishing when grain-boundary sliding becomes prominent is by the equicohesive temperature. Above this temperature the grain boundary region is weaker than the interior and strength increases with an increase in grain size. Below the equicohesive temperature the grain-boundary region is stronger than the grain interior and strength increases with a decrease in grain size (thereby increasing the grain boundary area). In this context, a determination of the creep mechanism would be fundamental to define the welding conditions aimed at the enhancement of joint performance. Furthermore, the activation energy was calculated from Arrhenius plots reaching 123.5 kJ/mol and 147.7 kJ/mol for lower and upper (ref.) samples respectively (see Figure 5.27). This contrasts with the activation energy values ranging from 121 kJ/mol to 171 kJ/mol as found by Guo *et al*. [179], with activation energy for lattice self-diffusion in Mg

(135 kJ/mol) or activation energy for diffusion of Al in Mg (143 kJ/mol). Thus the observed values are somewhat in a reasonable range. In the present work, the calculated activation energy for creep exhibits a clear increase in upper samples, which totally agrees with the higher creep resistance tendency of upper samples shown by creep curves.

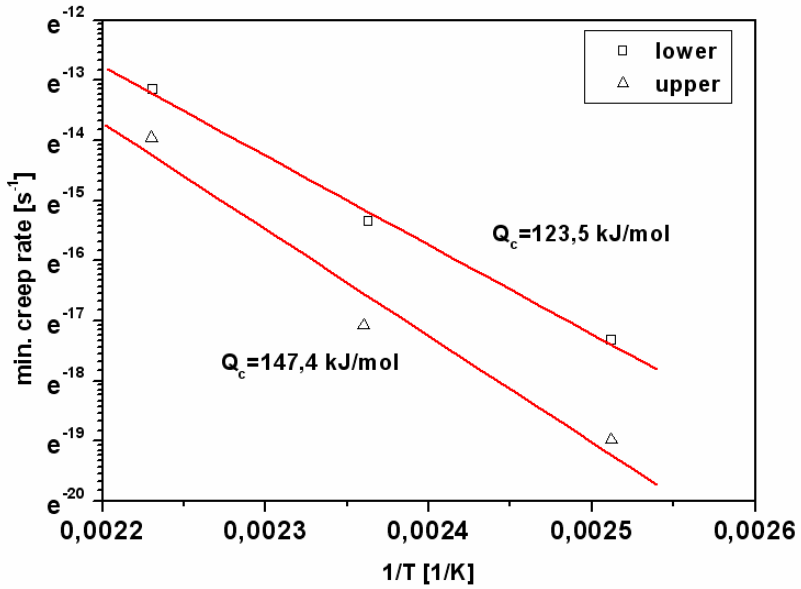

Figure 5.27: Plots of ln(dε/dt) against 1/T for AZ91D-T6 reinforcements in order to determine the activation energy for creep. Test conditions: 125 °C, 150 °C and 175 °C, under 80 MPa.

In addition, a brief comparison between the creep resistance of the three welded combinations and the AZ91D-T6 base material under different testing conditions was carried out (see Figure 5.28). Considering the particularities of the materials specifically used within this study (variable tensile strength, presence of voids, etc.) at lower temperatures one can observe a similar behaviour between AZ91 and MRI230D. However, at 175 °C the superior high-temperature properties of MRI230D become evident. Interesting in this context was the behaviour of the AE inserts, which always presented after welding an inferior creep resistance when compared with AZ91D-T6, even at higher temperatures. According to experiments carried out by Baake *et al.* [140] and by Aune and Ruden [36] creep strength of AE42 at 100 °C, 150 °C, 175 °C and 200 °C under different stresses always presented a superior resistance in comparison with AZ91. Changes imposed by the welding process cannot be used to justify the poor creep behaviour of AE42, since such differences were also evidenced in the reference samples (see Figure 5.23).

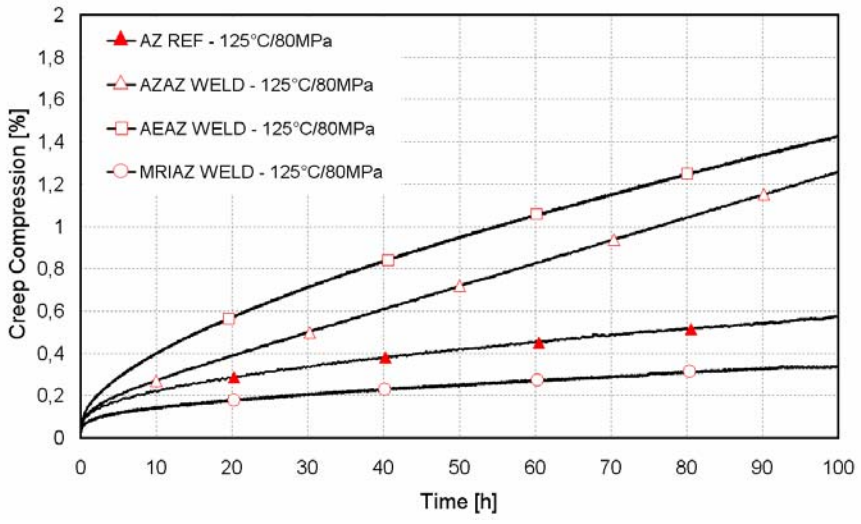

(a)

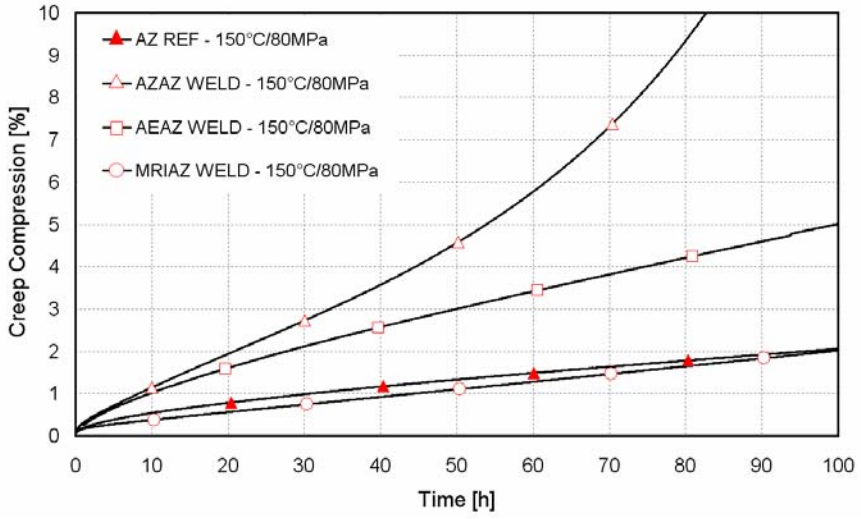

(b)

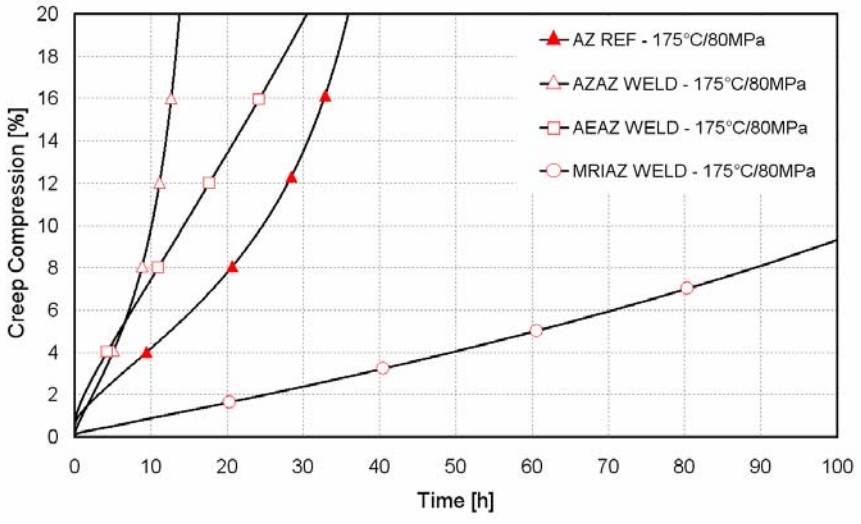

(c)

Figure 5.28: In (a), (b) and (c), the compression creep curves are plotted for similar and dissimilar welded samples at 125 °C, 150 °C and 175 °C respectively. Curves AZAZ REF were also plotted at different temperatures and represent the AZ-BM behaviour for further comparison.

Considering the objectives outlined within this study and the results of the creep tests, Mg-Al-Ca-Sr (MRI) alloys seems to be the most suitable to locally reinforce AZ91 components. Although high strength welds were produced, AE42 seems not to significantly contribute to increase the high temperature properties of AZ91 alloys locally. Furthermore, AZ91D-T6 inserts, which could improve high temperature properties locally, due to the formation of a highly recrystallised microstructure, have shown even poorer properties, indicating that grain boundary sliding plays a decisive role in the deformation mechanisms of these alloys.

5.5.2 BLR tests

In this study, bolt load retention tests in tension and in compression have partially confirmed the general tendency to have higher remaining load levels for Mg joints bolted with Al fasteners [9,34,35]. Further, a decreasing remaining load with torque for different bolt materials was also investigated and attested as reported in the literature [41,44]. As reported by many authors [9,34,35,41,44,45], the thermal expansion mismatch between joint and bolt material contributes significantly to relaxation, becoming even critical as the differences in thermal properties increase. Since the bolt and the component to be joined have different thermal expansion coefficients, during BLR tests, the bolt restricts the Mg from expanding freely and imposes higher stresses in the assembly. Therefore, the closer the thermal properties are, the higher the remaining load will be (see Figure 2.6). Furthermore, at higher preloads, the loss of load is increased, due to the higher compressive stresses in the assembly, which results in an increase in creep deformation of the Mg parts.

In both tensile and compressive BLR tests (see Section 4.4.2), reinforced joints have always shown intermediate remaining load values, i.e. superior to those of AZ91D-T6 and inferior to those of MRI230D/BM. Additionally, remaining load levels of joints welded with 8 mm tip diameter studs presented a clear advantage over those welded with 6 mm studs. This trend can be explained by the fact that the final state of load relaxation occurs when the stresses surrounding the bolt become less localised [38,42]. With the ∅8 mm welds, the stress field can, due to the larger reinforced area, propagate to a larger extent while remaining inside of the high creep resistance inserted material. Furthermore, Mg joints bolted with Al fasteners presented generally the same tendency to that observed with steel bolts. However, reinforced joints

presented on average more expressive results, with remaining load values up to 97 % of those from MRI230D/BM (see Figure 4.34). Optical microscope evaluation performed within the welded area after BLR tests revealed microstructures with none of the discontinuities or defects that could be induced by loads imposed during the tests.

For BLR tests in compression, the dependence of BLR behaviour on temperature and preload force is an important issue and should always be considered during high temperature tests of Mg alloys. Initial trials, where samples were tested at 125 °C with Al and steel screws, presented minor differences concerning remaining loads within this configuration. In these cases, no clear tendency could be observed involving remaining load between reinforced or non-reinforced material (BM and welded joints) or between different material reinforcements. This conflicts with the literature [180], which states that moderate creep resistant AZ91D alloy is prone to excessive creep deformation when exposed to even low levels of load at temperatures above 100 °C. However, Table 4.19 points out a significantly low value for remaining loads in tests carried out at 175 °C after 100 hours. Okechukwu [40] reported also P_F values (final load retained by the couple after returning to room temperature) around zero for MRI153 and MRI230D/BM tested at 175 °C and attributed the poor high temperature resistance of these alloys to the enlarged $Mg_{17}Al_{12}$ grain boundary phase at higher temperatures, which is unstable at temperatures above 120 °C. Moreover, remaining loads of up to 70 % for AE42 at 175 °C have been published in the literature [41,43,44], although under conditions different to those employed in this work. The AZ91D welded joint was also evaluated and clearly showed the lowest remaining load. The broad re-precipitation of β-phase along the grain boundaries, associated with its rupture inside the grains, seemed to facilitate grain boundary sliding, thereby decreasing creep resistance and consequently the remaining load for this combination.

According to Figure 4.36, the joint bolted with an Al fastener presented an untypically low remaining load of only 27 %, which is contrary to that reported in the literature [9,34,35]. BLR tests experience, during the initial period, a short load increase caused by the thermal expansion mismatch between the Mg sample and the steel bolt. The remaining load after testing is directly influenced by the initial load increase, which is

lower the more similar the couple and bolt materials are, i.e. similar couple and bolt materials causes lower load increases during initial heating and therefore higher remaining loads after the temperature cycle. Further BLR tests under these conditions should be performed to clarify the unexpected behaviour of Mg samples clamped with Al bolts.

Considering the results obtained from tensile and compressive BLR tests, one can confirm the feasibility of the process to reinforce Mg components locally. In both cases, the remaining load in welded joints exceeded that of the AZ91D BM, indicating a promising future for the technology proposed within this study.

6 SUMMARY AND CONCLUSIONS

Mechanisms of joint formation as well as metallurgical and mechanical properties of similar and dissimilar welds produced by Friction Hydro Pillar Processing (FHPP) were investigated, determined and assessed. The results and analyses obtained from these investigations lead to the following conclusions:

– In spite of it being a new welding technique, FHPP has demonstrated its suitability for joining different magnesium (Mg) materials. The selected combination of base materials was successfully joined in similar and dissimilar configurations using two different geometries and a large combination of welding parameters. Both geometries exhibited a high performance with good mechanical joint efficiency compared with the base material within the investigated range, i.e. there is a wide operating window for the production of satisfactory joints, considering their mechanical properties.

– A physical description of the process in terms of microstructural evolution supported by temperature results was proposed. Based on that, the bonding mechanisms for similar and dissimilar configurations were identified and determined, whose behaviour accorded with the microstructural changes observed during metallurgical characterisation.

– Welding equipment showed a high reproducibility, with a relatively low standard deviation within the investigated range of parameters. Since the stability of the process was proven, a further investigation of welding parameters was performed in order to establish a correlation between the process, the final microstructure and properties of the welded joints. In this context, the theoretical influence of the main important process parameters on the final welded joint was confirmed by experimental observations. The influence of those parameters on variables is presented in Section 4. The summarised conclusions for each variable studied in these joined materials combinations are presented below:

I. SIMILAR AZ91D-T6

Joint formation in similar AZ91D-T6 welds is characterised by the coalescence of the plasticised layer during the initial stages of the process, followed by the formation of a series of adiabatic shear planes with a refined dynamically recrystallised structure. The consumable is fully plasticised across the bore of the hole and the thickness of the work piece.

The microstructure within the recrystallised zone is characterised by refined equiaxed grains, which tends to increase with increasing upsetting, with a complete rupture of the lamellae β-phase. However, this phase is re-precipitated along the grain boundaries as a probable indication of local melting. Coarse AlMn and MgSi precipitates are not fragmented and remain in the composition of the microstructure of the extruded material. In a region around the final frictional plane in the upper welding area, the microstructure shows complex intercalated flow patterns, in which part of the former base material is recrystallised in some areas, while α-matrix islands without lamellae $Mg_{17}Al_{12}$ eutectics can be observed in between.

Maximum temperatures slightly decrease with pressure. Increasing welding pressure and upsetting slightly enhances the mechanical properties, achieving values similar to those from base material. Hardness profiles indicated a reduced scattering, as a consequence of the β-phase dissolution, with no hardness loss within the recrystallised zone. Welding pressure and upsetting were shown not to influence hardness values significantly.

II. DISSIMILAR AE42/AZ91D-T6

In dissimilar AE/AZ welds, joint formation was characterised by different bonding mechanisms. Within this combination, the stud yields and occupies the cavity before a plasticised layer is created, i.e. the consumable is inserted into the cavity at a rate faster than that at which the plasticised material develops. The consumable is therefore neither plasticised across the bore of the hole, nor through the height of the cavity. The joint formation can be defined as a variation of the Friction Taper Plug Welding (FTPW) process inside a non-through thickness hole.

The microstructure of the recrystallised zone in regions at the vicinity of the joint indicated a complete rupture of the coarse Aluminium-Rare Earth eutectics. In some locations in the upper stud areas, clusters of particles over the bonding line were observed. In regions towards the consumable centre, the microstructure seems to be unaffected by the welding process to some extent. In these regions, the typical dendritic structure with its lamellar second phase compounds remains almost unaltered, which suggests that the consumable was not fully plasticised through its diameter.

Mechanical tests showed the extruded material with hardness values up to 70 HV, which indicates an overmatching condition of the extruded material in relation to the AE42 BM. Tensile and pull-out tests revealed strengths similar or in some cases even higher than those of the AZ91 base material.

III. DISSIMILAR MRI230D/AZ91D-T6

Within this combination, joint formation follows the same sequence discussed for similar AZ welds. Due to the matching correlation of material/welding conditions, the plasticised layer is generated through the consumable diameter and rises along the hole, leaving behind a dynamically recrystallised deposited material. No bonding formation changes were observed with increasing upsetting.

The microstructure on the MRI side of the weld is dominated by equiaxed dynamically recrystallised grains. In particular regions of both the vicinity of the joint and the middle of the consumable, a complete degradation of the typical base material second phase particles Mg(Al,Ca) was observed. Additionally, dissimilar MRI/AZ welds show a severely deformed area in the vicinity of the joint on the AZ91 side of the weld, where dynamically recrystallised grains appear in an extension from 100 µm to 400 µm from the weld line, without the presence of the eutectic structure. In comparison with the BM, where grain size analyses indicate values ranging from 80 µm to 120 µm, in the deposit, grain size varies generally from a finer structure at the bottom, with an average grain diameter ranging from 5 µm to 13 µm, to a coarser structure at the top, where values varying from 18 µm to 22 µm were identified.

Mechanical properties of the welded joints showed values similar to those of the AZ91 BM. An increased upsetting indicates no clear variation in tensile strength. Hardness values achieve values up to 80 HV at some points, which means that in the extruded MRI230D material an overmatching condition was created.

IV. JOINT PERFORMANCE – SIMILAR AND DISSIMILAR CONFIGURATIONS

Performance tests confirmed the feasibility of the process to locally reinforce Mg based components. The strength of the reinforced joint relative to the BM in both tensile and compressive BLR tests was elevated, achieving in some cases 93 % of base material values. The higher efficiency of joints bolted with Al fasteners could not be confirmed, although a few tests were performed under this configuration.

Creep properties were demonstrated to be inferior within the extruded material in relation to reference base material samples. Possible formation of localised β-phase with different morphology and the complete disruption of the second phase intermetallic network, as a consequence of the microstructural changes imposed by the welding process, were attributed as the most plausible reason for the poor creep resistance on these regions. Nonetheless, the creep resistance of reinforced samples were significantly superior to those of pure unreinforced AZ91D-T6.

The principal motivation behind this study was to perform a systematic analysis of FHPP in Mg alloys, to understand the metallurgical phenomena and the consequent microstructural changes imposed by the welding process. As a second issue, the possibility of using the process to encourage a more widespread application of Mg based materials by industry was verified. The proposed methods and mechanisms, as well as the results of the joining parameters' influence on temperature development, joining mechanisms and mechanical performance of FHPP welded joints in commercial magnesium materials, provides an important pathway to further exploitation of scientific and technical fields of this new joining technique. Although joint features and joining mechanisms may vary slightly within different joining partners, owing to individual structural, thermo-physical and mechanical properties, the results obtained from this work can be extended to other combinations of lightweight alloys.

As summarised in Table 6.1, the establishment of the bonding mechanisms and their influences on microstructural and mechanical properties of similar and dissimilar welds was successfully achieved. The experimental methodology adopted at the onset of this work and the systematic approach, in which the scientific challenges of the subject matter have been addressed, also proved to be successful. The new and alternative joining technique developed, characterised and demonstrated in this work for magnesium materials, proved itself to be an interesting alternative for similar and dissimilar configurations. Furthermore, FHPP flexibility, short joining cycles, reduced process steps, simple machinery, due to the process robustness and possible robotic applications, suggest potential cost savings compared to the current state of the art. In addition, the absence of the need to develop new welding equipment, since friction welding machines are commercially available, and the possibility to adapt industrial machinery for FHPP make this new technology highly transferable for industrial applications.

Table 6.1: Summary of the work.

Base Plate / Reinforcement (Stud Material)					AE42	MRI230D	AZ91D-T6 ∅6mm/12mm Upsetting	AZ91D-T6 ∅8mm/10-20mm Upsetting
AZ91D-T6	Base Plate	Joint Quality	Process Stability		- +	+	+ +	+ +
			Metallurgical Characterization		Determined	Determined	Determined	Determined
					The consumable is not plasticized neither across the bore of the hole nor through the height of the cavity. The microstructure in the recrystallized zone is characterized by a complete fragmentation of the coarse Aluminium-Rare Earth eutectics.	The microstructure is dominated by equiaxed dynamically recrystallized grains combined with a complete degradation of the typical second phase Mg(Al,Ca) particles.	The consumable is fully plasticized across the bore of the hole and the thickness of the workpiece. Microstructure within the recrystallized zone is characterized by refined equiaxed grains with a complete rupture of the lamellae β-phase, which is re-precipitated along the grain boundaries.	
			Hardness		+ +	+ +	+	+
			Pull-Out		+ +	+ +	+ +	+ +
			Tensile		+ +	+ +	+ +	+ +
		Joint Performance	Creep Tests		-	+ +	N/E	- -
			Bolt Load Retention	Tension	N/E	+ +	N/E	N/E
				Compression	+	+ +	N/E	- -

7 SUGGESTIONS FOR FURTHER WORK

After the completion of this study, some points are recommended for further work.

– A supplementary study, focusing on creep properties and bolt load retention of joints reinforced with different materials, would provide further design information on joint durability and performance, which would help to accelerate the transition from laboratory to industrial scale.

– Further mechanical and metallurgical characterisation of welded joints by means of diverse analytical techniques, such as nanoidentation testing and TEM, would provide a better understanding of the joining mechanisms. Such characterisation would also be meaningful for precise characterisation of local mechanical behaviour and/or detailed investigation of microstructural zones. Changes to fine precipitates imposed by the welding process and their influence on the performance of the joint could be further understood.

– With the bonding mechanism in mind, a further development of the welding machine, incorporating a torque measurement system, would help the formulation of the FHPP process description based on energy input. With a torque measurement system integrated into the machine and using statistical methods, the quality of a joint could be monitored on-line as a further stage.

– Since the first approach involving the application of FHPP in Mg alloys has been initiated, an investigation of the joinability of high pressure die casting (HPDC) as well as of new advanced lightweight materials, such as MMCs would be very meaningful. Furthermore, the application of the proposed reinforcement method in real components, such as existing gearbox housings, would significantly increase the technical added value of the process.

8 REFERENCES

[1] MORDIKE B.L. and Ebert T., 2001, *"Magnesium: Properties, Applications and Potential"*, Materials Science and Engineering A302, pp.: 37-45.

[2] KAINER K.U. and von Buch F., 2003, *"The Current State of Technology and Potential for Further Development of Magnesium Applications"*, in Magnesium alloys and Technologies, WILEY-VCH Verlag GmbH & CO. KG aA, Weinheim, pp. 1-22.

[3] PARK S.H.C., Sato Y.S. and Kokawa H., 2003, *"Effect of Microtexture on Fracture Location in Friction Stir Welding of Mg alloy AZ61 During Tensile Test"*, in Scripta Materialia 49, pp.:161-166.

[4] EDGAR R.L., 2006, *"Global Overview on Demand and Applications for Magnesium Alloys"*, published in Proceedings of the 7th International Conference on Magnesium Alloys and Their Application, pp.: 3-8, 06-09 November, Dresden, Germany.

[5] JOHNSON R. and Threadgill P., 2003, *"Friction Stir Welding of Magnesium Alloys"*, TMS, Magnesium Technology 2003 – Edited by Howard I. Kaplan.

[6] FISCHERSWORRING-BUNK A., 2005, *„Das Neue BMW Aluminium-Magnesium-Verbundkurbelgehäuse",* DGM-Fortbildungsseminar, GKSS-Forschungszentrum, 22.-24. November.

[7] HOWARD-SMITH J., Teksid S.p.A., 2001, *"Magnesium – An Overview"*, Australian Journal of Mining.

[8] AGHION E. and Eliezer D., 2004, *"Magnesium Alloys - Science, Technology and Applications"*, published by The Israeli Consortium for the Development of Magnesium Technology, Israel.

[9] PFISTER U., 2005, *„Schraubverbindungen und Schraubtechnologie in der Powertrain-Serienmontage"*, Bad Nauheim / Frankfurt, 7. bis 9. März.

[10] LEITNER H., Godor I., Eichlseder W. und Hinteregger, 2005, *„Betriebsfeste Auslegung von Schraubverbindung im Leichtmetallguss",* Bad Nauheim 17. 18. November.

[11] DITZE A. and Scharf C., 2003, *"Recycling of Magnesium Alloys"*, in Magnesium alloys and Technologies, WILEY-VCH Verlag GmbH & CO. KG aA, Weinheim, pp. 254-278.

[12] JASCHIK C., Haferkamp H. and Niemeyer M., 2000, *"New Magnesium Alloys"*, in Proceedings of the conference Magnesium alloys and their applications, 26-28 September, München, pp. 41-46.

[13] CHUKO W.L. and Gould J.E., 2002, *"Magnesium Joining for Automotive Applications"*, EWI Research Report No. MR0217, Edison Welding Institute, Columbus, OH.

[14] ASM Specialty Handbook: Magnesium and Magnesium alloys; Ed. M.M. Avedesian ASM International (1999).

[15] http://www.efunda.com.

[16] http://www.matweb.com.

[17] KING J.F., 2000, *"Development of Practical High Temperature Magnesium Casting Alloys"*, in Proceedings of the conference Magnesium alloys and their applications, 26-28 September, München, pp. 14-22.

[18] V. BUCH F., Schumann S., Aghion E., Bronfin B. and Mordike B.L., 2000, *"Development of a Low-cost, Temperature and Creep Resistant Magnesium Die-Casting Alloy"*, in Proceedings of the conference Magnesium alloys and their applications, 26-28 September, München, pp. 23-28.

[19] PETTERSEN, K., Westengen, H., Skar, J.I., Videm, M. and Wie, L.Y., 2000, *"Creep Resistance Mg Alloy Development"*, in Proceedings of the conference Magnesium alloys and their applications, 26-28 September, München, pp. 29-34.
[20] MORDIKE, B.L., von Buch, F., 2000, *"Development of High Temperature Creep Resistant Alloy"*, in Proceedings of the conference Magnesium alloys and their applications, 26-28 September, München, pp. 35-40.
[21] V. BUCH F. and Mordike B.L., 2000, *"High-Temperature Properties of Magnesium Alloys"*, in Proceedings of the conference Magnesium alloys and their applications, 26-28 September, München, pp. 106-129.
[22] CELOTTO, S., 2000, *"TEM Study of Continuous Precipitation in Mg-9 Wt% Al-1 Wt% Zn Alloy"*, in Acta Materialia 48(2000), pp. 1775-1787.
[23] CHUNG, Y. and Shin, K.S., 2005, *"Effects of Alloying Elements on the Microstructure and High-Temperature Mechanical Properties of Mg-Al Alloys"*, in Magnesium Technology.
[24] SCHAFFER, P.L., Lee, Y.C. and Dahle, A.K., 2001, *"The Effect of Aluminium Content and Grain Refinement on Porosity Formation in Mg-Al Alloys"*, Magnesium Technology – TMS 2001.
[25] NAVE, M.D., Dahle A.K. and StJohn, D.H., 2000, *"The Role of Zinc in the Eutetic Solidification of Magnesium-Aluminium-Zinc Alloys"*, in Magnesium Technology – TMS 2000.
[26] WEI L.Y., Dunlop G.L. and Westengen H., 1996, *"Development of microstructure in cast Mg-Al-Rare Earth Alloys"*, in Materials science and technology, Vol. 12, September, pp. 741-750.
[27] DIERINGA H., 2006, *"Vergleichende Untersuchungen zum Zug- und Druckkriechverhalten der verstärkten und unverstärkten Magnesiumlegierung AE42"*, genehmigte Dissertation, Technische Universität Hamburg-Harburg.
[28] DIERINGA H., Bowles A., Hort N. and Kainer K.U., 2005, *"Microstructural Development in Tension and Compression Creep of Magnesium Alloy AE42"*, in Materials Science Forum, Vol. 482, pp. 271-274, Switzerland.
[29] POWELL, B.R., V. Rezhets, M.P. Balogh and R.A. Waldo, 2002, *"Microstructure and Creep Behaviour in AE42 Magnesium Die-Casting Alloy"*, JOM August 2002, p. 34-38.
[30] *"MRI 153 – New Magnesium Alloy for high Temperature Applications"*, DSM - Dead Sea Magnesium Prospect.
[31] *"Magnesium Alloys for high Temperature Applications"*, DSM - Dead Sea Magnesium Prospect.
[32] EBEL-WOLF B., Walther F. and Eifler D., 2006, *"Microstructure based characterization of the cyclic deformation behaviour of the magnesium die-cast Alloys MRI153M and MRI230D"*, in Proceedings of the 7th International Conference on Magnesium Alloys and Their Applications, 06-09 November, Dresden, Germany.
[33] http://www.lam.mw.tu-muenchen.de/Lehre/Download/WfMuA/5_Magnesium.pdf.
[34] WESTPHAL, K., Mulherkar, T. and Scheiding, W., 2005, *"Aluminium Fasteners for Magnesium Components"*, Fastener Technological International, August.
[35] WESTPHAL, K., 2003, *"Verschraubung von Magnesiumkomponenten"*, in Beitrag zur IIR Fachkonferenz „Magnesium im Fahrzeugbau", April, Marriot-Hotel Sindelfingen.

[36] AUNE, T.K. and Ruden, T., 1992, *"High Temperature Properties of Mg die Casting Alloys"*, SAE Technical paper, 920070.

[37] SHEN G. and XU S., 2007, *"Finite Element Simulation of Bolted Joints and Magnesium Bolt-Load Retention Behaviour"*, SAE Technical paper, 2007-01-1032.

[38] XU S., Sohn, K.Y., Dewhirst, D. and Allison, J.E., 2000, *"Finite Element Modeling of Bolt Load Retention of Die –Cast Magnesium"*, SAE Technical paper, 2000-01-1121.

[39] BERTILSSON, I., Fischersworring-Bunk, A., Marx, T., Bergman, F., Kunst, M., Thiele, J. and Tan, Z., 2006, *"Aluminium Bolts in Magnesium Engine Components"*, Proceedings of the 7th International Conference on Magnesium Alloys and Their Applications, 06-09 November, Dresden, Germany.

[40] OKECHUKWU, A., 2006, *"Investigation of Bolt Load Retention Behaviour of Mg-Alloys"*, Masters Thesis - Technische Universität Hamburg Harburg (TUHH), Hamburg.

[41] CHEN, F.C., Jones, J.W., McGinn, T.A., Kearns, J.E., Nielsen, A.J. and Allison, J.E., 1997, *"Bolt-Load Retention and Creep of Die-Cast Magnesium Alloys"*, SAE Technical paper, 970325.

[42] SOHN, K.Y., Jones, W., Berkmortel, J., Hu, H. and Allison, J.E., 2000, *"Creep and Bolt Load Retention Behaviour of die cast Magnesium Alloys for High Temperature Applications"*, SAE Technical paper, 2000-01-1120.

[43] LUO, A. and Shinoda, T., 1998, *"A new magnesium alloy for automotive powertrain applications"*, SAE Technical paper, 980086.

[44] MORENO I.P., Sohn K.Y. and Jones J.W., 2001, *"Bolt-Load Retention Behaviour of a Die Cast Magnesium Rare Earth Alloy"*, SAE Technical paper, 2001-01-0425.

[45] SOHN, K.Y., Yurko, J.A., Jones, J.W., Kearns, J.E. and Allison, J.E., 1998, *"Bolt-Load Retention Behaviour of Die-Cast AZ91D and AE42 Magnesium"*, SAE Technical paper, 980090.

[46] DRUSCHITZ A.P. and Showalter E.R., 2003, *"Bolt Load Compressive Stress Retention Testing of Magnesium Alloys"*, SAE Technical paper, 2003-01-0187, SAE World Congress, Detroit, Michigan, March 3-6.

[47] CROSSLAND, B., 1971, *"Friction Welding - Recommended Practices for Friction Welding"*. in Contemporary Physics, 12(6), pp. 559 - 574.

[48] KLOPSTOCK, H. and Neelands, A.R., 1941, *"An improved Method of Joining or Welding Metals"*, Patent nº. GB - 00572789.

[49] NCT Friction Welding website: http://www.nctfrictionwelding.com/process.php, 2005.

[50] VILL, V.I., 1962, "Friction Welding of Metals", Reinhold Publishing Corporation, American Welding Society, Inc, New York.

[51] GREWE, K., 1997, "The Friction Welding Takes on New Applications", Welding Journal, September, pp. 39-40.

[52] http://pdf.directindustry.com/pdf/thompson-friction-welding/friction-welding-applications-26030-8501.html

[53] http://www.mtiwelding.com/friction-welding-applications.cfm

[54] HAZLET, T.H., 1981, "Fundamentals of Friction Welding", Source Book on Innovative Welding Processes, American Society for Metals, pp. 11-36.

[55] ELMER, J. W. and Kautz, D., 1993, “Fundamentals of Friction Welding”, in Metal Handbook, vol. 6, American Society for Metals, pp. 150-155.

[56] BOWDEN, F.P. and Tabor, D., 1954, “The friction and Lubrication of the Solids”, Part 1, Oxford University Press.

[57] GODDARD, J. and Wilman, H., 1962, “A theory of Friction and Wear during the Abrasion of Metals”, Wear, Vol. 5.

[58] AWS Welding Handbook, 8th ed., Vol.2, American Welding Society, 1991, p. 739-763.

[59] Recommended Practices for Friction welding, ANSI/AWS C6.1-89, American Welding Society, 1989.

[60] ELLIS, C. R. G., 1972, *"Continuous Drive Friction Welding of Mild Steel"*, in Welding Journal: pp. 183s - 197s.

[61] LUCAS, W., 1973 *"Process Parameters and Friction Welds"*, Metal Construction and British Welding Journal - 5, pp.: 293-297.

[62] BÖHME, D. and Hermann, F.-D., 1992, "DVS - Handbuch der Schweißverfahren Teil II: Autogenverfahren - Thermisches Schneiden - Elektronenstrahl- und Laserstrahlschweißen, Reib-, Ultraschall- und Diffusionsschweißen" DVS Verlag, Fachbuchreihe Schweißtechnik.

[63] SPINDLER, D. E., 1994, "What Industry Needs to Know about Friction Welding", in Welding Journal, March, pp.: 37-42.

[64] DENNIN, G., 1979, *"Optimierung von Einstellwerten für das Reibschweißen mit kontinuierlichem Antrieb"*, in Schweißen und Schneiden, 31(7), pp. 283-289.

[65] MAZAC, K., 2000, *"Parameterfindung und Parameterüberwachung beim Reibschweißen"*, in 10. Erfahrungsaustausch Reibschweißen, SLV München, Germany.

[66] BETHLEHEM, W., 1984 (heft 01), "Geeignet zur Prozessüberwachung: Störungen des Momentverlaufes lassen fehlerhafte Reibschweißungen erkennen", in Schweißen und Schneiden, 36(01): pp. 23-28.

[67] DUFFIN F. D. and BAHRANI A.S., 1973, *"Friction welding of mild steel"*, Metal Construction and British Welding Journal, 05(04): pp. 125 - 132.

[68] SERGIN, S.A. and SABABTSEV, V.P., 1977, "The Distribution of Temperature along the length of a bar in relation to the speed of rotation in the friction welding of steels", in Welding Production (01): pp. 37-39.

[69] VOINOV, V.G., 1968, *"Mechanism of Joint Formation in Friction Welding"*, in Welding Production, 15: pp. 8 - 13.

[70] EICHHORN F. and SCHAEFER R., 1968, *"Beitrag zu den Vorgängen an der Verbindungsstelle beim konventionellen Reibschweißen von Stahl",* in Schweißen und Schneiden, 20(11): pp. 563-570.

[71] HOFMANN, W. and Thome, L., 1965, *"Einige Einflußgrößen auf das Reibungsschweißen von Stahl und von Aluminium"*, in Schweißen und Schneiden, 17(05): pp. 194 - 199.

[72] DREWS P. and Schmidt J., 1978, *"Steuerung des Reibschweißvorganges zum Erzielen eines vorbestimmten Endmaßes"*, in Zeitschrift für industrielle Fertigung, Springer Verlag, 68: pp. 387-393.

[73] PINHEIRO, G.A., Pankiewicz, C.G., dos Santos, J.F. and Kainer K.U., 2006, *"Rotational Friction Welding of a high Creep Resistance Magnesium Alloy"*, in Proceedings of the 7th International Conference on Magnesium Alloys and Their Applications, Dresden, November.
[74] PETRUCCI L. G., 1978, *"Temperature distribution in friction welding"*, in General Engineer, July and August, pp. 178-184.
[75] SUGA Y., Miyakawa S. and Ogawa K., 1999, *"Estimation of temperature distribution in the friction weld of carbon steel by the finite element method"*, in Welding International, 13(4): pp. 262 - 269.
[76] TUMULURU M.D., 1984, *"A Parametric Study of Inertia Friction Welding for Low Alloy Steel Pipes"*, Welding Journal, Welding Research Supplement. September: pp. 289s - 294s.
[77] PINHEIRO, G.A., Pankiewicz, C.G., Weis Olea, C.A., Dos Santos, J.F. and Kainer, K.U., 2007, *"Effects of Welding Conditions on Microstructural Transformations and Mechanical Properties in AE42HP Friction Welded Joints"*, presented and published on the III Workshop on Recent Advances in Friction Welding and Allied Processes, 3/4 July 2007, Dubrovnik, Croatia.
[78] MEYER A., *"Friction Hydro Pillar Processing - Bonding Mechanism and Properties"*, Fakultät für Maschinenbau und Eletrotechnik der Technischen Universität Carolo-Wilhelmina zu Braunschweig, 2003.
[79] ASM, 1993, "Metals Handbook". Vol. 6. American Society for Metals.
[80] NENTWIG, A.W.E., W. Welt et al, 1991, *"Analyse des Reibschweißablaufes beim Rotationsreibschweißen von metallischen Werkstoffen gleicher und unterschiedlicher Warmefestigkeit"*, DVS Bericht: 35-44.
[81] NEUMANN, A. and Schober, D., 1991, *"Reibschweißen von Metallen"*, Verlag Technik GmbH, Berlin.
[82] PAULY, D., 1999, *"Process development on an experimental Friction Hydro Pillar Processing system"*, Arbeitsbereich Schiffbau, Diplomarbeit - Technische Universität Hamburg-Harburg, Hamburg.
[83] ADAM, P., 1979, *"Ablauf der Verbindungsbildung beim Schwungradschweißen von hochwarmfesten Legierungen – Temperaturverlauf und Wulstbildung"*, in Schweißen und Schneiden, 31(7), pp. 279-283.
[84] KREYE, H. and Wittkamp I., 1977, *"Gefügeänderung und Bindemechanismus beim Reibschweißen"*. in Zeitschrift für Metallkunde, 68(4): p. 253-259.
[85] WICHELHAUS G., 1974, *"Messen der Stoßflächentemperatur beim Reibschweißen"*, in Schweißen und Schneiden, 26(3): pp. 97-100.
[86] BETHLEHEM, W., 1984 (heft 10), *"Schmelzpunkt wurde nicht erreicht: Untersuchungen des Gefüges beim Reibschweißen"*. in Schweißen und Schneiden, 36(10): pp. 479-483.
[87] KREYE, H., 1982, *"Verbindungsbildung beim Reibschweißen"*, in 2. Aachener Reibschweiß-Kolloquium, 10 – 11 March, Aachen.
[88] CHENG, C.J., 1962, "Transient temperature distribution during friction welding of two similar materials in tubular form", in Welding Research Supplement, pp. 542s-550s.
[89] SLUZALEC, A., 1990, *"Thermal effects in Friction Welding"*, International Journal of Mechanical Sciences, 32(06): pp. 467 - 478.

[90] BALASUBRAMANIAN, V., Li Y, Crompton, T., Katsube, A.S. and Soboyejo, W., 1999, *"A New Friction Law for the Modelling of Continuous Drive Friction Welding: Applications to 1045 Steel Welds"* Materials and Manufacturing Processes, Vol. 14, nº 06, pp. 845 - 860.
[91] NICHOLAS, E.D. and Ellis, C.R.G., 1969, *"Friction Welding of mild steel - Effect of deceleration time"*, The Welding Institute Report R/RB/P40/69.
[92] NICHOLAS, E.D. and Ellis, C.R.G., 1968, *"Equilibrium and deceleration characteristics of mild steel friction welds"*, The Welding Institute Report P/31/68.
[93] DUFFIN F.D. and Crossland B., 1970, *"Friction welding with sudden release of the fixed component"*, Proc. of Conf. on Advances in Welding Processes, Welding Institute, pp. 25.
[94] THOMAS, W., Nicholas, D., Jones, S.B., Lilly, R.H., Dawes, C.J. and Dolby, R.E., 1992, *"Friction Forming"*, TWI Cambridge, Patent N°.: EP 0 602 072 B1.
[95] THOMAS, W. and D. Nicholas, 1993, *"On trial - a new thick plate joining technique"*, in TWI Connect, April.
[96] THOMAS W.M. and Nicholas D., 1992, *"Leading Edge: Friction Hydro Pillar Processing (FHPP)"*. in TWI Connect, June 1992.
[97] NICHOLAS E.D., 1995, *"Friction Hydro Pillar Processing"*. in 11th Annual North American Welding Research Conference - Advances in Welding Technology, 07 - 09 November, 1995.
[98] PAULY, D., 1999, *"Process development on an experimental Friction Hydro Pillar Processing system"*, Arbeitsbereich Schiffbau, Diplomarbeit - Technische Universität Hamburg-Harburg, Hamburg.
[99] MEYER A., Pauly D., Santos J.F., Pinheiro G., Roos A., Gibson D. and Blakemore G.R., 2001, *"Considerations on Robotic Friction Stitch Welding for the Repair of Marine Structures"*. in 20th International Conference on Offshore Mechanics and Arctic Engineering. June 3-8, 2001, Rio de Janeiro, Brazil: The American Society of Mechanical Engineers.
[100] GIBSON D., Meyer A., Vennemann O., Santos J.F. and Blakemore G.R., 2001, *"Engineering Applications of Friction Stitch Welding"*. in 20th International Conference on Offshore Mechanics and Arctic Engineering, June 3-8, Rio de Janeiro, Brazil: The American Society of Mechanical Engineers.
[101] THOMAS, W. and Nicholas D., 1997, *"The need for gas shielding - Positive advantages for two friction processes"*, in TWI Bulletin, Sep/Oct 1997: pp. 84 - 88.
[102] PINHEIRO, G.A., 2007, „Ein neues Fügeverfahren zur Erhöhung der Gewindetragfähigkeit im modernen Automobilleichtbau“, InnoCarBody, Bad Nauheim / Frankfurt - 2007.
[103] THOMAS, W.M. and Nicholas, E.D., 1996, *"Emerging friction joining technology for stainless steel and aluminium applications"*, Presented at 'Productivity beyond 2000': IIW Asian Pacific Welding Congress, Auckland, New Zealand, February 1996.
[104] THOMAS, W.M., Nicholas, E.D. and Kallee, S.W., 2001, *"Friction based technologies for joining and processing"*, present at TMS Friction Stir Welding and Processing Conference, November 2001, Indianapolis.

[105] FRED DELANY, William Lucas, Wayne Thomas, Dave Howse, David Abson, Steve Mulligan, Colin Bird, 2005, *"Advanced joining processes for repair in nuclear power plants"*, presented at 2005 International Forum on Welding Technologies in Energy Engineering, September 21 – 23, Shanghai, China.

[106] SAYEE RAGHUNATHAN, 2006, *"Novel technologies for repair and refurbishment"*, presented at National Welding Seminar (NWS 2006) 24 - 26 November 2006, Chennai, India.

[107] HOWSE D., Lucas W., and Thomas W., 2002, *"Novel joining techniques for repair in the power generation industry"*, presented at EPRI Welding and Repair Technology for Power Plants Conference, Point Clear, Alabama, USA, 26-28 June.

[108] KALLEE S. and Nicholas D., 1999, *"Friction and Forge Welding Processes for the Automotive Industry"*, presented at International Body Engineering Conference, Detroit, USA, 28-30 September, (Paper No. 99-IBECC-13).

[109] ANDREWS, R.E. and Mitchell, J.S., 1990, "Underwater Repair by Friction Stitch Welding", Metals and Materials - Marine Technology, Dezember, pp. 796 - 797.

[110] BEAMISH, K., 2003, *"Friction taper plug welding of 10mm AA6082-T6"*, TWI internal report 768/2003.

[111] BRONSERT M., 2005, *"Prozessentwicklung und Bestimmung der Eigenschaften einer FHPP-Überlappverbindung"*, Diplomarbeit - Vorgelegt der Technischen Universität Hamburg-Harburg im Hochschulübergreifenden Studiengang Schiffbau, Oktober.

[112] BOWLES A., Hort N., Meyer A., dos Santos J.F. and Kainer K.U., 2003, *"Welding of Magnesium: Microstructural Characterization"*, in the 6th International Conference on Magnesium and their Applications, September 2003, 917-923.

[113] OGAWA K., Yamaguchi H., Ochi H., Sawai T., Suga Y. and Oki Y., 2003, *"Friction Welding of AZ31 Magnesium Alloy"*, Welding International, 2003, 17 (11), pp.: 879-885.

[114] KATO K. and Tokisue H., 1994, *"Friction Welding of Magnesium Alloys"*, Welding International, 08(6), 452-457.

[115] DRAUGELATES U., Schram A. und Kettler C., 1998, *"Laserstrahlschweißen und Reibschweißen von Magnesiumlegierungen"*, DVS-Ber., Band 194, Schweißen und Schneiden 98, Hamburg 9/1998.

[116] DRAUGELATES U., Schram A., Bouaifi B. and Kettler C., 1998, Institute of Welding and Machining (ISAF), TU-Clausthal, Germany.

[117] KATO K., Okuta M., Tokisue H. and Onoda T., 1989, Weldability of Magnesium Alloys by Friction, Lab. Eng., Shibaura - Inst. Technol., 4, pp.: 23-38.

[118] DRAUGELATES U. and Schram A., 2000, *"Prozessführung und Gestaltung für das Fügen komplexer Bauteile"*, Institut für Schweißtechnik und Trennende Fertigungsverfahren, Allgemeine Angaben zum Teilprojekt B3, TU-Clausthal, Germany.

[119] KATO K. and Tokisue H., 2004, *"Dissimilar friction welding of aluminium alloys to other materials"*, in Welding International, 2004, 18 (11), pp.: 861-867.

[120] KOHN G., Antonsson S. and Munitz A., 1999, *"Friction stir welding magnesium alloys"*, in TMS Annual Meeting and Exhibition Automotive Alloys.

[121] SATO Y, Hwan S., Michiuchi M., Kokawa H., 2004, *"Constitutional Liquation During Dissimilar Friction Stir Welding of Al and Mg Alloys"*, Scripta Materialia 50 (2004) 1233-1236.
[122] STERN A., Munitz A. and Kohn G., 2003, *"Application of Welding Technologies for Joining of Mg Alloys: Microstructure and Mechanical Properties,* Magnesium Technology 2003, TMS (The Minerals, Metals and Materials Society).
[123] SOMASEKHARAN A.C. and Murr L.E., 2004, *"Microstructures in Friction-Stir Welded Dissimilar Magnesium Alloys and Magnesium Alloys to 6060-T6 Aluminium Alloy"*, Materials Characterization 52 (2004) pp.:49-64.
[124] XUNHONG W. and Kuaishe W., 2006, *"Microstructure and Properties of Friction Stir Butt-Welded AZ31 Magnesium Alloy"*, Materials Science and Engineering A 431 (2006) 114-117.
[125] www.twi.co.uk/j32k/protected/band_10/bprfws02.html
[126] PINHEIRO, G.A., 2006, *"Friction Hydro Pillar Processing of Lightweight Alloys: Bonding Mechanisms and Joint Properties"*, Summer School WM, Institute for Materials Research, GKSS-Forschungszentrum, 27.-29 September.
[127] PINHEIRO, G.A., 2005, *DAAD-CNPq Annual Report Nr. 1,* Brazil-Germany Bilateral Scientific Cooperation.
[128] LIMA, D.B.A., 2006, *"Similar and Dissimilar Rotational Friction Welding of Magnesium AZ91D-T6 Magnesium alloy: Bonding Mechanisms and Joint Properties"*, Diplomarbeit - GKSS Internal Report.
[129] PINHEIRO, G.A., Olea, C.A., dos Santos, J.F. and Kainer, K.U., 2007, *"Microstructural and mechanical behaviour of friction welds in a high creep resistance magnesium alloy"*, published in Advanced Engineering Materials, Vol.9, Issue 9, September, pp. 757-763.
[130] DIN 65582 – Wärmebehandlung von Gußstücken aus Aluminium- und Magnesiumlegierungen (1990); pp. 1-8.
[131] ASTM-B-000661-03 – Standard Practice for Heat Treatment of Magnesium Alloys (2005); pp. 1-6.
[132] ASTM E 3-95, 2000, *"Standard Practice for Preparation of Metallographic Specimens"*, Annual Book of ASTM Standards Vol 03.03, pp. 1-8.
[133] ASTM E 340-95, 2000, *"Standard Test Method for Macroetching Metals and Alloys"*, Annual Book of ASTM Standards Vol 03.03, pp. 385-395.
[134] ASTM E 112-96, 2000, *"Standard Test Method for Determining Average Grain Size"*, Annual Book of ASTM Standards Vol 03.03, pp. 240-263.
[135] DIN EN ISO 6507, 2005, *"Metallische Werkstoffe: Härteprüfung nach Vickers"*, DIN – Deutsches Institut für Normung e.V.
[136] DIN EN 1043-2, 1996, *"Härteprüfung Teil 2: Mikrohärteprüfung an Schweißverbindungen"*. European Committee for Standardization.
[137] DOLLAR A. and Meade P., 2003, *"Modelling Pull-out tests of Dental Implants"*, Biomedical Engineering – Applications, basis and communications, Vol. 15, N°4, August.
[138] DIN 50125, 2003, *"Prüfung metallischer Werkstoffe - Zugproben"*, DIN - Deutsches Institut für Normung e.V.
[139] DIN EN 10002, 1991, *"Tensile testing of metallic materials"*, DIN - Deutsches Institut für Normung e.V., Berlin.

[140] BAKKE P., Westengen H., Sannes S. and Albright D., 2004, *"Powertrain Components – Opportunities for the Die Cast AE Family of Alloys"*, SAE Technical Paper, 2004-01-0655.

[141] XUMING S., Sohn K.Y., Dewhirst D. and Allison J.E., 2000, *"Finite Element Modeling of Bolt Load Retention of Die-Cast Magnesium"*, SAE Technical paper, 2000-01-1121.

[142] XU S., Williams G., Shen G., Bouchard R., Sahoo M. and Osborne R., 2006, *"Bolt-Load Retention Testing of Magnesium Alloys for Automotive Applications"*, SAE Technical paper, 2006-01-0072.

[143] DIN EN 20273, 1992, *"Mechanische Verbindungselemente; Durchgangslöcher für Schrauben (ISO 273:1979)"*, DIN - Deutsches Institut für Normung e. V., Berlin.

[144] ASTM E 328-86, 2002, *"Standard Test Method for Stress Relaxation for Materials and Structures"*, Annual Book of ASTM Standards Vol 03.01, pp. 379-390.

[145] BICKFORD J.H., 1995, *"An Introduction to the Design and Behaviour of Bolted Joints"*, 3rd Ed., New York, Marcel Dekker, Inc.

[146] DIN EN ISO 7089, 2000, *"Flache Scheiben - Normale Reihe, Produktklasse A (ISO 7089:2000); Deutsche Fassung EN ISO 7089:2000"*, DIN - Deutsches Institut für Normung e. V., Berlin.

[147] DIN EN ISO 4014 (DIN 931), 2001, *" Sechskantschrauben mit Schaft - Produktklassen A und B (ISO 4014:1999); Deutsche Fassung EN ISO 4014"*, DIN - Deutsches Institut für Normung e. V., Berlin.

[148] Krautkramer BoltMike III catalogue, GE Inspection Technologies.

[149] ASTM E1685-00, 2006, *"Standard Practice for Measuring the Change in Length of Fasteners Using the Ultrasonic Pulse-Echo Technique"*, ASTM International.

[150] HUANG, Y., Hort, N., Dieringa, H. and Kainer, K.U., 2004, Advanced Engineering Materials, 6(11), 883-888.

[151] DIERINGA, H., Hort, N. and K.U. Kainer, 2003, Kompozyty/ Composites, 3, 275.

[152] AWS Welding Handbook, 8th ed., Vol.2, American Welding Society, 1991, p. 739-763.

[153] AMANCIO, S.T., 2007, *"Friction Riveting: Development and Analysis of a new Joining Technique for Polymer-Metal Multimaterials structures"*, vorgelegte Dissertation, Technische Universität Hamburg-Harburg.

[154] SILVA, A.M., 2006, *"An Investigation on the Structure/Property Relationships of Solid State Welding Processes in a Titanium Matrix Composite Alloy (Ti6Al4V + 10wt.% of TiC)"*, Dissertation, Fachbereich für Ingenieurwissenschaften, Abteilung Maschinenbau, der Universität Duisburg-Essen.

[155] ZETTLER, R., Lomolino, S., dos Santos, J.F., Donath, T., Beckmann, F. Lippman, T. And Lohwasser, D., 2006, *"A Study on Material Flow in FSW of AA2024-T351 and AA6056-T4 alloys"*, GKSS Internal Report.

[156] SAKKINEN D.J., "Physical Metallurgy of Magnesium Die Cast Alloys", The Dow Chemical company.

[157] BAKKE, P., Bowles, A.L. and Westengen, H., 2006, 7th International Conference on Magnesium Alloys and their Applications, p. 53-66.

[158] FUTAMATA, M. and Fuji A., 1990, *"Friction welding of titanium and SUS304L austenitic stainless steel"*, in Welding International, 4(10), p. 23-28.

[159] BOWDEN F.P. and Ridler K.E., 1954, *"Physical Properties of Surfaces III – The surface temperature of solids sliding"*, Proceedings of the Royal Society of London, Series A, 223(1152), April.
[160] BOWDEN F.P. and Thomas P.H., 1954, *"The Surface Temperature of Sliding Solids"*, Proceedings of the Royal Society of London, Series A, Vol. 223(1152), April, pp. 29-40.
[161] GERLICH, A., Su, P. and North, T., 2005, *"Friction Stir Spot Welding of Mg-Alloys for Automotive Applications"*, Magnesium Technology 2005, TMS, p. 383-388.
[162] GERLICH, A., Su, P. and North, T., 2005, *"Peak Temperatures and Microstructures in Al and Mg Alloy FSW Spot Welds"*, in Welding and Joining 2005, Vol. 10, N°6, p. 647-652.
[163] SATO, Y.S., Hwan, S., Park, C., Muchiuchi, M. and Kokawa, H., 2004, *"Constitutional Liquation During Similar Friction Stir Welding of Al and Mg Alloys"*, Scripta Materialia, 9, p. 1233-1236.
[164] NORTH, T.H., Bendzsak, G.J., Gerlich, A., Su, P. and Cingara, G., 2007, *"Transient Local Melting in AL7075-T6 Friction Stir Spot Welds"*, in Materials Science Forum, Vols. 539-543, p. 3826-3831.
[165] NORTH, T.H., Bendzsak, G.J., Gerlich, A., Su, P. and Maldonado C., 2005, *"Understanding Friction Welding"*, IURS, Beijing, China.
[166] NORTH, T.H., Bendzsak, and C.B. Smith, 2000, *"Material Properties Relevant to 3D FSW Modelling"*, Proc. 2nd International Conference on Friction Welding, TWI, Gothenburg, 26-28 June.
[167] CAMPBELL J., 1997, *"Castings"*, Butterworth-Heinemann, 261-262, Oxford, UK.
[168] http://www.meridian-mag.com/jp/magnesium/datasheet.pdf
[169] http://www.thermocoax.com/9_Temperature_sensors/E196-0_Thermocouple_Type_K.pdf
[170] JÜTTNER, S., 1999, "Untersuchungen zum Schutzgasschweißen von Magnesiumlegierungen für Konstruktionsbauteile im Automobilbau", Dissertation, Fakultät für Maschinenbau und Elektrotechnik der Technischen Universität Carolo-Wilhelmina zu Braunschweig.
[171] SOMASEKHARAN, A.C. and Murr, L.E., 2004, *"Microstructures in Friction-Stir Welded Dissimilar Magnesium Alloys and Magnesium Alloys to 6061-T6 Aluminium Alloys"*, Materials Characterization, pp.: 49-64.
[172] XUNHONG, W. and Kuaishe W., 2006, *"Microstructure and Properties of Friction Stir Butt Welded AZ-31 Magnesium Alloy"*, Materials Science and Engineering A 431, pp.: 114-117.
[173] JOHNSON, R. and Threadgill, P., 2003, *"Friction Stir Welding of Magnesium Alloys"*, TMS, Magnesium Technology 2003 – Edited by Howard I. Kaplan.
[174] VDI2230, 2003, *"Systematic Calculation of high duty bolted joints – Joints with one cylindrical bolt"*, VDI-Handbuch Konstruktion, Gesellschaft Entwicklung Konstruktion Vertrieb, Düsseldorf.
[175] DURANDET, Y., Song. W., Cordini, P., Brandt, M. and Ostendorf, A., 2006, *"Effects of Strain Rate and Filler Alloy on the Properties of Laser Welded AZ31 Alloy Sheet"*, published in Proceedings of the 7th International Conference on Magnesium Alloys and Their Application, pp.: 871-876, 06-09 November, Dresden, Germany.
[176] BAI J., Sun Y., Xue F., Qiang J. And Zhu T., 2007, *"Effect of Al Contents on Microstructures, Tensile and Creep Properties of Mg-Al-Sr-Ca Alloy"*, Journal of alloys and Compounds, 437, pp. 247-253.
[177] *"Magnesium Alloys for high Temperature Applications"*, DSM - Dead Sea Magnesium Prospect.

[178] HIRAI K., Somekawa H., Takigawa Y. and Higashi K., 2005, *"Effects of Ca and Sr Addition on Mechanical Properties of a Cast AZ91 Magnesium Alloy at Room and Elevated Temperature"*, Materials and Engineering A 403, pp. 276-280.

[179] GUO, J.H., Chen, L.Q., Xu, Y.B. and Lian, F.Z., 2007, *"Investigation of the Compressive Creep Behaviour of AZ91D Magnesium Alloy"*, Materials and Engineering A 443, pp.: 66-70.

[180] ZHANG, J., Guo, Z.X., Pan, F., Li, Z. and Luo, X., 2007, *"Effect of Composition on the Microstructure and Mechanical Properties of Mg-Zn-Al Alloys"*, Materials Science and Engineering A 456, pp.: 43-51.

[181] SKLENICKA, V., Svoboda, M., Pahutova, M., Kucharova, K. and Langdon, T.G., 2001, *"Microstructural Processes in Creep of an AZ91 Magnesium-Based Composite and its Matrix Alloy"*, Materials and Engineering A319-321, pp.: 741-745.

[182] STJOHN, D., Qian, M., Easton, M.A., Cao, P. and Hildebrand, Z., 2005, *"Grain Refinement of Magnesium Alloys"*, Metallurgical and Materials Transactions A, Volume 36, number 7, Juli.